Advances in Science, Technology & Innovation
IEREK Interdisciplinary Series for Sustainable Development

Zeynal Abiddin Ergüler · Riheb Hadji · Helder I. Chaminé · Jesús Rodrigo-Comino · Amjad Kallel · Broder Merkel · Mehdi Eshagh · Haroun Chenchouni · Stefan Grab · Murat Karakus · Sami Khomsi · Jasper Knight · Mourad Bezzeghoud · Maurizio Barbieri · Sandeep Panda · Ali Cemal Benim · Hesham El-Askary *Editors*

Selected Studies in Geotechnics, Geo-informatics and Remote Sensing

Proceedings of the 3rd Conference of the Arabian Journal of Geosciences (CAJG-3)

IEREK RESEARCH & KNOWLEDGE ENRICHMENT

Springer

Advances in Science, Technology & Innovation

IEREK Interdisciplinary Series for Sustainable Development

Advances in Science, Technology & Innovation (ASTI) is a series of peer-reviewed books based on important emerging research that redefines the current disciplinary boundaries in science, technology and innovation (STI) in order to develop integrated concepts for sustainable development. It not only discusses the progress made towards securing more resources, allocating smarter solutions, and rebalancing the relationship between nature and people, but also provides in-depth insights from comprehensive research that addresses the **17 sustainable development goals (SDGs)** as set out by the UN for 2030.

The series draws on the best research papers from various IEREK and other international conferences to promote the creation and development of viable solutions for a **sustainable future and a positive societal** transformation with the help of integrated and innovative science-based approaches. Including interdisciplinary contributions, it presents innovative approaches and highlights how they can best support both economic and sustainable development, through better use of data, more effective institutions, and global, local and individual action, for the welfare of all societies.

The series particularly features conceptual and empirical contributions from various interrelated fields of science, technology and innovation, with an emphasis on digital transformation, that focus on providing practical solutions to **ensure food, water and energy security to achieve the SDGs.** It also presents new case studies offering concrete examples of how to resolve sustainable urbanization and environmental issues in different regions of the world.

The series is intended for professionals in research and teaching, consultancies and industry, and government and international organizations. Published in collaboration with IEREK, the Springer ASTI series will acquaint readers with essential new studies in STI for sustainable development.

ASTI series has now been accepted for Scopus (September 2020). All content published in this series will start appearing on the Scopus site in early 2021.

Zeynal Abiddin Ergüler · Riheb Hadji · Helder I. Chaminé · Jesús Rodrigo-Comino · Amjad Kallel · Broder Merkel · Mehdi Eshagh · Haroun Chenchouni · Stefan Grab · Murat Karakus · Sami Khomsi · Jasper Knight · Mourad Bezzeghoud · Maurizio Barbieri · Sandeep Panda · Ali Cemal Benim · Hesham El-Askary
Editors

Selected Studies in Geotechnics, Geo-informatics and Remote Sensing

Proceedings of the 3rd Conference of the Arabian Journal of Geosciences (CAJG-3)

Springer

ISSN 2522-8714 ISSN 2522-8722 (electronic)
Advances in Science, Technology & Innovation
ISBN 978-3-031-43758-8 ISBN 978-3-031-43759-5 (eBook)
https://doi.org/10.1007/978-3-031-43759-5

This Springer imprint is published by the registered company Springer Nature Switzerland AG
The registered company address is: Gewerbestrasse 11, 6330 Cham, Switzerland

Paper in this product is recyclable.

About the 2nd Springer Conference of the *Arabian Journal of Geosciences* (CAJG-3), Online November 2–5, 2020

The *Arabian Journal of Geosciences* (AJG) is a Springer journal publishing original articles on the full range of Earth sciences in partnership with the Saudi Society for Geosciences. The journal focuses on, but is not limited to, research themes which have regional significance for the Middle East, the Euro-Mediterranean, Africa, Asia, and some other regions of the world. The journal receives on average 3500 submissions a year and accepts around 800 papers for publication in its 24 annual issues (acceptance rate around 20%). It benefits from the participation of an editorial team of 15 topical chief editors and 100 international associate editors who generously help in evaluating and selecting the best papers.

In 2008, Prof. Abdullah Al-Amri, in close partnership with Springer, founded the *Arabian Journal of Geosciences (AJGS)*. In 2018, the journal celebrated its tenth anniversary. To mark the event, the founder and the editor-in-chief of the AJGS organized the 1st Conference of the *Arabian Journal of Geosciences* (CAJG) in close collaboration with Springer on November 12–15, 2018. The conference was an occasion to endorse the journal's long-held reputation and brought together 450 authors from 70 countries, who work in the wide-ranging fields of Earth sciences. The dynamic four-day conference in a stimulating environment in Hammamet, Tunisia, provided attendees with opportunities to share their latest unpublished findings and learn about the latest geosciences studies. The event also allowed attendees to meet and talk to the journal's editors and reviewers.

In a continuation of the successful 1st CAJG and 2nd CAJG, this year's conference aims to bring geoscientists from all over the world to present and discuss their most recent findings. The 3rd CAJG will continue to publish the newest findings in its proceedings and some special issues by Springer, with a clear mission to drive greater North–South (Europe-Africa) scientific cooperation and to open doors to new and enriching collaborations with geoscientists based in Asia and the Americas. Research studies from the wide-ranging fields of Earth sciences can be submitted for evaluation by the Conference Scientific Committee. In particular, the 3rd CAJG will devote a special session to studies focusing on unraveling the undiscovered oil and gas resources in the Mediterranean and North Africa. Many international experts will be invited to take part in the discussion, in particular we are expecting a massive participation of researchers from North Africa Research Group (NARG) of Manchester University (UK) and other scientists based in North Africa.

Conference Tracks

The scientific committee of the 3rd CAJG invites research papers on all cross-cutting themes of Earth sciences, with a main focus on the following 15 conference tracks:

- Track 1. Atmospheric Sciences, Meteorology, Climatology, Oceanography
- Track 2. Biogeochemistry, Geobiology, Geoecology, Geoagronomy
- Track 3. Earthquake Seismology and Geodesy
- Track 4. Environmental Earth Sciences
- Track 5. Exploration and Theoretical Geophysics, Seismic and Well-Logging Methods, Mathematical Geosciences
- Track 6. Geo-Informatics and Remote Sensing
- Track 7. Geochemistry, Mineralogy, Petrology, Volcanology
- Track 8. Geological Engineering, Geotechnical Engineering
- Track 9. Geomorphology, Geography, Soil Science, Glaciology, Geoarcheology, Geoheritage
- Track 10. Hydrology, Hydrogeology, Hydrochemistry
- Track 11. Marine Geosciences, Historical Geology, Paleoceanography, Paleoclimatology
- Track 12. Numerical and Analytical Methods in Mining Sciences and Geomechanics
- Track 13. Petroleum and Energy Engineering, Petroleum Geochemistry
- Track 14. Sedimentology, Stratigraphy, Paleontology, Geochronology
- Track 15. Structural Geology, Tectonics and Geodynamics, Petroleum Geology

About the Conference Steering Committee

General Chair

Abdullah Al-Amri

Founder and Editor-in-Chief,

Arabian Journal of Geosciences,
King Saud University, Saudi Arabia

Conference Supervisor

Nabil Khélifi

Senior Publishing Editor, MENA program,
Journal Publishing Manager,
Arabian Journal of Geosciences,
Springer, a part of Springer Nature, Germany

Advisory Co-chair

Walter D. Mooney

Guest of Editorial Board,
Arabian Journal of Geosciences,
United States Geological Survey Western Region, USA

Advisory Co-chair

Giovanni Bertotti,

Guest of Editorial Board,
Arabian Journal of Geosciences,
Geoscience and Engineering, Delft University of Technology, The Netherlands

Scientific Committee Co-chair

François Roure,

Chief Editor—Track 15,
Arabian Journal of Geosciences,
IFP—Energies Nouvelles, France

Scientific Committee Co-chair

Biswajeet Pradhan,

Chief Editor—Track 6,
Arabian Journal of Geosciences,
University of Technology Sydney, Australia

Local Organizing Co-chair

Mohamed Soussi,

Former Associate Editor,
Arabian Journal of Geosciences,
Tunis El Manar University, Tunis, Tunisia

Local Organizing Co-chair

Mounir Medhioub,

Guest of Editorial Board,
Arabian Journal of Geosciences,
University of Sfax, Sfax, Tunisia

Publications Co-chair

Beatriz Bádenas,
Chief Editor—Track 14,
Arabian Journal of Geosciences,
University of Zaragoza, Zaragoza, Spain

Publications Co-chair

Marina Rabineau,
Chief Editor—Track 11,
Arabian Journal of Geosciences,
University of Brest, Brest, France

Program Co-chair

Amjad Kallel,
Chief Editor—Track 4,
Arabian Journal of Geosciences,
ENIS, University of Sfax, Tunisia

Program Co-chair

Sami Khomsi,

Georesources Lab,
CERTE, University of Carthage
Tunis, Tunisia

Proceedings Editorial Manager

Mourad Amer,

Editor of Springer/IEREK ASTI Series,
Guest of Editorial Board of AJGS,
IEREK, Alexandria, Egypt

Communication Chair

Zakaria Hamimi,

Associate Editor,
Arabian Journal of Geosciences,
Benha University, Benha, Egypt

Public Relations Chair

Faïez Gargouri,

Director of the Higher Institute of Computer Science and Multimedia,
President of the AIG,
University of Sfax, Tunisia

Conference Manager

Mohamed Sahbi Moalla,

Journal Coordinator,
Arabian Journal of Geosciences,
ISET, University of Sfax, Tunisia

Preface

The proceedings of the 3rd Springer Conference of the *Arabian Journal of Geosciences* (CAJG-3) which was held online in November 2020 consists of four volumes titled:

Proceedings Volume 1: New Prospects in Environmental Geosciences and Hydrogeosciences
Proceedings Volume 2: Advances in Geophysics, Tectonics, and Petroleum Geosciences
Proceedings Volume 3: Recent Research on Geomorphology, Sedimentology, and Geochemistry
Proceedings Volume 4: Research developments in Geotechnics, Geo-Informatics and Remote Sensing

These volumes are based on the accepted conference papers for either oral/poster presentations or selected for online publication during the CAJG-3.
The first volume offers a broad range of recent studies that discuss the latest advances in geoenvironmental and hydrogeosciences from diverse backgrounds including climate change, geoecology, biogeochemistry, water resources management, and environmental monitoring and assessment. It shares insights of experienced scientists from, but not limited to, research institutes worldwide, focused the Mediterranean and Middle East regions on how the understanding of ecological, climatological, oceanic, and hydrological processes is the key for improving practices in environment management, including the eco-responsibility, scientific integrity, and social and ethical dimensions.

The second volume includes a series of research methods that are nowadays in use for measuring, quantifying, and analyzing the targeted geological domains. Remote sensing with high-resolution satellite imagery, seismology, geochemistry, theoretical geophysics and related profiles with tomographic images, earthquake geology with times series radar interferometry and related geodetic-GPS campaigns, and well-logging contribute to scrutinizing the Earth tectonic architecture. Fundamental questions that address the genesis and evolution of our planet are built upon data collection and experimental investigations under physical constitutive laws which are the conditions for a successful scientific research. These multidisciplinary approaches combined with the geodynamics of tectonic provinces and investigations of potential zones of natural resources (petroleum reservoirs) provide the basis for the economic development.

The third volume presents an updated unique view in conjugating field studies and modeling to better quantify the process-product binomial unusual in geosciences. Earth systems require a comprehensive understanding of processes and dynamics of geology, morphotectonics, sedimentology, stratigraphy, and geochemistry. In the geomorphology section, several studies deal with topics related to fault slip and incision rates, soil science, landslides and debris flows, coastal processes, and geoarcheology and geoheritage. Under the sedimentology section, researchers present recent advances in stratigraphy, environmental, tectonic and diagenetic processes, together with evolutionary, biostratigraphic and paleoenvironmental significance of paleontology are presented. Additionally, this section also contains papers on marine geosciences, from molecular proxies related to climate to geophysical surveys. Last but not least, the third section on geochemistry focuses on sedimentary geochemistry and mineralogical characterization, magmatic and metamorphic processes and products, and the origin and exploration of mineral deposits. This volume resumes the current situation related

to the above-mentioned topics mainly in the Mediterranean realm, testifying the geological importance of this area and surroundings.

The fourth volume contains research studies in the fields of three sections; (1) geological and geotechnical engineering, (2) geomechanical studies based on numerical and analytical methods, and (3) geo-informatics and remote sensing. The content of these research studies would provide new scientific knowledge for further understanding on landslides, new stabilization techniques, importance of geophysics for engineering geology investigations as well as new empirical approaches for easily predicting some physical and hydrogeomechanical properties of geomaterials.

The proceedings of the CAJG-3 is of interest to all researchers, practitioners, and students in all fields of geosciences, including the environmental geosciences.

Kütahya, Türkiye — Zeynal Abiddin Ergüler
Setif, Algeria — Riheb Hadji
Porto, Portugal — Helder I. Chaminé
Granada, Spain — Jesús Rodrigo-Comino
Sfax, Tunisia — Amjad Kallel
Freiberg, Germany — Broder Merkel
Quebec, Canada — Mehdi Eshagh
Khenchela, Algeria — Haroun Chenchouni
Johannesburg, South Africa — Stefan Grab
Adelaide, Australia — Murat Karakus
Tunis, Tunisia — Sami Khomsi
Johannesburg, South Africa — Jasper Knight
Évora, Portugal — Mourad Bezzeghoud
Rome, Italy — Maurizio Barbieri
Gandhinagar, India — Sandeep Panda
Düsseldorf, Germany — Ali Cemal Benim
Orange, USA — Hesham El-Askary
July 2021

Contents

About the Editors

Dr. Zeynal Abiddin Ergüler Kutahya Dumlupinar University, Kutahya, Turkey.

Dr. Ergüler is a full professor at the geological engineering department at Kutahya Dumlupinar University (Turkey). He holds a B.Sc. (1998), an M.Sc. (2001), and a Ph.D. degree (2007) in Geological Engineering from Hacettepe University (Turkey). His research interests mainly focus on rock mechanics, engineering geology, environmental geology, and soil mechanics. His current investigation is to understand and model the thermo-hydro-mechanical behavior of shale rocks in the area of shale gas production. In addition to performing many types of research and industry-funded projects, he has also been teaching and supervising undergraduate and graduate students. In 2017, he joined the *Arabian Journal of Geosciences* (AJGS) as an editor responsible for evaluating submissions in the fields of rock mechanics, engineering geology, environmental geology, and soil mechanics.

Prof. Riheb Hadji University of Sétif 1, Setif, Algeria.

Prof. Riheb Hadji is a professor in Geological Sciences in the Department of Earth Sciences, Institute of Architecture and Earth Sciences, Setif 1 University, Algeria. Specialized in Applied Geology, Geomatics, and Environment, he does research in geomorphology, hydrogeology, and natural hazards. His current project is about "Risk management in North Africa". He is the head of the Laboratory of Applied Research in Engineering Geology, Geotechnics, Water Sciences, and Environment, Setif 1, University, Algeria, and the co-chairman of the International Association of Water Resources in the Southern Mediterranean Basin. He has published more than 100 scientific papers in peer-reviewed journals, edited two books on soil mechanics, and has an RG-score of 23.21, an H-index of 24, and an i10 of 34. He has also been involved in four international collaboration projects and several national projects. An editorial board member in peer-reviewed journals, he is an internationally known expert in RS-GIS, natural hazard, and environmental issues.

Helder I. Chaminé School of Engineering (ISEP), Polytechnic of Porto, Portugal.

Helder I. Chaminé is a skilled geologist and professor of engineering geosciences at the School of Engineering (ISEP) of the Polytechnic of Porto, with over 32 years of experience in multidisciplinary geosciences research, consultancy, and practice. He studied geological engineering and geology (B.Sc., 1990) at the Universities of Aveiro and Porto (Portugal), respectively. He received his Ph.D. in geology at the University of Porto in 2000 and spent his postdoctoral research in applied geosciences at the University of Aveiro (2001–2003). In 2011, he received his Habilitation (D.Sc.) in geosciences from the University of Aveiro. Before joining the academy, he worked for over a decade on international projects for mining, geotechnics, groundwater industry and/or academia related to geodynamics and regional geology, hard rock hydrogeology and water resources, engineering geosciences and applied geomorphology, rock engineering, and georesources. His research interests span fundamental to applied fields: GIS mapping techniques for applied geology, structural geology and regional geology, engineering geosciences and rock engineering, slope geotechnics, mining geology and hydrogeomechanics, hard rock hydrogeology, exploration hydrogeology, urban groundwater, and hydromineral resources. He is interested in mining geoheritage, history of cartography, military geosciences and higher-education dissemination, skills, and core values. Presently, he is the head of the Laboratory of Cartography and Applied Geology (LABCARGA | ISEP), a senior researcher at Centre GeoBioTec | U.Aveiro and Centre IDL | U.Lisbon, as well as belongs to the executive board of the M.Sc. + B.Sc. Geotechnical and Geoenvironmental Engineering Programs (OE + EUR-ACE Label) and the Department of Geotechnical Engineering (ISEP). He currently belongs to the board of the Technical Commission of Environmental Geotechnics from SPG. He was a board member of APGeom—Portuguese Association of Geomorphologists (2009–2013), SPG—Portuguese Geotechnical Society (2016–2020), APG—Portuguese Association of Geologists (2020–2021), and AIH-GP—Portuguese Chapter of the International Association of Hydrogeologists (2019–2022). He was a consultant and/or responsible for over 75 projects of applied geology, hydrogeomechanics, slope geotechnics, mining geology, exploration hydrogeology, hard rock hydrogeology, water resources, urban groundwater, and applied mapping (Mozambique, Portugal, and Spain). He has co-authored over 210 publications in indexed journal articles, conference proceedings/full papers, chapters, and technical and professional papers. He co-edited over 15 special volumes and is presently involved in editing themed issues for some international journals (e.g., *Environmental Earth Sciences*—Springer, *Springer Nature Applied Sciences*, *Discover Water*—Springer, *Arabian Journal of Geosciences*—Springer, *Water*—MDPI). As a referee for several international journals in applied mapping, geosciences, geotechnics, hydrogeology, water resources, and geohazards, he has a broad activity. He served as an invited expert evaluator of Bologna Geoscience Program for DGES (Portugal) and Scientific Projects Evaluation for NCST, 2017–2019 (Kazakhstan), and NRF |

RISA, 2019 (South Africa), as well as a coordinator of "Geology on Summer|Ciência Viva" Program at ISEP (2005–2019) for geoscience dissemination. He has also been active in teaching and supervising many Ph.D., M.Sc., and undergraduate students. He has been on the editorial board, among others, of the *Arabian Journal of Geosciences* (SSG + Springer), *Hydrogeology Journal* (IAH + Springer), *Euro-Mediterranean Journal for Environmental Integration* (Springer), *Springer Nature Applied Sciences* (Springer), *Mediterranean Geoscience Reviews* (Springer), *Discover Water* (Springer), *Geotechnical Research* (ICE), *Geosciences* (MDPI), *Revista Geotecnia* (Portugal), and *Geología Aplicada a la Ingeniería y al Ambiente* (Argentina). He integrates as a moderator or a session chair in several conferences, workshops, and meetings. He was the scientific chair of the 1st International Conference on Georesources, Geomaterials, Geotechnologies and Geoenvironment, 4GEO (Porto, Portugal, November 7–8, 2019). He is currently on the organizing and scientific committees of the 3rd International Workshop on Natural Hazards—NATHAZ'22 (Terceira Island, Azores, May 2022), supported by Springer.

Dr. Jesús Rodrigo-Comino University of Granada, Granada, Germany.

Dr. Jesús Rodrigo-Comino, graduated in Geography, currently works as an assistant professor at the University of Granada. He carried out a thesis with an extraordinary degree award with the work: "The soils of the province of Malaga: Revision according to the classification criteria of FAO-WRB (2006)". He holds a Master's degree in Territorial Planning and Geographic Information Systems (2013) from the University of Granada, whose final work was divided into three national publications and a monograph. During his predoc stage, he obtained three scholarships for doctoral studies: DAAD (German Academic Exchange Service), La Caixa Foundation and FPU (Ministry of Education, Spain). During this period, he completed his doctoral thesis between the University of Trier (Germany—2 years) and Malaga (2 years), and Doctor in Geography (2018) from the University of Malaga with a doctoral thesis consisting of eight international publications, international mention and outstanding cum laude: "Actual geomorphological processes in sloping vineyards. A comparison between Ruwer-Mosel Valley (Trier, Germany) and Montes de Málaga (Málaga, Spain)". Currently, he is also preparing a second doctorate in geomatics engineering at the Polytechnic University of Valencia. His research career consists of four full monographs (Nova, Springer, etc.) and one edited alone (Elsevier), 171 indexed publications (Scopus)/130 JCR, leading international collaborations with research teams from Iran, China, Kazakhstan, Sudan, India, Brazil, Croatia, Iraq, or the USA. He is a regular reviewer in more than 140 international indexed journals (e.g., *Scientific Reports*, *Science of the Total Environment*, *PlosOne*, *Catena*, *Geoderma*, *Agriculture*, *Ecosystem* and *Environment or Earth-science Review*), a member of the panel of two doctoral theses, and an evaluator of projects for the Ministries of Science of Chile, Peru, the USA, Serbia, Switzerland, Kazakhstan or Poland, and postgraduate scholarships for DAAD. He has organized several scientific meetings and congresses (e.g., Action Cost, V

Biohydrology, Fire in the Earth, etc.), sessions at international conferences (EGU, TerraEnvision, Conference of the *Arabian Journal of Geosciences*, etc.), oral presentations, and conferences magisterial (Germany, Bulgaria, Norway, etc.). He is the editor-in-chief of the indexed journal (Scopus and ESCI; Q2) *Air Soil and Water Research* (SAGE). In addition, he is an associate editor at *Scientific Reports* (Nature-Springer), *Hydrological Science Journal* (Taylor & Francis), *Arabian Journal of Geosciences* (Springer), *Euro-Mediterranean Journal for Environmental Integration* (Springer), and *Journal of Mountain Science* (Springer). He has participated as a researcher in R&D&I projects on social issues related to housing or the census, or transfer and knowledge at European level such as the INTERREG Smart-Light HUB project (light pollution) or COST FIRElinks (fires). He has been invited to give lectures on agriculture, sustainable management, and erosion in several universities. He has supervised five final degree projects and three completed Master's degrees in Germany. He has taught regulated and certified teaching at the Universities of Granada, Valencia, Malaga, León, Oviedo, and Trier (in German) on development, geomorphology, Geographic Information Systems, remote sensing, and statistical techniques. He was recently awarded with a Leonardo Grant (BBVA Foundation).

Dr. Amjad Kallel ENIS, University of Sfax, Sfax, Tunisia.

Dr. Amjad Kallel is currently an associate professor of Environmental Geology in the Sfax National School of Engineers at the University of Sfax, Tunisia. He holds a B.Eng. in Georesources and Environment (1998) from the University of Sfax (Tunisia) and an M.Sc. degree and a Ph.D. degree in Georesources and Environment (2004) from Hokkaido University (Japan). He joined Venture Business Laboratory (VBL) at Akita University, Japan (2005–2006), as a researcher focusing on refining and recycling technologies for the recovery of rare elements from natural and secondary sources. On his return to Tunisia, he worked at the University of Gabes from 2006 to 2011, where he contributed to the elaboration of teaching programs at the Higher Institute of Water Sciences and Technologies of Gabes. Since 2011, he has joined the Sfax National School of Engineers. There, he has also been involved in various research projects related to Environmental Geology and Environmental Geotechnics. He has co-organized many prestigious workshops, seminars, and international conferences. In 2016, he joined the *Arabian Journal of Geosciences* (Springer) and the *Euro-Mediterranean Journal for Environmental Integration* (Springer) as the chief editor and the managing editor, respectively.

Broder Merkel TUBAF, Freiberg, Germany.

Broder Merkel did his Dissertation (Ph.D.) Dr. rer.nat. as Hydrogeologist (TU München) and Habilitation (Dr. habil) at Christian-Albrechts Universität Kiel. Broder Merkel is a full professor for Hydrogeology at TUBAF (1993–2015) for hydrogeology, hydrochemistry, modeling chemical thermodynamics and reactive transport, geo-statistics, GIS and remote sensing. Broder Merkel is the dean of the Faculty Geoscience, Geotechnics and Mining, a DFG liaison officer of TUBAF, the vice rector of TUBAF, and the head of the Scientific Diving Center of TUBAF. Broder Merkel's field work is in Bolivia, China, Chile, Czech Republic, Iraq, Iran, Israel, Italy, Jordan, Hungary, Mexico, Mozambique, Namibia, Palestine, Russia, Spain, and the USA. Broder Merkel has organized of seven international conferences on uranium mining and hydrogeology.

Mehdi Eshagh University West, Sweden.

Mehdi Eshagh, 1977, born in Tehran, Iran, completed his M.Sc. degree in Geodesy from KNToosi University of Technology in Iran and Ph.D. in Geodesy at Royal Institute of Technology (KTH) under supervision of Prof. Lars E. Sjöberg in 2009. He became docent (habilitation) in Physical Geodesy and Space Geodesy at KTH and worked there as a senior researcher until 2016 and since September 2013 as a professor of Geodesy at University West in the western part of Sweden. He has about 22 years of activities in teaching diversity of courses in surveying engineering and geodesy, research and supervision of students at all levels of educations. He is the author of 120 articles in peer-reviewed international journals and the book *Satellite Gravimetry and the Solid Earth, Mathematical Foundations*, published by Elsevier in 2020. He is the founder of *Journal of Geodetic Science* in 2010 and its editor-in-chief since 2018. He is interested in collaboration in teaching and research internationally, e.g., Affiliated Professor at the Ethiopian Space Science and Technology Institute and Adjunct Professor at KNToosi University of Technology, and habilitated with University of Sherbrooke.

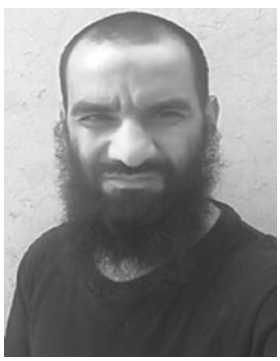

Dr. Haroun Chenchouni Higher National School of Forests, Khenchela, Algeria.

Dr. Haroun Chenchouni is an associate professor and a research scientist (Ecologist) at the Higher National School of Forests (Khenchela, Algeria). He is a former associate professor at the University of Tebessa (Algeria). He holds an M.Sc. (Magister) in Dryland Ecology from the University of Ouargla (Algeria) and a doctorate degree in Ecology and Environment from the University of Batna. He graduated as an engineer in Plant Ecology and Forest Ecosystems from the Department of Biological Sciences (University of Batna, Algeria). His research interests are fairly broad; he uses statistical modeling approaches to understand how natural environments, mainly climatic and edaphic factors, and anthropogenic perturbations influence biological interactions, shape trends in population dynamics, and influence community diversity. He uses various biological models to investigate biological interactions and community ecology of arid and semiarid ecosystems of North Africa. At various universities in Algeria, he

teaches forest ecology, biostatistics, and ecological modeling. He has published more than 100 peer-reviewed publications and internationally recognized research papers. He is also involved in national and international research projects. In 2017, he joined the *Arabian Journal of Geosciences* (AJGS) as an associate editor. Then in 2019, he was assigned as a chief editor of Topic 2 (biogeochemistry, geobiology, geoecology, geoagronomy) to handle submissions dealing with various fields of biogeosciences, geoecology, climate change, plant and soil science, agricultural and forest environment, and environmental sciences.

Stefan Grab School of Geography, Archaeology and Environmental Studies, University of the Witwatersrand, South Africa.

Stefan Grab is Swiss by birth but grew up in Pietermaritzburg, South Africa. Stefan Grab studied geomorphology at the University of Natal with specialization in periglacial geomorphology. Today, Stefan Grab works in both geomorphology and historical climate change sectors. Stefan Grab's research regions include southern and eastern Africa, the mid-Atlantic and Iran (Middle East).

Prof. Murat Karakus University of Adelaide, Adelaide, Australia.

Prof. Karakus holds a B.Sc. in Mining Engineering (1991) from Hacettepe University (Turkey) and a Ph.D. degree in Rock Mechanics (2000) from the University of Leeds, UK. He is currently a chair professor at the China University of Geosciences, Wuhan, and an associate professor of the School of Civil, Environmental and Mining Engineering. His research area is the field of experimental rock mechanics; fracture and damage mechanics, numerical analysis, plasticity, and constitutive modeling in rock mechanics and strainburst/rockburst mechanisms for deep tunnels and mining. He established a Cave Mining Research Centre at the University of Adelaide and has been investigating many aspects of cave mining including mud-rush problem, cave backpropagation, preconditioning by hydraulic fracturing, and cave flow modeling. He attracted and is currently leading several research projects including ARC—Australian Research Council grants, CRC—Deep Exploration Technologies, ACARP—Australian Coal Association Research, and Industry supported projects. He has published several chapters and over a hundred papers in international journals and conferences He is a member of the ISRM Commission on Rockburst and the ISRM Commission of Deep Mining. He has been serving as the editorial board member of several journals including the *International Journal of Rock Mechanics and Mining Sciences*, *Rock Mechanics and Rock Engineering*, *Tunnelling and Underground Space Technology*, *Journal of Rock Mechanics and Geotechnical Engineering*, *International Journal of Mining, Reclamation, and Environment*, *Bulletin of Engineering Geology and the Environment*. He is currently serving as the chief editor of Track-12; *Numerical and Analytical Methods in Mining Sciences* and *Geomechanics of Arabian Journal of Geosciences*.

Sami Khomsi Georesources Lab, CERTE, University of Carthage, Tunis, Tunisia.

Sami Khomsi is a structural-petroleum geologist. He got his Ph.D. at Tunis University in 2004 and his HDR (Habilitation à Diriger des Recherches) in the same university in 2015. Since 2011, he works in the department of petroleum geology and sedimentology, and in the Geoexploration department in the faculty of Earth Sciences, King Abdulaziz University, Jeddah, Saudi Arabia. He worked also in different universities in Tunisia and France. Past employment within academia (research and teaching) and industry in the exploration activities involved in many international programs, regional exploration assets, regional synthesizes, sites survey, prospects evaluation and professional expert training (field trip leader for professionals, coaching of geoscientists) in basin analysis involving basin modeling, structural analysis, and balanced cross sections. He collaborated with major oil companies in Eastern Maghreb on field studies, structural analysis of fold-thrust structures, subsurface reservoir characterizations, and seismic interpretations. He has also experience in geophysical methods involving fast processing and interpretation of seismic reflexion sections in terms of structural geology-investigation-evaluation of plays, characterization of fractured reservoirs, and subsurface mapping. His main research interests are geometry, kinematics and dynamics of fold-thrust systems and foreland basins in North Africa, Middle East and the Mediterranean realm, fractured reservoir analogues, applying structural analysis and subsurface techniques in the characterizations of drillable structures and structural evaluation of traps using regional cross sections at large scale as well as structural subsurface based on regional seismic reflection profiles in different basins. https://www.scopus.com/authid/detail.uri?authorId=16175410900.

Jasper Knight University of Witwatersrand, South Africa.

Professor of Physical Geography, University of the Witwatersrand, Johannesburg, South Africa.

Jasper Knight is a geoscientist with research interests in the spatial and temporal variability in landscape system responses to climate and environmental changes during the late Pleistocene and Holocene, looking at sediments and geomorphology. Jasper Knight focuses thematically on glaciers, rivers, coasts, and mountains. Jasper Knight focuses geographically on the UK and Ireland, northwest USA, Australia, European Alps, various locations in Asia, and across both southern and northern (Saharan) Africa. Jasper Knight is an editor of three major international journals (*Sedimentary Geology*, *Journal of Maps*, *Land Degradation and Development*). Jasper Knight's teaching and student supervision focus on the interconnections between the physical and human environments, landscape change, and environmental resources of the past, present, and future.

Mourad Bezzeghoud Universidade de Evora, Évora, Portugal, Portugal.

Mourad Bezzeghoud is a full professor at the University of Évora (Professor in the Physics Department/School of Sciences and Technology and a researcher at the ICT/IIIFA). He has published dozens of articles in specialized revues and journals, and several books and chapters in book. He works in the area of Earth Sciences (Solid Earth Geophysics) with an emphasis in seismology. He interacted with 198 collaborators in co-authorship of scientific works. In his curriculum, Ciência Vitae (FCT, Portugal), the most frequent terms in the context of scientific and technological production are seismicity, focal mechanisms, nonlinear dynamics, seismic risk, seismic source, Azores, broad band seismic network, chaos, earthquake faults, and seismic instrumentation.

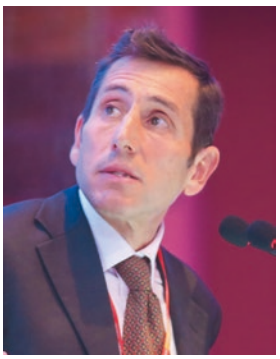

Prof. Maurizio Barbieri Department of Chemical Engineering Materials Environment, Faculty of Engineering, Sapienza University of Rome, Italy, Italy.

Prof. Barbieri holds a degree in Geological Sciences (1994) and a Ph.D. degree in Earth Sciences (1998) from Sapienza University of Rome, (Italy). He is currently a full professor of Environmental Geochemistry and Hydrogeochemistry at Sapienza University of Rome (Italy). His job-related skills are geochemical tracers in hydrological studies; interactions between water and the geological and chemical environment; quantitative understanding of chemically based processes in hydrogeochemical environments and complementary physical and biological processes and conditions; kinetics and equilibria of geochemical reactions; the movement of isotopes and soil chemistry; freshwater-seawater interactions in coastal aquifers; basic and applied research on speciation and transformation of trace metals and metalloids during biogeochemical processes in both natural and anthropogenic environments; radiogenic and stable isotope geochemistry. Other fields of expertise are ion chromatography, ICP-MS, water, soil and geological mapping, univariate and multivariate analysis of geochemical datasets, isotope analyses of Sr, H, O, and B.

He is an editorial board member for Springer, Elsevier and MPDI Journals (topics: Geochemistry, Water and Environment). Water Quality Advisory for the LIFE ACTION GRANTS: Restoration, management and valorisation of PRIority habitats of MEDiterranean coastal areas—LIFE17 NAT/GR/000511. His coordinating beneficiary is Hellenic Society for the Protection of Nature (2018–2020) and International Project (2018–2020) LIFE17NAT/GR/000511 “Restoration, management and valorisation of PRIority habitats of MEDiterranean coastal areas”. He is an environmental advisor (Hydrogeochemistry) for the International Project (2016–2019) SECOSUD II—Conservation and equitable use of biological diversity in the SADC region. The project is financed by the Italian Agency for Development Cooperation and implemented through Eduardo Mondlane University, South African National Park, and Sapienza University of Rome. He is the scientific coordinator (2014–2016) for the geochemical model of the Vico Lake (Central Italy), with particular regard to environmental arsenic. His client includes Regional Agency for Environmental Protection of Lazio. He is an

environmental advisor (Hydrogeochemistry) for the International Project (2012–2014) "Institutional Support to the management of Protected Areas in Albania". His project was supported by the International Union for Conservation of Nature (IUCN).

Dr. Sandeep Panda is currently working as an Assistant Professor at the Department of Industrial Biotechnology, Gujarat Biotechnology University, Gujarat, India. His main research areas include (Bio) hydrometallurgical approaches for metal extraction from primary and secondary resources, Bio-desulphurization of Coal, Bio and Chemical approaches for Mine Water treatment and application of eco-friendly approaches for sustainable mineral-metal waste recycling and management. He has been involved as Principal/Co-principal Investigator and as Team Member in several R&D and Industrial research projects (at both National and International level) since 2009. As of 2023, he has published 55 International journal papers; 4 book chapters and 5 Editorial books of high quality and impact that have received nearly 1950 citations (h-index—25). One of his articles published in the journal *NATURE* related to Tech-Metal supply is receiving much attention and appreciation from global leaders working in his area. His research works have invited the attention of several press and media. He has been featured in the WORLD RANKING OF THE TOP 2% SCIENTISTS in the Domain of Mining and Metallurgy (Sub Domain—Environmental Sciences) as per the Standford University list of top-cited scientists in 2020, 2021, 2022. He is an active member of several prestigious professional bodies and technical/scientific committee member in several reputed international conferences. He has served as a reviewer in over 40 reputed International Journals and is currently serving as: (1) Associate Editor of the *Arabian Journal of Geosciences* and *Euro-Mediterranean Journal of Environmental Integration* (Springer Nature) and Editorial Board Member of: (2) *Frontiers in Microbiology* and *Frontiers in Environmental Sciences* (Frontiers Publications), (3) *Mineral Processing and Extractive Metallurgy Review Journal* (Taylor & Francis Group) and (4) Editorial Advisory Board of *Detritus Journal* (IWWG).

Prof. Dr.-Ing. habil. Ali Cemal Benim Düsseldorf University of Applied Sciences, Düsseldorf, Germany.

Prof. Dr.-Ing. habil. Ali Cemal Benim received his B.Sc. and M.Sc. degrees in Mechanical Engineering at the Boğaziçi University, Istanbul, Turkey. He received his Ph.D. degree at the University of Stuttgart, Germany, in 1988, on the topic "Finite Element Modeling of Turbulent Diffusion Flames" with "Degree of Distinction". Following a postdoctoral period at the University of Stuttgart, in 1990 he joined ABB Turbo Systems Ltd. in Baden, Switzerland, where he was the manager of the "Computational Flow and Combustion Modeling" group. Since January 1996, he is a professor for Energy Technology and the head of Center of Flow Simulation at the Dusseldorf University of Applied Sciences, Dusseldorf, Germany.

Prof. Hesham El-Askary Chapman University, USA.

Prof. El-Askary received his Ph.D. in Computational Sciences and Informatics from George Mason University in 2004. He is the 2015 recipient of the Chapman University's elite Senior Wang-Fradkin Professorship award. In 2016, he was named as the regional coordinator on a $3 million Euro grant from the European Union's (EU) Horizon 2020. The three-year project, known as GEO-CRADLE, deals with coordinating and integrating state-of-the-art Earth Observation Activities in the regions of North Africa, Middle East, and Balkans and Developing Links with GEO-related initiatives toward GEOSS. Through this work, he with the research team were able to deliver the first analytical solar Atlas of Egypt that is now considered to be the official document of the government for solar investment. This work was recently presented at Planet Earth Institute at the Royal Society in London during a seminar that discussed the future of solar energy in Africa. His research interests include dust storms monitoring and detection using different remote sensing technologies as well as studying other extreme events. He is also involved in studying air pollution problems over mega cities due to natural and man-made effects as well as climate change and its impacts on sea level rise and coral reefs for coastal areas. His research also included using Earth observations in studying impact of sever dust storms anomalous chlorophyll outbreaks in the marine environment, hurricanes intensification as well as transport of microbes' causing Kawasaki disease outbreaks. Recently, he has been focusing on using Earth observations for water resources management, precision agriculture along the sustainable development goals. Today, he views himself as an Earth system scientist with a major interest in natural hazards, atmospheric events, and using renewable energy as the only way to address global climate change issues. He has published over a 100 refereed research publications, conferences, full paper, and chapters in these research areas. His research has been supported by National Science Foundation, NASA, United States Department of Agriculture and European Union. He has received the Saudi Arabia award hosted by the Arab Administrative Development Organization (ARADO) affiliated with the League of Arab states for the best published article in Environmental Management among 150 articles in 2006. He is also a member of the Institute of Electrical and Electronics Engineers (IEEE), AGU, EGU, COSPAR, and Phi Beta Delta Honor Society.

SAR Simulation for Vegetation Roughness to Monitor the Phenology of Oryza Sativa

Shoba Periasamy, Kokila Priya Ravi, Ramakrishnan S. Shanmugam and Kalaranjini Velappan Sasikala

Abstract

This research explores the potential of the proposed vegetation roughness model from Synthetic Aperture Radar (SAR) (C-band) in discriminating the phenological stages of *Oryza sativa*. The influence of incidence angle on the backscattering coefficient in mid- and far-range was significantly controlled by employing the optimization model. The temporal sequence of Sentinel-1 data in 12 days' time-lapse was acquired to investigate the relationship between the temporal variation of radar backscattering coefficient and the phenological stages of *Oryza sativa*. The study was executed by simulating the backscattering values of VH polarization as a cumulative function of vegetation scattering and vegetation moisture, where the soil roughness and dielectric constant were assumed to be constant throughout the crop cycle. By employing DPSVI as a descriptor of vegetation, the vegetation moisture content was extracted from the total available moisture content. The model for vegetation roughness/scattering coefficient was proposed by scaling down the influence of vegetation moisture from VH polarization. The simulated vegetation roughness model was applied to discriminate the phenological stages of *Oryza sativa*, and the results had shown adequate statistical significance with the in situ vegetation roughness ($R^2 = 0.78$) measures. Furthermore, the deployed model has been found to have the potential of measuring the crop height ($R^2 = 0.80$) indirectly without employing interferometric techniques.

Keywords

SAR · *Oryza sativa* · Incidence angle optimization · Vegetation moisture · Vegetation roughness

1 Introduction

Mapping and periodic monitoring of the phenological stages of *Oryza sativa* (Paddy) are necessary for its effective management and to ensure food security. *Oryza sativa* is a crop grown in a tropical climate (Kaur, 2019) that limits the potential of optical and hyperspectral remote sensing data to be applicable in investigating the plant parameters throughout the entire crop cycle. Microwave remote sensing has a higher potential in monitoring the temporal variations in the phenological stages of *Oryza sativa* (Minh et al., 2019) due to the depolarization nature of the signal, based on the structure and orientation of the target. The backscattering values are generally controlled by two indispensable parameters: moisture content and roughness (Ulaby, 1975).

Various studies in the past have proved the potential of Quad-pol SAR data in monitoring the growth stages of *Oryza sativa* (Wu et al., 2011) and interferometric techniques in estimating crop height (Srivastava et al., 2006). In the present study, a novel simulation approach has been proposed to investigate the different phenological stages from dual-polarized (VV and VH) SAR data by assuming dielectric and roughness values of soil as constant throughout the crop cycle. The objective of the present study is to propose a simple but robust simulation for vegetation roughness to discriminate the phenological stages and the corresponding crop height of *Oryza sativa* using C-band (5.36 GHz) Sentinal-1 data product.

S. Periasamy (✉) · R. S. Shanmugam
Institute of Remote Sensing, Department of Civil Engineering, College of Engineering, Anna University, Chennai, India
e-mail: shobap@annauniv.edu

K. P. Ravi
CGG Satellite Mapping, Crawley, UK

K. V. Sasikala
Geospatial Technologies, LTIMindtree, Chennai, India

Z. A. Ergüler et al. (eds.), *Selected Studies in Geotechnics, Geo-Informatics and Remote Sensing*, Advances in Science, Technology & Innovation, https://doi.org/10.1007/978-3-031-43759-5_1

2 Materials and Methods

The research was performed in Thanjavur district, Tamil Nadu, India, commonly known as the "Rice bowl of India" because of its active agricultural activities in the delta region of the Cauvery River. The temporal development of *Oryza sativa* was continuously monitored from sowing to harvest period (110–150 days) which includes vegetative phase (Phase I–Seedling/ transplantation to stem elongation), reproductive phase (Phase II–Panicle initiation to flowering), and ripening phase (Phase III–Milk to mature stage). The decrease in the backscattering coefficient in VV and VH polarization with the increasing incidence angle (θ) from near- to far-range was controlled by employing the optimization model (Periasamy & Ravi, 2020) in the multi-temporal Sentinel-1 data (5.36 GHz). The backscattering values of VH polarization are dominantly controlled by the vegetation scattering/depolarization effect (Patel et al., 2006) and partially influenced by vegetation water content. The effect of vegetation water content was decoupled from their contribution to total backscattering values using DPSVI (Periasamy, 2018) as a vegetation descriptive parameter. The vegetation roughness model was proposed by reducing the influence of vegetation moisture from backscattering values of VH polarization. It should be noted that the dielectric values of the soil were assumed to be constant in the paddy field irrespective of different growth stages.

Similarly, the resultant product of the proposed model was examined with the field measured crop height (H_{crop}) based on which the relationship between h_{veg} and H_{crop} was simulated through a simple linear regression. The simulation for vegetation roughness and simple regression was performed for all the acquired imageries to discriminate the phenological stages and attain crop height.

3 Results

The increased standard deviations in the backscattering values of various features in mid- and far-range have been significantly controlled in both the polarization $\left(\sigma^0_{VV-opt}\ \&\ \sigma^0_{VH-opt}\right)$ after optimization. From the temporal investigation of backscattering coefficient values of VV $\left(\sigma^0_{VV-opt}\right)$ and VH $\left(\sigma^0_{VH-opt}\right)$ polarization with the phenological stages of *Oryza sativa*, we found that VH polarization is highly sensitive to the growth stages of *Oryza sativa* compared to the VV polarization (Table 1). The values of h_{veg} have shown promising statistical consistency with the in situ roughness measurements ($R^2 = 0.78$) till the heading stage ($h_{veg(\mu)} = 0.910$) when the crops have attained the maximum height. Similarly, the resultant product of h_{veg} demonstrated a good correlation with the field measured crop height (H_{crop}) in different phenological stages ($R^2 = 0.80$) till the heading stage.

However, the gradual decline in the h_{veg} values was observed from flowering ($h_{veg(\mu)} = 0.84$) to mature stage ($h_{veg(\mu)} = 0.61$). The proposed model finds difficulty measuring the vegetation roughness and height from flowering to the mature stage as the plant's needle structure and arrangement get disturbed by the rice grains.

4 Discussion

In σ^0_{VH-opt}, the sensitivity of plant growth is higher because the backscattering coefficient increases gradually from flooding to the heading stage and decreases with the change in leaves orientation. The consistent decrease in σ^0_{VV-opt} was due to attenuation of radar signal into leaves, stems, and secondary tillers of *Oryza sativa*. During the initial vegetative phase, the flooded field acts like a specular surface (Nguyen et al., 2015) and results in low backscattering

Table 1 Statistical consistency of the SAR simulation for vegetation roughness (h_{veg}) with the in situ measurements

Phenological stages		σ^0_{VH-opt} (dB)	σ^0_{VV-opt} (dB)	H_{crop} (μ) (cm)	h_{veg}		
					μ	rmse	Bias
Phase I	Transplanting	− 20.220	− 13.235	16	0.162	0.060	− 0.001
	Tillering	− 18.172	− 11.067	28	0.337	0.081	0.002
	Stem elongation	− 16.238	− 7.435	41	0.585	0.102	0.019
Phase II	Panicle initiation	− 15.359	− 8.996	63	0.816	0.057	0.001
	Heading/booting	− 14.776	− 10.247	102	0.910	0.093	0.062
	Flowering stage	− 16.110	− 8.245	96	0.84	0.136	0.023
Phase III	Milk stage	− 16.785	− 7.601	94	0.766	0.100	− 0.014
	Dough stage	− 17.036	− 8.920	89	0.694	0.194	0.031
	Mature stage	− 17.672	− 8.925	85	0.613	0.201	− 0.002

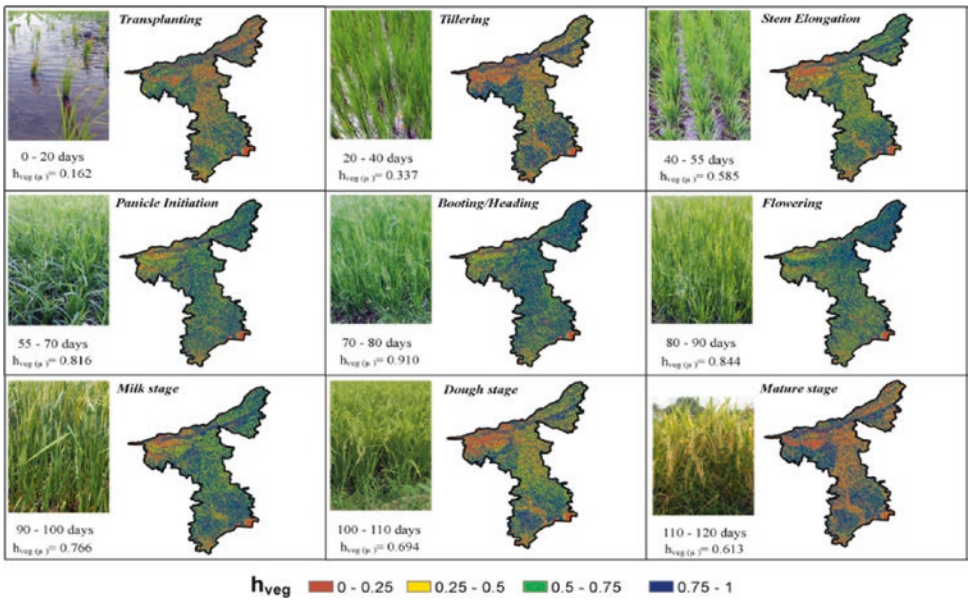

Fig. 1 Vegetation roughness maps against each growth stage

($h_{veg(\mu)}=0.162$). During the process of attaining the reproductive phase, the volumetric scattering effect dominates in the backscattering values (Singha et al., 2019). Thus, the maximum vegetation roughness values ($h_{veg(\mu)}=0.3$ to 0.91) in the heading stage resulted from increased volumetric scattering (Fig. 1). After the flowering stage, the measurements from the simulation were negatively biased. This was due to the paddy plant gradually descending on the surface from the flowering phase to the mature stage due to rice grains' increased weight. Furthermore, a positive correlation between h_{veg} and H_{crop} exists by virtue of variations in the scattering nature in different growth stages with the corresponding height of *Oryza sativa*. The proposed simulation is well suited to determine the different phenological stages and height of *Oryza sativa* without employing complex interferometric techniques. However, the crop condition and yield estimation could not be studied with the proposed SAR vegetation roughness model.

5 Conclusions

The research investigated the sensitivity of the proposed vegetation roughness model from dual-polarized Sentinel-1 data in discriminating the phenological stages of *Oryza sativa*. The influence of incidence angle variation on the backscattering coefficient was significantly controlled by employing the optimization model. The study emphasized the plant's depolarization effect by keeping the influence of dielectric constant and the soil roughness constant. The simulation was demonstrated to be effective in examining the different growth stages and determining the height of *Oryza sativa* until the crop reaches the heading stage.

References

Kaur, R. (2019). Climate change impacts on rice (*Oryza sativa*) productivity and strategies for its sustainable management. *Indian Journal of Agricultural Sciences, 89*(2), 171–180.

Minh, H. V. T., Avtar, R., Mohan, G., Misra, P., & Kurasaki, M. (2019). Monitoring and mapping of rice cropping pattern in flooding area in the Vietnamese Mekong Delta using Sentinel-1 data: A case of an Giang Province. *ISPRS International Journal of Geo-Information, 8*(211), 1–22.

Nguyen, D. B., Clauss, K., Cao, S., Naeimi, V., Kuenzer, C., & Wagner, W. (2015). Mapping rice seasonality in the Mekong Delta with multi-year Envisat ASAR WSM data. *Remote Sensing, 7*(12), 15868–15896.

Patel, P., Srivastava, H. S., Panigrahy, S., & Parihar, J. S. (2006). Comparative evaluation of the sensitivity of multi-polarized multi-frequency SAR backscatter to plant density. *International Journal of Remote Sensing, 27*(2), 293–305.

Periasamy, S. (2018). Significance of dual polarimetric synthetic aperture radar in biomass retrieval: An attempt on Sentinel-1. *Remote Sensing of Environment, 217*, 537–549.

Periasamy, S., & Ravi, K. P. (2020). A novel approach to quantify soil salinity by simulating the dielectric loss of SAR in three-dimensional density space. *Remote Sensing of Environment, 251*, 1–17.

Singha, M., Dong, J., Zhang, G., & Xiao, X. (2019). High resolution paddy rice maps in Cloud-prone Bangladesh and Northeast India using Sentinel-1 data. *Scientific Data, 6*(26), 1–10.

Srivastava, H. S., Patel, P., & Navalgund, R. R. (2006). Application potentials of synthetic aperture radar interferometry for land-cover mapping and crop-height estimation. *Current Science, 91*(6), 783–788.

Ulaby, F. (1975). Radar response to vegetation. *IEEE Transactions on Antennas and Propagations, 23*(1), 36–45.

Wu, F., Wang, C., Zhang, H., Zhang, B., & Tang, Y. (2011). Rice crop monitoring in South China with RADARSAT-2 quad-polarization SAR data. *IEEE Geoscience and Remote Sensing Letters, 8*(2), 196–200.

Wind-Wave Relationship Compared Between the Arabian Sea and Bay of Bengal Regions Using Numerical Ocean Models, Genetic Algorithm, and Scatterometer Wind Fields

Mourani Sinha and Susmita Biswas

Abstract

The wind-generated surface wave heights impact all those venturing into the deep oceans and also those dwelling near the coasts. The two basins, the Arabian Sea (AS) and the Bay of Bengal (BB), located at either side of the Indian Ocean exhibit distinct features although located in the same latitudinal band receiving the same amount of heat from the sun. The wind-wave variability in the two basins having striking differences is studied in this paper. WAVEWATCH III model was run for the Indian Ocean region using scatterometer daily wind fields. Empirical orthogonal function analysis was applied on the model generated significant wave height (SWH), zonal, and meridional wind components to generate the temporal patterns (PCs) for both the regions separately. The maximum variability of the dominant PC for all the parameters was more in the AS than the BB. Then, multivariate genetic algorithm (GA) was applied on the PCs to generate the explicit forecast equations which were used along with SCATSAT-1 wind product to generate forecasted SWH fields. Scatter plots generated and the coefficient of determination calculated between the actual and GA predicted PCs showed the performance of the algorithm was better for the AS than the BB basin. The root mean square error spatial maps generated between the actual and GA reconstructed SWH values were compared for both basins. For the BB region, the maximum error was observed in the head and central Bay regions. For the AS region, the maximum error was along the Findlater Jet.

Keywords

Wind-waves · Scatterometer · Genetic algorithm · Arabian Sea · Bay of Bengal

1 Introduction

Prediction techniques using genetic algorithm (GA) based on developments in chaos theory and function approximation (Alvarez et al., 2001; Takens, 1980) require only past values to generate future ones. These alternative methods are much more promising using less computing resources compared to numerical models. Previous studies reveal a combination of genetic algorithm, and empirical orthogonal function (EOF) analysis has been employed satisfactorily to forecast scatterometer observed surface winds in the north Indian Ocean (Basu et al., 2005; Sinha et al., 2013). In this work, EOF analysis and GA have been applied to forecast and compare wave height fields in the AS and BB regions using scatterometer wind speed fields.

2 Materials and Methods

The study region covering the Indian Ocean extends from 30º E to 120° E and 30° N to 70° S. The WAVEWATCH III model was run from 2009 to 2018 using ASCAT daily 25 km wind fields and 2017–2018 SCATSAT-1 daily 25 km wind fields. For the BB and AS regions, EOF analysis was applied on 8 years (2009–2016) model generated SWH, zonal (U), and meridional (V) wind components to generate the PCs. Multivariate GA was applied on the PCs of SWH, U and V and further to test the accuracy of the analytical explicit equations generated, independent validation sets were utilized. Scatter plots were generated between the

M. Sinha (✉)
Department of Mathematics, Techno India University, West Bengal, India
e-mail: mou510@gmail.com

S. Biswas
Department of Computer Science and Engineering, Techno India University, West Bengal, India

Z. A. Ergüler et al. (eds.), *Selected Studies in Geotechnics, Geo-Informatics and Remote Sensing*, Advances in Science, Technology & Innovation, https://doi.org/10.1007/978-3-031-43759-5_2

actual and GA predicted PCs, and finally, root mean square error maps to study the basin's features.

3 Results

The dominant mode of the PCs for SWH exhibited 79% variability for BB and 90% for AS. The PCs were of annual variability with maximum values during the southwest monsoon months. Multivariate GA was applied on the PCs of the SWH, U, and V parameters to generate a relationship among them. After training the algorithm for BB, the maximum strength index of the best equation was 0.68. The explicit analytical equation obtained for the BB region is given as follows:

$$\begin{aligned}\mathrm{SWH}(t) = (u(t-1)/(((.02) * ((((-4.65)\\ + ((-9.54)/((u(t-1)/(-9.54))/(-9.40))))\\ * (-9.37)) - v(t-1))) - (9.54))).\end{aligned}$$

Similarly for the AS region, the explicit equation with strength index 0.7 is given as

$$\begin{aligned}\mathrm{SWH}(t) = ((u(t-1) + (u(t-1)\\ + (((v(t-1) - (u(t-1)/(-2.68)))\\ - u(t-1))/((-4.79)/(-2.09)))))/((-4.79) * (2.65))).\end{aligned}$$

The accuracy of the above equations was tested by applying them to an independent validation dataset. In this work, 4 such datasets were considered. The 4 datasets contain model outputs using 2017 ASCAT and SCATSAT-1 wind fields and then 2018 ASCAT and SCATSAT-1 wind fields. Figure 1 gives the scatter plots of the actual and GA predicted PCs using independent dataset comprising of 2017 ASCAT and SCATSAT-1 wind fields, respectively, for BB.

Figure 2 gives similar plots for the AS region. Considering 2017 and 2018, the coefficient of determination R^2 between the actual and GA predicted PC is between 0.5 and 0.7 for the BB region and between 0.7 and 0.8 for the AS region. Thus, the performance of the algorithm is better for the AS region compared with the BB region.

The SWH fields were next reconstructed using the original EOFs and the genetically forecasted PCs for the validation sets. Root mean square error (RMSE) maps were generated giving the spatial error distribution between the actual and GA reconstructed SWH values. Figure 3 illustrates the RMSE maps for the BB region for the 2017 ASCAT and SCATSAT-1 validation data, respectively. The error between the actual and GA reconstructed SWH values was more than 0.5 m for the ASCAT set whereas more than 0.8 m for the SCATSAT-1 set. Figure 4 gives similar plots for the AS region which shows along the Findlater Jet the maximum error was around 0.8 m for the 2017 ASCAT set and around 1 m for the 2017 SCATSAT-1 set.

4 Discussion

For all the parameters SWH, U, and V, the variability of the dominant mode of the PCs was more in AS than BB. This may be due to the strong winds over AS during the summer monsoon. The annual pattern of the first PC corresponds to the monsoonal oscillation with maximum values during the southwest monsoon months. Similar results were obtained by Rao et al. (2011) as they performed EOF analysis over 9 years of SWH data in the BB and AS regions. Multivariate GA applied to the PCs to generate the explicit analytical equations showed again a better strength index for the AS region compared to the BB region, while training

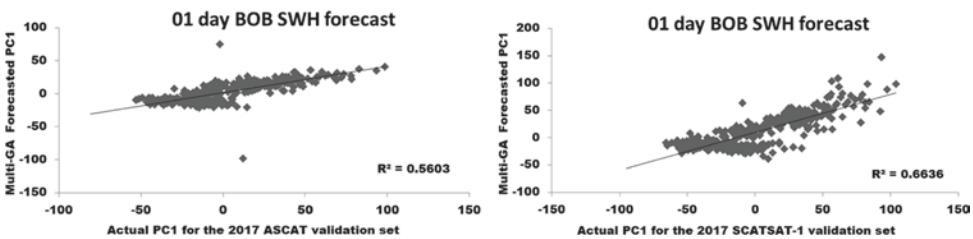

Fig. 1 Scatter plot for BB SWH forecast using 2017 ASCAT and SCATSAT-1 set

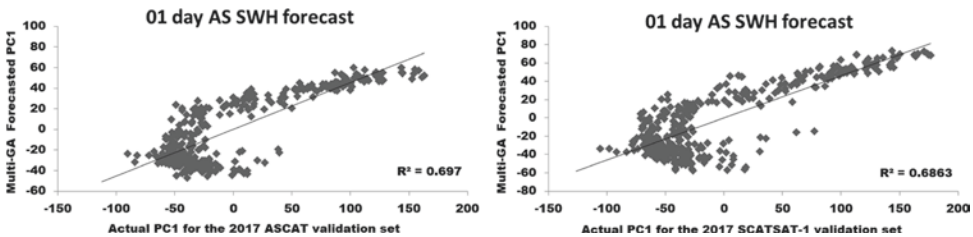

Fig. 2 Scatter plot for AS SWH forecast using 2017 ASCAT and SCATSAT-1 set

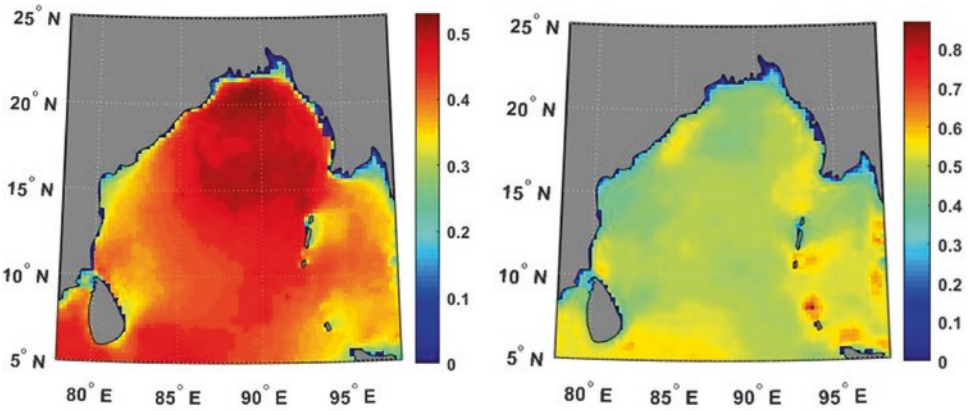

Fig. 3 RMSE map for BB SWH using 2017 ASCAT and SCATSAT-1 data

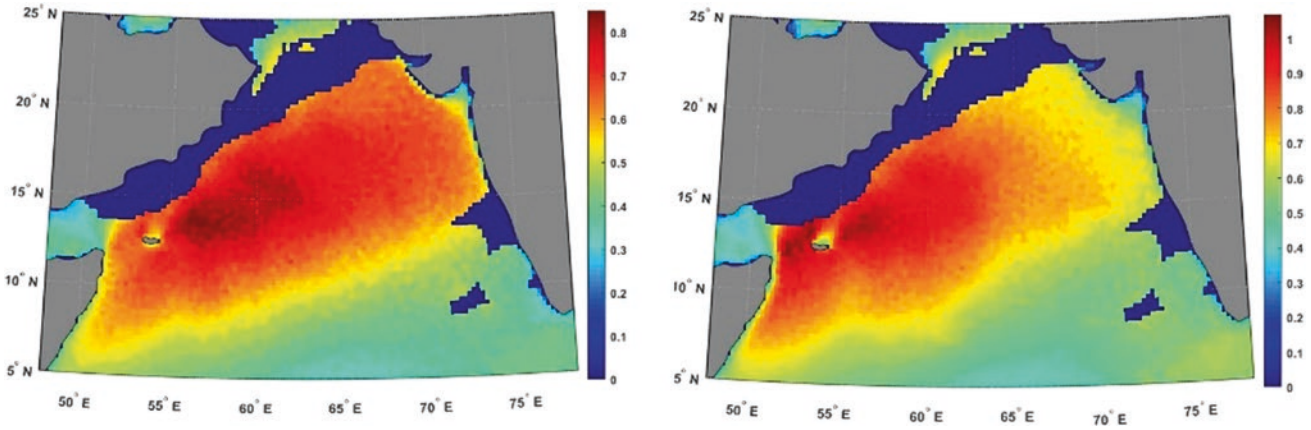

Fig. 4 RMSE map for AS SWH using 2017 ASCAT and SCATSAT-1 data

the algorithm. Previously, similar experiments were conducted by Rao et al. (2013) only for the BB region. Scatter plots generated and the coefficient of determination calculated between the actual and GA predicted PCs showed that the performance of the algorithm was better for the AS than the BB basin. This may be due to the higher percentage of variability of the dominant PC in the AS than the BB. Finally, root mean square error maps were generated between the actual and GA reconstructed wave height values for both basins to study the features. It was observed that the error was more with the SCATSAT-1 sets than the ASCAT sets. This was due to the fact that the training of the algorithm to generate the explicit analytical equations was done with the ASCAT datasets. Comparing AS and BB, the error was more along the Findlater Jet due to its rough characteristics.

5 Conclusion

For the BB and AS regions, multivariate GA was applied to the SWH, U, and V dominant PCs to generate explicit equations for a 01-day forecast. The algorithm performed better for the AS region than the BOB region as the variability of the dominant PC was more in the former case. After testing the equations with independent

validation sets, it was found that for the BB region, the maximum error was in the head and central Bay regions, and for the AS region, the maximum error was along the Findlater Jet.

References

Alvarez, A., Orfila, A., & Tintore, J. (2001). DARWIN: An evolutionary program for nonlinear modeling of chaotic time series. *Computer Physics Communications, 136*(3), 334–349.

Basu, S., Sarkar, A., Satheesan, K., & Kishtawal, C. M. (2005). Predicting wave heights in the north Indian Ocean using genetic algorithm. *Geophysical Research Letters, 32*, L17608.

Rao, A. D., Sinha, M., Neetu, & Basu, S. (2011). Variability of significant wave height over the Indian Ocean using empirical orthogonal function analysis. *The International Journal of Ocean and Climate Systems, 2*(2), 75–85.

Rao, A. D., Sinha, M., & Basu, S. (2013). Bay of Bengal wave forecast based on genetic algorithm: A comparison of univariate and multivariate approaches. *Applied Mathematical Modelling, 37*, 4232–4244.

Sinha, M., Rao, A. D., & Basu, S. (2013). Forecasting space-time variability of wave heights in the Bay of Bengal: A genetic algorithm approach. *Journal of Oceanography, 69*, 117–128.

Takens, F. (1981). Detecting strange attractors in turbulence. In D. Rand, & L. S. Young (Eds.), *Dynamical systems and turbulence*, Warwick 1980. Lecture Notes in Mathematics (Vol. 898). Springer.

A Benchmark InSAR Simulator for Phase Filtering and Coherence Estimation

Xinyao Sun, Aaron Zimmer, Navaneeth Kamballur Kottayil, Subhayan Mukherjee, Parwant Ghuman and Irene Cheng

Abstract

Over the past decade, Interferometric Synthetic Aperture Radar (InSAR) has become a widely accepted and effective remote sensing technique for ground displacement monitoring. InSAR phase filtering and coherence estimation are two key steps to achieve an accurate outcome. However, the challenge is how to precisely validate and eventually optimize the developed algorithms, as no ground truth data with controlled noise is available. In this work, we introduce an InSAR simulator that provides a highly configurable simulation framework to generate a wide variety of phase fringes and coherence distributions. It allows researchers to customize the key configuration parameters and then adopt a mechanism to randomly generate InSAR data with a collection of distinct synthetic features. In addition, our simulator has been used for extensive analysis of several state-of-the-art conventional and deep learning approaches using a pre-configured benchmark dataset with 1800 simulated interferograms. Our simulator can help researchers to compare the strengths and weaknesses of existing algorithms, and guide directions in future studies.

Keywords

InSAR · Simulation · Benchmark · Filtering · Coherence

1 Introduction

Over the years, Interferometric Synthetic Aperture Radar (InSAR) has been widely used for measuring precise wide-area earth's surface displacements with millimetre precision (Deledalle et al., 2010). It has been used in various applications like earth subsidence and uplift detection, gas and oil extraction, estimation of deterioration of roads and railways lines. Accurate measurement of ground displacement requires InSAR data with a high signal-to-noise ratio (SNR). Unfortunately, microwave reflections are usually disturbed by non-stationary noise when recorded by satellite sensors. It results in a noisy single-look complex (SLC) SAR image degrading their interferometric phase. There are many filtering and coherence estimation studies that have been invented in the past decade, from conventional signal processing algorithms (Deledalle et al., 2010, 2014) to recent artificial intelligent models (Mukherjee et al., 2020; Sun et al., 2020). A remaining challenge is how to precisely validate and eventually optimize the developed algorithms, as no ground truth data with controlled noise is available. To date, the most commonly adopted evaluation strategy is using a couple of synthetic interferometric phases with simple geometric shape fringes or simulating the radar signals according to the pre-given digital evaluation model (DEM). Note that there is a lack of large-scale data sets and benchmarks for this research field. Large-scale data is important especially if an application wants to take advantage of the recent learning-based approaches. It is known that the robustness of a trainable model's learning capacity requires diversity in data sets for sufficient training and testing in terms of the types of signal features and noise characteristics. Otherwise, a model could easily suffer from overfitting, which biases the evaluation results. To this end, we introduce a new stochastic 2D InSAR simulator specifically for generating large-scale benchmarks for InSAR phase filtering and coherence estimation studies.

X. Sun (✉) · N. K. Kottayil · S. Mukherjee · I. Cheng
University of Alberta, Edmonton, AB T6G 2R3, Canada
e-mail: xinyao1@ualberta.ca

I. Cheng
e-mail: locheng@ualberta.ca

A. Zimmer · P. Ghuman
3vGeomatics Inc, Vancouver, BC V5Y 0M6, Canada

Z. A. Ergüler et al. (eds.), *Selected Studies in Geotechnics, Geo-Informatics and Remote Sensing*,
Advances in Science, Technology & Innovation, https://doi.org/10.1007/978-3-031-43759-5_3

2 Methods

2.1 Phase Noise Model

SAR satellites produce single-look complex (SLC) images. The returning radar echo from the ground is represented as a complex number in each SLC pixel. The signal model and its degradation version can be characterized by:

$$\begin{aligned} \mathrm{SLC}_{\mathrm{clean}} &= A\cos(\theta) + jA\sin(\theta), \\ \mathrm{SLC}_{\mathrm{noisy}} &= A\cos(\theta) + v_r + j(A\sin(\theta) + v_i) \end{aligned} \tag{1}$$

where A is clean amplitude and θ is clean phase. Noise components v_r and v_i are additive white Gaussian noise (AWGN) in real and imaginary channels, respectively (Deledalle et al., 2014). The corresponding clean interferogram is calculated as:

$$I = (A_{\mathrm{SLC1}} \odot A_{\mathrm{SLC2}})e^{j(\theta_{\mathrm{SLC2}} - \theta_{\mathrm{SLC1}})} \tag{2}$$

2.2 Stochastic Simulator

As illustrated in Eq. 2, the interferometric phase is the wrapped phase difference between two SLCs. Hence, we set one of SLCs' phase components to 0 and only generate synthetic signals on the other one. The key steps of our simulator are: (1) Generate SLC_1 as a $H \times W$ two-dimensional complex image with 0 phase value and with amplitude value growing from $r_{\min}$ to $r_{\max}$ moving from the left-most column to the right-most side following a Rayleigh distribution. (2) Generate SLC_2 with the same resolution and amplitude value as SLC_1, then add a set of signals S to the phase. (3) Add independent additive white Gaussian noise v with standard deviation σ to the real and imaginary channels of both SLC_1 and SLC_2. (4) Generate ground truth clean and noisy interferogram as defined by Eq. 2.

Our simulator focuses on the following InSAR signal features with configurable parameters: (1) Gaussian bubble: range of *spatial scale* and range of Gaussian *amplitudes*. (2) Ellipse: range of *heights* and range of *radii* for both ellipse's first and second axis. (3) Polygon: range of *heights and* range of *radii* for the edges and the range of *number* of polygon edges. (4) Buildings: range of *height*, *width* and *depth_factors* which are used to simulate the height of a building. (5) Amplitude stripes: the approximate *thickness* of the amplitude that is altered in a band region of the *SLC*. (6) Phase stripes: the approximate thickness of the phase band in the interferometric phase. Furthermore, the simulator is designed to add signals in random locations, and there is an extra parameter n defining the number of such types of signals added to the SLC. Lastly, the ground truth coherence is calculated with Monto Carlo approximation by maximum-likelihood coherence metric:

$$\mathrm{cohernece} = \frac{\sum_i^N z_1^{(i)} z_2^{*(i)}}{\sqrt{\sum_i^N \left|z_1^{(i)}\right|^2 \sum_i^N \left|z_2^{(i)}\right|^2}} \tag{3}$$

where z is sampled with amount of N (set to a large number to reduce bias) for each location (r, c) in the synthetic interferogram.

$$z = A_{slc}^{r,c} e^{j} + v_r + jv_i, \text{ where } (v_r, v_i) \sim N\left(0, \sigma^2\right) \tag{4}$$

We adopt an empirical relationship between amplitude and coherence for a specific noise σ to convert the amplitude to coherence for each point.

3 Results

3.1 Visual Samples

After fixing the random seed as well as the configuration, we generated 1800 samples with 1000×1000 resolution as a benchmark data set. Visualization of selected patches' simulated phase (under different configurations) of clean and noisy interferograms as well as the coherence are shown in Fig. 1.

Our proposed benchmark data set has been adopted to evaluate widely used and latest techniques (Sun et al., 2020). Root mean square error (RMSE) (lower is better) and mean structural similarity index map (SSIM) (higher is better) are employed to assess both pixel level accuracy as well as structural level robustness as given in Table 1. Implementation and experimental details can be found in Sun et al. (2020).

4 Discussion

During the simulating process, different types of signals are stochastically generated based on the predefined configurations and summed together to achieve a closely infinite amount of combinations that result in different irregular fringes in the interferometric phase. Our simulator provides various options to control the complexity of the interferometric phase and different distortion levels. It has been successfully adopted in various established works (Mukherjee et al., 2018, 2020; Sun et al., 2020).

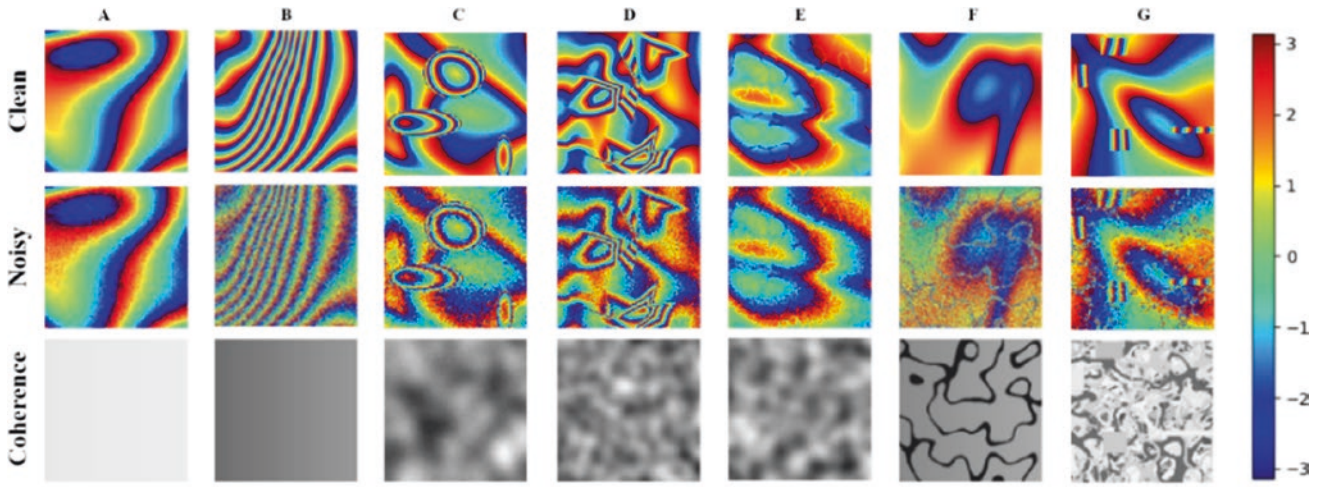

Fig. 1 Column A: low base noise, sparse fringes; B: median base noise, dense fringes; C: ellipse signals; D: polygon signals; E: phase bands; F: low amplitude bands; G: plenty of amplitude bands with building blocks

Table 1 Overall results for each of the tested algorithms (Sun et al., 2020)

Measure	BoxCar (Seymour & Cumming, 1994)	NL-SAR (Deledalle et al., 2014)	NL-INSAR (Deledalle et al., 2010)	DeepInSAR (Sun et al., 2020)
Phase RMSE (Radians)	1.0202	1.0988	1.0020	0.8536
Phase SSIM	0.7223	0.6677	0.7273	0.8666
Coherence RMSE	0.4240	0.4971	0.3139	0.2167
Coherence SSIM	0.3126	0.3935	0.5192	0.7984

5 Conclusions

To the best of our knowledge, this work represents the largest scale performance evaluation benchmark for InSAR filtering and coherence estimation. The source code can be found at https://github.com/Lucklyric/InSAR-Simulator. By introducing our simulator and benchmark, our goal is to help researchers to compare the strengths and weaknesses of existing or new algorithms, and guide the future direction of InSAR phase filtering and coherence estimation.

References

Deledalle, C. A., Denis, L., & Tupin, F. (2010). NL-InSAR: Nonlocal interferogram estimation. *IEEE Transactions on Geoscience and Remote Sensing, 49*(4), 1441–1452.

Deledalle, C. A., Denis, L., Tupin, F., Reigber, A., & Jäger, M. (2014). NL-SAR: A unified nonlocal framework for resolution-preserving (Pol)(In) SAR denoising. *IEEE Transactions on Geoscience and Remote Sensing, 53*(4), 2021–2038.

Mukherjee, S., Zimmer, A., Kottayil, N. K., Sun, X., Ghuman, P., & Cheng, I. (2018, October). CNN-based InSAR denoising and coherence metric. In *2018 IEEE SENSORS* (pp. 1–4). IEEE.

Mukherjee, S., Zimmer, A., Sun, X., Ghuman, P., & Cheng, I. (2020). An unsupervised generative neural approach for InSAR phase filtering and coherence estimation. In *IEEE geoscience and remote sensing letters*.

Seymour, M. S., & Cumming, I. G. (1994, August). Maximum likelihood estimation for SAR interferometry. In *Proceedings of IGARSS'94–1994 IEEE International Geoscience and Remote Sensing Symposium* (Vol. 4, pp. 2272–2275). IEEE.

Sun, X., Zimmer, A., Mukherjee, S., Kottayil, N. K., Ghuman, P., & Cheng, I. (2020). DeepInSAR—A deep learning framework for SAR interferometric phase restoration and coherence estimation. *Remote Sensing, 12*(14), 2340.

Optimized GPR Signals for Improved Buried Cylindrical Objects Detection

Rim Ghozzi, Samer Lahouar and Chokri Souani

Abstract

Ground Penetrating Radar (GPR) is a non-destructive technique based on the analysis of electromagnetic waves propagation phenomena (refraction, reflection, and diffraction) in the underground. It is possible to extract images of underground buried structures by analyzing the received signals (A-scans). In order to obtain accurate GPR measurements, different incident waveforms have been considered, namely: Gaussian, Gaussiandotnorm (normalized first derivative of Gaussian), and Ricker. The source signal at frequency 500 MHz. For the evaluation of the quality of the received signals, a bistatic ground-coupled antenna system is used. In this paper, to optimize the GPR signal that guarantees accurate detection of GPR pulses reflected by a buried cylindrical object, the Finite Difference Time Domain (FDTD) technique is applied. Additionally, GPR scans were obtained by FDTD simulations using two antenna configurations: perpendicular broadside and perpendicular end-fire. The studied object is a cylindrical tube (polyethylene with inner air), with various depths and different diameters, buried in dry sand. The collected data (A-scans) have been generated using the GprMax simulator. The obtained results proved that Ricker is the best incident waveform for the broadside and end-fire antenna. In fact, for the end-fire antenna configuration, the Mean Absolute Percentage Errors (MAPEs) are 12.49%, 3.16%, and 0.53%, while for the broadside antenna configuration, the MAPEs are 13.94%, 6.87%, and 4.59% for Gaussian, Gaussiandotnorm, and Ricker waveforms, respectively. Therefore, for accurately detecting a buried cylindrical tube with GPR, the best configuration is the end-fire antenna with a Ricker incident waveform.

Keywords

Ground Penetrating Radar (GPR) · Non-destructive inspection · Incident waveform · Finite-Difference Time-Domain (FDTD) · Broadside antenna · End-fire antenna

1 Introduction

Owing to Ground Penetrating Radar (GPR) devices, the identification of buried objects and measurement of their depths has become simpler in the recent years. These devices were successfully used on the basis of electromagnetic (EM) analysis methods to find and classify utilities (Eisenmann, et al., 2016; Lai et al., 2017; Prego et al., 2017; Zhao & Al-Qadi, 2017).

The rising curiosity and the use of GPR systems have increased the importance of improving the GPR calculation accuracy. Several studies have been performed in that sense. For example, additional devices have been incorporated with GPR systems in Ferrara et al. (2018), Pilecki et al. (2017) to get higher image resolution. This method was tested, and better measurements were collected, successfully. In (Ghozzi et al., 2018), the authors integrated the findings of the GPR study with visual inspection data to increase the measurement accuracy. In addition, multiple

R. Ghozzi (✉) · S. Lahouar · C. Souani
Laboratoire de Micro-électronique et Instrumentation, Faculté des Sciences de Monastir, Université de Monastir, Av. de l'Environnement, 5000 Monastir, Tunisia
e-mail: ghozzi.rym@gmail.com

R. Ghozzi
École Nationale d'Ingénieurs de Sousse, Université de Sousse, 4023 Sousse, Tunisia

S. Lahouar
Center for Research in Microelectronics and Nanotechnology, CRMN, Technopole of Sousse, 4054 Sousse, Tunisia

C. Souani
Institut Supérieur des Sciences Appliquées et de Technologie de Sousse, Université de Sousse, 4003 Sousse, Tunisia

Z. A. Ergüler et al. (eds.), *Selected Studies in Geotechnics, Geo-Informatics and Remote Sensing*, Advances in Science, Technology & Innovation, https://doi.org/10.1007/978-3-031-43759-5_4

types of incident waveforms were evaluated in Ghozzi et al. (2020) to get better subsurface-reflected GPR signals. This method is the basis of the analysis provided in this paper because the accuracy of data obtained by GPR systems is highly dependent on incident field parameters.

The goal of this paper is to pick the best incident waveforms (Gaussian waveform, Mexican hat waveform, etc.) that can detect buried cylindrical artifacts with enhanced GPR reflections. This is done with the GprMax computational simulator, which is based on the Time-Domain Finite-Difference (FDTD). In this paper, simulation data are used because they enable rapid and reliable testing of various incident GPR waves and configurations without the burden of hardware implementations, particularly in Shangguan and Al-Qadi (2015), it was proven that the FDTD method can be accurately used to simulate GPR waves propagation in dielectric media.

2 Geometry and Antennas Configuration

The GprMax software is a computational simulator used to model GPR structures propagating waves. Dr. Giannopoulos developed it in 1996 based on the FDTD method principle (Giannopoulos, 2005).

With a spatial discretization of $\Delta x = \Delta y = \Delta z = 0.01$ m, the dimensions of the studied model are 0.6 m × 2 m × 2 m. The object studied is a cylindrical tube (polyethylene with inner air), buried in the dry sand of relative permittivity $\varepsilon_r = 3$ with different depths 'h' and various diameters.

Both antennas are 20 cm apart, although they are still 2 cm away from the ground surface. The time window is set to 12 ns. The cylinder radius 'r' is set at 10 cm, 20 cm, and 30 cm, with varying depths of 25 cm, 30 cm, 35 cm, and 40 cm, respectively.

The proper polarization of the GPR system during the scan is important. According to Benedetto and Pajewski (2015), the polarization of the transmitted wave must be parallel to the direction of the target in order to be properly identified. Therefore, the antenna is located in the broadside antenna or end-fire antenna. The underground geometry 3D model along with the transmitter (Tx) and receiver (Rx) antenna location is shown in Fig. 1. A-scans are taken by positioning the GPR antennas above the target and collecting GPR data for a set period of time.

3 Data Analysis and Results

The simplest technique for analyzing the reflected signal based on a trace is to calculate the reflection's peak-to-peak time (Coster et al., 2018; Ghozzi et al., 2017). That is the difference in time between those peaks. The time-delay for each of the A-scans collected is calculated. It is possible to measure the two-way travel time using Eq. (1).

$$\Delta t = \frac{2d\sqrt{\varepsilon_r}}{c} \tag{1}$$

where c is the velocity of the electromagnetic wave ($c = 0.3$ m/ns), ε_r is the relative permittivity of the propagation medium (dry sand $\varepsilon_r = 3$) and d is the depth of target. By calculating the MAPE error (see Fig. 2), defined as follows, the precision of the calculated travel times with different source types and with the broadside and end-fie antenna is assessed:

$$\text{MAPE}(\%) = \frac{100}{N}\sum_{i=1}^{N}\left|\frac{\Delta t_i - \widehat{\Delta t_i}}{\Delta t_i}\right| \tag{2}$$

where $\widehat{\Delta t_i}$ is the estimated value, Δt_i is the real value, and N is the number of scans.

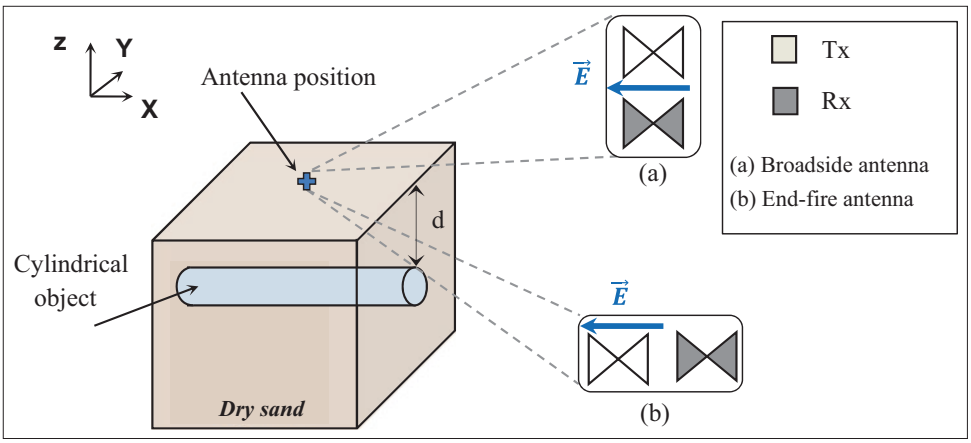

Fig. 1 3D geometry model with configuration of GPR Tx and Rx antenna

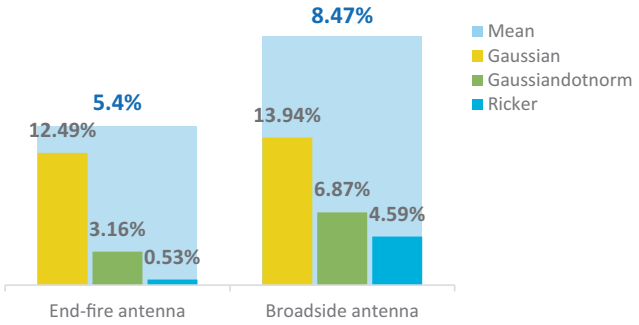

Fig. 2 MAPE results summary for A-scan analysis

4 Discussion

Therefore, we can infer that the Ricker waveform produces the best results for a broadside and end-fire configuration. Furthermore, the end-fire is the optimum configuration for A-scan tests. In truth, the average MAPE is found to be 5.4% for the three kinds of incident waveforms for the perpendicular end-fire configuration, whereas for broadside configuration, the average MAPE of 8.47% is found to be approximately 3% higher.

5 Conclusions

Various types of Ground Penetrating Radar (GPR) incident waveforms and GPR antenna configurations were analyzed and tested in this article. The goal was to identify the best GPR incident signals to ensure that the GPR pulses represented by a buried cylindrical tube are measured accurately and precisely. FDTD simulations of different forms of incident GPR signals were performed accordingly. Simulations of FDTD were then acquired using two configurations of the antenna: broadside and end-fire. The best results were obtained when the incident waveform was Ricker in end-fire and broadside antenna configurations with a Mean Absolute Percentage Error (MAPE) of 5.4% and 8.47%, respectively. Further investigation should be carried out using B-scan.

References

Benedetto, A., & Pajewski, L. (2015). Civil engineering applications of ground penetrating radar. In *Springer transactions in civil and environmental engineering, Italy* (p. 373). https://doi.org/10.1007/978-3-319-04813-0

De Coster, A., Van der Wielen, A., Gregoire, C., & Lambot, S. (2018). Evaluation of pavement layer thicknesses using GPR: A comparison between full-wave inversion and the straight-ray method. *Construction and Building Materials, 168*, 91–104. https://doi.org/10.1016/j.conbuildmat.2018.02.100

Eisenmann, D., et al. (2016). Effects of position, orientation, and metal loss on GPR signals from structural rebar. In 43rd Annual Review of Progress in Quantitative Nondestructive Evaluation (QNDE), 2016 Jul 17–22. Atlanta, GA. https://doi.org/10.1063/1.4974630

Ferrara, V., Pietrelli, A., Chicarella, S., & Pajewski, L. (2018). GPR/GPS/IMU system as buried objects locator. *Measurement, 114*, 534–541. https://doi.org/10.1016/j.measurement.2017.05.014

Ghozzi, R., Lahouar, S., Souani, C., & Besbes, K. (2017). *Peak detection of GPR data with Lifting WaveletTransform (LWT) Advanced Systems and Electric Technologies (IC_ASET)*. IEEE, Hammamet, Tunisia. https://doi.org/10.1109/ASET.2017.7983663

Ghozzi, R., Lahouar, S., Besbes, K., & Souani, C. (2018). Mapping of sewer lines using GPR: A case study in Tunisia. *Data, 3*. https://doi.org/10.3390/data3040040

Ghozzi, R., Lahouar, S., & Souani, C. (2020). *Data quality of the information collected from GPR on a 3D structure* (pp. 66–76). Springer International Publishing. https://doi.org/10.1007/978-3-030-21009-0_6

Giannopoulos, A. (2005). Modelling ground penetrating radar by GprMax. *Construction and Building Materials, 19*, 755–762. https://doi.org/10.1016/j.conbuildmat.2005.06.007

Lai, W. W. L., Ho, M. L. Y., Chang, R. K. W., Sham, J. F. C., & Poon, C. S. (2017). Tracing and imaging minor water seepage of concealed PVC pipe in a reinforced concrete wall by high-frequency ground penetrating radar. *Construction and Building Materials, 151*, 840–847. https://doi.org/10.1016/j.conbuildmat.2017.06.148

Pilecki, Z., et al. (2017). Capabilities of seismic and georadar 2D/3D imaging of shallow subsurface of transport route using the seismobile system. *Journal of Applied Geophysics, 143*, 31–41. https://doi.org/10.1016/j.jappgeo.2017.05.016

Prego, F. J., Solla, M., Puente, I., & Arias, P. (2017). Efficient GPR data acquisition to detect underground pipes. *NDT & E International, 91*, 22–31. https://doi.org/10.1016/j.conbuildmat.2017.06.103

Shangguan, P., & Al-Qadi, I. L. (2015). Calibration of FDTD simulation of GPR signal for asphalt pavement compaction monitoring. *IEEE Transactions on Geoscience and Remote Sensing, 53*, 1538–1548. https://doi.org/10.1109/tgrs.2014.2344858

Zhao, S., & Al-Qadi, I. (2017). Pavement drainage pipe condition assessment by GPR image reconstruction using FDTD modeling. *Construction and Building Materials, 154*, 1283–1293. https://doi.org/10.1016/j.conbuildmat.2017.06.103

Forest Stand Height Estimation Using Inversion of RVoG Model Over Forest of North-Eastern India

Ankita Mungalpara, Sanid Chirakkal, Deepak Putrevu and Suman Mitra

Abstract

Multiple studies have been carried in the recent years to estimate forest height using remote sensing techniques. The forest height is an essential forest resource parameter that is usually used in biomass estimation contributing to carbon sequestration studies. Polarimetric Interferometric SAR (PolInSAR) is a remote sensing technique that combines SAR Polarimetry (PolSAR) with SAR Interferometry (InSAR) and has demonstrated tremendous ability for forest height extraction as it is sensitive to the vertical arrangement of the scattering media. In this paper, we examine the Random Volume over Ground (RVoG), the polarimetric canopy scattering model for the forward modeling, and the three-stage inversion (TSI) for retrieving vegetation stand height. We investigate the performance of the inversion algorithm for forest height estimation using single-baseline L-band ALOS-2 PALSAR data collected on December 17, 2018, and December 31, 2018, over the Saipung Reserve Forest, Meghalaya, over North-Eastern India. The correlation between the field-measured forest height, and the estimated tree height using the TSI technique is 0.81 with an RMSE of 5.05 m. The study suggests that the PolInSAR approach has significant potential for the retrieval of forest biophysical parameters such as stand height.

Keywords

Synthetic Aperture Radar (SAR) · Forest Height Estimation · Polarimetric Interferometric SAR (PolInSAR)

1 Introduction

Vegetation parameter estimation (using remote sensing techniques), at large scale, is very critical to perform ecosystem modeling effectively and to address essential science questions related to climate change, global warming, etc. (Simard et al., 2006). In this short paper, we showcase an algorithm based on single-baseline Polarimetric SAR Interferometry (PolInSAR) to retrieve one of the vital vegetation parameters, viz., the canopy height.

PolInSAR combines the utilities of two SAR technologies: Polarimetry and Interferometry. PolSAR (Fully Polarimetric Synthetic Aperture Radar) provides the three complex scattering matrices at each image pixel, which provides insight into the structural information of the scatterer (geometry, shape, and dielectric constant). Interferometric SAR (InSAR) leads to interferogram generated out of SAR images acquired with an appropriate baseline (spatial or temporal). A common problem for all estimation techniques emerges from the nature of the scattering process. In terms of the interferometric observables, it does not provide an effective separability of the physical forest parameters. This limits a straightforward parameter estimation and requires the inversion of a scattering model, which relates the interferometric observables to the physical parameters of the scattering process (Cloude et al., 1998; Papathanassiou & Cloude, 2001). This is where combining PolSAR with InSAR becomes advantageous. In this paper, we examine the Random Volume over Ground (RVoG), the polarimetric canopy scattering model for the forward modeling, and the three-stage inversion (TSI) for retrieving vegetation stand height. This inversion also estimates other forest parameters

A. Mungalpara (✉) · S. Mitra
DA-IICT, Gandhinagar, Gujarat 382007, India
e-mail: mungalpara.ankita@gmail.com

S. Mitra
e-mail: suman_mitra@daiict.ac.in

S. Chirakkal · D. Putrevu
SAC, ISRO, Ahmedabad, Gujarat 380015, India
e-mail: sanid@sac.isro.gov.in

D. Putrevu
e-mail: dputrevu@sac.isro.gov.in

Z. A. Ergüler et al. (eds.), *Selected Studies in Geotechnics, Geo-Informatics and Remote Sensing*,
Advances in Science, Technology & Innovation, https://doi.org/10.1007/978-3-031-43759-5_5

such as canopy extinction, ground-to-volume amplitude, and ground topographic phase (Cloude & Papathanassiou, 1998).

The study was conducted in Saipung Reserve Forest, East Jantia Hills district (25°11′E to 25°18′E Latitude to 92°34′N to 92°52′N Longitude), which covers 144 km^2, located in Meghalaya, a state situated in the North-Eastern corner of India.

2 Methodology

A realistic scattering model has to consider both the vegetation layer and ground interactions in the case of forest scattering at L-band. A standard model to describe such a scenario is the Random Volume over Ground (RVoG) scattering model (Papathanassiou & Cloude, 2001). This model containing six unknown parameters is optimally inverted using the three complex coherences from the monostatic PolInSAR system, viz., $\tilde{\gamma}_1$, $\tilde{\gamma}_2$, and $\tilde{\gamma}_3$. In this model, the vegetation layer is modeled as a layer of thickness h_V containing a volume with randomly oriented particles and scattering amplitude per unit volume m_V. This cloud of particles is located above a ground scatterer with scattering amplitude m_g. The complex interferometric coherence $\tilde{\gamma}$, after range spectral filtering, written as (Treuhaft et al., 1994; Treuhaft & Siqueira, 2000),

$$\tilde{\gamma}(\omega) = e^{j\phi}\frac{\tilde{\gamma}_v + m(\vec{\omega})}{1 + m(\vec{\omega})} \tag{1}$$

where $\vec{\omega}$ is a unit vector that describes the polarization, $\tilde{\gamma}_v$ is the volume coherence, ϕ is the phase related to the ground topography, and m is the effective ground-to-volume scattering ratio. $\tilde{\gamma}_v$ is defined as (Treuhaft et al., 1994; Treuhaft & Siqueira, 2000),

$$\tilde{\gamma}_v = \frac{I}{I_0}\begin{cases} I = \int_0^{h_V} \exp\left(\frac{2\sigma x}{\cos\theta_0}\right)\exp(i\kappa_z x)dx \\ I = \int_0^{h_V} \exp\left(\frac{2\sigma x}{\cos\theta_0}\right)dx \end{cases} \tag{2}$$

where σ is the wave mean extinction, κ_z is the vertical wavenumber, and θ_0 is the mean incidence angle.

Inversion on Eq. (1) involves taking observations of the complex coherence at several different polarizations and minimizing the difference between the model predictions and observations in the least square manner. Three-stage inversion (TSI) follows three stages, according to Cloude and Papathanassiou (1998) is (1) Least square line fitting, (2) Vegetation bias removal, and (3) Height Estimation. The end-to-end workflow of the forest height estimation technique is given in Fig. 1.

For this analysis, a pair of fully polarimetric ALOS-2 PALSAR data is procured over the Saipung forest region of Meghalaya state in North-East India. We follow the methodology outlined in Fig. 1. The pre-processing involves co-registration of the two PolSAR imagery, up to sub-pixel level accuracy. The complex coherences are estimated for the PolInsAR data and plotted on the complex plane. To invert the model, the three-stage strategy introduced earlier is employed.

3 Results and Discussion

The results of TSI are given in Table 1 for a subset of ground truth points. It shows the estimated height for different field locations in meters collected during the December 2018 expedition to the national reserve forest (carried out through the Principal Chief Conservator of Forests, Meghalaya). It is clear from the table that TSI performs

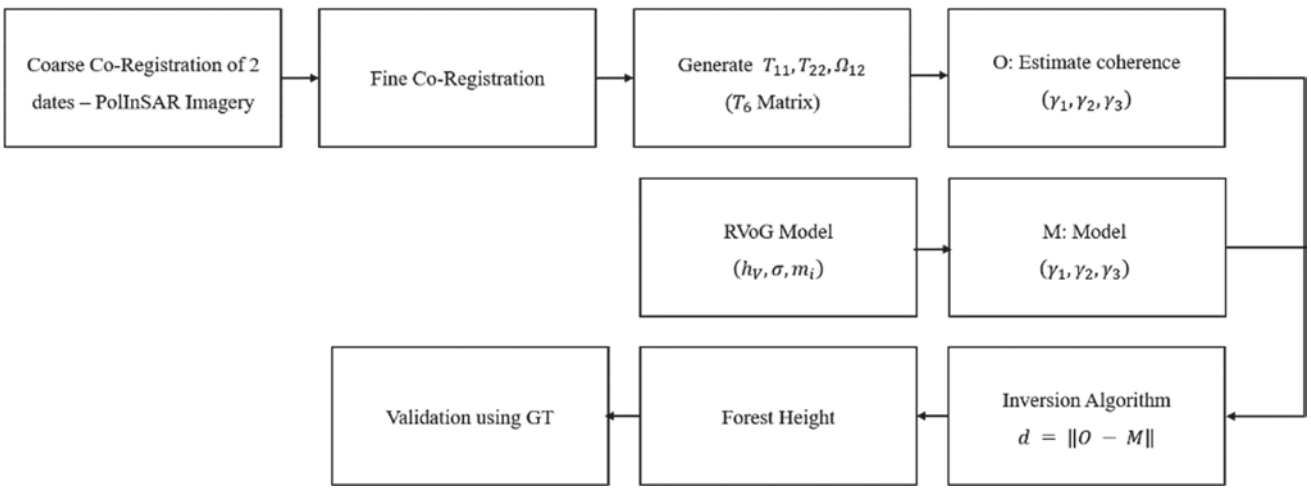

Fig. 1 PolInSAR processing flow for the forest height retrieval using RVoG model

well for our study area with enough sensitivity to the low and high end of the vegetation stand height.

The algorithm has been run for the whole study area to prepare the height map. Figure 2 shows the forest stand height map for Saipung Reserve Forest over the North-Eastern part of India. As can be seen, most of the reserve forest is quite dense with an average height shooting above 25 m.

This research's primary purpose is to estimate forest height from the PolInSAR inversion. A regression analysis was carried out to appraise the accuracy of the TSI method. For this, we use the ground truth data of field-measured height, some of which were already given in Table 1. The correlation coefficient between estimated and field-measured tree height is 0.81 for three-stage inversion. It indicates that the modeled height provides a statistically significant relationship with the field-measured height (Fig. 3).

The RMSE of the retrieval is found to be approximately 5 m. This is in agreement with other studies reported in the literature using single-baseline PolInSAR. This figure can be improved by using multi-baseline techniques or using more sophisticated canopy scattering models.

4 Conclusions

In this work, PolInSAR forest height estimation is established from the L-band dataset acquired from ALOS-2 PALSAR system. The RVoG canopy scattering model and the three-stage inversion have been implemented (Python 3) to estimate vegetation stand height. This study suggests that the PolInSAR technique has significant potential for retrieving forest biophysical parameters such as stand height,

Table 1 Estimated height in meters for the study area

Lat	Long	Field height (m)	Retrieved height (m)
92.74064	25.352757	24	24.76
92.74287	25.34275	27	28.88
92.74774	25.39293	4.3	6.4
92.7491	25.38815	6.1	6.36
92.70664	25.34185	14.6	13.94
92.72391	25.32471	21.2	21.01
92.71197	25.32915	24.4	19.45
92.64638	25.41916	20	21.08
92.63165	25.31202	11.8	4.75
92.64669	25.2713	8.7	5.72

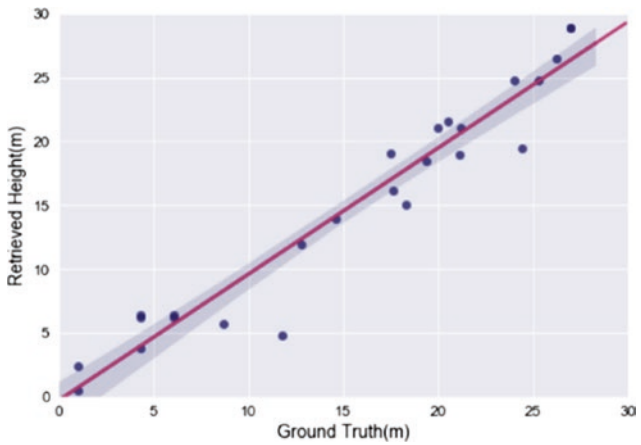

Fig. 3 Retrieved height using three-stage inversion (TSI)

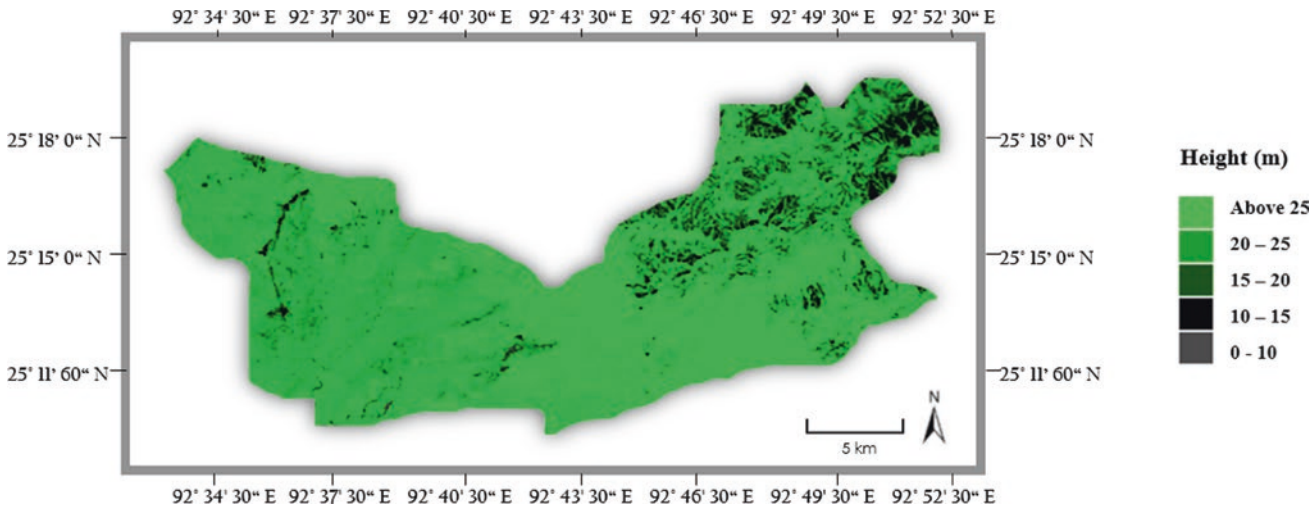

Fig. 2 Saipung Reserve Forest height map derived using the PolInSAR-based technique outlined in the paper. It shows the sensitivity of retrieval to the varying height zones of the reserve forest

and can substantially augment the biomass estimation over areas like reserve forests, where accessibility for field data collection remains difficult.

References

Cloude, S. R., & Papathanassiou, K. P. (1998). Polarimetric SAR interferometry. *IEEE Transaction on Geoscience and Remote Sensing, 36*.

Cloude, S., & Papathanassiou, K. (2003). Three-stage inversion process for polarimetric SAR interferometry. In *Radar, sonar and navigation, IEE proceedings* (Vol. 150, pp. 125–134).

Papathanassiou, K. P., & Cloude, S. R. (2001). Single-baseline polarimetric SAR interferometry. *IEEE Transactions on Geoscience and Remote Sensing, 39*.

Simard, M., Zhang, K., Rivera-Monroy, V. H., Ross, M., Ruiz, P., Castaeda-Moya, E., Twilley, E., & Rodriguez, E. (2006). Mapping height and biomass of mangrove forests in the ever glades National Park with SRTM elevation data. *Photogrammetric Engineering & Remote Sensing, 72*(3), 299–311.

Treuhaft, R. N., Madsen, S. N., Moghaddam, M., & van Zyl, J. (1996). Vegetation characteristics and underlying topography from interferometric radar. *Radio Science, 31*, 1449–1485.

Treuhaft, R., & Siqueira, P. (2000). Vertical structure of vegetated land surfaces from interferometric and polarimetric radar. *Radio Science, 35*.

Monitoring Ground Deformation Through Time-Series Analysis of SAR Data: An Application to Chalkidiki Peninsula, Greece

Stavroula Alatza, Ioannis Papoutsis, Demitris Paradissis and Charalampos Kontoes

Abstract

The objective of the present study is to extract information about the displacement field in the central part of Chalkidiki peninsula, an area poorly investigated by means of SAR interferometry. InSAR time-series analysis was performed on datasets from ERS-2 and Sentinel-1 SAR sensors. Validation was provided by GPS observations near Polygyros city. For Sentinel-1 data, a combination of ascending and descending satellite imaging geometries was performed, to estimate the vertical motion components. SAR results indicate low-rate deformation around Polygyros city, not exceeding − 2 mm/y to 2 mm/y. Negative displacement rates with a maximum value of − 5 mm/y are observed near Olynthos village, indicating the continuation of aquifer overexploitation phenomena near the Moudania watershed after 2014 and the importance of their mitigation.

Keywords

Chalkidiki · InSAR · Time-series · Ground deformation · Aquifer overexploitation

1 Introduction

Chalkidiki peninsula is part of Central Macedonia, in northern Greece. The broader area is very seismically active. In the Chalkidiki region and northern Greece in general, several geodetic networks have been established and operated for various time spans, ranging from 1994 to 2016, with the objective to estimate the kinematic behavior of northern Greece (Mouslopoulou et al., 2014; Rontogianni, 2010). Also, the broader area around Thessaloniki city in the western part of the Chalkidiki peninsula has been studied by means of SAR interferometry, with the objective to map geophysical and anthropogenic deformation phenomena (Mouratidis et al., 2009; Raucoules et al., 2008; Svigkas et al., 2016). This study focuses on monitoring ground deformation phenomena in the central part of the Chalkidiki peninsula and specifically, the broader area around Polygyros city, by means of SAR interferometry by exploiting both historical and recent satellite data.

2 Materials and Methods

For the InSAR time-series analysis, SLC/level-1 data, from 1992 to 2002 and 2014 to 2018 were employed, to extract deformation in the area of interest (see Fig. 1). Twenty-seven (27) SLC images from the ERS-2 sensor of descending track no.7 were selected and analyzed with the combined InSAR method for PS and SBAS of StaMPS/MTI (Multi-Temporal InSAR) (Hooper, 2008) software package. The Stanford Method for Persistent Scatterers was implemented on 34 Sentinel-1A and 1B images, of descending track no.7 and 30 images of ascending track no.102 to map deformation from 2014 to 2018. Specifically, for Sentinel-1 data, the Parallelized Persistent Scatterer Interferometry (P-PSI) (Papoutsis et al., 2020), a processing chain that parallelizes several processing steps of ISCE and StaMPS/MTI software, was employed. To minimize decorrelation phenomena and phase-unwrapping errors, introduced by high relief and dense vegetation, special handling of the parameters during PS processing was required. This approach resulted in a trade-off between the number of the selected PS scatterers and a low signal-to-noise ratio. The open-source Toolbox for Reducing Atmospheric InSAR Noise (TRAIN) (Bekaert et al., 2015) was employed

S. Alatza (✉) · I. Papoutsis · C. Kontoes
National Observatory of Athens, 15236 Athens, Greece
e-mail: alatza@noa.gr

D. Paradissis
National Technical University of Athens, 15780 Athens, Greece

Z. A. Ergüler et al. (eds.), *Selected Studies in Geotechnics, Geo-Informatics and Remote Sensing*,
Advances in Science, Technology & Innovation, https://doi.org/10.1007/978-3-031-43759-5_6

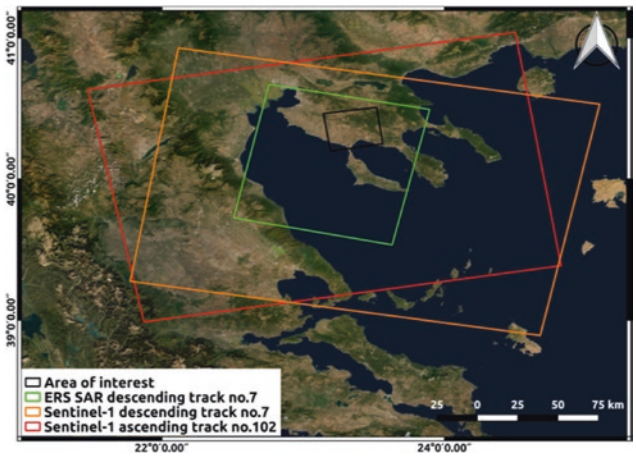

Fig. 1 Map of the area of interest in the Chalkidiki peninsula and the corresponding satellite footprints. The broader area of Polygyros city is depicted with the black rectangle, while the colored rectangles represent the satellite footprints

for the estimation and removal of the tropospheric contribution from the deformation phase. Since the area around Polygyros is characterized by intense topography, the linear correction provided a satisfying accuracy.

3 Results and Discussion

Low-rate velocities, not exceeding 2 mm/y toward and away from the satellite, are observed in the majority of the area under investigation (see Fig. 2). No alterations in the LOS deformation pattern between the two time periods are observed (see Fig. 2a–c). Low mean standard deviation LOS velocities (0.5 mm/y for Sentinel-1 data of ascending track no.102, 0.6 mm/y for Sentinel-1 data of descending track no.7 and 0.7 mm/y for ERS-2 data) hint that low-rate linear deformation occurs and that there is no bias in the estimated displacements. As expected, a higher rate of PS scatterers per km^2 (188 PS/km^2 for ERS data, 354 PS/km^2, and 260 PS/km^2 for Sentinel-1 data of ascending and descending tracks, respectively) is detected in the city of Polygyros. The PS density is significantly reduced (19 PS/km^2 for ERS data, 14 PS/km^2, and 5 PS/km^2 for Sentinel-1 data of ascending and descending tracks, respectively), near Mt. Cholomon Forest, to the north of Polygyros. An area around a GPS station, located near Vrastama village was selected as a reference, based on its stability in the north motion component. A subsiding area is identified near the Olynthos site, with a maximum deformation of −5 mm/y (see Fig. 2b, c). For

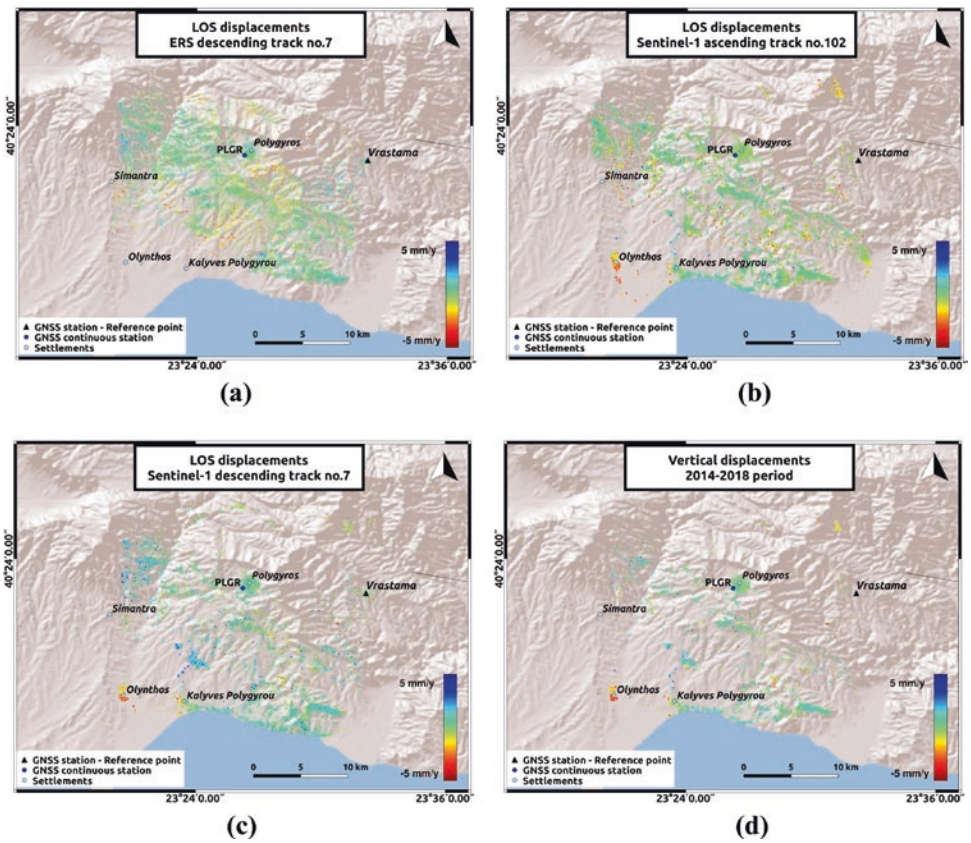

Fig. 2 **a** PS-SBAS combination LOS displacements for ERS data. **b** PS LOS velocities of Sentinel-1 data (ascending track 102). **c** PS LOS velocities of Sentinel-1 data (descending track 7). **d** Vertical displacements for the 2014–2018 period. The reference area near Vrastama village is marked with the black triangle. Also, the location of the GNSS continuous station PLGR is presented

Sentinel-1 results, a decomposition of the line-of-sight displacements in the descending look direction was performed to estimate the vertical displacements (see Fig. 2d) by implementing the system of equations of Samieie-Esfahany et al. (2009) and the methodology proposed by Papoutsis et al. (2017). Available observations from the PLGR GNSS station from 2013 to 2016 were compared to SAR results for the 2014–2018 time period. An absolute comparison between these two datasets is unfeasible. However, a transformation of the PLGR NEU motion components ($N = 0.00526$ m/y, $E = 0.00251$ m/y, $U = -0.00077$ m/y) to the slant range direction, using Eq. 1 by Hanssen and Interferometry (2001), resulted to 0.1408 mm/y in the LOS direction, which also denotes a non-deforming area around Polygyros city.

$$u = u_{\mathrm{Up}} \cos(\theta_{\mathrm{inc}}) - \sin(\theta_{\mathrm{inc}}) \left[u_N \cos\left(\alpha_h - \frac{3\pi}{2}\right) + u_E \sin\left(\alpha_h - \frac{3\pi}{2}\right) \right] \quad (1)$$

where $\alpha_h - \frac{3\pi}{2}$ corresponds to the perpendicular to the satellite heading angle in the azimuth look direction, for a right-looking satellite and θ_{inc} corresponds to the incidence angle.

Considering the geodynamic field of the western Chalkidiki region, which belongs to a weakly deformed block (Kougoulis et al., 2007), the stability observed in the broader area of Polygyros city, during both time periods, appears to be a reasonable conclusion. Evidence that the aquifer of Nea Moudania, in the western part of the Chalkidiki region, is overexploited which is provided by several piezometric studies (Siarkos & Latinopoulos, 2016; Veranis et al., 2016). Olynthos is among the sites where a piezometric decline is observed for the 2003–2014 time period. Negative LOS (see Fig. 2b, c) and vertical (see Fig. 2d) displacements, estimated for the 2014–2018 time period, near Olynthos village, clearly depict that water balance in the area might not have been restored after 2014, and that overexploitation of the Moudania watershed continues. This observation is also highlighted in Svigkas et al. (2396), through an InSAR analysis from 2015 to 2019, validated by ground truth data.

4 Conclusions

An extensive study was performed focused on the central part of Chalkidiki with the objective to identify the type of deformation that occurs and its relation with natural processes or human activities. SAR results indicate low-rate deformation in most parts, around Polygyros city, not exceeding − 2 mm/y and 2 mm/y, an observation which is also verified by GPS measurements. A noteworthy phenomenon is subsidence near Olynthos village with a maximum rate of − 5 mm/y, attributed to overexploitation of the Moudania watershed, denoting a continuous phenomenon from 2003 to 2018, which needs to be addressed. Finally, with the addition of SAR results for the intermediate time period between 2002 and 2014, which is a work in progress, we aim to achieve a complete overview of the deformation field in the central part of the Chalkidiki peninsula and its association with tectonic or anthropogenic activities.

References

Bekaert, D. P. S., Walters, R. J., Wright, T. J., Hooper, A. J., & Parker, D. J. (2015). Statistical comparison of InSAR tropospheric correction techniques. *Remote Sensing of Environment, 170*, 40–47.

Hanssen, R. (2001). Radar interferometry: Data interpretation and error analysis. In F. van der Meer (Ed.), *Remote sensing and digital image processing* (2nd ed.). Kluwer Academic Publishers.

Hooper, A. (2008). A multi-temporal InSAR method incorporating both persistent scatterer and small baseline approaches. *Geophysical Research Letters, 35*, L16302.

Kougoulis, C., Arvanitis, A., Kolios, N., Koutsinos, S., & Kougoulis, J. (2007). Geothermal exploration in the Sani-Afytos area of the Kassandra peninsula (Chalkidiki peninsula, Northern Greece). *Bulletin of the Geological Society of Greece, 40*(3), 1162–1176.

Mouratidis, A., Briole, P., Ilieva, M., Astaras, T., Rolandone, F., & Baccouche, M. (2009). Subsidence and deformation phenomena in the vicinity of Thessaloniki (N. Greece) monitored by Envisat/ASAR interferometry. In *Proceedings of the Fringe 2009 Workshop: Advances in the Science and Applications of SAR Interferometry*, Frascati, Italy, 30 November–4 December 2009.

Mouslopoulou, V., Saltogianni, V., Gianniou, M., & Stiros, S. (2014). Geodetic evidence for tectonic activity on the Strymon fault system, Northeast Greece. *Tectonophysics, 633*, 246–255.

Papoutsis, I., Kontoes, C., Alatza, S., Apostolakis, A., & Loupasakis, C. (2020). InSAR Greece with parallelized persistent scatterer interferometry: A national ground motion service for big copernicus sentinel-1 data. *Remote Sens., 12*, 3207.

Papoutsis, I., Kontoes, C., & Paradissis, D. (2017). Multi-track persistent scatterer interferometry analysis in wider Athens, Greece. *Remote Sensing, 9*(3), 276.

Raucoules, D., Parcharidis, I., Feurer, D., Novalli, F., Ferretti, A., Carnec, C., Lagios, E., Sakkas, V., Le Mouélic, S., Cooksley, G., et al. (2008). Ground deformation detection of the greater area of Thessaloniki (Northern Greece) using radar interferometry techniques. *Natural Hazards and Earth Systems Sciences, 8*, 779–788.

Rontogianni, S. (2010). Comparison of geodetic and seismic strain rates in Greece by using a uniform processing approach to campaign GPS measurements over the interval 1994–2000. *Journal of Geodynamics, 50*, 381–399.

Samieie-Esfahany, S., Hanssen, R., van Thienen-Visser, K., & Muntendam-Bos, A. (2009). On the effect of horizontal deformation on InSAR subsidence estimates. In *Proceedings of the Workshop Fringe 2009, Frascati, Italy*, 30 November–4 December 2009.

Siarkos, I., & Latinopoulos, P. (2016). Modeling seawater intrusion in overexploited aquifers in the absence of sufficient data: Application to the aquifer of Nea Moudania, Northern Greece. *Hydrogeology Journal, 24*, 2123–2141.

Svigkas, N., Loupasakis, C., Papoutsis, I., Kontoes, C., S. Alatza, S., Tzampoglou, P., Tolomei, C., & Spachos, T. (2020) Insar campaign reveals ongoing displacement trends at high impact sites of Thessaloniki and Chalkidiki, Greece. *Remote Sensing, 12*(2396).

Svigkas, N., Papoutsis, I., Loupasakis, C., Tsangaratos, P., Kiratzi, A., & Kontoes, C. H. (2016). Land subsidence rebound detected via multi-temporal InSAR and ground truth data in Kalochori and Sindos regions, Northern Greece. *Engineering Geology, 209*, 175–186.

Veranis, N., Nimfopoulos, M., Christidis, C., & Chrysafi, A. (2016). Granular aquifer system of West Chalkidiki area, region of Central Macedonia, Northern Greece. *Bulletin of the Geological Society of Greece, 50*(2), 1016–1026.

The Applicability of Reflectance Spectral Features and Remote Detection for Radioactive Mineral Exploration in Mamuju, West Sulawesi, Indonesia

Arie Naftali Hawu Hede, Yogi La Ode Prianata, Syafrizal, Mohamad Nur Heriawan and Heri Syaeful

Abstract

Mamuju region in West Sulawesi, Indonesia, has the highest radiation dose rate of naturally occurring radioactive materials in Indonesia. The high radioactivity in Mamuju is derived from tertiary alkaline volcanic rocks. This research aimed to assess the applicability of reflectance spectroscopy analysis to identify minerals, develop a spectral database, and then use Sentinel-2 multispectral satellite imagery integrated with digital elevation model data to map potential areas. Reflectance spectra were measured and developed into a spectral database used for spectral-based analysis in remote detection using Sentinel-2 imagery. Several mapping methods, including spectral angle mapper, linear spectral unmixing, band composite, and directed principal component analysis were applied to generate mineral distribution maps. The identification of geological structures was completed using a lineament analysis-based method. The reflectance analysis revealed strong absorption in visible, near-infrared ranges potentially related to the iron oxide/hydroxide. Clay minerals, including sulfates, NH_4 species, and phyllosilicate minerals were successfully identified in the shortwave infrared range. However, target radioactive minerals, such as davidite, thorianite, gummite, and autunite, were difficult to identify using spectral analysis. The altered areas were mapped using Sentinel-2 in certain areas, and the geological structures extracted from the lineament analysis showed that radioactive mineralization occurs in the southeast-northwest. Results demonstrated that the application of a remote sensing-based method for identifying and mapping potential areas could be a key for future radioactive mineral exploration.

Keywords

Reflectance spectroscopy · Radioactive mineral · Remote sensing · Exploration

1 Introduction

The foremost radioactive mineral prospect in Indonesia is in Mamuju, West Sulawesi, with high radiation dose rates from naturally occurring radioactive materials, in some areas higher than 5 mSv/y (Syaeful et al., 2014). This region's high radioactivity is related to tertiary alkaline volcanic rocks of the Adang volcanic complex (Syaeful et al., 2014). Thus, mapping potential areas for radioactive minerals is an essential part of exploration phases. Remote sensing has proven its applicability for mapping various types of mineral deposits.

The goal of this research was to assess remote detection applicability to identify radioactive mineral prospect areas. Two basic principles were used in this research: reflectance spectroscopy and lineaments analysis. Reflectance spectra of samples were measured to develop a spectral database for imaging spectroscopy analysis. An assessment of optical imaging Sentinel-2 was used to examine alteration zones that might be related to radioactive mineral distribution. Since uranium and thorium mineralization is controlled by tectonic activities which may create structures, the identification of geological structures was needed. Geological

A. N. H. Hede (✉) · Syafrizal · M. N. Heriawan
Earth Resources Exploration Research Group, Faculty of Mining and Petroleum Engineering, Bandung Institute of Technology, Bandung 40132, Indonesia
e-mail: ariehede@itb.ac.id

Y. L. O. Prianata
Graduate Program of Mining Engineering, Faculty of Mining and Petroleum Engineering, Bandung Institute of Technology, Bandung 40132, Indonesia

H. Syaeful
Research Center for Nuclear Fuel Cycle and Radioactive Waste Technology, Research Organization for Nuclear Energy (ORTN), National Research and Innovation Agency (BRIN), South Tangerang 15314, Indonesia

Z. A. Ergüler et al. (eds.), *Selected Studies in Geotechnics, Geo-Informatics and Remote Sensing*, Advances in Science, Technology & Innovation, https://doi.org/10.1007/978-3-031-43759-5_7

structure interpretation was completed using the Digital Elevation Model Nasional (DEMNAS; Indonesian DEM) data with a lineament analysis-based method.

2 Materials and Methods

The study area is situated in Mamuju, West Sulawesi, Indonesia, and samples were collected from several locations (Fig. 1a). Reflectance spectra were measured using the Analytical Spectral Device FieldSpec4 within the visible near-infrared (VNIR) to shortwave infrared (SWIR) ranges (350–2500 nm). Analysis of radioactive (uranium and thorium) and rare earth elements was performed using inductively coupled plasma mass spectrometry. In addition, this research also used geochemical data of near-surface soils (Mu'awanah et al., 2018).

Remotely sensed data of Sentinel-2 acquired on August 3, 2018 and DEMNAS were used for spectral-based analysis and extract lineaments for geological structure interpretation, respectively. Image preprocessing involved standard generic procedures and was completed using Sentinel Application Platform (SNAP). Spectral-based analyses such as spectral angle mapper, linear spectral unmixing, band composite, and directed principal component analysis were applied for mapping minerals. Structural mapping relied on the processing of DEMNAS by lineaments extracted using semi-automated algorithms (Msaddek et al., 2019).

3 Results

3.1 Geochemical and Spectral Reflectance Analyses

Mamuju's average uranium and thorium contents were relatively higher compared with the earth's crust. Based on the previous research, radioactive minerals formed as davidite, thorianite, gummite, and autunite (Sukadana et al., 2018). These minerals also contain rare earth elements. The high radioactive soil content also suggested that these elements experienced a surface reaction in weathering, washing, and secondary enrichment (Mu'awanah et al., 2018).

Reflectance spectra pattern identification showed at least two pattern types, which related to strong absorption features (Fig. 1b). The first type was related to iron/oxide/hydroxide that showed definitive features in the VNIR region (e.g., sample ID MJU_25_2013, MJU_33_2013, and MJU_A_36511). The second type was related to the presence of clay dominated by phyllosilicate minerals (biotite and chlorite), which was identified in the SWIR region (e.g., sample ID TKD-026, MJU_50_2013, MJU_A_36752, and MJU_26_2013). Another common clay mineral including sulfates and NH_4 species was also identified within this range.

3.2 Image Analyses

Two area sectors indicated anomalous radioactive contents: Ahu in the southwest and Tapalang in the northeast (Mu'awanah et al., 2018; Syaeful et al., 2014) (Fig. 2a). The intensive hydrothermal alteration occurred and was widespread in this region, indicating the emergence of altered mineral assemblages. Moreover, the presence of biotite, chlorite, actinolite, adularia, and other clay minerals indicated the alteration zone was the potassic type (Sukadana et al., 2018). Sentinel-2 mineral band ratios used to stimulate minerals related to iron oxide/hydroxide, clay minerals, and phyllosilicate (biotite and chlorite) were band4/band3, band11/12, and band 12/11, respectively. Figure 2b illustrates the interpretation of alteration related to phyllosilicate after band ratio method combined with directed principal component analysis to suppress

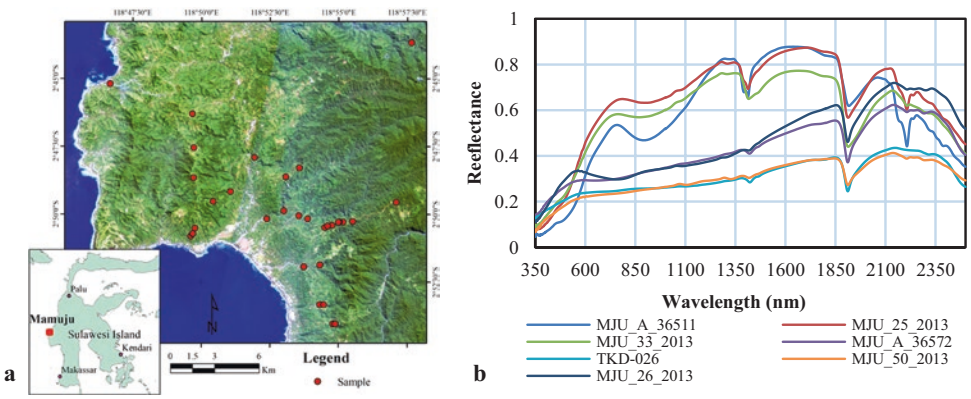

Fig. 1 **a** Location of the study area in Mamuju, West Sulawesi based on Sentinel-2 true color composite. **b** Typical reflectance spectra of samples (7 of the 30 samples)

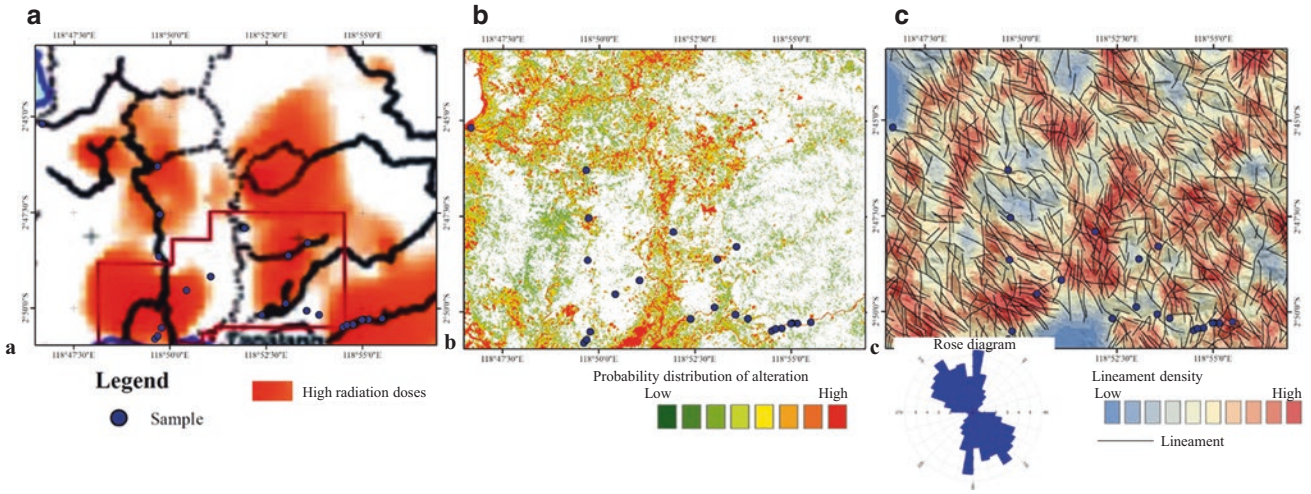

Fig. 2 Comparison between maps of **a** high radiation doses (Syaeful et al., 2014), **b** probability distribution of alteration, and **c** lineaments and lineament density

vegetation components. Lineaments analysis demonstrated that radioactive mineralization occurred in the southeast-northwest trending structure (Fig. 2c).

4 Discussion

Reflectance spectroscopy successfully identified mineral assemblage, which can be related to alteration. By knowing the zone of alteration, uranium exploration can be developed in deeper areas or areas with reductive conditions, allowing the formation of uranium oxide deposits (Sukadana et al., 2018). Imaging spectroscopy using Sentinel-2 following several procedures such as spectral angle mapper, linear spectral unmixing, band composite, and directed principal component analysis was applied. However, spectral angle mapper and linear spectral unmixing were not successful in mapping the mineral distribution due to dense vegetation conditions. As an alternative, band ratio combined with principal component analysis can be used and successfully enhance the alteration zones. Lineament analysis showed that geological structures control the distribution of radioactive anomalies in Mamuju.

5 Conclusions

This research demonstrated the application of reflectance spectroscopy for detecting the mineralogical information of samples from Mamuju, West Sulawesi, Indonesia. In addition, the research illustrated the application of a remote sensing-based method for identifying and mapping potential areas that can be a key for future radioactive mineral exploration.

References

Msaddek, M. H., Moumni, Y., Chenini, I., & Dlala, M. (2019). Applicability of developed algorithm for semi-automated extraction and morphotectonic interpretation of lineaments using remotely sensed data, Southwestern Tunisia. *Remote Sensing in Earth Systems Sciences, 2*(4), 292–307.

Mu'awanah, F. S., Priadi, B., Widodo, Sukadana, I. G., & Ardiansyah, R. (2018). Uranium mobilty on active stream sediment in Mamuju area, West Sulawesi. *Eksplorium, 39*(2), 95–104.

Sukadana, I. G., Indrastomo, F. D., & Ngadenin. (2018). Distribution of rock alteration based on Th/U ratio in Tapalang, Mamuju, West Sulawesi. *Riset Geologi Dan Pertambangan, 28*(2), 141–155.

Syaeful, H., Sukadana, I. G., & Sumaryanto, A. (2014). Radiometric mapping for naturally occurring radioactive materials (NORM) assessment in Mamuju West Sulawesi. *Atom Indonesia, 40*(1), 33–49.

Comparative Analysis of Different Vegetation Indices and Analysis of the Effects of Heavy Metals on Vegetation Using Sentinel Data

Khaoula Ben Attia Zrouga, Faiza Allouche khebour, Maria Paula Mendes, Ana Paula Falcão and Bouthaina Dridi Almohandes

Abstract

Dust emissions from the cement plant of Gabes (south of Tunisia) can affect vegetation cover. A methodological approach based on remote sensing data analysis was employed. Three satellite images (Sentinel-2 data) and four remote sensing-based indices (NDVI, SAVI, EVI, and ARVI) were calculated to establish the relation between spectral response and different heavy metals concentration and/or aerosols contents in the air. Three heavy metals (Cu, Pb, and Zn) contents were evaluated in 30 leaf samples for six plant species considering the distance from the cement plant. The results showed that EVI, NDVI, and SAVI gave similar results with lower values in 2018 (dryer year). On the other hand, ARVI showed higher values in 2018, which can be attributed to the emissions of the cement plant. CPA's analysis showed that *Helianthemum kahiricum* and *Zygophyllum* album presented high values of these four indices in 2018, although revealing high contents of Cu and Zn on the leaves. This steppic vegetation has a high capability to bioaccumulate these two metals. Results suggest that ARVI could be used to assess the state of vegetation in areas affected by dust deposition, allowing precise monitoring and management of vegetated areas.

Keywords

Vegetation indices · Plant species · Remote sensing · Heavy metals · Gabes-Tunisia

1 Introduction

Dust pollution caused by the cement plant of Gabes (south of Tunisia) affects several ecosystem compartments including soil and vegetation. Vegetation indices have been used to identify spectral vegetation changes under heavy metal pollution and to measure the effects of heavy metal environmental stress in plants (Asmaryan et al., 2013; Van Deventer & Cho, 2014, Amer et al., 2017; Zhou et al., 2018). In order to understand these effects on natural vegetation cover, a methodological approach based on remote sensing data analysis was employed. Three free satellite images (Sentinel-2A MSI; pixel size around 10 m; multispectral bands 2, 4, and 8), obtained on 12/12/2016, 22/12/2018, and 22/12/2019, were used. The use of Sentinel-2A images is explained by the fact that it has high time resolution providing a significant advantage in the collecting of complex knowledge about vegetation conditions (Shivangi and Kumari, 2020). Radiometric indices (NDVI, SAVI, EVI, and ARVI) were estimated in order to assess indirectly the effect of heavy metals (Cu, Zn, and Pb) in plant cover reflectance. These indices were estimated in sites covered by six plant species (*Olaea europaea, Zygophyllum album, Helianthemum kahiricum, Ficus carica, Prunus persica vulgaris, and Medicago sativa*). Variations between the three-year vegetation indices will be estimated to assess a relationship between the spectral response and the proximity of the cement plant.

K. B. A. Zrouga (✉) · B. D. Almohandes
Department of Horticultural Sciences and Landscape, High Institute of Agronomic Sciences of Chott Meriem (ISA-CM), Sousse University, B.P. 47, 4042 Chott Mariem, Sousse, Tunisia
e-mail: kbenattia2017@gmail.com

F. A. khebour
Lr GREE TEAM (LR17AGR01), High Institute of Agronomic Science-Chott Meriem, University of Sousse, ISA CM, BP 47, 4070 Sousse, Tunisia

M. P. Mendes · A. P. Falcão
CERIS, Civil Engineering Research and Innovation for Sustainability, Instituto Superior Técnico, Universidade de Lisboa, Av. Rovisco Pais, 1049-001 Lisbon, Portugal
e-mail: mpaulamendes@tecnico.ulisboa.pt

A. P. Falcão
e-mail: ana.p.falcao@tecnico.ulisboa.pt

Z. A. Ergüler et al. (eds.), *Selected Studies in Geotechnics, Geo-Informatics and Remote Sensing*, Advances in Science, Technology & Innovation, https://doi.org/10.1007/978-3-031-43759-5_8

2 Materials and Methods

Significant work has been done to automate the retrieval of time series of data available directly over the Internet (Sentinel-2A data and meteorological data) (Hardy et al., 2020). After downloading data, the first step consists of the atmospheric correction by the method of dark objective subtraction (DOS) (Schläpfer et al., 1998; Richter et al., 2011). Following this pretreatment step, four vegetation indices (Normalized Different Vegetation Index-NDVI, Soil Adjusted Vegetation Index-SAVI, Enhanced Vegetation Index-EVI and, Atmospherically Resistant Vegetation Index-ARVI) are calculated using Qgis software based on the equations listed in Table 1.

Considering the distance from the cement factory, 30 leaf samples from six species such as *Olea europaea, Zygophyllum album, Helianthemum kahiricum, Ficus carica, Prunus persica vulgaris, and Medicago sativa* were sampled in December 2018 to measure their heavy metal contents (Cu, Zn, and Pb). Twenty-four leaf samples were collected near the cement plant, and six control samples were taken farther, at an approximate distance of 10 km from the plant. The leaf samples were grouped in 11 clusters, according to their location, identified by alphabetical order, from A to K (Fig. 1). To establish potential relations between radiometric indices and the content of each metal on the leaves, the average contents of the latter were estimated. A principal component analysis (PCA) was performed to identify patterns between spectral response, vegetation, and heavy metals contents in the leaves.

3 Results

3.1 Multi-temporal Evaluation of Radiometric Indices

At a local scale, EVI, NDVI, and SAVI vegetation indices maps gave similar results (Fig. 2) with a higher average in 2016 (EVI = 0.30, NDVI = 0.26, and SAVI = 0.19 for 2016; EVI = 0.11, NDVI = 0.11, and SAVI = 0.09 for 2018; EVI = 0.12, NDVI = 0.17, and SAVI = 0.14, for 2019). The PM10 values were higher in December 2018 (0.07 mg/m^3) than in December 2016 (0 mg/m^3). 2016 presented the higher values of these three indices.

Table 1 Vegetation indices and respective equations and references

Vegetation indexes	Sentinel-2 bands used	Original author
NDVI	(B8 − B4) / (B8 + B4)	Tucker (1979)
SAVI	[(B8 − B4)/(B8 + B4 + L)] ∗ (1 + L); ***L**: Soil adjustment parameter (In our study case L = 0.5)*	Huete (1988)
EVI	G* (B8-B4) / (B8 + C1*B4-C2*B2 + L), ***G**: Gain factor (equal to 2.5)*; ***L**: Soil adjustment factor (=1); **C1** and **C2**: correction coefficients of atmospheric diffusion (In our study case **C1** = 6 and **C2** = 7.5)*	Huete et al. (1999)
ARVI	((B8) − (2B4 − B2) / (B8) + (2B4 − B2))	Kaufman and Tanré (1992)

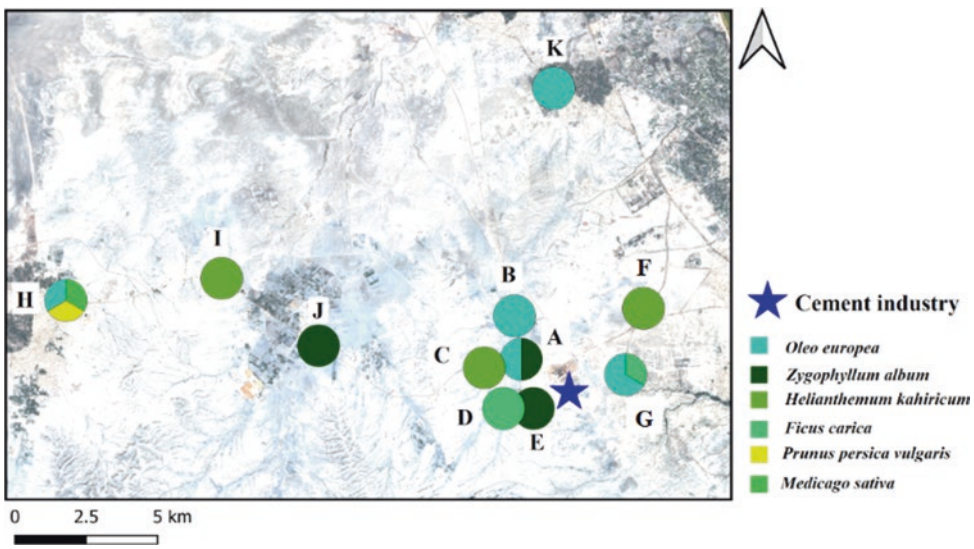

Fig. 1 Spatial distribution of the plant species in the study area

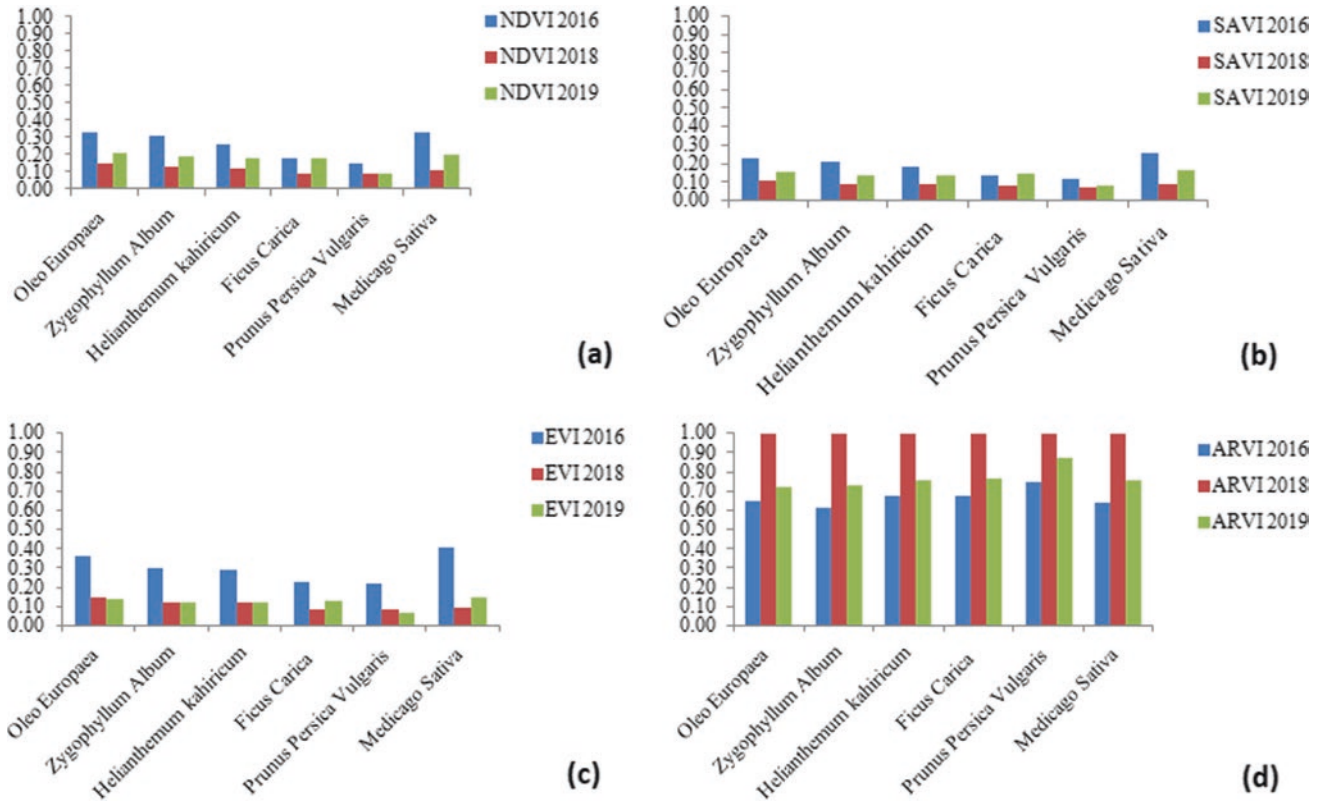

Fig. 2 Temporal variation of the different radiometric indices **a** NDVI, **b** SAVI, **c** EVI, and **d** ARVI for the plant species studied

The ARVI results (Fig. 2d) were different, showing sparser vegetation covering for the years 2018 and 2019 (average values of 0.67, 1.00, and 0.77 for 2016, 2018, and 2019, respectively).

Prunus persica vulgaris presented the highest peaks of ARVI during the three years. This species showed the lower peaks for EVI, SAVI, and ARVI. These results can be in part explained by the precipitation amounts during these three years. In December of 2016, precipitation was 61.02 mm/year (higher radiometric indices), decreasing in 2018 to 1.67 mm/year, and recovering in December of 2019 to 19.83 mm/year (renewed increasing of radiometric indices). The PM10 values recorded in 2016 were 0.05 and 0.00 mg/m^3 for November and December in 2016. In 2018, the values were equal to 0.03 and 0.07 mg/m^3 for these two consecutive months.

The highest values of NDVI and SAVI indices were obtained in the year 2016 (0.85 and 0.63, respectively; Fig. 3a). In the case of EVI and ARVI, 2018 presented higher and the same values (1.00; Fig. 4b). This fact may be due to the increase of annual precipitation from 2016 to 2018 (146.75 to 189.29 mm/year, respectively). Finally, clusters K and H covered by *Olea europaea, Prunus persica vulgaris,* and *Medicago sativa* presented the highest values of NDVI, SAVI, and EVI for all studied periods. These clusters are located on the control sites.

3.2 Application of Principal Component Analysis (ACP)

The first (F1) and second principal components (F2) contained 80.5% of the variance in the data subset (Fig. 4). ARVI had a distinct behavior compared to the other three vegetation indices (NDVI, SAVI, and EVI). The 2019 and 2016 vegetation indices are more correlated than the 2018 indices. Cu and Zn contents in the leaves were correlated. *Medicago sativa* and *Olea Europaea* presented a very distinct spectral response, showing the last plant with higher values of NDVI, SAVI, and EVI for the three years. *Helianthemum kahiricum* and *Zygophyllum album* showed higher contents of Cu and Zn. *Ficus Carica* had high contents of Pb on the leaves.

4 Discussion

The temporal analysis of SAVI, EVI, and ARVI indices may be related to the meteorological and agro-pedological factors of the environment which are decisive in the growth cycle of plants and, therefore, in the variation of the intensity of the chlorophyll activity measured by these indices (Diello et al., 2005). In 2016 and 2019, they were

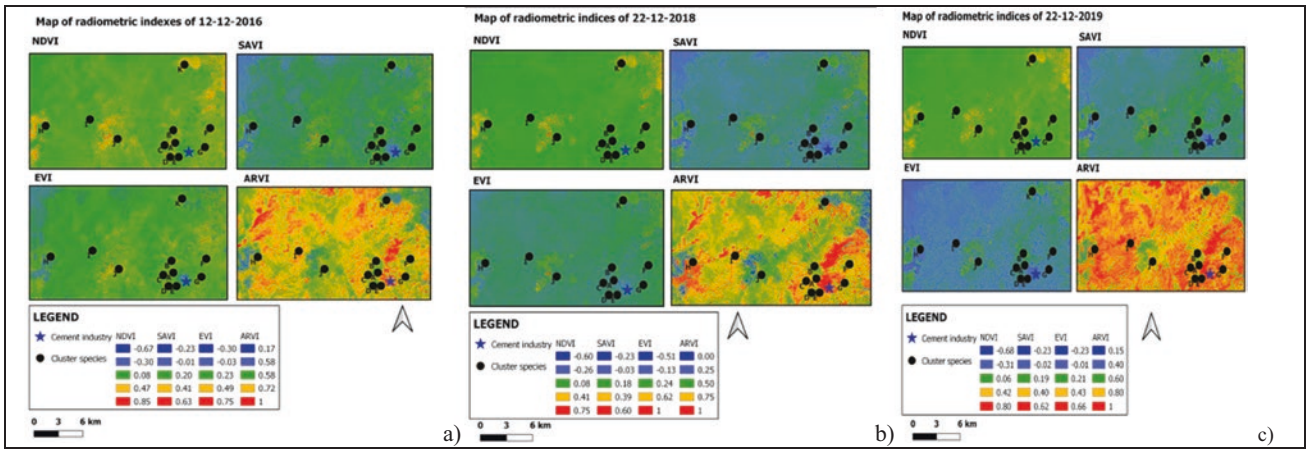

species studied.

Fig. 3 Maps of radiometric indices of 2016 (**a**), 2018 (**b**), and 2019 (**c**)

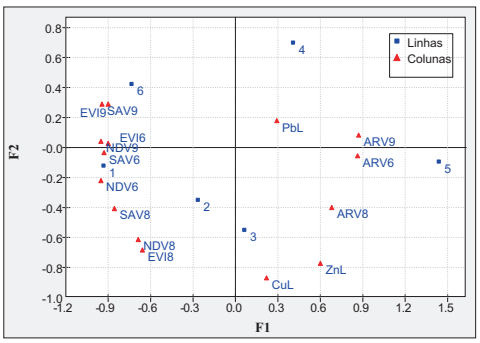

Fig. 4 PCA's results for the first two components F1 (62.0%) and F2 (18.5%)

LEGEND

EVI6: EVI 2016
NDV6: NDVI 2016
SAV6: SAVI 2016
ARV6: ARVI 2016
EVI8: EVI 2018
NDV8: NDVI 2018
SAV8: SAVI 2018
ARV8: ARVI 2018
EVI9: EVI 2018
NDV9: NDVI 2019
SAV9: SAVI 2019
ARV9: ARVI 2019

1: *Olea europaea*
2: *Zygophyllum album*
3: *Helianthemum kahiricum*
4: *Ficus carica*
5: *Prunus persica vulgaris*
6: *Medicago sativa*

associated with greener plants such as *Medicago sativa* (Alfalfa) and *Olea Europaea* (olive tree). 2018 was a dryer year that had repercussions on the spectral response of the plants (Walker et al., 2014). 2018 had higher PM10 values in December when compared to 2016. ARVI is considered more robust for regions with a high content of atmospheric aerosol (e.g., dust, smoke, air pollution) (Kaufman & Tanré, 1996; Fan et al., 2015). *Helianthemum kahiricum* and *Zygophyllum album* presented high values of the four indices in 2018, although revealing high contents of Cu and Zn on the leaves. This fact is related to these species' higher capability to bioaccumulate these two metals in their leaves (Gamoun et al., 2018; Jalali et al., 2019). *Ficus Carica* showed low values of NDVI and EVI in 2018 and high contents of Pb in the leaves. ARVI of 2016 and 2019 is more correlated than 2018, although the PM10 value was not available, one can hypothesize that aerosols decreased from 2018 to 2019.

5 Conclusions

As a perspective, it would be interesting to use satellite images at higher resolutions and to use spectro-radiometric measurements in the field to validate the radiometry measured at the level of satellite images. The aerosol content in the air and SAVI seem related, and further study should be performed. In the future work, the number of samples will be increased in order to obtain more accurate and representative results.

References

Amer, M., Tyler, A., Fouda, T., Hunter, P., Elmetwalli, A., Wilson, C., & Vallejo-Marin, M. (2017). Spectral characteristics for estimation heavy metals accumulation in wheat plants and grain. *Scientific Papers Series: Management, Economic Engineering and Rural Development, 17*(3), 47–55.

Asmaryan, S., Warner, T. A., Muradyan, V., & Nerisyaan, G. (2013). Mapping tree stress associated with urban pollution using the WorldView-2 Red Edge band. *Remote Sensing Letters, 4*(2), 200–209. https://doi.org/10.1080/2150704X.2012.715771

Diello, P., Mahe, G., Paturel, J. E., Dezetter, A., Delclaux, F., Servat, E., & Ouattara, F. (2005). Relations indices de Végétation–Pluie au Burkina Faso: Cas du Bassin Versant du Nakambé/Relationship between Rainfall and Vegetation Indexes in Burkina Faso: A case study of the Nakambé Basin. *Hydrological Sciences Journal, 50*(2).

Gamoun, M., Belgacem, A. O., & Louhaichi, M. (2018). Plant Diversity of desert rangelands of Tunisia. *Plant Diversity, 40*(5), 217–225. https://doi.org/10.1016/j.pld.2018.06.004

Huete, A. R. (1988). A soil-adjusted vegetation index (SAVI). *Remote Sensing of Environment, 25*(3), 295–309.

Huete, A. R., Justice, C. O., & Van Leeuwen, W. J. D. (1999). *MODIS Vegetation Index (MOD 13)*. Version 3. Algorithm Theoretical Basis Document, 129p.

Fan, H., Fu, X., Zhang, Z., & Wu, Q. (2015). Phenology-based vegetation index differencing for mapping of rubber plantations using landsat OLI data. *Remote Sensing, 7*, 6041–6058. https://doi.org/10.3390/rs70506041

Jalali, J., Gaudin, P., Capiaux, H., Ammar, E., & Lebeau, T. (2019). Fate and transport of metal trace elements from phosphogypsum piles in Tunisia and their impact on soil bacteria and wild plants. *Ecotoxicology and Environmental Safety, 174*, 12–25. https://doi.org/10.1016/j.ecoenv.2019.02.051

Kaufman, Y. J., & Tanré, D. (1992). Atmospherically resistant vegetation index (ARVI) for EOS-MODIS. *IEEE Transactions on Geoscience and Remote Sensing, 30*, 261–270.

Kaufman, Y. J., & Tanré, D. (1996). Strategy for direct and indirect methods for correcting the aerosol effect on remote sensing: From AVHRR to EOS-MODIS. *Remote Sensing of Environment, 55*, 65–79.

Richter, R., Wang, X., Bachmann, M., & Schlaepfer, D. (2011). Correction of cirrus effects in Sentinel-2 type of imagery. International Journal of Remote Sensing*, 32*, 2931–2941.

Schläpfer, D., et al. (1998). Atmospheric precorrected differential absorption technique to retrieve columnar water vapour. *Remote Sensing of Environment, 65*, 353366.

Hardy, T., Franceschini, M. D., Kooistra, L., Novani, M., & Richter, S. (2020). Automated processing of Sentinel-2 products for time-series analysis in grassland monitoring. In *13th IFIP WG 5.11 International Symposium on Environmental Software Systems*. Data Science in Action, ISESS 2020, Wageningen, The Netherlands, February 5–7, 2020.

Tucker, C. J. (1979). Red and photographic infrared linear combinations for monitoring vegetation. *Remote Sensing of Environment, 8*, 127–150.

Van Deventer, H., & Cho, M. A. (2014). Assessing leaf spectral properties of *Phragmites australis* impacted by acid mine drainage. *South African Journal of Science, 110*(7–8), 1–12. https://doi.org/10.1590/sajs.2014/20130184

Walker, J. J., Beurs, K. M. D., & Wynne, R. H. (2014). Dryland vegetation phenology across an elevation gradient in Arizona, USA, investigated with fused MODIS and Landsat data. *Remote Sensing of Environment, 144*, 85–97.

Zhou, C., Chen, S. B., Zhang, Y. Z., Zhao, G. H., Song, D. R., & Liu, D. W. (2018). Evaluating metal effects on the reflectance spectra of plant leaves during different seasons in post-mining areas. *Remote Sensing, 10*(8), 1211. https://doi.org/10.3390/rs10081211

Combination of Several Techniques and Remote Sensing for Mapping the Shallow Seabed of Algeria Bay

Nour El Islam Bachari and Souad Lamouti

Abstract

Biokinetic maps are the basis of the biodiversity richness of a region. By knowing the fauna and flora in a region, we can conclude on the quality of the region's waters. The objective of this work is the combination of all coastal observation techniques. satellite images, scuba diving, marine video and echosounder. Satellite images have been used to delimit the search space for areas of high biological interest. These areas of interest are subject to observation by scuba diving, video film and bathymetric measurements. The result is a 3D biocenotic map to describe the nature of the habitat and the habitat stages of the species/space. The map species/space can used as a reference map on water quality, biodiversity and climate change.

Keywords

Underwater mapping · Classification image · Species identification

1 Introduction

Mapping of benthic biocoenoses implies the visualization of the spatiotemporal distribution of the quality and quantity of benthic resources. The interest of this mapping is environmental monitoring, coastal management, improving our knowledge on the functioning of ecosystems and the rational and sustainable use of the coastal zone and its resources within the framework of an integrated management policy (Ardizzone, 2016). The cartographic representation of benthic biocenoses allows the spatiotemporal distribution of the quality and quantity of benthic resources to be visualized. Mapping methods are divided into two categories. The first includes methods of direct visual observation by the researcher: diving, apnea, dumping, underwater video, prospecting on foot and observation from a boat (Fourier, 2006). The second category uses the technique of remote sensing following the process of acquisition and processing of satellite images. Each method has particularities, advantages, disadvantages and limitations. The ideal is to carry out a cartography with very high spatial resolution on the one hand and on the other hand that it's repetitive to observe temporal changes. The objective of our work is to contribute to the elaboration of biocenotic maps, carried out by in situ observation (diving, prospecting on foot and by boat) and by remote sensing at very high spatial resolution.

2 Methodology

The proposed methodology is based on the combination of several techniques to map the seabed. Figure 1 shows the methodology developed to produce a seabed map. On the one hand, an algorithm specific to in situ observation, and on the other hand, an algorithm specific to the use of satellite images.

2.1 Conventional Techniques

The method adopted is largely inspired by the work of Fornes et al. (2005). It allows for the mapping of small areas on a very large scale and with great precision with a minimum of human and material resources. Several juxtaposed corridors, materialized by ropes identified by letters and subdivided into several numbered squares, are traversed

N. E. I. Bachari (✉) · S. Lamouti
Laboratory of Oceanography Biologic and Marine Environment (LOBME), Department of Ecology and Environment, University of Sciences and Technology Houari Boumediene (USTHB), El Alia, BP 32, 16111 Bab Ezzouar, Algeria
e-mail: nbachari@usthb.dz

Z. A. Ergüler et al. (eds.), *Selected Studies in Geotechnics, Geo-Informatics and Remote Sensing*, Advances in Science, Technology & Innovation, https://doi.org/10.1007/978-3-031-43759-5_9

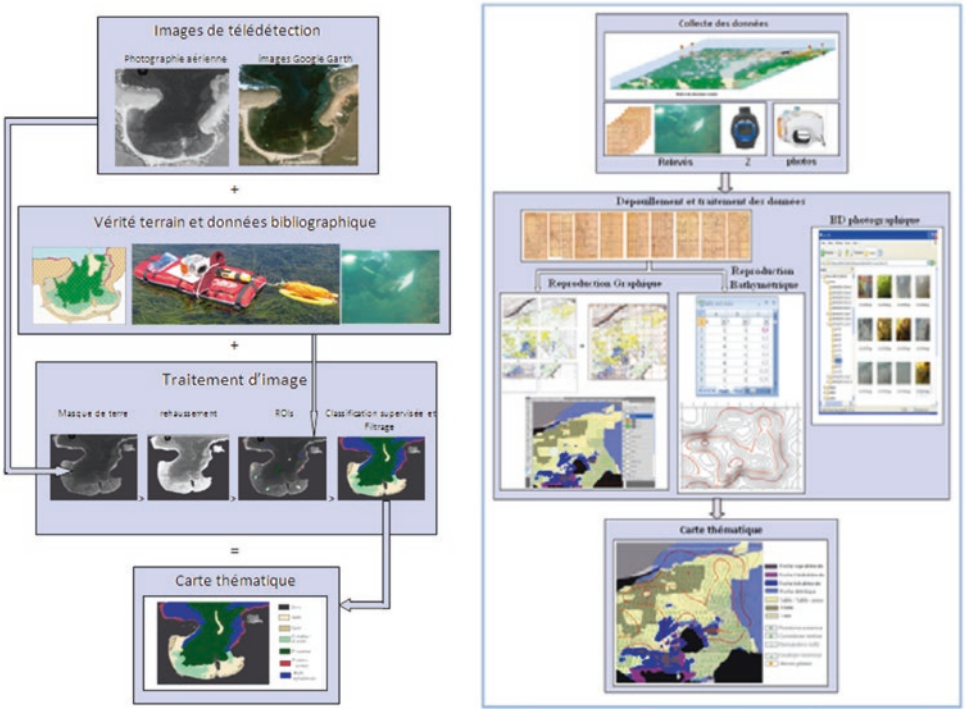

Fig. 1 Methodology developed

one after the other by free diving or scuba diving, and the limits of each biocenosis are noted as they are traversed. The different classes of maps representing bottom types, settlements and species are reproduced separately and represented by independent tiles, so that layers can be displayed as needed. This method is precise but very expensive since to make a map of one hectare surface area it was necessary to make 60 dives.

2.2 Satellite Image Observation

Optical remote sensing can be used for depths between 10 and 20 m, depending on water clarity (Toure et al., 2019; De Vaugelas et al., 1999). The interpretation of satellite and photo-aerial images makes it possible to locate the limits of the main coastal marine biocenoses at shallow depths. The supervised and unsupervised classification implemented on SDDS (Houma et al., 2006; Meharrar & El Islam Bachari, 2014) allowed us to distinguish the upper limit of the Posidonia meadow, the intertidal biocenoses from the other components. These maps can be used as a guide to delineate areas of prospecting and research for areas of high interest. The GIS-integra table thematic map is obtained by integrating in situ (ground truth) observation data into the image processing process and performing a supervised classification. A map very high resolution and three dimensions is produced. The processed images are aerial photographs and satellite images reconstructed from Google Earth.

2.3 Topography Map

Making a 3D nautical chart is possible using LIDAR. The problem is spatial resolution. In our case, we are interested in developing a centimetric map (Valentini et al., 2020). Faced with this problem, we developed a mechanical support and we installed together a digital camera and an echosounder. The camera produces a continuous georeferenced video observation and the echosounder produces bathymetric information. The echosounder gives us the depth Z_S directly by considering the speed of sound in water 1500 m/s. The actual depth is corrected real speed of sound C:

$$Z = Z_S + \frac{C}{1500} \tag{1}$$

$$C = 1449.2 + 4.6 \times T - 0.055 \times T^2 + (1.34 - 0.01 \times T) \times (S - 35) \tag{2}$$

where temperature (T) and salinity (S) are measured in situ.

3 Biocinosis Map

A Geographic Information System consists in making a digital map interact with a database. In our work for georeferencing, we used the coordinates of remarkable points surveyed by Google Earth and/or in the field. The table produced is composed by the following variables: latitude,

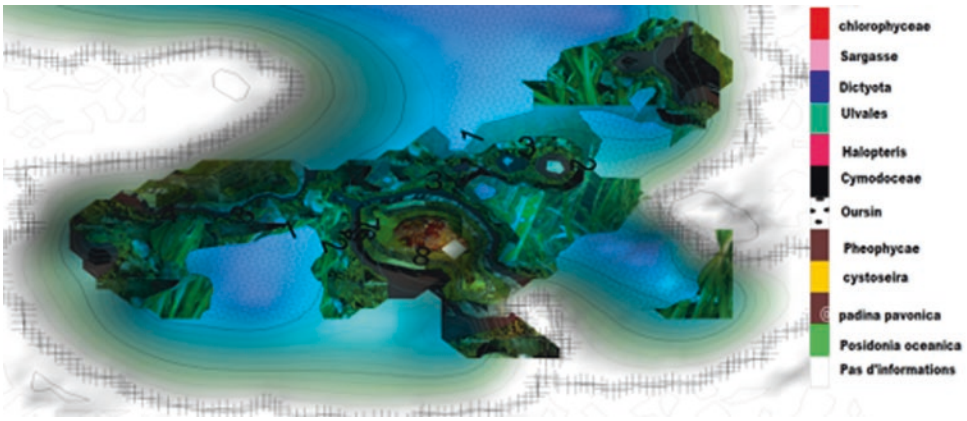

Fig. 2 3D map of biocinos

longitude, depth, temperature and salinity. For the video, we fix the interesting images and we try to identify the nature of the background. All data integrated in GIS, for spatial interpolation, we have opted for the method by natural neighbors. We produced the map in three dimensions, and all species composed the seabed. The result is a map 3D with twelve classes (Fig. 2).

4 Conclusions

Mapping by in situ observation has enabled us to obtain fine maps on the distribution of biocenoses but expensive therefore not adequate for spatiotemporal studies. Satellite methods have enabled us to optimize our research space and produce maps made up of groups. Inspired by the two methods, we have developed a mechanical support to put a camera and an echosounder. The objective is to produce a very high resolution biocenosis map specifying the levels of the habitats. The whole difficulty lies in the synchronization of the bathymetric data and the video images. Experimental pumpers are made to find the orientation of the sensors on the one hand and the choice of the speed of the boat. All data is integrated into geographical information system QGIS. The combination of the different layers allowed us to make a 3D map. The produced map contains the bathymetric level of habitat, the nature of the flora and nature of fauna that inhabit it.

References

Ardizzone, G.D. (2016). La rappresentazione cartographica nelle richerchi di biologia marina in Mediterranéo. In *ATTI XXX congresso SIBM*. Vibo Valentia, pp. 361–347.

De Vaugelas, J., Meinesz, A., Antolic, B., Ballesteros, E., Belsher, T., Cassar, N., Ceccherelli, G., Cinelli, F., Cottalorda, J., Frada'Orestano, C. M., Grau, A., Jaklin, A., Morucci, C., Rellini, M., Sandulli, R., Span, A., Tripaldi, G., Van Klaveren, P., Zavodnik, N., & Zuljevic, A. (1999). Proposition for a standardization of map representation of *Caulerpa taxifolia* expansion in the Mediterranean sea. *Oceanology Acta, 22*, 85–94.

Fornes, A., Basterretxea, G., Orfila, A., Jordi, A., Alvarez, A., & Tintore, J. (2005). Mapping Posidoniaoceanica from Ikonos. *ISPRS Journal of PhotoGrammetry and Remote Sensing, 60*, 315–322.

Fourier, J. (2006). Quelques méthodes de cartographie des biocénoses benthiques en plongée subaquatique: Application à la baie de Lannion (Bretagne). *Le Monde Des Cartes, 181*, 45–54.

Houma, F., Belkessa, R., & Bachari, N. (2006). Contribution of multispectral satellite imagery to the bathymetric analysis of coastal sea bottom. *Revue Des Energies Renouvelables, 9*, 165–172.

Meharrar, K., & El Islam Bachari, N. (2014). Modeling of radiative transfer of natural surfaces in the solar radiation spectrum: Development of a satellite data simulator (SDDS). *International Journal of Remote Sensing, 35*, 1199–1216.

Toure, S., Diop, O., Kpalma, K., & Seidou, A. (2019). MaigaShoreline detection using optical remote sensing. *ISPRS International Journal of Geo-Information, 8*, 75.

Valentini, E., Taramelli, A., Cappucci, S., Filipponi, F., & Nguyen Xuan, A. (2020). Exploring the dunes: The correlations between vegetation cover pattern and morphology for sediment retention assessment using airborne multisensor acquisition. *Remote Sensing, 12*, 1229.

Development of a Compressive Dewatering Management Software-Based system—A Case Study in Qatar

Hernan Vigil, Jorge Vigil, Alvaro Casado and Miguel Garcia

Abstract

Lusail CP07B is one of the mega projects being developed in Lusail City, close to the seaside in the Northern part of the State of Qatar. The project has 410,000 m^2 of excavation pit with variable depths between − 10 and − 30 mbgl (metres below ground level) and around 105,000 m^2 of slopes with different configurations and slopes stability methods. To maintain the phreatic level (groundwater level) under control, a massive dewatering system that usually plays an important role is required, and sometimes, it might negatively impact the project itself, from a safety, economic, quality, and schedule point of view. During the execution of Lusail CP07B, a complex Dewatering Management System (DMS) was implemented, based on a software platform tool. The software, based on the Civilworks Web Services (CWS), is able to work in real time, semi-real time, and manual mode. In this paper, the most important functions and capabilities of the platform are evaluated.

Keywords

Dewatering · Management · Monitoring · System · Civilnova · CWS · Software

1 Introduction

The execution of the CP07B project required the implementation of a massive dewatering system to lower the groundwater level from 2 to 30 mbgl to proceed forward with the excavation, shoring, and finally the permanent structures.

The main components of the dewatering system can be summarized in 210 dewatering wells with a diameter of 800 mm and variable depths from 20 to 30 mbgl; 95 sump pits.

As enabling components of the dewatering system can be mentioned, 50 piezometers, 22 generator sets of 550 KVA each, 10 km of drain lines, 6 km of ditches, along with sedimentation tanks, instrumentation, and monitoring.

During the operation of the dewatering system, a number of problems associated with its management were identified. These problems were: lack of traceability, current condition, control of consumables and system components, decentralized and disorganized documentation, absence of maintenance schedules, deficiencies in the quality control in general, and in particular, the water at the point of discharges into the sea, delays and sluggishness in the monitoring of the groundwater levels.

This latter point was associated with a series of collapses and instabilities (Kallash & Vigil, 2018) on the excavated slopes; during the excavation, it led to the slowdown of the project and compromised the security in some cases.

The idea to develop a software tool arose to solve the problems mentioned above. A tool that encompasses all aspects related to the management of the dewatering system, integrating and interpreting the geotechnical monitorization to determine the level of the risk of each area and send out alerts.

H. Vigil (✉)
University of Oviedo, Civilnova, Oviedo, Spain
e-mail: hernanvigil@hotmail.com

J. Vigil · A. Casado · M. Garcia
Civilnova, Oviedo, Spain

Z. A. Ergüler et al. (eds.), *Selected Studies in Geotechnics, Geo-informatics and Remote Sensing*,
Advances in Science, Technology & Innovation, https://doi.org/10.1007/978-3-031-43759-5_10

2 Geology and Hydrology Aspects

The geological conditions at the site can be summarized as superficial deposit or soil unit; Simsima Limestone which is considered moderately weak to moderately strong, off-white, moderately to slightly weathered and fractured microcrystalline limestone with inclusion of light green clay, voids and vugs and silty materials. Fractures display very close to medium apertures and are filled with silty and clay materials. A subclass within Simsima Limestone is Weathered Simsima Limestone classified based on the criteria: low RQD (typically < 20%).

Finally, Rus formation is moderately (partially) to distinctly weathered or fractured, light grey to off-white, weak to moderately weak limestone, or chalky to marly limestone. Fractures are very close to medium size, occasionally filled with silty and clay materials.

Simsima Limestone is highly fractured with RQD values being 0% especially in the top 2 m. Hence, such highly fractured limestone suggests that a karstic feature (mainly small cavities) may be present in the area. Such features typically lead to systems of major joints in the limestone within the affected area.

In contrast, the Rus formation comprises a number of weak zones as evident from the geological cross sections with SPT N values around or below 50 (some locations have N-SPT between 20 and 30) as well as very low rock recovery (TCR) and rock quality (RQD), with some locations as RQD = 0 and TCR = 0. This indicates a soillike rock behaviour.

It should be noted that systems of joints in the limestone will often be water bearing and are able to produce very large quantities of water. The quantity of water which can move through these fissures and fractures will be a function of the hydraulic driving head, the size of the flow path, and the presence of fine material within the flow path.

3 The Platform

Civilworks Web Services (CWS) is a platform in the cloud, developed by open-source software. It is multi-parametric, scalable, and adaptable to customer needs. In addition, the platform encompasses an ecosystem of applications developed for civil engineering works (see Scheme 1).

Overall, it is a large database that feeds on sensors in real time (regardless of the manufacturer or type) by means of manual data entry or a combination of both. In addition, it has a GIS integrated with CAD and BIM for the management of graphics and dynamic maps and is able to work with IoT elements (see Figs. 1 and 2).

Finally, it has been incorporated into the platform the business technology (Kaufman, 2015) and data mining for the interpretation, data analysis, and decision making in real time (Ramesh et al., 2021), based on the established risk criteria (Max & Kjell, 2020) (see Fig. 3).

Table 1 gives the main items considered and managed by the platform regarding dewatering and geotechnical monitoring.

Finally, it has been incorporated into the business smart technology and data mining for the interpretation, data analysis, and decision making in real time, based on the established risk criteria.

4 Usability and Utility

The access to the information is done in a direct way through the GIS view, being able to consult both data related to the elements and documentation. The layering of the different instances also helps to facilitate access to information (Fig. 4).

The visual alert system allows us to locate any problem at a glance, and then access the detail of the incident.

These functions, together with the sending of alerts via SMS or email, ensure a prompt action on the emergency situation detected by the measurement devices.

The system allows real-time access to the information of the monitoring system, the processing of all data together to obtain valuable information for decision making, and generates an increase in safety during the construction process that results in fewer accidents with the resulting reduction of economic costs and personnel injury.

5 Conclusions

Significant improvements and cost savings are the results obtained following the platform integration. Indeed, the integration on a single platform of the different types of monitoring equipment that are from different manufacturers allows an orderly operation of the resources, a uniform surveillance system which results in a reduction in staff requirements needed to control the drainage system.

The data integration also enables the exploitation of such information through business intelligence tools that optimize decision making based on data obtained from the system. Cost savings by the increase in sound decision making are always important.

In real time, the alarm systems increase the security of the complex and prevent accidents, which can result in both material expenses and what is most serious, a grave danger to human life.

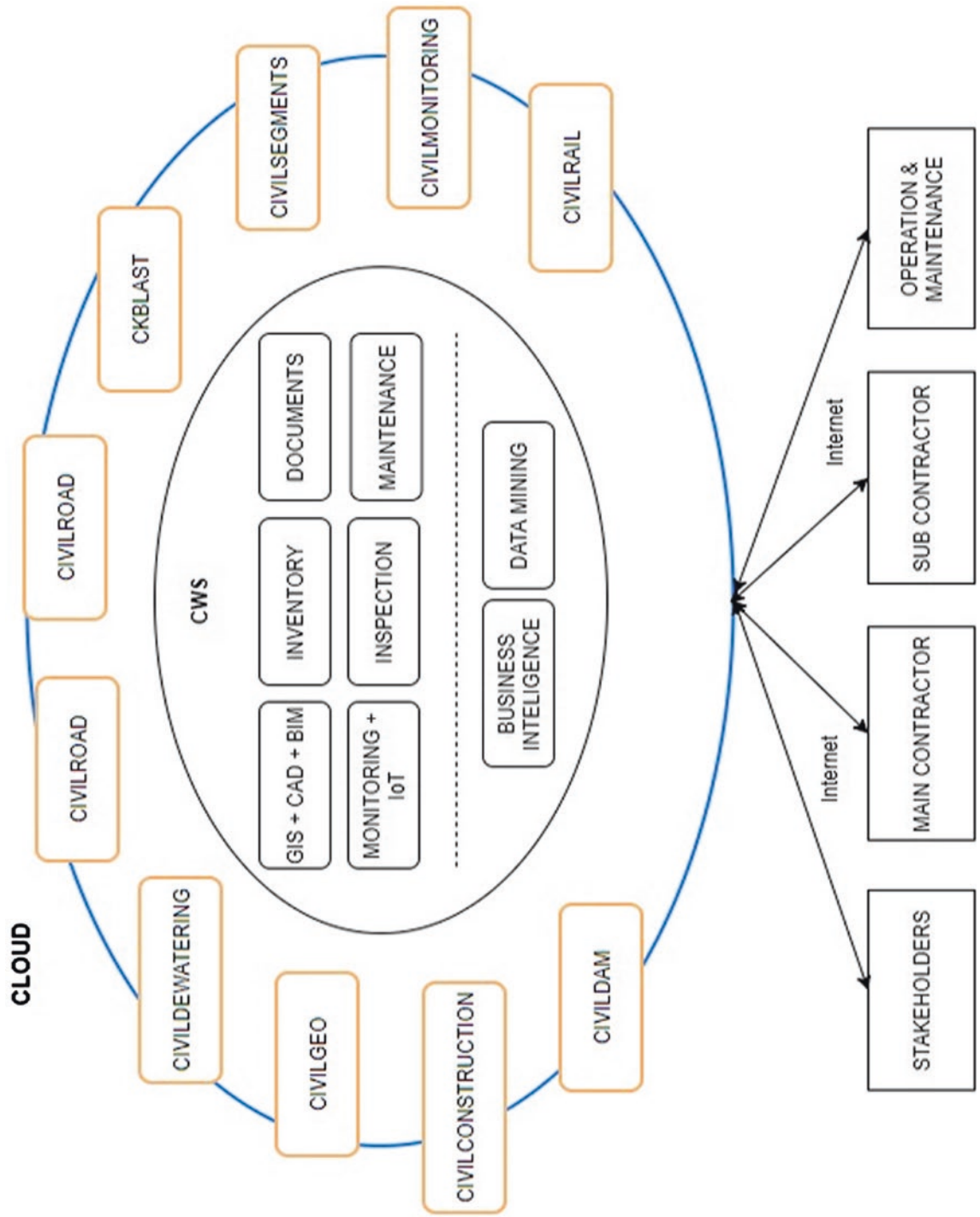

Scheme 1 CWS ecosystem and interaction with other tools over the platform

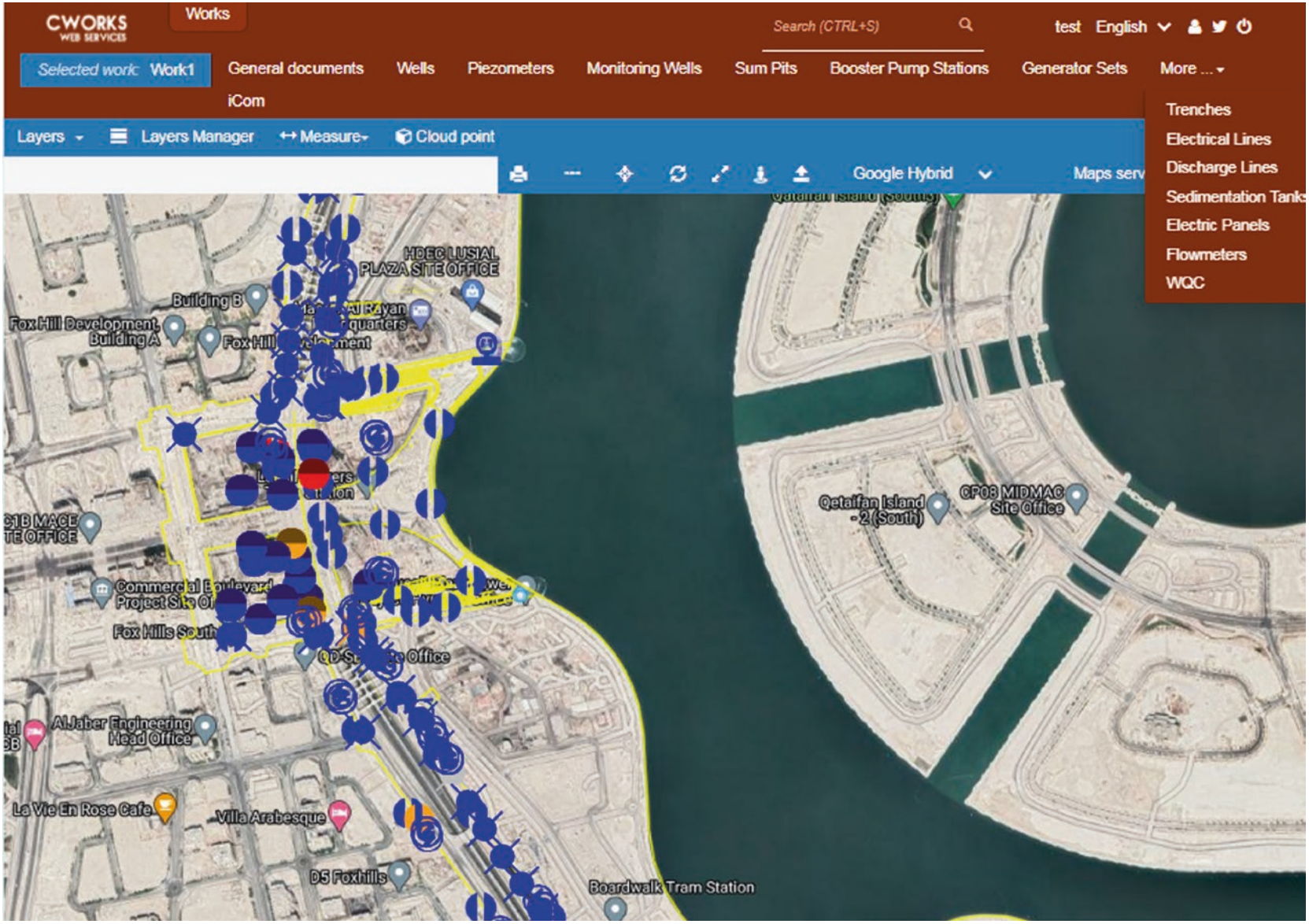

Fig. 1 CWS general dashboard and GSI windows detail

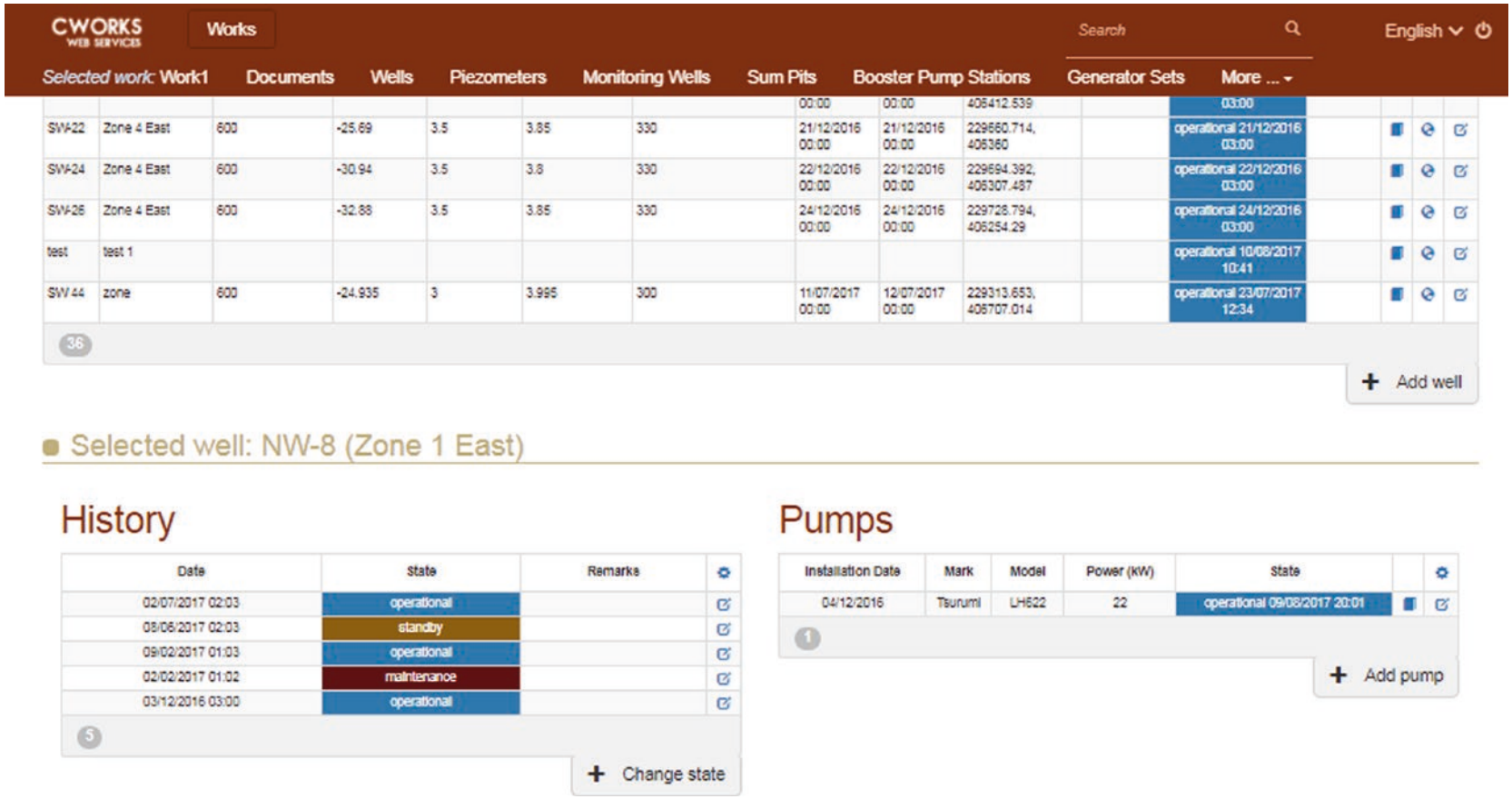

Fig. 2 CWS window of dewatering wells information

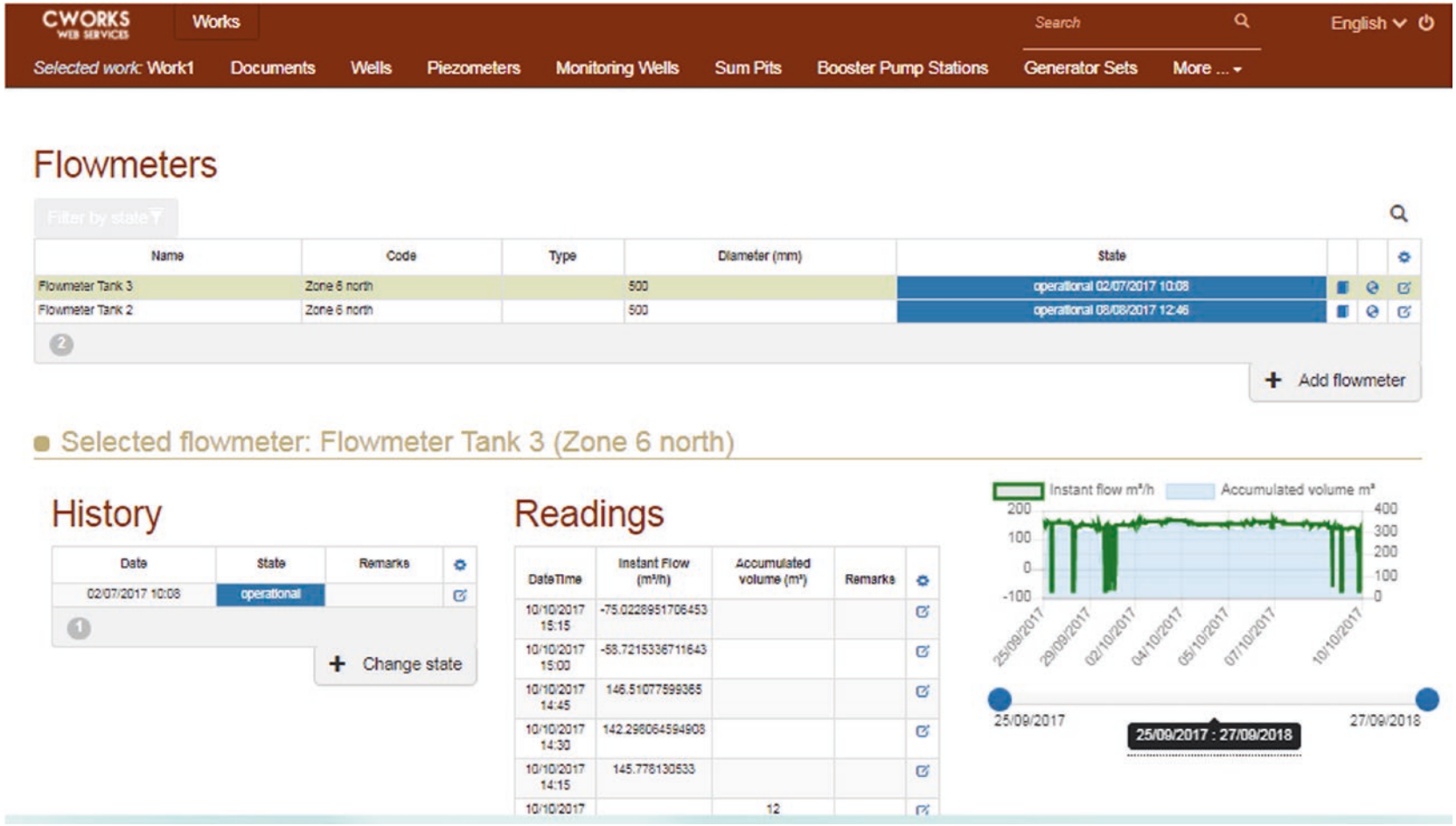

Fig. 3 CWS window of flowmeters, detailed information

Table 1 Dewatering items and aspect managed by the platform

Main items of dewatering system	Aspects managed
Wells and sum pits management	• General data and • Georeferencial location • Historical activity and actual status • Pump tracking • Maintenance calendar and records • Documents control • Tooltips
Booster pump stations management2019	
Generator sets management	
Trenches management	
Electrical lines and panels management	
Discharge lines	
Sedimentation tanks	
Piezometers and monitoring well duality management	• General data • Historical data • Readings, manual, semi-real, and real time • Charts • Alarms • Documents management (plans, photographs, etc.)
Flowmeters	
Main items of geotechnical monitoring	
Pressure cells	
Prisms	
Inclinometers	

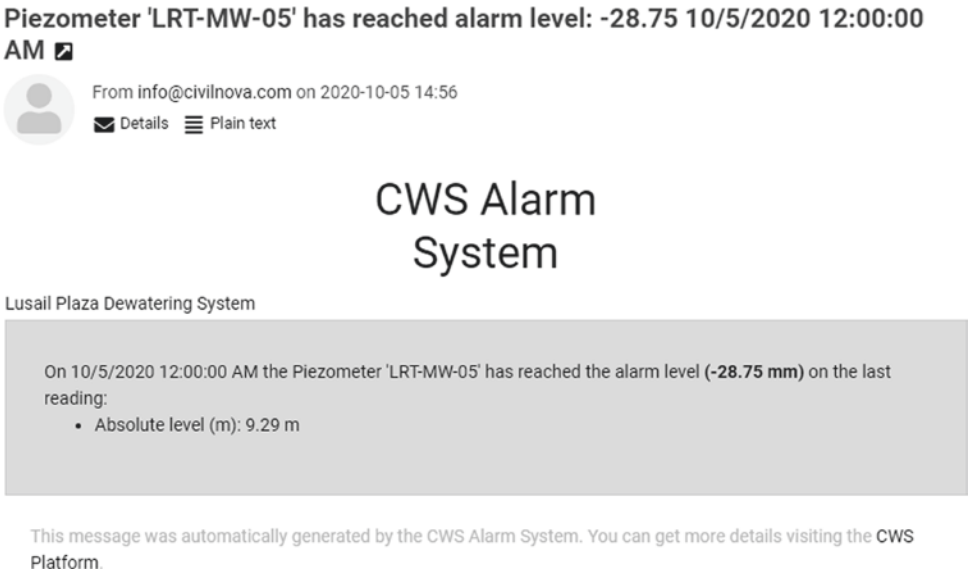

Fig. 4 CWS dewatering alert notification

The implementation of the platform in the construction phase also constitutes the origin of the maintenance platform. To this, we must add the inspection and control processes of the construction elements and equipment.

The information collected by the system is also compatible with other BIM tools, provided they are compatible with the IFC standard, therefore, such information is reusable for other operations.

The incorporation of IoT devices on the platform forms the basis of digitization of the infrastructure, connecting in this way with the concept of the smart city that we are so concerned about nowadays.

References

Kallash, A., Vigil, H. (2018). Recent advances in geo-environmental engineering, geomechanics and geotechnics, and geohazards. In *Observation on failure behavior of cut slope in Chalky Limestone, case studies in Rus formation proceedings of the 1st Springer conference of the Arabian journal of geosciences (CAJG-1)*, pp. 407. Springer.

Kaufman, R. (2015). *Business intelligence guidebook from data integration to analytics*. Elsevier.

Max, K., & Kjell, J. (2020). *Feature engineering and selection*. Chapman and Hall/CRC.

Ramesh, S., Dursun, D., & Efraim, T. (2021). *Analytics, data science and artificial intelligence. System for decision support* (11th edn.). Pearson.

Impact of Climate Change and Human Activities on the Urban Wetland of Tunisia

Rania Ajmi, Safa Bel Fekih Boussema, Souleima Dammak, Balkis Chaabane and Faiza Khebour Allouche

Abstract

Wetlands constitute a natural buffer for rainwater buffers and the places where most urbanization occurs. In Tunisia, these ecosystems suffer from malfunction and significant degradation. This is the case of the "Sebkha of Sousse" which represents the green lung of the industrial area of "Sidi Abd Elhamid" located in the center of Tunisia. This study seeks to analyze the impact of climate change and human activities on the seasonal and pluriannual behavior of this Sebkha by using multitemporal Landsat satellite imageries and Google Earth snippets. Shorelines from 2003 to 2019 were delineated on the multitemporal snippets in the Google Earth software by visual interpretation. LULC change between 2008 and 2019 was detected by using ENVI software. The analysis of LULC revealed, for example, that built-up and cultivated areas have increased by 4.285 and 18.53%, respectively, in the north and east sides of the zone. However, the Sebkha area decreased from 0.12 to 0.10%. The visual interpretation of Google earth snippets shows significant seasonal and multiannual variations of the Sebkha water volume. Then, climatic changes during the seasons lead to changes in the soil occupation which contribute to the variation of agricultural needs by stimulating pumping for irrigation. The water supply from the water table to surface aquatic systems may therefore decrease significantly, modifying the ecological functioning of wetlands, interfaces between groundwater and area. Hence, the importance of setting up strategies to preserve this brittle ecosystem and think about its sustainable development taking into account human well-being.

Keywords

Urban wetland · Climate change · LULC · Environment · Human activities

1 Introduction

Wetlands are vital for the survival of humanity. However, their area continued to decline, especially during the second half of the twentieth century (Hettiarachchi et al., 2014). Urbanization and changing climatic patterns are likely to negatively affect wetland conditions, such as permanency and productivity (Lisa et al., 2012). The main research objective was to characterize the behavior of the Sebkha, its state, and dynamics as a function of climatic and anthropogenic factors.

2 Materials and Methods

The Sebkha of Sousse is located in the south of the Sousse governorate (Fig. 1). It covers an area of 62 ha. Its coordinates compared with the North latitude, and the East longitudes are 35° 74′ and 10° 38′, respectively.

This research work was carried out using "ENVI 5.1" and "QGIS 2.2" software. A Garmin 64 S GPS was used in the field to locate spaces. Two high-resolution Landsat satellite images were downloaded (https://earthexplorer.usgs.gov/), namely Landsat 5Thematic Mapper and Landsat

R. Ajmi (✉) · S. Bel Fekih Boussema · S. Dammak · B. Chaabane · F. Khebour Allouche
High Institute of Agronomic Science of Chott Mariem (ISA-CM), Departement of Horticultural Sciences and Landscape, Sousse University, B.P 47, 4042 Chott Meriem Sousse, Tunisia
e-mail: ajmi.rania.ep.ismail@gmail.com

R. Ajmi · S. Bel Fekih Boussema · F. Khebour Allouche
National Agronomic Institute of Tunis, Lr GREEN TEAM (LR17AGR01), Carthage University, B.P 43, Avenue Charles Nicolle 1082, Tunis Mahrajène, Tunisia

Z. A. Ergüler et al. (eds.), *Selected Studies in Geotechnics, Geo-Informatics and Remote Sensing*, Advances in Science, Technology & Innovation, https://doi.org/10.1007/978-3-031-43759-5_11

Fig. 1 Localization map of the study area (@Google Earth, 2020). http://www.canalmonde.fr/

8 Operational Land Imager dating from 23/08/2008 to 06/03/2019, respectively. We also used images from the Google Earth platform from 2008 to 2019. We analyzed the current state of the study area and the land-use change based on a conceptual framework (Fig. 2). The framework represents the landscape diagnosis, namely a physical and anthropogenic analysis. The framework also represents the land-use change, using the mapping wetland conversion and habitat distribution.

3 Results and Discussion

3.1 Land-Use Change Analysis

The analysis of LULC revealed that between 2008 and 2019: on the north and east sides of the zone, there is an increase in built-up areas (Fig. 3). The area of urbanization between 2008 and 2019 increased by 4.285%. The area occupied by the Sebkha of Sousse between these 2 years indicates a slight regression of 0.12–0.10%. The imagery obtained from the Google Earth platform shows that in August 2009, the Sebkha is almost dry while, in January 2014, it is engorged with water (Fig. 4). This is due to climate change during these periods, in fact in August 2009, the precipitation is equal to 0.08 mm, and the average temperature is 32.73 °C, while in January 2014, the precipitation is equal to 0.16 mm, and the average temperature is at 10.37 °C.

3.2 Survey Analysis

The results of the survey carried out among farmers showed that the urban extension caused the instability of the current state of the sebkha. For example, there is a decrease in the area of olive groves in the surroundings and a deterioration of the life quality in the outlying districts.

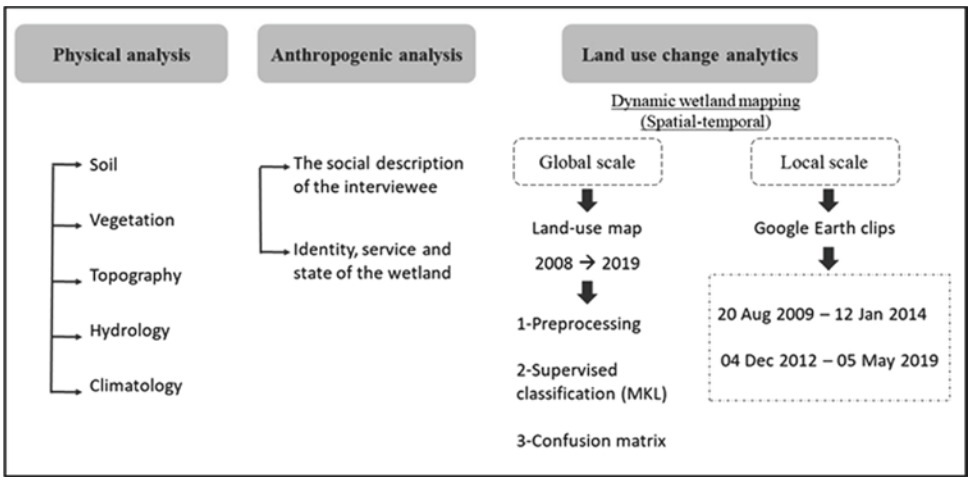

Fig. 2 Conceptual framework of research methodology

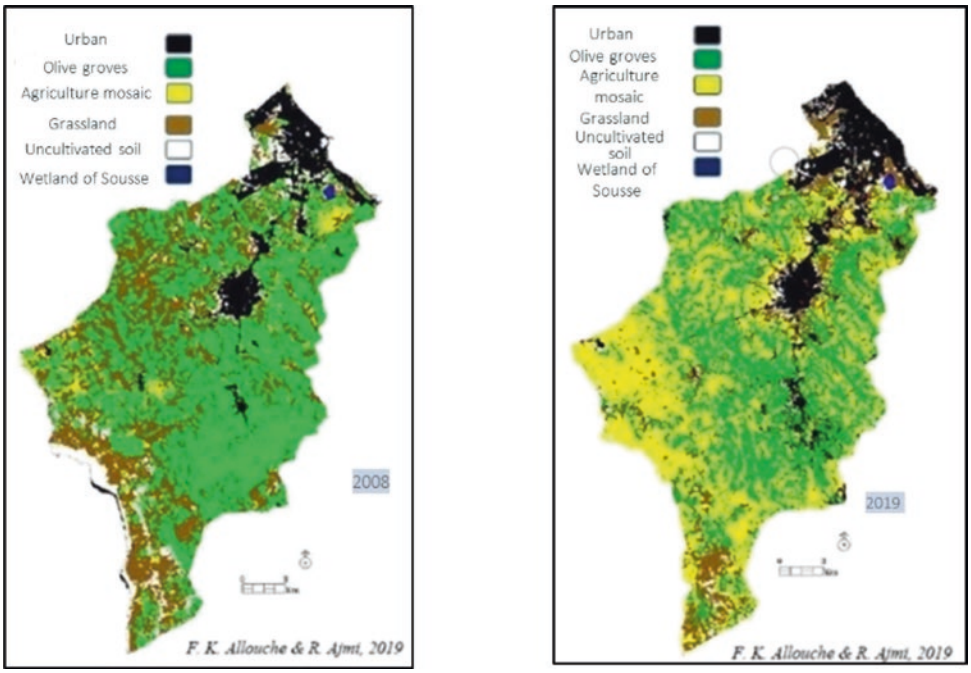

Fig. 3 Land-use maps of Sousse region (at left in 2008, at right in 2019)

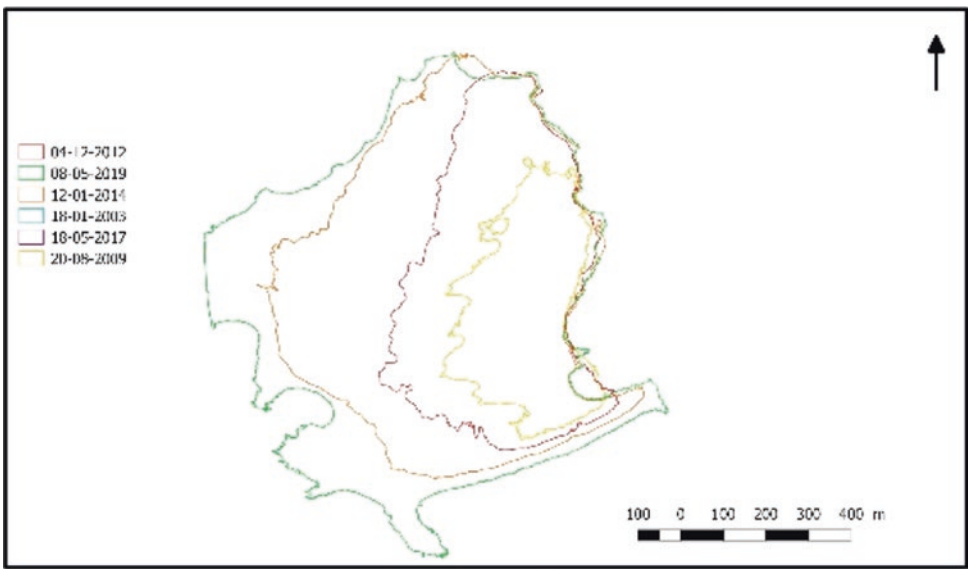

Fig. 4 Spatiotemporal variation of Sebkha Sousse shorelines between 2009 and 2019

This research work has clearly shown the importance of urban sprawl and its impacts around the Sebkha of Sousse. An exceptionally anarchic extension on the banks of the sebkha is detected, associated with a spontaneous nibbling of the agricultural belt and a deterioration of the quality of life in the disadvantaged peripheries. This process was also identified in the study prepared by Chouari (2013) on the Sijoumi wetland and many other Mediterranean wetlands (Bel Fekih Bousemma et al., 2020). This requires the development of a management plan and a sustainable strategy for these fragile areas in order to preserve them.

4 Conclusions

The urban wetland of Sousse represents the green lung of "Sidi Abd Elhamid" and the only virgin space where the inhabitants can refuge. The use of remote sensing and GIS tools has made it possible to detect its spatiotemporal dynamics and to show the usefulness of these tools in decision support. The location of entities at risk of degradation will help decision-makers to properly propose sustainable management scenarios for the preservation of this ecosystem.

References

Bel Fekih Bousemma, S., Khebour Allouche, F.,Chaabane, B. (2020). Tools and Indicators for Integrated Wetland Monitoring Case of Hergla Wetland Tunisia. *European Academic Research, 8*(6), 3230–3245.

Chouari, W. (2013). Problèmes d'environnement liés à l'urbanisation contemporaine dans lesystème endoreïque d'Essijoumi (Tunisie nord-orientale). *Physio-Géo, 7*(1), 111–138.

Hettiarachchi, M., et al. (2014). The eco-social transformation of urban wetlands: A case study of Colombo, Sri Lanka. *Landscape and Urban Planning, 132*(14).

Lisa, L. A., et al. (2012). Isolated Wetland loss and degradation over two decades in an increasingly urbanized landscape. *Wetlands, 33*(11).

Spatiotemporal Investigation of Surface Urban Heat Island (SUHI) Using Landsat: Application on African Cities

Mohammed N. Assaf, Assal Selma and Mirna Gharbi Dit Kacem

Abstract

The high rate of population growth and the expansion of urbanization have been affecting the environment, resulting in rising temperatures, decreasing green areas and vegetation land cover, and increasing urban impervious surfaces. This rapid urbanization has led to a series of environmental problems such as Urban Heat Island (UHI) phenomenon. Investigating Surface Urban Heat Islands (SUHIs) has taken attention worldwide. Despite the unprecedented urbanization that has been experienced in many African cities, little attention has been given to SUHIs in Africa. This paper is dedicated to study the relationship between the spatial and temporal pattern of land use and land cover (LULC) and land surface temperature (LST) to analyze the characteristics of SUHI in four African cities: Casablanca (Morocco), Tunis (Tunisia), Kampala (Uganda), and Windhoek (Namibia). Our choice was based on the following criteria: location and size of the city, high population and urbanization rates, and its economic status. Therefore, Landsat time-series data were acquired during summers between 2000 and 2020 to monitor the formation of SUHI. The results have shown significantly strong correlations between LST and the built-up regions distribution (positive) and green space (negative) in the four cities. This study may provide significant information to policymakers to ease making mitigation strategies for the urban ecological restoration and creating new patterns for a sustainable urbanization.

Keywords

Urban heat island (UHI) · Surface urban heat islands (SUHIs) · Sustainable urbanization · Land used and land cover (LULC) · Land surface temperature (LST)

1 Introduction

Urban heat islands have appeared during the last century and have been spreading ever since (Hussein & Assaf, 2023). Effects vary from one area to another, making it important to mention that its effect is more relevant to developing countries, which are often unwilling to face the consequences of rapid urbanization (Alkhalidi et al., 2023). Despite the fast urbanization in Africa, it has been relatively uncontrolled. This study serves to provide better insight to the critical environmental situation associated with rapid and poorly controlled urbanization. Several perversely research have mentioned the importance of such studies to support future scenarios of climate change mitigation for a sustainable urbanization(Abdelal et al., 2022; Assaf, 2019; Hussien & Assaf, 2020; Hussien et al., 2021).

2 Data and Methods

2.1 Study Areas

The chosen study areas are all located in Africa and include four cities. The first is Casablanca (Morocco) located along the Atlantic coast of Morocco. The climate here is cold, rainy, and humid in winter, and dry/hot during summers from May to September. The driest conditions are in September when the average maximum temperature is 25 °C (HCP, 2019). The second city is Tunis, the capital and largest city of Tunisia. Winters are generally rainier than summers, and the average annual temperature is 18.1 °C (HCP,

M. N. Assaf (✉)
Department of Civil Engineering and Architecture, University of Pavia, 27100 Pavia, Italy
e-mail: MA.Mohammed.Assaf@gmail.com

A. Selma · M. G. D. Kacem
The National Institute of Oceanography and Experimental Geophysics (OGS), Trieste, Italy

Z. A. Ergüler et al. (eds.), *Selected Studies in Geotechnics, Geo-Informatics and Remote Sensing*, Advances in Science, Technology & Innovation, https://doi.org/10.1007/978-3-031-43759-5_12

2019). The third is Kampala (Uganda) located on the northern shore of Lake Victoria. On average, the temperatures are high, with February the warmest month averaging 23 °C, while the coolest is June at 21 °C (HCP, 2019). The fourth city is Windhoek, the capital and largest city of Namibia. The average temperature around the coast is 23 °C, while in the wet season it is around 30 °C. Nevertheless, it rarely falls below 4 °C or exceeds 34.4 °C (HCP, 2019).

2.2 Satellite Data

Seven Landsat 8 OLI/TIRS and thirteen Landsat 7 ETM + operational satellite cloud-free (< 10%) data were downloaded from the US Geological Survey (USGS) Global Visualization Viewer for each study area. All the Landsat 8 OLI/TIRS and Landsat 7 ETM + data used were acquired during the dry season.

2.3 Pre-processing

The pre-processing included radiometric and atmospheric corrections for each satellite image. It consists of using PCI Geomatica software-ATCOR to convert the digital number (DN) values of the multispectral bands (bands 1–7 and 9, 1–5 and 7) for Landsat 8-OLI and Landsat 7 ETM +, respectively, into surface reflectance values. DN values of the thermal bands (bands 10 and 11, 6) for Landsat 8-OLI and Landsat 7 ETM +, respectively, are converted to at-satellite brightness temperature [TB (degrees Kelvin)].

2.4 Retrieval of LST

The retrieval of LST consists, first, of converting DNs of the thermal bands (i.e., Band 6 in Landsat 7 ETM+) to absolute units of at-sensor spectral radiance (Hussein et al., 2023). For Landsat 7 ETM + data from 2000 to 2020, the spectral radiance scaling method was used following the equation by Salah and Saleh (2010). For Landsat 8 OLI/TIRS data collected for the period 2000–2020, the radiance scaling factors provided in the metadata file were used following the approach found by Abu Ahmed et al. (2020). Second, under the assumption that the Earth's surface is a black body (i.e., spectral emissivity = 1), the thermal band data for both Landsat 7 ETM + and Landsat 8 OLI/TIRS was converted from at-sensor spectral radiance to top of atmosphere brightness temperature using the Equation from Saleh (2010). Finally, the top of atmosphere brightness temperature has been used to determine the land surface temperature (LST) following the approach of Zhang et al. (2017).

2.5 Retrieval of Land Surface Parameters

To calculate the normalized vegetation index (NDVI), remote sensing reflectance R_{rs} in the red and near infrared (NIR) regions of the spectrum for Landsat 7 ETM + and Landsat 8 were used following the relationship according to Baret and Guyot (1991). The normalized difference built-up index (NDBI) from Landsat 7 ETM + and Landsat 8 was calculated using remote sensing reflectance measurements in the red and mid infrared (MIR) regions of the spectrum as expressed by Liu and Weng (2011). To understand the Urban Heat Island Index (UHT) patterns, the UHT index has been estimated using the equation by Mathew et al. (2016).

2.6 Statistical Analysis

Statistical analysis was conducted using correlation analysis to investigate the relationship between the mean LST and both NDVI and NDBI calculated for each studied city for the period 2000–2020.

3 Results and Discussion

The spatial distribution of LST, NDVI, NDBI, and UHT was compiled for the four cities. In this study, only the results corresponding to Casablanca are presented as a case study. This example is presented on the basis of the significant spatial variation each index measured for the period 2000–2020.

3.1 Spatiotemporal Analysis of LST, NDBI, and NDVI

Based on Fig. 1, it is observed that the temperature ranged between 17.33 and 45.88 °C in June 2000, with a mean LST of 37.3 °C. In 2020, the temperature was ranging between 20.14 and 41.14 °C, with a mean LST of 38.1 °C in Casablanca. As Fig. 1 illustrates, the highest values of LST are recorded mainly in the built-up regions, where the NDBI index is reportedly found to be high in both 2000 and 2020. Also, it is found that the built-up index has increased. This may be explained by the fact that the various building materials used nowadays are better trapping radiation, thus contributing to the increase of LST. The NDVI index has decreased from 2000 to 2020, which may be explained by the rapid increase of urbanization in Casablanca. This contributed to the replacement of green areas, which demonstrates the high values of temperature in areas where the green cover has decreased in 2020.

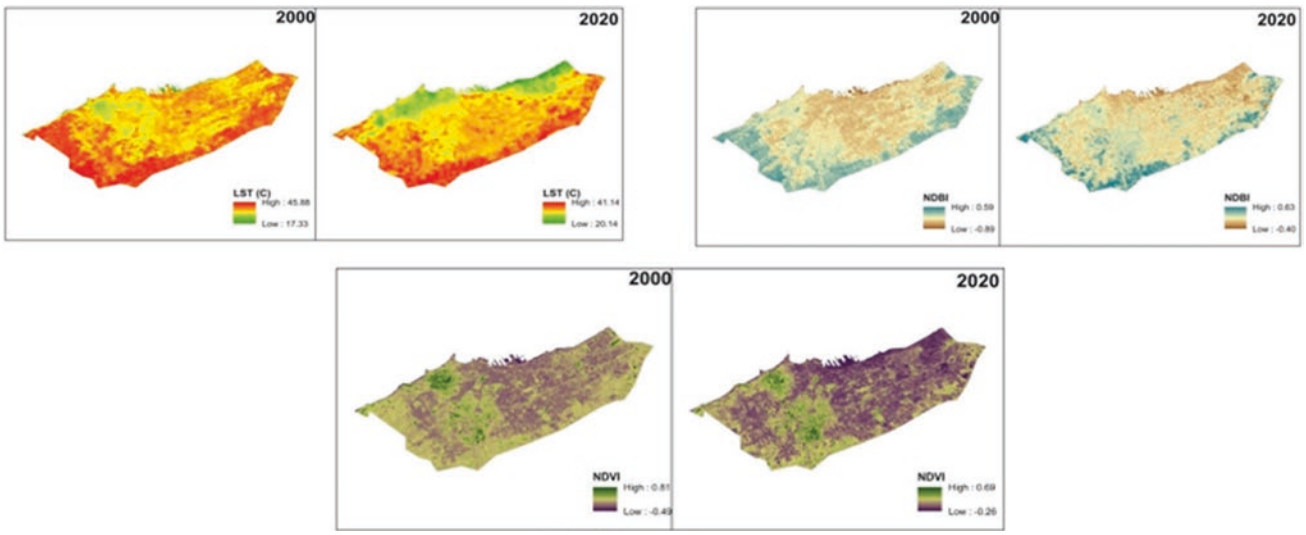

Fig. 1 Spatiotemporal distribution maps of LST, NDBI and NDVI, respectively, for June 2000 and 2020 in Casablanca

3.2 UHT Index

As Fig. 2 illustrates, it is observed that the UHT index values have slightly increased from 2000 to 2020, ranging from 0.01 to 0.99. In the city center, the UHI index values are around 0.6 or more, whereas the values increase considerably in the South-East of the city in 2020. Based on Fig. 1, it is noted that the UHI index is higher in areas, where the built-up index increases and the vegetated areas in the South-East of Casablanca decrease. The low UHT index values recorded in the coastal area of Casablanca can be explained by the moderating oceanic control, which reduces the UHI effect in summer.

3.3 LST Relationship with Land Surface Parameters

Correlation analysis between the LST, NDVI, and NDBI was elaborated for establishing relationships as shown in Fig. 3. The analyses have shown a strong positive linear correlation of mean LST with NDBI in both 2000 and 2020 ($r^2 = 0.853$). This reflects the proportional relationship between the variation of the land surface temperature and built-up areas. The results obtained through the correlation between LST and NDVI show a negative correlation. This demonstrates that in areas with high NDVI, the temperature is found to be lower than areas with low NDVI values.

4 Conclusions

This study set out to investigate the spatial and temporal variation of land use and land cover (LULC), with that of land surface temperature (LST). The purpose is to analyze the characteristics of SUHI in four selected cities of Africa. Our results show the following: (1) The LST is in constant increase since 2000, changing the ranges in temperature. This is a manifestation of increasing urbanization, decreasing green areas, and the rapid growth rate in

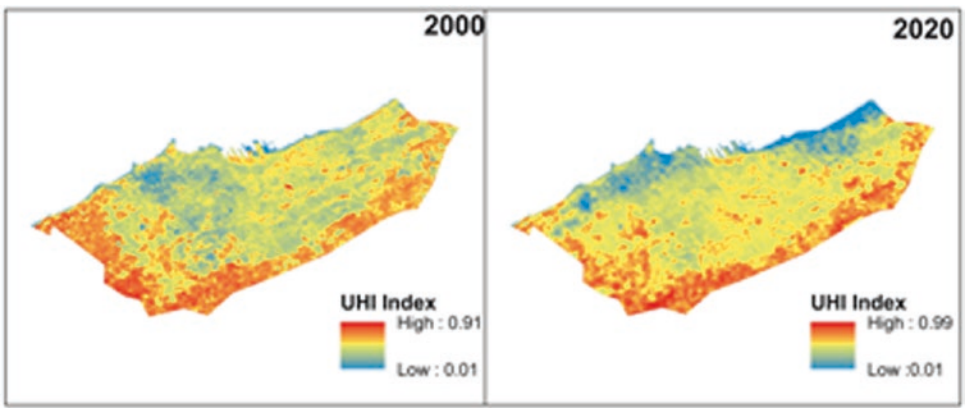

Fig. 2 Spatiotemporal distribution map of UHT for June 2000 and 2020 in Casablanca

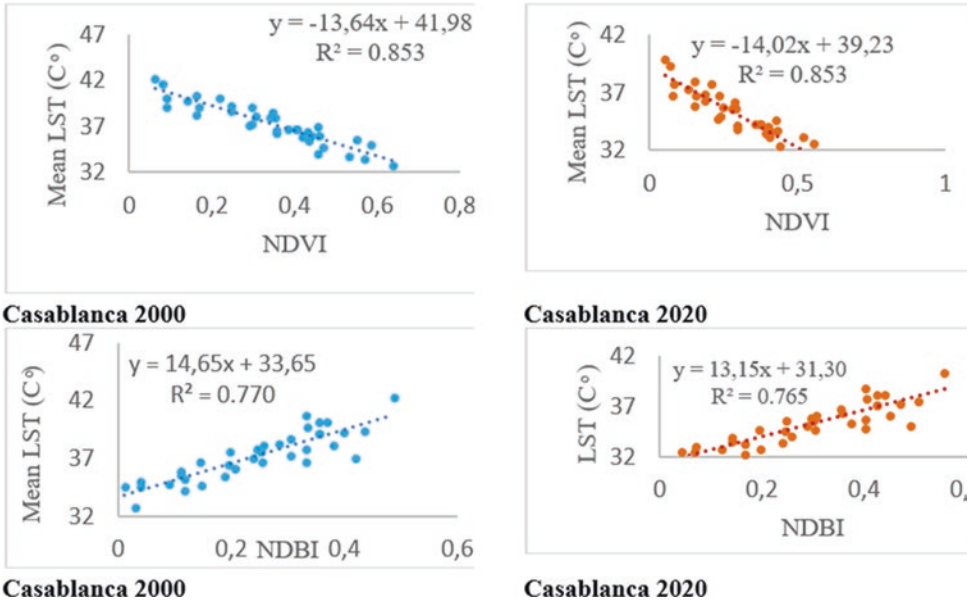

Fig. 3 Correlation between the LST, NDVI, and NDBI for 2000–2020 in Casablanca

built-up regions. (2) Taking the Casablanca case, it is evident that oceanic influences help regulate the UHT. Despite an increasing UHI index, the UHT index's values were low, which explains the natural climate regulatory effects by the sea.

References

Abdelal, Q., Assaf, M. N., Al-Rawabdeh, A., Arabasi, S., & Rawashdeh, N. A. (2022). Assessment of Sentinel-2 and Landsat-8 OLI for small-scale inland water quality modeling and monitoring based on handheld hyperspectral ground truthing. *Journal of Sensors*, 2022. https://doi.org/doi.10.1155/2022/4643924

Alkhalidi, A., Assaf, M. N., Alkaylani, H., Halaweh, G., & Salcedo, F. P. (2023). Integrated innovative technique to assess and priorities risks associated with drought: Impacts, measures/strategies, and actions, global study. *International Journal of Disaster Risk Reduction, 94*, 10380010. https://doi.org/1016/j.ijdrr.2023.103800

Assaf, M. N. (2019). *Utilizing Landsat 8 and sentinel 2 satellites images for water quality evaluation in King Tala Dam*. German Jordanian University.

Baret, F., & Guyot, G. (1991). Potentials and limits of vegetation indices for LAI and APAR assessment. *Remote Sensing of Environment, 35*(2), 161–173.

Hussein, N. M., & Assaf, M. N. (2020). Multispectral remote sensing utilization for monitoring chlorophyll-a levels in inland water bodies in Jordan. *The Scientific World Journal, 2020*, 7.

Hussein, N. M., & Assaf, M. N. (2023). Assessment of spatial and temporal distribution of Urban Heat Islands (UHI) in semi-arid climate. *Journal of Environmental Engineering and Landscape Management, 31*(1), 52–66. https://doi.org/10.3846/jeelm.2023.18482

Hussein, N. M., Assaf, M. N., & Abohussein, S. S. (2021). Application of sentinel 2 to evaluate colored dissolved organic matter algorithms for inland water bodies in Jordan. In *Proceedings of the 9th Jordan international chemical engineering conference (JICHEC9)* (Vol. 12, p. 14).

Hussein, N. M., Assaf, M. N., & Abohussein, S. S. (2023). Sentinel 2 analysis of turbidity retrieval models in inland water bodies: The case study of Jordanian dams. *The Canadian Journal of Chemical Engineering, 101*(3), 1171-1184. https://doi.org/10.1002/cjce.v101.3 10.1002/cjce.24526

Liu, H., & Weng, Q. (2011). Enhancing temporal resolution of satellite imagery for public health studies: A case study of West Nile Virus outbreak in Los Angeles in 2007. *Remote Sensing of Environment, 117*, 57–71.

Mathew, A., Khandelwal, S., & Kaul, N. (2016). Spatial and temporal variations of urban heat island effect and the effect of percentage impervious surface area and elevation on land surface temperature: Study of Chandigarh city, India. *Sustainable Cities and Society, 26*, 264–277. https://doi.org/10.1016/j.scs.2016.06.018

Saleh, S. A. H. (2010). Impact of urban expansion on surface temperature in Baghdad, Iraq using remote sensing and GIS techniques. *Journal of Al-Nahrain University, 13*, 48–59.

Zhang, X., Estoque, R. C., & Murayama, Y. (2017). An urban heat island study in Nanchang City, China based on land surface temperature and social-ecological variables. *Sustainability Cities in Society, 32*, 557–568.

Study of the Urban Extension of Laghouat (Algeria) Between 2007 and 2020 Using the Modified Built-Up Index (MBAI) from Spot-5 and Sentinel-2 Images

Kamel Hachemi and Fatiha Benkouider

Abstract

For years, Laghouat city (Algeria), a semi-arid area, has experienced an urbanization rate of 93% and urban sprawl constrained by topography and hydrology. Laghouat is exposed to many natural hazards as wind erosion, siltation, and inundation. Faced with these hazards, its vulnerability is intensified following the challenges of population growth and necessarily the increase in construction in recent years. The objective of this work is to follow the urban expansion of Laghouat city between two dates using the modified built-up area extraction index (MBAI). For this purpose, two 10 m resolution satellite images were used; the first one is a Spot-5 image acquired in 2007 and the second a Sentinel-2 image acquired in 2020. The MBAI index has been applied to these two images and has shown its effectiveness. The two highlighted built-up spaces are used to analyze the evolution of Laghouat city over this period. The built-up spaces are, respectively, estimated to be 21 km^2 in 2007 and 27 km^2 in 2020, corresponding to an urban extension rate of 28% over a period of 13 years with an average annual speed of 0.45 km^2/year. The risk map produced shows that Laghouat city is exposed to a rapid urban sprawl directed toward risk areas which are exposed to silting and flooding in old wadis.

Keywords

SPOT · Sentinel-2 · Urban sprawl · Semi-arid zone · Spectral index

1 Introduction

Laghouat city (Algeria) has experienced floods and silting risks for many decades. The increase in the population with a rate of 81.20% between 1998 and 2012 did therefore lead to an increase in buildings, which will necessarily increase the stakes and amplify the risks. This region already has 3083 constructions in flood zones (Aissa Madaoui & Aissa Madaoui, 2016). Laghouat station recorded a volume of sand of 20.7 m^3/year moved on a line one meter long by southwest and southeast winds (Dubief, 2001). The annual average sand winds duration in Laghouat is 37.1 h in all directions, and newly built spaces are at the foot of sand accumulation areas without any protective structure (Abdellaoui & Marmi, 2010). Following these problems, monitoring the urban sprawl seems to be the first task. In this paper, a study of urban sprawl in Laghouat city (Algeria) in a period of 13 years (between 2007 and 2020) from two images (Spot-5 and Sentinel-2) was carried out. The methodology consists of extracting built-up areas using the modified built-up area extraction index (MBAI) (Benkouider et al., 2019), quantifying, comparing, evaluating, and analyzing the obtained results.

K. Hachemi
Laboratory MEDIATIONS, Sorbonne University and Paris-Est University, Maison de La Recherche, 28 Rue Serpente, 75006 Paris Cedex, France
e-mail: kamel.hachemi@u-pec.fr

F. Benkouider (✉)
Telecommunications, Signals and Systems Laboratory, Department of Electronics, Faculty of Technology, University Amar Telidji of Laghouat, BP 37G, Bd des Martyrs, 03000 Laghouat, Algeria
e-mail: f.benkouider@lagh-univ.dz

Z. A. Ergüler et al. (eds.), *Selected Studies in Geotechnics, Geo-Informatics and Remote Sensing*, Advances in Science, Technology & Innovation, https://doi.org/10.1007/978-3-031-43759-5_13

2 Materials and Methods

2.1 City of Laghouat and Its Characteristics

The city of Laghouat (Algeria), known as the gateway to the desert, is located on the border between the high steppe plateaus and the Saharan region, about 330 km as the crow flies from the Mediterranean coast, at an altitude of 751 m and at a latitude of 33°47′59″ North and a longitude of 2°52′59″ East (see Fig. 1). Laghouat covers an area of 400 Km^2 including a growing population with an average density of 384 inhabitants/km^2, i.e. between 2007 and 2012 (Table 1).

This city is bounded to the northeast by the Oued M'zi, to the south by the vast Algerian desert (sandy area), and to the northwest by Jebel Ahmar (862 m) from the Pre-Saharan Atlas. The Oued M'zi passes between Jebel Ahmar in the west and Jebel Dakhla in the east (see Fig. 1). These two structures form the same chain which was cut in two by a fault in the direction of southwest/northeast. The city is also limited in the south by Oued M'saad, one of the tributaries of Oued M'zi.

2.2 Methodology

In order to properly carry out this study of monitoring the urban extension of Laghouat city, we proceeded as follows:

Fig. 1 Geographical characteristics of Laghouat city, produced from Sentinel-2A image (2020)

Table 1 Population of the city of Laghouat (Abdellaoui & Marmi, 2010)

Year	1830	1977	1987	1998	2003	2007	2008	2012
Inhabitants number	6000	42,800	69,435	96,342	119,043	132,891	144,747	174,575
Density hab./km^2	15.00	107.00	173.59	240.86	297.61	332.23	361.87	436.44

(1) extract the built-up area using the modified built-up area index (MBAI) from Spot-5 and Sentinel-2 images; (2) map these areas; (3) draw up a risk map. The choice of this MBAI index is based on three reasons: (1) has already been applied to Laghouat; (2) has been applied to the spot images; and (3) gave good results. The MBAI index proposed by Benkouider et al. (2019) was applied to the spot image using the following Eq. (1):

$$\mathrm{MBAI} = \frac{B_{\mathrm{NIR}} + 1.57B_G + 2.4B_{\mathrm{SWIR}}}{1 + B_{\mathrm{NIR}}} \quad (1)$$

where $\boldsymbol{B_G}$, $\boldsymbol{B_{\mathrm{NIR}}}$, and $\boldsymbol{B_{\mathrm{SWIR}}}$ indicate the digital number of the green, near infrared, and SWIR band, respectively.

3 Results

3.1 Application of the MBAI Index

The MBAI index has been successfully tested on Laghouat using Spot-5 images and was able to serve as a worthwhile alternative for quickly and objectively mapping built-up areas (Benkouider et al., 2019). Sentinel-2 carries a super-spectral sensor with 13 bands in the visible and near infrared (VNIR) and short wave infrared (SWIR) wavelength bands, and they are given in central wavelength. The extraction of built-up areas from Sentinel-2 imagery was recently developed. A large number of indices have been tested along with the individual spectral bands, and target discrimination was possible in most of them (Randu et al., 2016; Sabo et al., 2017). Overall, results for Sentinel-2 highlight the critical importance of a good compromise between the spatial and spectral resolution. The resolutions of the spectral bands used for the MBAI index are shown in Table 2.

The response of bare soil generally results in a low increasing interval (0.4–0.6 μm) corresponding to blue and green. The infrared (MIR), which corresponds to band 4 in the spot image and to SWIR in Sentinel-2 image, is associated with a high contrast level for detecting built-up and bare land areas (Bhatti & Tripathi, 2014). The MBAI is, therefore, higher and hence has increasingly white shades. The MBAI is applied to images of Laghouat (Spot-5 and Sentinel-2) (Fig. 2). In the MBAI, built-up areas appear in white.

Table 2 Spectral resolution of used bands in Spot-5 and Sentinel-2

Band	Image	Spot-5	Sentinnel-2
	Absorption	Spectral resolution (μm)	Spectral resolution (μm)
B_G	Green	0.50–0.59	0.5598
B_{NIR}	Near infrared	0.79–0.89	0.8328
B_{SWIR}	Short-wave infrared	1.58–1.75	1.665

3.2 Cartography

In order to clearly highlight the changes, a simple way to perform change detection between two satellite images is to put a composition of colors. The algorithm chosen for the detection of changes in our case is the simplest possible, i.e., the color composite and thresholding MBAI images dates. We assigned two colors, the blue for the image of March 26, 2007 (Fig. 3a), and the red for the image of March 5, 2020 (Fig. 3b).

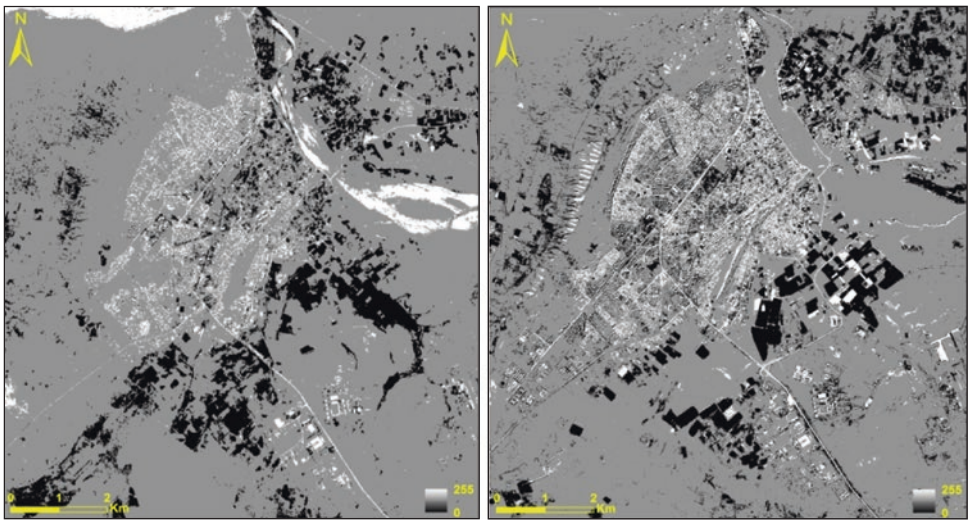

Fig. 2 Built-up areas identified by MBAI index, **a** Spot-5 image (2007), **b** Sentinel-2 image (2020)

(a) **(b)**

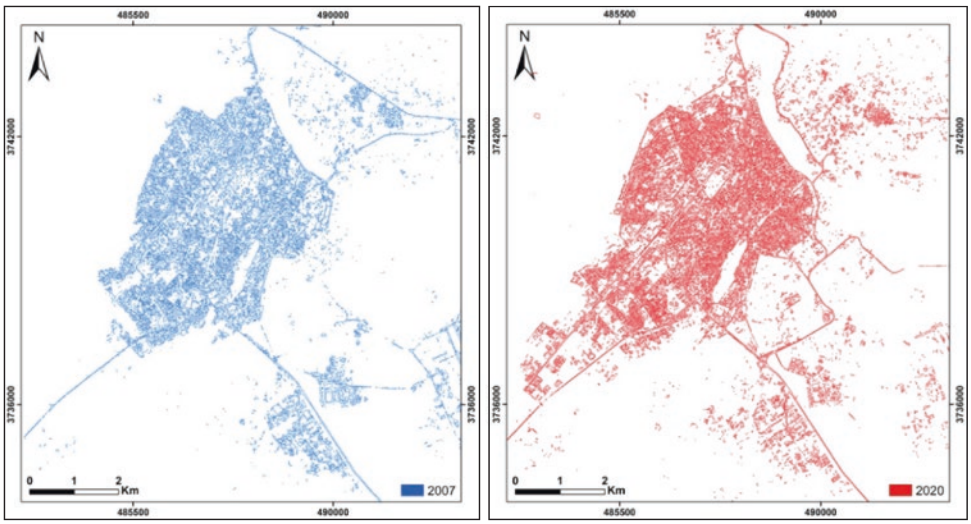

(a) (b)

Fig. 3 Binary map of built-up area, **a** Spot-5 (2007), **b** Sentinel-2 (2020)

3.3 Evolution of the City of Laghouat Between 2007 and 2020

These two binary images have provided an urban sprawl evolution map for thirteen years (Fig. 4). We also estimated the occupied areas at approximately 21.07 km^2 in 2007 and 26.88 km^2 in 2020. These results thus enabled us to calculate the rate of change of this expansion at 28% in this period of 13 years (Table 3), i.e., an annual average speed of 0.45 km^2/year. Table 3 summarizes the parameters extracted from the city between 2007 and 2020 (Table 3). Subsequently, we produced a thematic map (Fig. 4b) showing the bed of the Oued Msaad.

4 Discussion

The comparison of the obtained results from two sensors HRG (Spot-5) and MSI (Sentinel-2A) allowed us to conduct some comments: for Spot-5 image, some built-up areas are confused with water, unlike the case of Sentinel-2 image where there is total discrimination between built-up area features and water (Fig. 2). It should be noted that there are also parts of the areas of Jebel Ahmar and Jebel Dakhla that showed the same signals as the built-up area is due either to: (i) meteorological conditions of the shooting dates, 2007 and 2020, which left the imaged materials to have the same reflectance signals close to the spectral

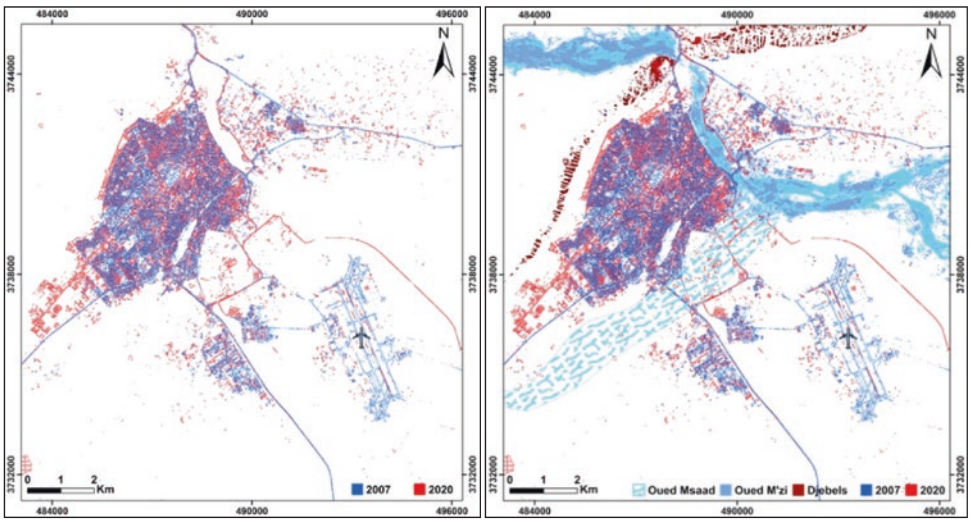

(a) (b)

Fig. 4 Evolution maps of Laghouat city, **a** Map of the built-up area evolution between 2007 and 2020; **b** Laghouat thematic map

Table 3 Results of the parameters extracted by the analysis for the city of Laghouat

City of Laghouat 2007		City of Laghouat 2020		Speed of annual evolution		Amount of growth between 2007 and 2020	
Perimeter (km)	Area (km^2)	Perimeter (km)	Area (km^2)	Perimeter (km/an)	Area (km^2/an)	Perimeter (%)	Area (%)
49.2	21.1	59.,3	26.9	0.8	0.45	20.4	27.6

bands used by the MBAI index (B_G, B_{NIR}, B_{SWIR}); or (ii) differences in the spectral resolutions used by the two sensors, HRG and MSI. These differences of a few hundredths (1/100) of a μm of the wavelengths used by the two satellites, Spot-5 and Sentinel-2A (Table 2), can have different discriminating power, so more classes are possible.

This study enabled us to produce a risk map showing the threats to the city of Laghouat (Fig. 4b). These are caused by two major phenomena characterizing this region. The first includes the problem of silting up, which accelerates with the increase of the average wind speed and is dependent on wind direction. The southwest/northeast wind direction coincides with the major axis of the urban sprawl of Laghouat city. This map also shows another direction of urban sprawl toward the northwest at the foot of the sand accumulation areas where new constructions are visible. The second risk consists of the phenomena of seasonal flooding, repeated in this city. This threat comes from Oued Msaad which is a tributary of Oued M'zi. During periods of rainfall, the Oued M'zi overflows, occupying its major bed, thus, obstructing the outflow of the Oued Msaad, and causing significant damage.

5 Conclusions

In this paper, the MBAI index is used to analyze the urban growth of the city of Laghouat (Algeria) over a period of thirteen years and also to produce the risk maps of this city. Built-up areas were extracted for two dates 2007 and 2020 from two different sensors, Spot-5 and Sentinel-2A, respectively. We have produced accurate maps showing the urban sprawl of Laghouat city as well as the constraints and risks that threaten it. This study reveals a rapid urban sprawl oriented toward the risk zones caused by population growth. We have recorded constructions in sandy areas, exposed to silting risks, and in areas susceptible to flooding such as old wadis.

References

Abdellaoui, A., & Marmi, R. (2010). Mise en évidence de mouvements de sable à partir d'images satellitales; application au piémont sud de l'atlas saharien (Algérie). *Analele Universitatii Bucuresti Geografie, 10*, 2–14.

Aissa Madaoui, A., & Aissa Madaoui, R. (2016). *Protection des villes contre les inondations cas du centre d'Ain Fezza Tlemcen*. Master thesis in Hydrolic, Option: Eau, Sol et Aménagement, pp. 1–135.

Benkouider, F., Abdellaoui, A., & Hamami, L. (2019). New and improved built-up index using SPOT imagery: Application to an arid zone (Laghouat and M'Sila, Algeria). *Journal of the Indian Society of Remote Sensing, 47*, 185–192.

Bhatti, S. S., & Tripathi, N. K. (2014). Built-up area extraction using Landsat 8 OLI imagery. *Giscience and Remote Sensing, 51*(4), 445–467.

Dubief, J. (2001). *Données météorologiques du Nord de l'Afrique à l'équateur*. Edition Karthala.

Randu, J., Chomé, G., Christophe Jaque, D., Waldner, F., Bellmans, N., et al. (2016). Sentinel-2's potential for sub-pixel landscape feature detection. *Remote Sensors, 8*(6), 488.

Sabo, F., Corbane C., & Ferri S. (2017). *Inter-sensor comparison of built-up derived from Landsat, Sentinel-1, Sentinel-2 and SPOT5/SPOT6 over selected cities*. EUR 28520 EN, European Union.

Spatial Analysis of Mobile Communication Coverage in Rural and Urban Areas of Jodhpur District, Rajasthan (India)

Aswathy Puthukkulam, Sanjay Gaur and Anand Plappally

Abstract

Mobile towers or antennas installed by the only government company in the urban and rural areas of the Jodhpur district were surveyed. In this study, a total of 341 towers installed by the government were spatially overlayed on the shapefile of the district. This article provides a specific case study on the type of distribution of the communication coverage provided by these installations. The acquired data from Bharat Sanchar Nigam Limited (BSNL), India, included spatial coordinates of the towers, frequencies, and antenna heights. Using Okumura-Hata model for path loss prediction, coverage of individual towers was calculated using a MATLAB software code. The coverage area of each tower or antenna is overlaid on the district's shapefile using ARCMAP toolbox. Coverage of rural government towers in the district of Jodhpur was found to follow a logistic distribution with an average radius of 7.20118 km. A three-parameter Gamma distribution of mobile tower coverage in urban areas confirms an extremely large density of small antennas existing within a small land surface area. The implication of the study provides newer insights into the spread of communication coverage in a specific geography which would enable innovative opportunities to improve communication businesses.

Keywords

Coverage · Antenna · Distributions · Rural · Urban

A. Puthukkulam (✉) · S. Gaur
Jodhpur Institute of Engineering and Technology, RTU, Kota, Rajasthan, India
e-mail: aswathyp87@gmail.com

A. Plappally
Indian Institute of Technology Jodhpur, Jodhpur, Rajasthan, India

1 Introduction

Communication researchers across the globe have started working on models which improve connectivity while deciding spatial locations to install cellular towers (Amaldi et al., 2008). Milli-metric waves, high altitude platforms, and cellular planning have been of importance in providing better coverage for densely populated areas across the world (Thornton et al., 2003). Rural locations of Asiatic nations like India have geographies which will take a long time to adapt to such technologies (Yarkoni et al., 2007). The coverage bias can create a development bias in providing services in rural and urban locations. Therefore, a deep understanding of topography, the density of users, coverage distribution, and individual antenna specifications become pertinent (Puthukkulam et al., 2020). Antenna location, mobile user location, operating frequencies, and environmental factors are used to envisage coverage for a location. This article aims to comprehend coverage distribution in rural and urban locations in semi-arid landscape and depict it.

2 Settings and Methods

The study area lies between 25° 50′ 34″ N to 27° 37′ 59″ N latitude and 71° 45′ 37″ E to 73° 56′10″ E longitude. Its shapefile illustrated in Fig. 1a has been prepared using ARCMAP 10.2. The administrative boundary files are extracted from the Web site entitled indianremotesensing.com.

In the Jodhpur block, the contour lines are closely spaced at a specific area toward its north-west as specified in Fig. 1b. The undulating district is dotted by 341 governmental towers extending across rural and urban parts. The data on governmental towers was obtained from Bharat Sanchar Nigam Limited (BSNL) India, Jodhpur division. The heights of the towers provided by them ranged between 15 and 80 m. The maximum height of the urban towers is

Z. A. Ergüler et al. (eds.), *Selected Studies in Geotechnics, Geo-informatics and Remote Sensing*, Advances in Science, Technology & Innovation, https://doi.org/10.1007/978-3-031-43759-5_14

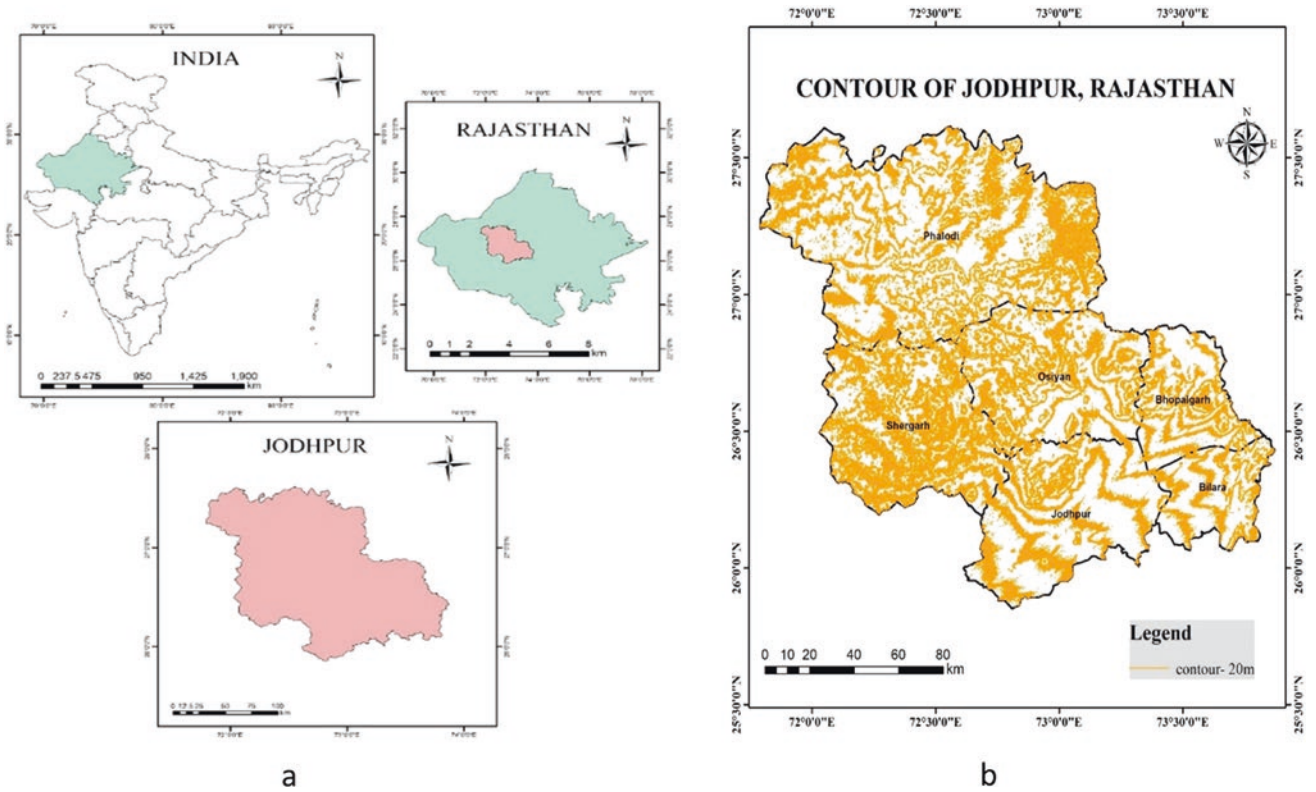

Fig. 1 Shapefile of Jodhpur district **a** Depicts the shapefile **b** Delineates the contours within the six blocks of the district

around 60 m, and the average is 30 m. The indoor coverage thresholds with 90% location probability in urban and rural areas are − 74.2 and − 82.2 dBm, respectively. The maximum allowed path loss can be calculated using the formula (Yarkoni et al., 2007),

$$\text{Path Loss} = \text{EIRP} - \text{RSSI} \tag{1}$$

where RSSI is received signal strength intensity, and EIRP is effective isotropic radiated power. The provided value of EIRP is 43 dBm (Yarkoni et al., 2007). The Okumura-Hata model is used for predicting signal propagation and path loss. From Eq. 1, the coverage of 341 towers was calculated in a MATLAB coding environment (Puthukkulam et al., 2020). The detailed procedure for coverage calculation can be referred from Puthukkulam et al. (2020). The coverage is then spatially plotted and analyzed using a buffer tool in ARCMAP 10.2 environment.

3 Results

3.1 Coverage

Using Okumura-Hata model, coverage distances for all the 341 towers were calculated. The coverage in the rural area of the Jodhpur district tends to follow a logistic distribution. It means that a binary classification is prevalent while developing a strategy for installing antennas in rural locations. This supports the government's view of installing towers in the Dhanis or villages which are separated by large inter-spacings (Puthukkulam et al., 2020).

Inferring from the logistic distribution in Fig. 2a, the users of wireless coverage will have only the option of using their mobile devices at specific locations in the rural areas. In order to validate that, Anderson Darling (AD) test was used. The AD statistic is smallest (24.395) for distribution in Fig. 2a, confirming coverage to be logistic in nature.

The value of AD statistic is the smallest (18.138) as illustrated in Fig. 2b for the urban data. Now, this coverage data can be accepted to follow the three-parameter Gamma distribution. Likelihood-ratio test (LRT) p-value is $< 95\%$ confidence level (0.05), and thus, three-parameter Gamma offers significantly better goodness-of-fit than the other distributions for this univariate data of Fig. 2b.

4 Discussion

From the above discussion, the coverage followed a distinct behavior in rural and urban locations of the Jodhpur district. Figure 3a shows the coverage of 15 randomly selected towers in rural parts of Jodhpur. The randomness in coverage

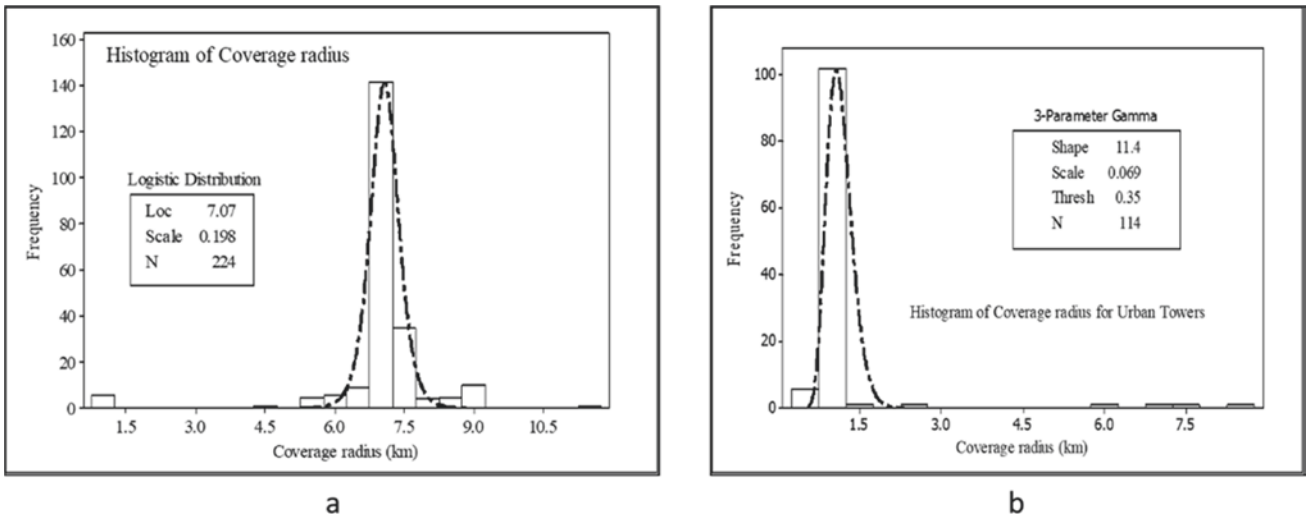

Fig. 2 **a** The logistic distribution fitted histogram of coverage of towers mapped across rural parts. **b** The three-parameter Gamma distribution fitted histogram of coverage of towers mapped across urban parts

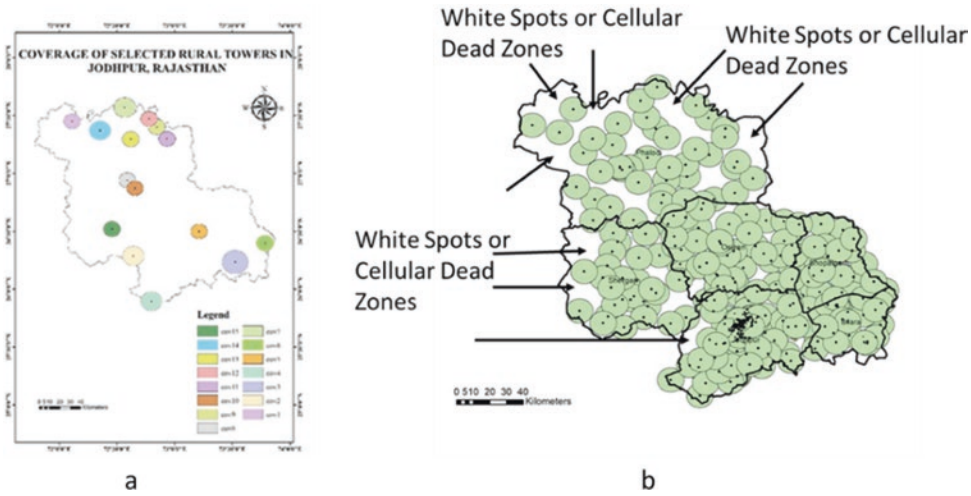

Fig. 3 **a** Coverage plotted utilizing buffer tool in ArcMap on randomly selected communication antennas in rural parts of the district. **b** Depiction of white spots

radii within rural locations is also illustrated. The average rural coverage radii were found to be 7.20118 km and that of urban towers was 1.02388 km. These values were used for depicting the coverage provided by each tower as illustrated in Fig. 3b. This plot helps to enumerate the approximate cellular dead zones or white spots in the Jodhpur district.

5 Conclusions

The coverage overlaps in Fig. 3 support the view of interference as an unavoidable risk in wireless networks in rural and urban Jodhpur. Rural and urban coverage was found to follow logistic and three-parameter Gamma distribution, respectively. It is also clear that there are locations which do

not have the coverage in the pastoral reaches of the district which are white spots.

Prior knowledge of coverage distribution and white spots in the district will help to establish future antenna business opportunities.

References

Amaldi, E., Capone, A., & Malucelli, F. (2008). Radio planning and coverage optimization of 3G cellular networks. *Wireless Networks, 14*, 435–447.

Puthukkulam, A., S. Gaur, Vinod, T. R., Plappally, A. (2020) Establishing relationships of cellular communication coverage provided by governmental and non-governmental companies as a function of digital elevation, population density, and transport infrastructure in Jodhpur District, Rajasthan. In *Proceedings of the XIV IGU-INDIA, Burdwan*.

Thornton, J., Grace, D., Capstick, M. H., & Tozer, T. C. (2003). Optimizing an array of antennas for cellular coverage from a high altitude platform. *IEEE Transactions on Wireless Communications, 2*(3), 484–492.

Yarkoni, N., Blaunstein, N., & Katz, D. (2007). Link budget and radio coverage design for various multipath urban communication links. *Radio Science., 42*(2), 12867.

Integrating Biophysical Parameters Into the Identification of Soil Map and Pedological Characteristics: Application to the Western High Atlas Mountains, Morocco

Adnane Labbaci, Said Moukrim, Said Laaribiya and Ouafae Abdelouahab Reddam

Abstract

Soil maps have paramount importance as they enable scientists, as well as decision-makers, to make relevant choices in areas ranging from agronomy to land use planning. In this paper, we consider three main factors of soil differentiation: the materials, resulting from a lithological synthesis made from the geological maps; morpho-landscapes, extract from the digital elevation model (DEM); and land cover map, developed from the Sentinel image. Several methods are proposed to make better use of the information available on soils. Four approaches can be distinguished: the reference sector method, the exploitation of soil-landscape relations, statistical and geostatistical modeling, and the contribution of the geographic information system (GIS) in soil mapping. Among these four approaches for mapping soils, the landscaping approach and the use of GIS and remote sensing modeling will be adopted. For this article, we have crossed three layers of mono-factorial information, whose weighting is estimated to be the same, to arrive at a pedological sketch representing the homogeneous zones. Ninety-four homogeneous units were identified, from which we have developed an implementation map of 51 soil profile sites. The aim of this study is to identify the portions of sand, clay, and silt for each site through laboratory analysis. The results help determine seven pedological units represented in six cartographic units.

Keywords

Soil map · Geology · Lithology · GIS remote sensing · Site · Pedological sketch

1 Introduction

For elaborating soil maps, the following cartographic documents are most often used: geological maps; topographic maps and/or DEM; vegetation maps and aerial photographs and/or satellite images. Duchaufour (Duchaufour, 1991; Emberger, 1955) emphasizes the role of geology in the preparation of soil maps. Maps are synthesized with the help of the neighborhood relations of the map units to arrive at a map of the materials. Several authors have recognized that relief is a predominant factor in several pedogenetic processes (Aandahl, 1948; Baize & Jabiol, 1995; Moore et al., 1991). The DEM is used in the GIS software to derive the other morphological attributes (slope and exposure), the whole expresses the relief of the zone, which constitutes an important factor for the development of soil distribution in the landscape (Moore et al., 1991). Currently, remote sensing data processing software focuses on the textural analysis of pixel-to-pixel data but does not include methods for processing organizations (Girard, 1989). Structural methods have since been developed to fill this gap. They consider for analysis, the pixel and its neighborhood: OASIS (Gilliot, 1992, 1994; Girard & Girard, 2004; Gomez, 2004), PAPRI (Borne, 1990), CLAPAS (Robbez-Masson, 1994) which give a good result from the renderings cartography, visual and statistical analyses. The information from the satellite

A. Labbaci (✉)
Geosciences and Geo environment lab, Faculty of Sciences of Agadir, Ibn Zohr University, 80000 Agadir, Morocco
e-mail: labbaciadnane@gmail.com

S. Moukrim
High Commission On Water Forests and Combating Desertification, Quartier Administratif, Challah Rabat, Morocco

S. Laaribiya
Geography Department, Chouaib Doukkali University, El Jadida, Morocco

O. A. Reddam
Geography Department, Jaume I University, Castellon, Spain

Z. A. Ergüler et al. (eds.), *Selected Studies in Geotechnics, Geo-Informatics and Remote Sensing*, Advances in Science, Technology & Innovation, https://doi.org/10.1007/978-3-031-43759-5_15

images makes it possible to produce the land cover map that we have introduced into the model for the elaboration of the soil sketch and identify the different soils existing in the study area.

2 Materials and Methods

To establish this pedological sketch map, we have used cartographic data that will allow the differentiation of soils. The study area is covered by the geological map of the Argana corridor at 1/100,000. The map was scanned, and different geological layers were digitized. To obtain the DEM, the contours were digitized from topographic maps. The altimetric accuracy of these maps is 20 m. These data also permit the derivation of elevational and slope maps that can be integrated into the model for the realization of the site pedological sketch. The Sentinel-2 image, after atmospheric and radiometric correction, was used to develop the land cover map by using a supervised classification with the maximum likelihood algorithm. The lithological map is obtained from the interpretation of the different origins and characteristics of rocks. After interpreting the legend of the geological map, the homogeneous units were grouped and built into a new class. Next, the formations according to their physico-chemical characteristics were differentiated. The development of the physiographic unit map makes it possible to visualize the information concerning the altitudes and reliefs of the study area. To determine physiographic units, classes of slopes and altitudes were extracted from the DEM. These classes will be combined to extract the map of physiographic units. The overlaying of the different maps generated (lithological map, land use map, and morphological map) provides for a map of homogeneous units. These units are defined as surfaces having the same lithological, morphological, and occupancy characteristics.

3 Results

The development of the soil cartographic sketch is the result of the overlaying of maps corresponding to the extrinsic factors of soils, geology, morphology, and land use.

3.1 Derivation of the Lithological Map from Geological Data

According to the geological map of the corridor of Argana (Western High Atlas), which covers our study area, 14 geological units can be distinguished. This zone is dominated by Jurassic and Permo-Triassic formations, with the presence of quaternary terraces resulting from the alluvial and colluvial phenomena of the latter. Six lithological units are distinguished, and the range of each unit is represented by a sub-total. The most representative entities are limestones, clay limestones, conglomerates, and alluviums, with a recovery rate of 51, 20, 13, and 10%, respectively.

Table 1 Land use classes of the study area

Classes	Area (Ha)	%
Dense forest	6012.27	25.51
Moderately dense forest	12,122.11	51.44
Shallow forest	4687.11	19.89
Cultivated land	666.96	2.83
Bare soil	75.78	0.32

3.2 Derivation of the Land Cover Map

The classification of the Sentinel imagery yields five classes. Forest formation is made up of three categories: dense forest, moderately dense, and shallow forest. The other classes are cultivated lands and bare soil (Table 1).

3.3 Derivation of the Physiographic Units' Map

The overlay of the slope map and elevations permits the establishment of the physiographic unit's map. Thereafter, a cartographic generalization of the classes was obtained by eliminating small surfaces, considering the norm of a quarter (1/4) cm^2 as the smallest mapped surface representable on paper charts (Gadas, 2001). In our study, we considered a scale representation of 1/100,000, hence eliminating areas < 25 ha. The results of overlaying the slope map (5 classes) and the elevation map (6 classes) yielded 26 physiographic units instead of 30 units.

3.4 Derivation of the Homogeneous Units' Map and Implementation of Soils Profiles

The map of homogeneous units represents the distribution of soil types. It is obtained from the superposition of the three mono-factorial maps previously described. The superposition of the three maps and the map processing of the results by assigning units smaller than 25 ha to neighboring units of larger size yields 51 homogeneous units.

3.5 Soil Profile Implantation

For a scale of 1/100,000, we will have to plant a profile for every 250 ha. For the study area, this equates to 94 profiles. With the use of homogeneous units and respecting the rule of 250 ha per unit of a large area, 51 profiles are analyzed. The remaining 43 profiles are only for observational purposes. The study identified several soil units, some of which exist as simple map units, while others exist in association with one or more units as complex map units.

4 Discussion and Conclusion

The purpose of this soil study, using modern soil mapping tools and methods, is to develop prospection plans. From a methodological point of view, the landscape approach favoring soil differentiation factors and their interactions is the basis of the results obtained. Unlike conventional long and expensive methods, this approach makes it possible to make the most of soil formation factors and to establish a soil mapping. Parallel to the methodology adopted in this study, the tools used in spatial data processing software, the powerful computer support as well as the raster documents rich in raw and useful information, allowed an excellent manipulation of the data and results in good accuracy. To facilitate the reading of the data, a cartographic generalization has been chosen for the filtering of the units obtained to eliminate the problem of multiplicity of combinations which increases the interpretation and increase the cartographic detectability. This generalization has been coupled with a grouping process of units associated with neighborhood relations (high landscape affinity) or constitutional kinship.

Three layers of mono-factorial information were overlayed, whose weighting weight is estimated to be the same to arrive at a pedological sketch representing the homogeneous zones. Ninety-four homogeneous units were identified, based on these results, and referring to the norm of a profile per 250 ha for a scale of 1/100,000, we have developed an implementation map of the soil profiles on 51 sites. Despite the advantages of the method adopted for this study, disadvantages arise. Indeed, the choice of the data, their interpretations, and their scales can influence the results; adding to this, the overlaying of factors whose weighting remains a subject to discuss. In addition to these limiting factors, we consider it necessary to have poly-disciplinary knowledge and know-how, both technically and thematically.

References

Aandahl, A. (1948). *The characterization of slope positions and their influence on the total nitrogen content of a few virgin soils of Western I.*

Baize, D., & Jabiol, B. (1995). Guide pour la description des sols.

Borne, F. (1990). *Developing a method to map coconut agrosystems from high-resolution satellite images*.

Duchaufour, P. (1991). *Pédologie: Sol, végétation, environnement* (3rd edn.). Masson, p. 289.

Emberger, L. (1955). Une classification biogéographique des climats. *Revista Travelled in Factory Science Montpellier, 7*, 3–45.

Gadas, F. (2001). *Proposition d'une méthode de cartographie des pedopaysages application a "la moyenne vallée du Rhône"*. Thèse Institut National Agronomique Paris-Grignon.

Gilliot, P. (1992). *Surface polarization instabilities of electron-hole states in quantum dots*.

Gilliot, P. (1994). *Nanocrystals of Cds dispersed in a sol-gel silica glass: Optical properties*.

Girard, M. C., & Girard, C. M. (2004). *Traitement des Données de Télédétection*. INRA, p. 552.

Girard, M.-C. (1989). La cartographie en horizons. *Science Du Sol, 27*, 41–44.

Gomez, C. (2004). *Potentiels des données de télédétection multi-sources pour la cartographie géologique: Application à la région de Rehoboth (Namibie)* (p. 210). Thèse de Doctorat, Université Caude Bernard.

Moore, I. D., et al. (1991). Digital terrain modeling: A review of hydrological, geomorphological, and biological applications.

Robbez-Masson, S. (1994). *Implementation of a new algorithm for Clapas in R language in order to improve efficiency of soil survey*.

Study of the Flood Risk in the Middle Valley of the Medjerda Watershed Using GIS and Remote Sensing: Case of the Plain of Jendouba–Boussalem

Wiem Benali and Abd Esslem El Guali

Abstract

The objective of this study is the prediction of the flood risk in the Jendouba–Bousselem plain by using two approaches to verify the obtained maps, for the first one, we combined the parameters DTM, slope, permeability, drainage density, and land use, while for the second one, we crossed the hazard to the vulnerability. The risk simulation shows that the study area is at medium risk at the level of the city of Jendouba; this risk evolves downstream to become very high at the level of the city of Boussalem, noting that the areas near the channels and the urban areas are the most floodable and that the areas located in the periphery of the plain have the lowest risk of flooding.

Keywords

Flood risk · Vulnerability · Alea · GIS · Remote sensing

1 Introduction

Tunisia is periodically affected by floods causing loss of life and significant material damage, especially in the Medjerda watershed.

Despite the construction of several dams, the most important of which is that of Sidi Salem, and the existence of some facilities that have reduced the severity of floods, these efforts remain insufficient given the high risk, especially in the plain of Jendouba–Boussalem whose most important floods occurred in September 1969, March 1973, 1976, 2000, and January 2003, 2010.

It is important to locate and specify the gradient of the flood risk, previous works are carried out in some localities, near the wadi or in the whole catchment area of Madjerda, and for our project, we chose to study the plain.

2 Data and Methods

The agricultural map and the Commissariat of Regional Development and Agricultural Activity of Jendouba are the main sources of data in the study of the Jendouba–Bousselem plain which is located in the middle valley of Medjerda. It is worth noting that its main tributaries in the right bank are Mellègue at 10,700 km^2 and Tessa 2420 Km^2, and in the left bank, there are two tributaries, namely Bouhertma at 550 Km^2 and Kasseb at 270 Km^2. The region is characterized by a Mediterranean climate with mild and humid winters and hot and dry summers, a rainfall between 354 and 556 mm during 60–120 days, a maximum temperature of 38 °C in August and July, and a minimum of 6 °C in January. Almost all of the surface does not exceed 3°, with a medium to low permeability, a flat geomorphologic structure (Table 1), and dominance of agricultural land.

To elaborate the flood risk maps, two methods have been applied based on the classification of the issues at different levels. The first one is a superposition of the slope, relief, permeability, and drainage density parameters without having weighted them. The second one is a cross between the vulnerability of the territory obtained from the slope, the permeability, and the drainage density with the Hazard obtained from the rainfall of 1973 and the land use.

Flood risk maps are based on the following formulas (Haddad, 2012)

$$RI = MNT + 2HS + S + 1/2P + 1/2GO \quad (1)$$

$$RI = \underbrace{(HS + S + P)}_{a} \times \underbrace{(GO + R)}_{b} \quad (2)$$

W. Benali (✉) · A. E. E. Guali
Faculty of Sciences of Bizerte, 7021 Jarzouna, Bizerte, Tunisia
e-mail: wiembenali3@gmail.com

Z. A. Ergüler et al. (eds.), *Selected Studies in Geotechnics, Geo-Informatics and Remote Sensing*,
Advances in Science, Technology & Innovation, https://doi.org/10.1007/978-3-031-43759-5_16

Table 1 Geomorphology of the plain Jendoub–Boussalem

Total watershed area (km^2)	Perimeter of the watershed (km)	Shape index	Characteristics of the watershed	Length (km)	Width (km)	Specific elevation (m)
537	242	2.92	Lengthened to very lengthened	83	37	10

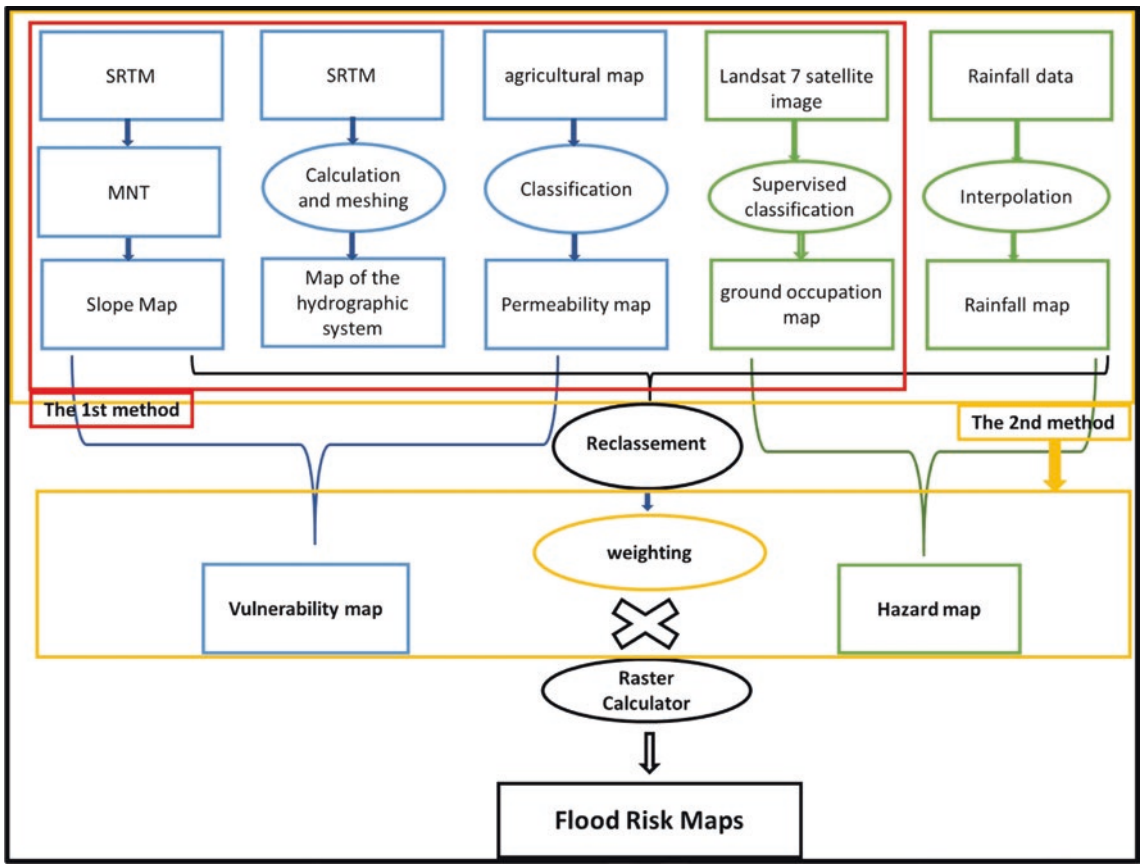

Fig. 1 Methodology for flood risk mapping

(1) First method without weighting, (2) Second method with weighting, FR—Flood risk, RS—River system, S—Slope, P—Permeability, R—Rainfall, GO—Ground Occupation, (a) Vulnerability of the land to flooding and (b) Hydro-climatic hazard (Fig. 1).

3 Results

To highlight the seriousness of the risk, the red color was used, the darker the color, the greater the probability of occurrence of the risk of flooding. The very dark red concerns areas characterized by the presence of several factors that trigger the risk.

The maps of the flood risk elaborated by the two approaches coincide summarily noting that the intensity of the risk increases by going toward the North East where the downstream zones of the catchment area of the middle valley of the Medjerda, and these zones form the front dam of Sidi Salem. They are characterized by important precipitations, a weak slope, weak permeability, and a bad location of the stakes, particularly the habitats of the populations, the urban zones of which mainly the city of Bousselem, which is the most threatened by the flood (Fig. 2).

4 Discussion

Flooding increases the number of water resources, and the exchanges between the water table and the surface are much more intense during the flood than during the rest of the year. In addition, it improves the quality of this water

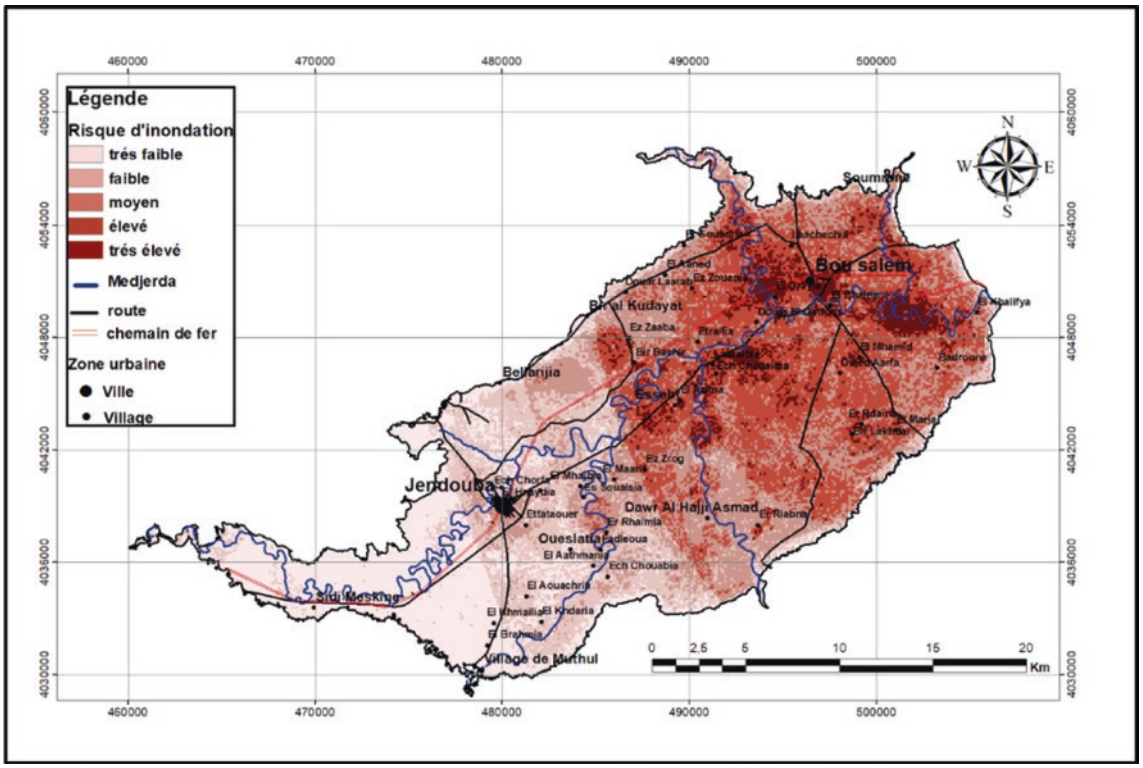

Fig. 2 Flood risk map of the Jendouba–Boussalem plain of the second method

by dilution effect; the distribution of rainfall, in space and time, is, therefore, a significant factor that conditions the variations in the O18 and H2 contents of rainwater and consequently of groundwater (Mokadem et al., 2016).

The differences in several localities between the two maps produced are understandable because the flood risk map developed by the first method seems to be the same as the drainage density map since it has the highest coefficient in the risk calculation formula. However, for the second method, the main factor that favors the appearance of flood risk is rainfall. For this reason, the flood risk map visibly reproduces the appearance of the 1973 Hazardrainfall map which reflects the greatest flood that hit Tunisia. We chose this date to predict what will happen now with the current urban development and the presence of the retention structure of Sidi Salem which will aggravate the unfathomability under the effect of the braking and the accumulation of water and sediments.

The correlation between the data provided by the cartography and the history of floods in the Jendouba–Bousselem plain shows that the flood risk map elaborated by the second method with a weighting of the parameters and crossing of the vulnerability to the hazard better reflects the reality.

The urban areas most at risk from flooding are impermeable surfaces due to the effect of the materials used such as concrete and tar. These materials inhibit infiltration and increase the speed of water rise and the violence of the runoff. The solution may, therefore, be to replace these materials with other permeable materials, which requires research.

5 Conclusions

The simulation and comparison of the two maps of flood risk show that the risk is average at the city of Jendouba, increasingly important downstream, and very high at the city of Boussalem. The areas near the channels and urban areas are the most floodable. The areas located at the periphery of the plain have a very low risk of flooding.

The maps of flood-prone areas that were obtained will be used as a tool to assist urbanization strategies and flood protection plans. The installation of facilities reduces the severity of the risk such as hydrometric stations that detect the sudden rise in the level of wadis early and the construction of other gabions to reduce the speed of flows.

Finally, I propose the creation of a telephone application to warn the inhabitants.

References

Haddad, A. (2012) *Design of a GIS application for the identification of flood risk areas in the Greater Tunis area*, pp. 63.

Japan International Cooperation Agency (JICA). (2009). *Study on integrated basin management focusing on flood regulation in the Medjerda river basin*, pp. 1–104.

Kotti, F. C., Mahe, G., Habaieb, H., Dieulin, C., & Calvez, R. (2017). *Impact of anthropogenic developments on the hydrological regime in the Medjerda river basin, Tunisia*.

Mokadem, N., Demdoum, A., Hamed, Y., Bouri, S., Hadji, R., Boyce, A., Laouar, R., & Saad, A. (2016). Stable hydrogeochemical and isotopic groundwater data of a multi-aquifer system: Northern Gafsa basin e Central Tunisia. *Journal of African Earth Sciences, 114*, 174–191.

Use of Remote Sensing and GIS to Study the Evolution of Irrigated Areas and Their Impact on Groundwater in a Semi-Arid Region (Morocco)

Naïma El Assaoui

Abstract

The availability of historical images with different spatial and spectral resolutions allowed us to map the irrigated surfaces, follow their evolution, and analyze the impact of these water withdrawals for irrigation on groundwater resources and on the acquifer's piezometry. The methodology used was based on Landsat 5, 7, and 8 images from August to the end of September; for the years 1973, 1987, 2005, 2009, 2012, and 2015, which underwent radiometric and geometric corrections, and a combination of different methods. Rectified and georeferenced images were obtained, which made it possible to geographically position the results extracted from the processed images and determine the corresponding areas. The extraction of irrigated areas was based essentially on the normalized vegetation index. In addition, the imagery obtained by field and survey data was used. The chosen methodology enabled us to map the irrigated areas over the entire surface covering the water table and to quantify the irrigated surface area. Those irrigated areas were integrated into a global GIS. Analysis of results shows the evolution of the areas irrigated by groundwater pumping from 2200 ha in 1973 and 5000 in 1980 to more than 20,000 ha in 2005. The drawdown of aquifer's water level, for the periods 1980–1998 and 1980–2005, can reach 10 m. In addition, the 2015 land use drawn-up map has highlighted the reduction or even disappearance of pivots and intense growth of the built constructions and the road network.

Keywords

Landsat imagery · Remote sensing · Irrigated areas · GIS · Groundwater

1 Introduction

The different Intergovernmental Panel on Climate Change (IPCC) reports, Moroccan's climate trends, indicate warming in the future and decreasing of rainfall and runoff. As a semi-arid to arid country, water resources will be vulnerable to climate change in the future, with a threat of an important decrease in groundwater resources. This climate change phenomenon is generally coupled with the water demand increase, especially for agricultural needs. So, the problem to resolve is: How can we detect and quantify these surfaces for more than 1500 farms?

Spatial images have become an efficient tool for the management of irrigated areas. They allow a synoptic view and a spatiotemporal coverage of the studied surfaces. The availability of spatial image archives and the acquisition of current images of different spatial and spectral resolutions allow better management of land use. The GIS and remote sensing have become efficient tools to help managers investigate land use areas for agriculture's modification and the response of aquifer's groundwater resources. The availability of the history of images of different spatial and spectral resolutions allows the development of precise mapping of irrigated surfaces. The monitoring of their evolution is helpful for the analysis of the impact of groundwater withdrawal for irrigation on the piezometry of the water table, as well as their correlation with the corresponding rainfall trajectories.

The study area is located in the North West of Africa in the center of Morocco (Fig. 1a) and is located in the Bouregreg Chaouia watershed which contains five principal aquifers including Chaoui Cotiere, Sehoul, and Tanoubert (Fig. 1b); but the most important and biggest is the

N. E. Assaoui (✉)
Water and Environment Geosciences Laboratory, Center CERNEDDS, Department of Life and Earth Sciences, Faculty of Sciences, Mohammed V University, Rabat, Morocco
e-mail: n.elassaoui@um5r.ac.ma

Z. A. Ergüler et al. (eds.), *Selected Studies in Geotechnics, Geo-informatics and Remote Sensing*, Advances in Science, Technology & Innovation, https://doi.org/10.1007/978-3-031-43759-5_17

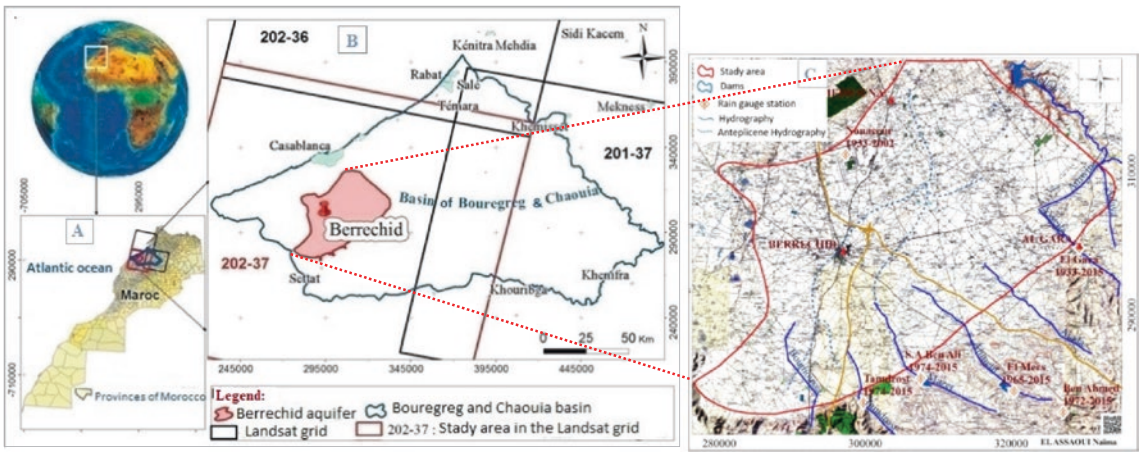

Fig. 1 Localion map of the study area

Berrechid aquifer. It is a plain of 1600 km^2 area, with fertile soil where agriculture is the most important economic activity, serving several cities in Morocco (Fig. 1).

The hydrological network is endoergic and crosses the plain in its Southern and South-eastern parts by rivers downstream which go down from the plate, crossing the plain on less than 20 km and disappear in the center of the plain (Fig. 1c).

Precipitation generally occurs between October and May for a relatively small number of days and is highly variable depending on the season. The rainy period extends from November to May. During this period, rainfall is irregularly distributed with a predominance of January or December and, even in some years, of March. From June, the rains become increasingly rare, and in July and August, there is almost no rainfall.

The average annual rainfall in the study area fluctuates between 150 and 550 mm, depending on whether it is a dry year or a wet year.

2 Methodology and Data Preparation

The study area is located in the Berrechid Plain in the Bouregreg Chaouia Basin (West of Morocco). To study Landsat 5, 7, and 8 images for the years 1973, 1987, 2005, 2009, 2012, and 2015, the methodology used was a combination of several methods which are: the visual interpretation method; post-classification comparison for change detection on multidate images; evaluation of the accuracy of the change detection method and interpretation; and the Tasseled Cap transformation that reduces redundant information between bands. It mainly provides three bands of clues: brightness, greenness, and moisture, and habitat using the fourth band (Elhag et al., 2013; Jaiswal et al., 1999; Naima, 2017; Singh et al., 2010).

The satellite image has been corrected radiometrically and geometrically to remove the effects of the atmosphere and distortion in the image and link it to a projection system. Rectified and georeferenced images were obtained. This made it possible to geographically position the results extracted from the processed images and the knowledge of the corresponding areas. Then, the results obtained were transferred to a global geographic information system integrating the communes of the region (Elhag et al., 2013; Jaiswal et al., 1999; Naima, 2017).

Finally, using the calibrated groundwater model in MODFLOW/GMS interface, the results obtained are used for the simulation of the piezometry of different periods and different scenarios (Naima, 2017).

3 Results

3.1 Extraction of Irrigated Areas

Moreover, we can clearly see the concentration of pivots on the Landsat 2005 image and their disappearance in the 2015 image extract, which clearly shows a change in the irrigation mode (see Fig. 2).

The extraction of irrigated areas was based essentially on the calculation of the normalized vegetation index (Jaiswal et al., 1999). It has shown its efficiency for mapping and space and temporal monitoring of irrigated perimeters. The date of image capture is judiciously chosen (August to the end of September). Irrigated areas result in a very high vegetation index (see Fig. 3).

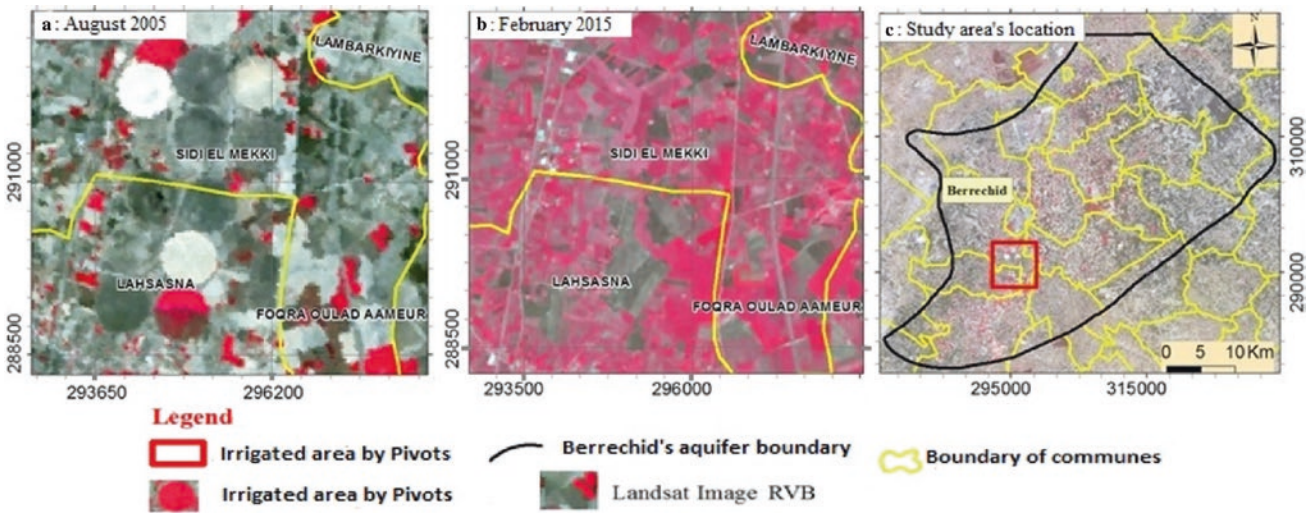

Fig. 2 Extracts from landsat images showing the change in irrigation mode from 2005 **a** to 2015 **b** in the municipalities of Sidi El Mekki and Lahsasna

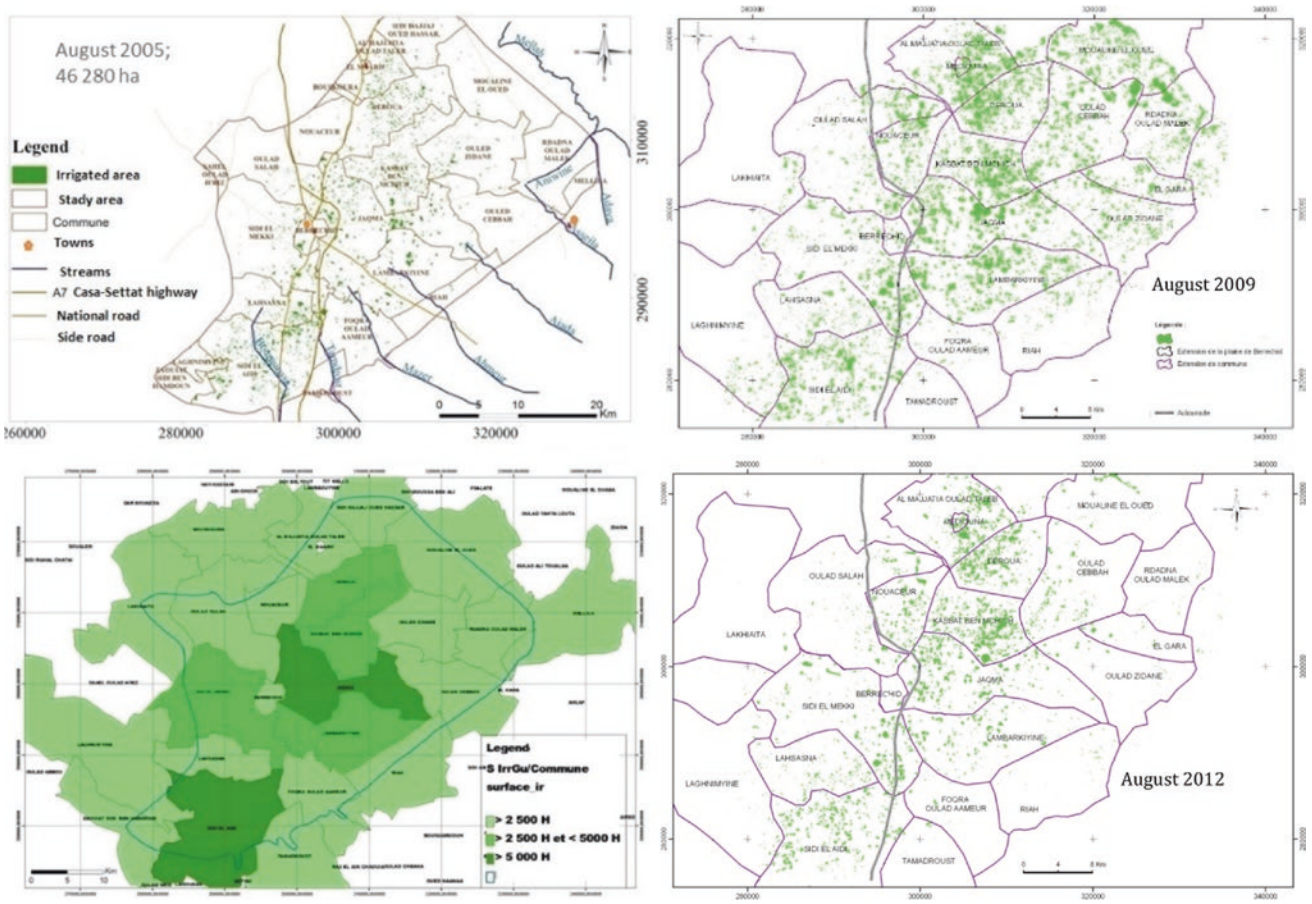

Fig. 3 Represents, respectively, a map of irrigated areas of the Berrechid aquifer extracted from the TM landsat August 2005, 2009, and 2012 images and irrigated areas per municipality

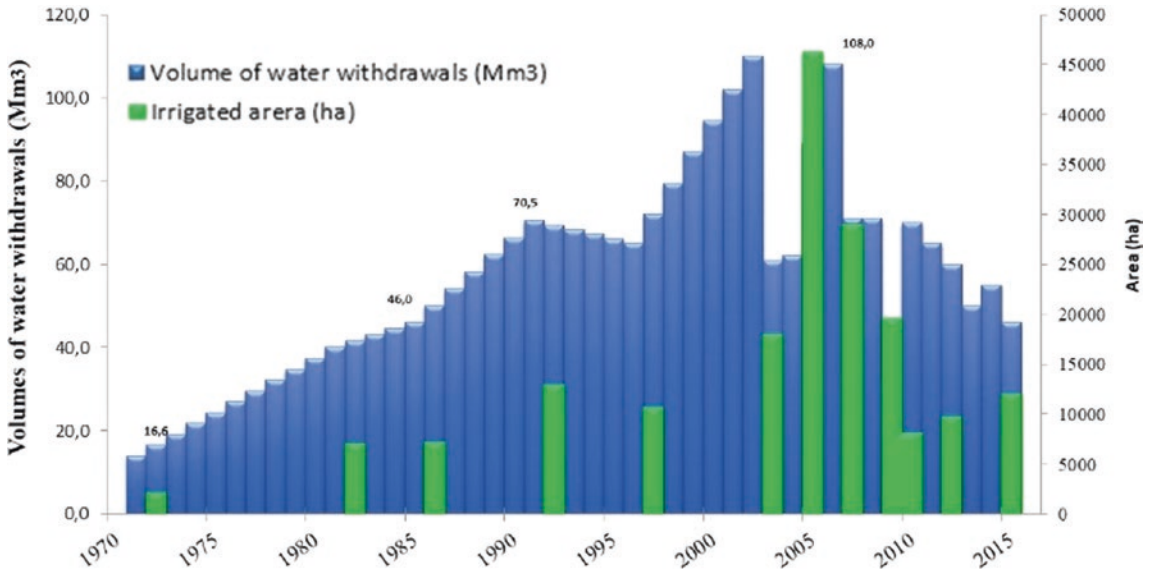

Fig. 4 Evolution of volumes of water withdrawal and irrigated area

3.2 Pumped Water Withdrawal for Irrigation

These withdrawals from the irrigation system have a significant influence on the groundwater balance (Naima, 2017; Othman et al., 2018; Singh et al., 2010), as noted above. Compared to agricultural withdrawals, their monitoring is not easy, relying on the surveys carried out regularly by the Watershed Agency (ABHBC), the updated studies, as well as the elaboration of land use maps; particularly in relation to the irrigated areas established using remote sensing (Naima, 2017) (see Fig. 4).

Moreover, we can clearly see the concentration of pivots on the Landsat 2005 image and their disappearance in the 2015 image extract, which clearly shows a change in the irrigation mode (see Fig. 2).

4 Discussion

The analysis of the results has allowed us to trace an evolution of the areas irrigated by groundwater pumping from 2200 ha in 1973, 5000 ha in 1980, 46,278 ha in 2005, and 28,975 ha in 2009 to more than 20,000 ha in 2015. In 2005, the irrigated area, as well as the volume of water, is the most important because it was a dry year (see Fig. 3.).

It should be emphasized that this methodological approach can be used to carry out the temporal monitoring and mapping of irrigated areas on the extension of the Berrechid plain. The dominant irrigation methods are gravity used in 57% of the total irrigated area and drip irrigation in 41%. Sprinkler and pivot irrigation remain marginal, representing nearly 2% (respectively, 1.26% and 0.77%).

These withdrawals have a significant influence on the groundwater balance. Compared to agricultural withdrawals, their monitoring is a difficult task, taking into account the surveys carried out regularly by the ABHBC, the updated studies; as well as the elaboration of land use maps, particularly in relation to the irrigated areas established using remote sensing (Naima, 2017; Othman et al., 2018; Singh et al., 2010).

In Fig. 5a, b, we can observe the evolution of the drawdown of the water table level, for the periods 1980–1998 and 2005–2015, which can reach 10 m.

5 Conclusion

The analysis using satellite images, of the evolution of the irrigated surfaces under the effect of intense irrigation, allowed us to note the negative impact on the groundwater reserves of the aquifer whose water table level dropped between 8 and 10 m. Finally, this methodology enabled us, on the one hand, to map the irrigated areas over the entire area covering the Berrechid aquifer and, on the other hand, to quantify the irrigated area of each plot. The irrigated areas are integrated into a global GIS integrating the communes, especially the distribution of irrigated areas at each commune (El-Assaoui, 2017).

To improve this methodology and to better understand the extraction of irrigated areas from the vegetation index, it must be supplemented with field data (surveys).

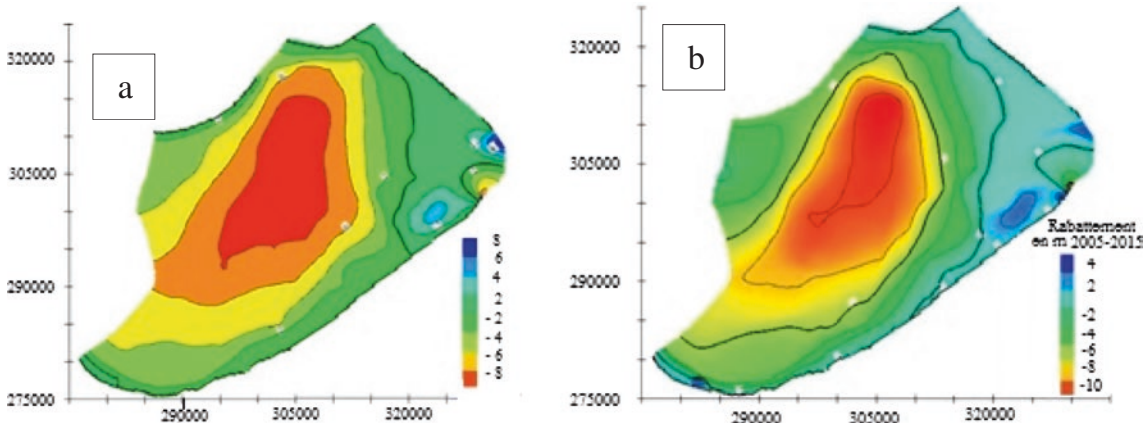

Fig. 5 Drawdowns of the water table during the periods 1980–1998 and 2005–2015

References

El-Assaoui, N. (2017). *Contribution to the méthodological study of the impact of climate change on groundwater resources* Ph.D. thesis, Ain Chock Science School, Hassan II University, (Morocco). https://orcid.org/0000-0003-1811-6274

Elhag, M., Psilovikos, A., & Sakellariou-Makrantonaki, M. (2013). Land use changes and its impacts on water resources in Nile Delta region using remote sensing techniques. *Environment, Development and Sustainability, 15*, 1189–1204.

Jaiswal, R. K., Saxena, R., & Mukherjee, S. (1999). Application of remote sensing technology for land use/land cover change analysis. *Journal of the Indian Society of Remote Sensing, 27*(2).

Othman, A., Sultan, M., Becker, R., Alsefry, S., Alharbi, T., Gebremichael, E., Alharbi, H., & Abdelmohsen, K. (2018). Use of geophysical and remote sensing data for assessment of aquifer depletion and related land deformation. *Surveys in Geophysics, 39*, 543–566.

Singh, S. K., Singh, C. K., & Mukherjee, S. (2010) Impact of land-use and land-cover change on groundwater quality in the Lower Shiwalik hills: A remote sensing and GIS based approach. *Central European Journal of Geosciences, 2*(2), 124–131.

Study of Soil Degradation by Integrating Multi-temporal Topographic Data and Digital Images into a GIS: The Case Study of the Oued Siliana Catchment (Northern Tunisia)

Nassira Zouaoui, Radhia Mansour and Abdessalem ElGhali

Abstract

The agricultural land in the North of Tunisia represents the main resource of fertile soils of the country. The scarcity and limitation of these natural resources require a strategy to both preserve and protect them from threats like hydric erosion, which causes the loss of a large area during each rainy season. This hydric erosion is all the more aggressive since the downpours are torrential and the rivers are poorly protected by erosion control works. This destructive phenomenon is potentially active along the banks of watercourses, and it causes changes in the hydrographic network morphology as well as in the geometry of cultivable surfaces and plots. Therefore, the catchments are overall in degrading spatial–temporal evolution, always reflecting a transport of considerable masses of soil into the wadis and their tributaries. In this context, the Oued Siliana basin (northern Tunisia) constitutes a demonstrative example of the study of this kind of phenomenon, where the analysis of altimetric and multi-date spectral data from the field and the interpretation of results allow the detection of geometric changes of surfaces and, therefore, spatio-temporal evolution of the phenomenon studied.

Keywords

Morphometric index · GIS · Remote sensing · Soil loss · Hydric erosion · Multi-date DEM

1 Introduction

The soil degradation due to hydric erosion is a constantly increasing phenomenon (Maimouni et al., 2011) representing a complex issue in Tunisia (Hossain & Akter, 2018). Overall, it is the result of several natural and anthropogenic factors (Jebari & Bensalah, 2014; Tahiri & al., 2017), and it constitutes one of the most destructive phenomena of fertile soils, affecting goods and people (Ouvry, 2012).

The presented research investigates the spatial–temporal evolution of this natural phenomenon by focusing on the Oued Siliana watershed (northern Tunisia), a sub-unit of the Oued Mejerda basin.

The study consists in using multi-temporal altimetric and spectral data in order to allow the evaluation of the natural risk of water erosion and that, from the morphometric indices (using the derived DEM SRTM of 90 m of resolution for the year 2000) to give the potentially threatened areas.

2 Materials and Methods

The adopted methodology in this study makes it possible: (i) to identify the risk zones which are threatened by the hydric erosion and (ii) to quantify the rate of erosion (reference time period: 1985–2015), according to the adopted methodological flowchart (Fig. 1).

In detail, the adopted approach consists of:

(1) Spatial analysis of a 90 m resolution SRTM-derived digital elevation model (DEM) for the year 2000 in order to derive morphometric indexes like: Stream Power Index «SPI», Sediment Transport Index «STI», Debris Flow Topographic Index «DFTI» which represent the logical crossover between STI and SPI (Dehni et al., 2015), and Topographic Wetness Index «TWI»;
(2) Spectral analysis of Landsat 5 and Landsat 8 OLI-TIRS satellite images for the years 1985 and 2017, which

N. Zouaoui (✉) · R. Mansour · A. ElGhali
Faculty of Sciences of Bizerte, Carthage University, 7021 Bizerte, Tunisia
e-mail: nassira.zouaoui.2020@gmail.com

Z. A. Ergüler et al. (eds.), *Selected Studies in Geotechnics, Geo-Informatics and Remote Sensing*, Advances in Science, Technology & Innovation, https://doi.org/10.1007/978-3-031-43759-5_18

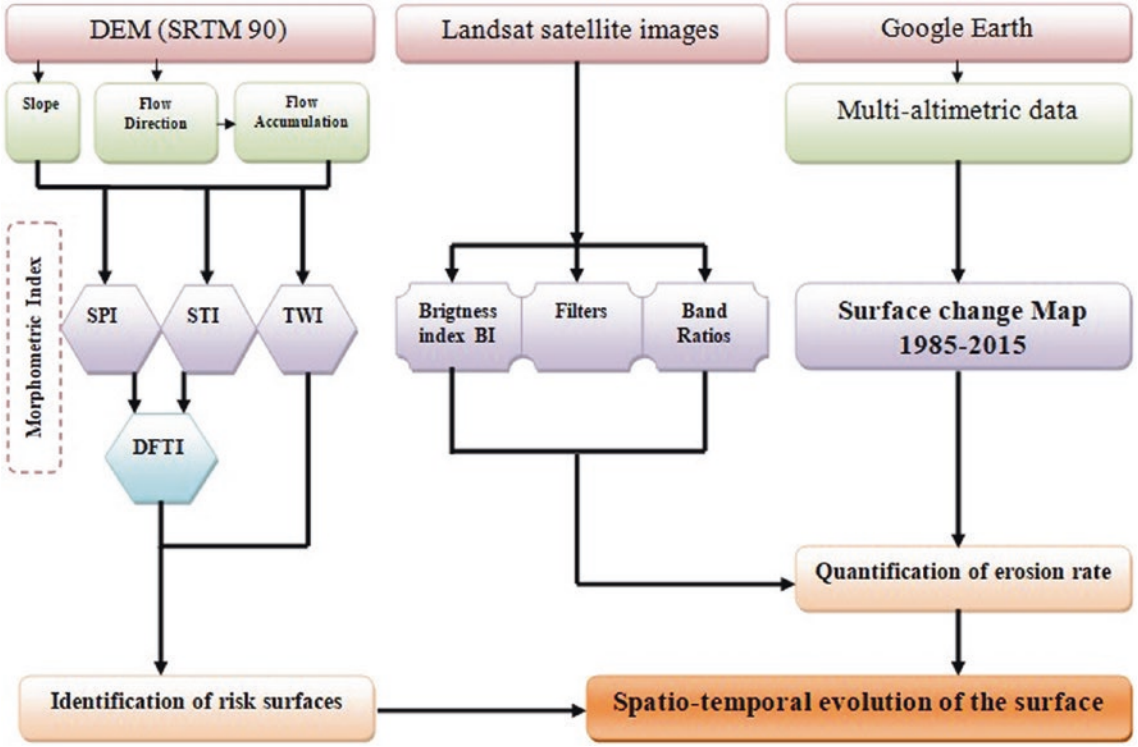

Fig. 1 Adopted methodological flowchart

made it possible to calculate the brightness index (BI), which in turn makes it possible to clearly distinguish between vegetated surfaces and bare soil (EnvCAL-Suivi), as well as the use of filters and ratio bands. It allowed good discrimination between the water and vegetation, thus highlighting the spatial–temporal evolution of Oued Siliana catchment.

(3) Comparison and combination of the results of the previous steps, (1) and (2), with those obtained by a difference of DEMs analysis (reference time period: 1985–2015) allow the detection of surface changes as well as a quantification of eroded surfaces and accumulations surfaces. In detail, the employed topographic data were obtained from Google Earth ™ first by choosing the study area and then digitizing as many points as possible within the study area. These points were then converted by means of the "GPS Visualizer" software into geographic coordinates (φ, λ, z) with the WGS 1984-UTM-Zone 32 coordinate system. Finally, the multi-temporal DEMs corresponding to the years 1985, 1990, 1995, 2000, 2005, 2010, and 2015 were interpolated within the ArcGIS ™ package.

3 Results

Hydric erosion is a risk to property and people involving many issues, namely economic, agricultural, and drinking water issues (Ouvry, 2012). The agricultural lands which represent 57.95% of the Oued Siliana catchment, of which 60% for growing cereals, are characterized by uneven relief (Jebari & Bensalah, 2014) and are the most threatened by this degradation which continues to increase. The calculated morphometric indexes showed that 37.66% of the basin is characterized by a medium to very high erosion power (SPI) (Fig. 2a), 21.25% by a very high erosion sensitivity (STI) (Fig. 2b), 91.91% by a strong debris flow (DFTI) (Fig. 2c), and 41.52% of the soils of the basin have medium to very high humidity (TWI) (Fig. 2d).

As most of the natural land surfaces are made up of mixtures of vegetation, soil, and bedrock (Salamba et al., 2019), the use of Landsat images and topographic data allowed the quantification of accumulation and erosion rates (Fig. 3) that reached 70,012 ha during the period 2000–2005 (Fig. 4) due to the presence of sloping land and poor vegetation cover.

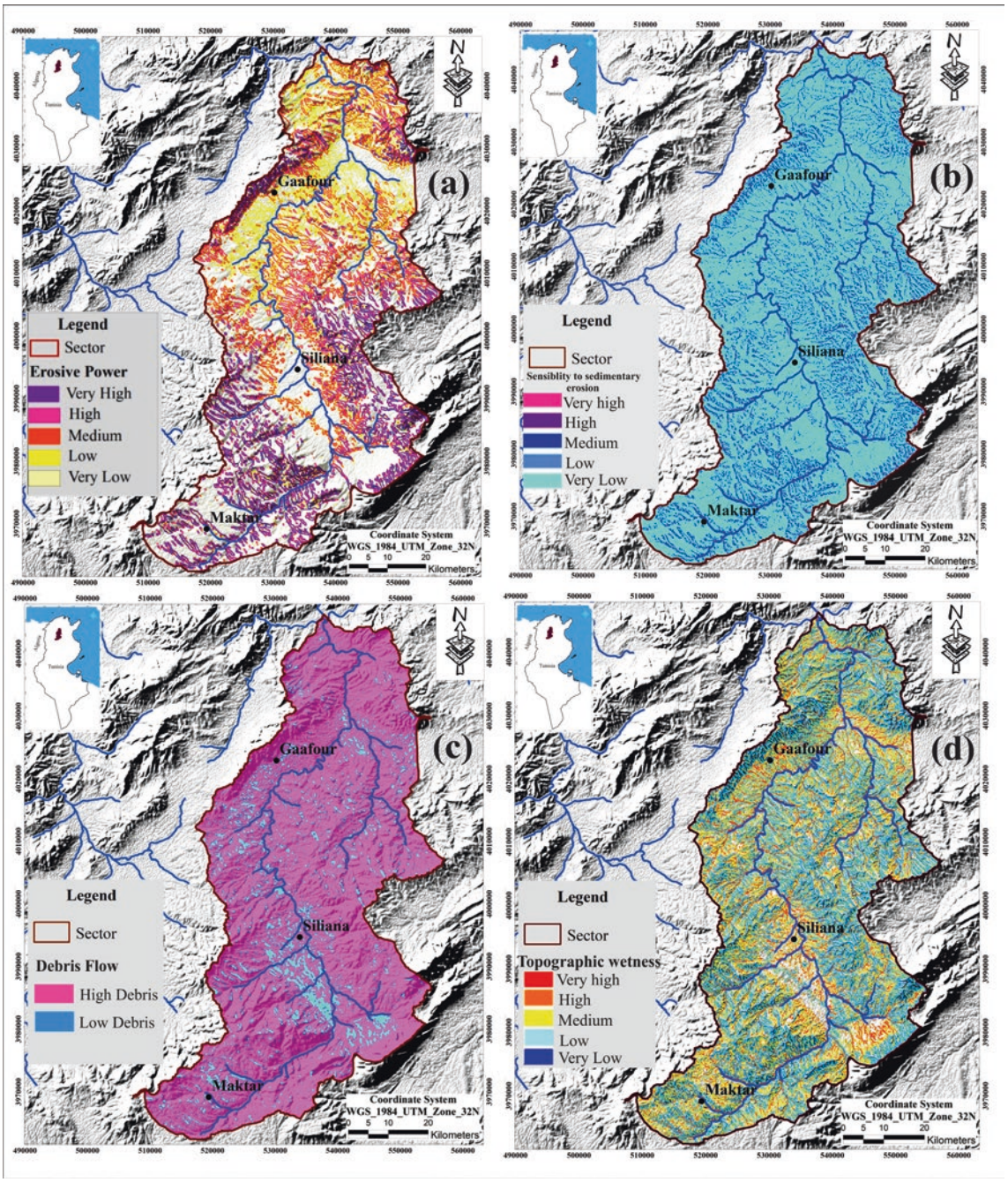

Fig. 2 Morphometric indexes maps: **a** stream power index (SPI), **b** sediment transport index (STI), **c** debris flow topographic index (DFTI), and: **d** topographic wetness index (TWI)

As shown in Fig. 4, within the reference time period 1985–2015, the Siliana catchment experienced a dynamic cycle "of erosion, transport, and sedimentation", causing the upstream loss of an area of about 40,000 ha and the downstream accumulation of soil matter covering an area of about 38,000 ha. Noteworthy, this accumulation area is devoid of the layer of topsoil essential for agricultural crops.

4 Discussion

The adopted methodology allowed the localization of areas potentially threatened by hydric erosion through the use of morphometric indexes that have currently become reference tools in the field of geomorphology (Gaucherel, 2003).

The quantification of erosion rates during the reference time period, 1985–2015, highlighted remarkable erosion

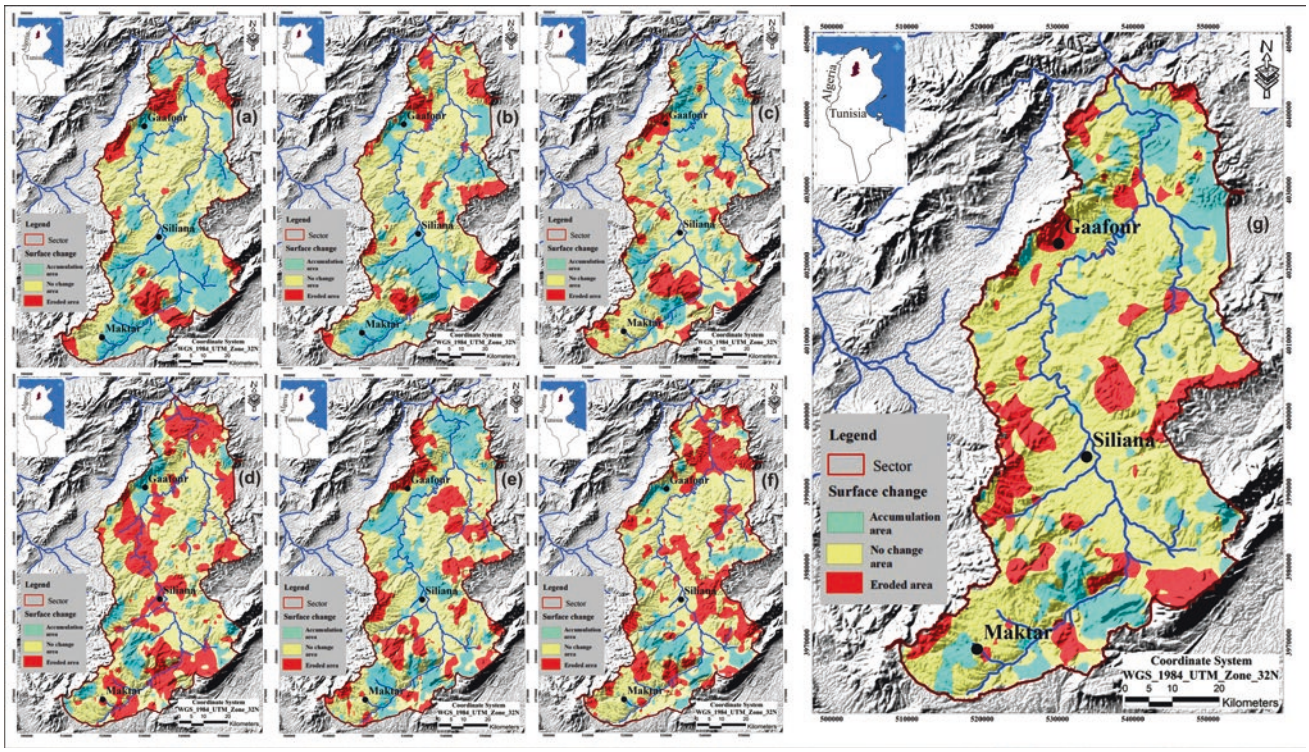

Fig. 3 Difference of DEM maps of the Oued Siliana watershed: **a** period 1985–1990, **b** period 1990–1995, **c** period 1995–2000, **d** period 2000–2005, **e** period 2005–2010, **f** period 2010–2015, and, **g** period 1985–2015

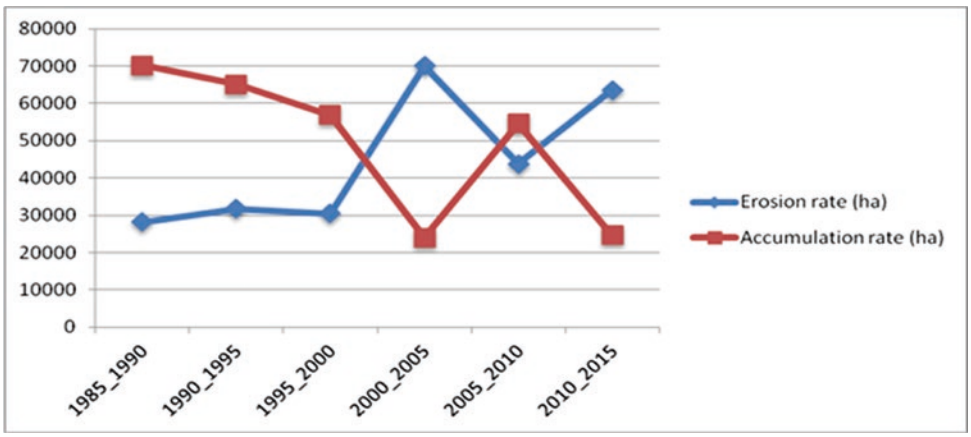

Fig. 4 Erosion and accumulation rates for the Oued Siliana watershed (reference time period: 1985–2015)

rates for the flood periods 2003, 2012, and 2015 (Abidi & al., 2019) (70,012 ha and 63,649 ha lost during the period 2000–2005 (Fig. 3d) and 2010–2015 (Fig. 3f), respectively). The results show the effectiveness of multi-date DEMs obtained from Google Earth, which is characterized by data quality similar to DEM (SRTM90) (Hossain & Akter, 2018; Rusli et al., 2014), for detecting surface change.

In order to protect the areas most threatened by hydric erosion, a series of developments are considered very useful to save property and people from this natural physical degradation. This protection can be reinforced by the construction of recharging works and gabion protection, as well as by the earthwork and the benches and plant fixings.

5 Conclusions

The presented research represents an example of digital processing of multi-source and multi-temporal data allowing the qualitative and quantitative analysis of the physical soil degradation due to hydric erosion. In this context, the

resulting maps highlighting the areas most threatened by water erosion can help decision-makers to control this natural phenomenon, thus reducing soil loss rates and protecting the country's food sector.

References

Abidi, S., al. (2019). Flood risk mapping of Medjerda High Valley with Hec- Ras model. *Journal International Sciences et Technique de l'Eau et de l'Environnement (JISTEE)*, *4*(1).

Dehni, A., Lounis, M., Hassani, M. I. (2015). *Geoprocessing of hydromorphometric indices for the automation of sedimentary and erosive models* (Application on the BV of Tafna—North-West Algeria) conference.

Cours EnvCAL-Suivi de l'environnement par télédétection- Les indices simples. https://e-488%20cours.univ-paris1.fr/modules/uved/envcal/html/vegetation/indices/qques-indices/indices-489 simples.html

Gaucherel, C. (2003). Pertinence de la notion d'indicateur pour la caractérisation du bassinversant. *Espace Géographique*, 3, 265–281.

Hossain F., Akter S., AhshanA. (2018). Digital elevation modeling of Saint Martin Island, Bangladesh: A method based on open source Google Earth data. *International Journal of Advanced Research*, *6*(2), 379–389.

Jebari, S., et Bensalah R. (2014). Protection des terres céréalières contre l'érosion hydrique. *Journée Nationale sur la valorisation des Résultats de la Recherche dans le Domaine des Grandes CulturesTunis*, le 17 avril.

Maimouni, S., et al. (2011). Potentiels et limites des indices spectraux pour caractériser la dégradation des sols en milieu semi-aride. *Canadian Journal of Remote Sensing, 37*(3), 1–18.

Ouvry J. F. (2012). *Dégradation des sols par l'érosion hydrique: Quels remèdes en région de grands*. https://www.cairn.inforevue-pour-2012-1-page-163.htm.

Rusli, N., Majid, M. R., & Din, A. H. M. (2014). Google Earth's derived digital elevation model: Acomparative assessment with Aster and SRTM data. *IOP Conf. Series: Earth and Environmental Science*, *18*, 012065.

Salamba, K. E., Hede A. N. H., Heriawan M. N. (2019). Identification of alteration zones using a Landsat 8 image of densely vegetated areas of the Wayang Windu Geothermal field, West Java, Indonesia. In *IOP Conference Series: Earth and Environmental Science* (Vol. 254, p. 012004IOP).

Tahiri, M., et al. (2017). Quantification of water erosion and sedimentation using empirical models in the Tahaddart watershed (Northwestern Rif, Morocco). *Bulletin de l'Institut Scientifique, Rabat, Section Sciences de la Terre*, 2017(39), 87–101.

OPENCoastS: A Tailored Coastal Forecasting WebGIS Service

Anabela Oliveira, Alberto Azevedo, André B. Fortunato, Marta Rodrigues, João Rogeiro, Pedro Lopes, Samuel Bernardo, Jorge Gomes, João Pina and Mario David

Abstract

Predicting the circulation in coastal systems requires a combination of knowledge of physical processes, accurate numerical models that represent all relevant processes, and a computational tool that automates the prediction procedures and results' visualization. The OPENCoastS service addresses these challenges in a comprehensive way. Freely available to all, OPENCoastS allows any user with a basic knowledge of coastal dynamics and computational grids of his/her system of interest, to build a forecast system through a very simple interaction with a WebGIS platform. This platform serves the whole forecast roadmap: deployment, management, and visualization of results. Depending on the characteristics of the coastal system at study, distinct modeling approaches can be taken, with associated requirements of computational power to guarantee timely delivery of the forecasts. Initially developed as a simple forecast engine for 2D circulation, OPENCoastS has become a full-fledged service that addresses different issues of coastal circulation. Three options are available: the original 2D barotropic simulations without short waves; 2D barotropic simulations with wave–current interaction; and 3D baroclinic simulations including salinity and water temperature. OPENCoastS is demonstrated to understand how distinct physical processes can impact velocities in a real application in the Albufeira coast using a 3D baroclinic circulation and a 2D wave and current circulation deployments.

Keywords

OPENCoastS · WebGIS · SCHISM · Wave and currents · Baroclinic flow

1 Introduction

Coastal forecast systems have been under development for several decades (Baptista et al., 2008) and have now a solid role in coastal management procedures for all entities with responsibilities or economic activities in these areas. Their setup, usage, and continuous maintenance are, however, limited by technological evolution constraints and personnel cost (Oliveira et al., 2019), thus preventing their broad use for many systems.

OPENCoastS (https://opencoasts.ncg.ingrid.pt/) was designed to address these challenges in a comprehensive way. It was developed as a proof of concept that operational systems can be open to all, and every coastal system should have a forecast implementation, anchored on the availability of relevant computational resources. Since 2018, this platform has attracted over 200 users from over 20 countries, in spite of allowing only for simple 2D tidal dynamics. The simple way to build, manage, and visualize results in a WebGIS platform is considered a major advantage by the users.

Most coastal problems, however, cannot be addressed without accounting for wave interactions or the vertical structure of the flow. Therefore, OPENCoastS was extended to a multimodal strategy where the user can select the most adequate physical configuration. Building from the first service version (Oliveira et al., 2019), the user can now deploy 2D or 3D runs, with or without wave interaction. Each mode requires the user to upload different information and select different forcing options, along 7 steps in a WebGIS platform. Each step is customized for the selected mode, and help is available at every step.

A. Oliveira (✉) · A. Azevedo · A. B. Fortunato · M. Rodrigues · J. Rogeiro · P. Lopes
Hydraulics and Environment Department, National Laboratory for Civil Engineering, Lisbon, Portugal
e-mail: aoliveira@lnec.pt

S. Bernardo · J. Gomes · J. Pina · M. David
Laboratório de Instrumentação, Física Experimental de Partículas, Lisbon, Portugal

Z. A. Ergüler et al. (eds.), *Selected Studies in Geotechnics, Geo-Informatics and Remote Sensing*, Advances in Science, Technology & Innovation, https://doi.org/10.1007/978-3-031-43759-5_19

2 The OPENCoastS Service and Its Current Functionalities

2.1 Summary of the OPENCoastS Service

OPENCoastS is a computational service of the H2020 EOSC-hub project, designed to build circulation forecast systems for any coastal system in the world. To facilitate its use by users that are not modeling experts, it requires the minimum information from the user and is supported by a simple workflow of 7 steps in a WebGIS interface. All the data required at each step is clearly identified and often available as a dropdown menu. For the setup of each simulation, pre-defined modeling parameters are provided, retaining the ability for most experienced users to define their own values.

OPENCoastS evolution to more complete physics was made possible by the comprehensive representation of physical processes available in the SCHISM modeling suite (http://ccrm.vims.edu/schismweb), the open-source modeling engine behind OPENCoastS. Three options are now available, depending on the relevant physics:

(1) 2D barotropic simulations—these simulations output water levels and depth-averaged velocities. Forcings are tides, wind, atmospheric pressure, and river flow.
(2) 2D barotropic simulations with wave–current interaction (2D W&C)—these simulations provide additional wave parameters. Wave–current interactions are simulated and forcings also include short waves. It can only be used in the North Atlantic.
(3) 3D baroclinic simulations—these simulations provide 3D fields of velocity, salinity, and water temperature, besides water levels. They can be forced by tides, river flow, temperature, and salinity at all the boundaries and also by the atmospheric surface forcing (wind, air temperature, pressure, humidity, solar radiation, and downwelling longwave radiation). These forecasts can be generated anywhere in the world.

As more complex physics required additional computational power, the availability of computational resources and IT services from the European Open Science Cloud community, through project EOSC-hub, was also fundamental to open the use of the enhanced OPENCoastS to all coastal communities.

The OPENCoastS interface also allows for deployment management. Duplicate, pause, restart, and end are some of the actions to be taken in the management board. Finally, a flexible visualization board is available to (i) display model layers for each variable, (ii) probe over the results, and (iii) download the output files. Automatic comparison with field data validates the quality of the predictions and supports the usefulness of the tool for researchers and managers alike. OPENCoastS is linked to EMODNET Physics elevation data hub. The user selects the stations for the model/data comparison for each deployment and then visualizes the results in the viewer.

Unlike 2D forecasts, the setup of a 3D run requires an additional file at Step 2: the 3D vertical grid, in the SCHISM modeling suite format. Given the need to provide input forecasts for other variables, new sources of boundary conditions were added, for usage in all forecast options. OPENCoastS now integrates two CMEMS deployments: global and IBI models. The outputs viewer was also extended to allow the users to visualize maps, probe results, and download data for the 3D output variables. Outputs are also extended to the vertical dimension, with results at each node and at each vertical layer of the new 3D variables: velocity, temperature, and salinity.

3 Understanding the Circulation Drivers at the Albufeira Coast

The city of Albufeira, located on the southern Portuguese coast, has a complex drainage network that includes a vast system of pipes, several coastal outfalls, and wastewater treatments plants and pumping stations. Discharges at the coast only occur during severe precipitation events which lead to inundation downtown and the contamination of urban beaches. This combined problem has led to massive investments from several end-users to redirect pluvial flows and treat and dispose of wastewater far away from the urban beaches. LNEC is building a modeling and forecasting deployment for this region to support the decision-makers to deal simultaneously with inundation and beach contamination, and reduce energy consumption.

Given the complexity of the modeled system, from the upstream basins to the ocean, a careful definition of relevant physical processes is necessary for coastal modeling to avoid prohibitive computational resources. Each day, a series of hydrodynamic and water quality forecast runs will be done, modeling the upper basins, wastewater and stormwater pipe networks, and the adjacent coast for several water infrastructure operation options. In order to define which processes have the most impact on the contamination plumes from the land discharges and the outfalls, OPENCoastS was used in two distinct modes: 2D with wave and current interaction and 3D baroclinic modes. This strategy also helps to define the coastal monitoring program to be undertaken this fall, to provide data for model calibration and validation for the final modeling effort.

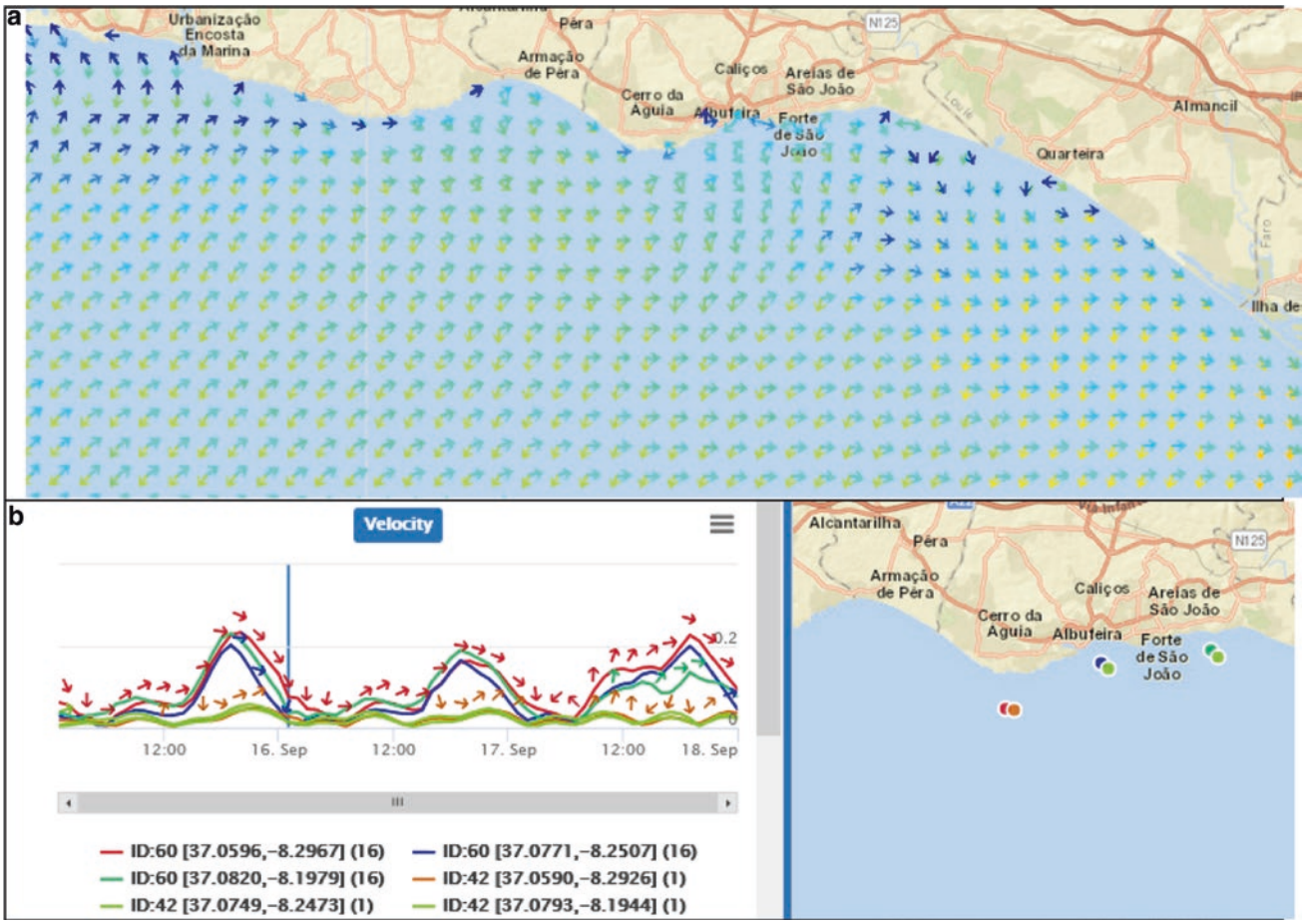

Fig. 1 16/9/2020, 0:00, **a** velocity, **b** velocity time series (ID60: 3D; ID42: 2D W&C)

Results show that velocity magnitudes and directions are quite distinct in each run. In particular, the directions are almost opposite in the area near Albufeira, making any plume simulations lead to transport to East or West depending on the chosen forcing conditions (illustrative layer shown in Fig. 1). These differences would be even more relevant under stormy conditions, with large waves. These differences show that both wave/current interaction and the 3D structure of flow need to be accounted for in the simulation of the urban outflow plumes. Since neither process can be neglected, simulations must include both baroclinic and wave effects. As SCHISM already includes these very complex physics, the WIFF forecasting infrastructure (on which OPENCoastS is based) needs to be extended too.

4 Conclusions

OPENCoastS, an on-demand coastal forecast service, is presented here to address multiple types of circulation physics and demonstrated in the Albufeira region.

Acknowledgements Funding: European Commission by H2020 project EOSC-hub (No 777536) and ANI through project SINERGEA (Project 33595, program 03/SI/2017).

References

Baptista, A. M., Howe, B., Freire, J., Maier, D., & Silva, C. T. (2008). Scientific exploration in the era of ocean observatories. *Computing in Science & Engineering, 10*(3), 53–58.

Oliveira, A., Fortunato, A. B., Rogeiro, J., Teixeira, J., Azevedo, A., Lavaud, L., Bertin, X., Gomes, J., David, M., Pina, J., Rodrigues, M., & Lopes, P. (2019). OPENCoastS: An open-access service for the automatic generation of coastal forecast systems. *Environmental Modelling & Software 124*, https://doi.org/10.1016/j.envsoft.2019.104585.

Sustainability Transitions of Cities in the Global South Experiencing Severe Plastic Pollution: A Geospatial Perspective

Ugonna C. Nkwunonwo and Elijah S. Ebinne

Abstract

Plastic pollution is an issue of global significance, although its knowledge is elusive for places in the Global South. Take Africa as an example, where policy and action are yet to demonstrate a readiness to tackle the crisis, which is one of the fundamental reasons it is now a critical research theme. As a major destination of most inorganic wastes through coastal and oceanic pathways from various world geographies, Africa's experience of plastic waste threatens, among other variables, the continent's marine environment. On a more localized scale, spatial densities of land-based plastic wastes generated from day-to-day transactions in urban environments increasingly cause scenic distortion in cities but also end up in seas because of poor waste management systems, improper waste disposal, and a lack of adequate waste recycling process. These realities offer a reasonable ground for action and motivate research to focus on the sustainable transition of cities in the Global South experiencing severe plastic solutions. The 2019 UN global sustainable development report considers these issues as an obvious threat to the progress toward sustainable development. Thus, it is important to develop strategies for managing plastic wastes in the Global South. This paper presents ongoing research into plastic pollution of the marine ecosystem. Our aim is to use geospatial infrastructure to analyze and visualize the current state of five African countries—South Africa, Kenya, Nigeria, Egypt, and Cameroun—in terms of plastic waste and management, but here we only review some literature to present an up-to-date knowledge of plastic pollution in Africa. We expect this research to assist in policy and politics toward the global plastic revolution mission, but also to provide the needed intellectual and interdisciplinary response to the persistent environmental issues in Africa that are mitigating the rapid transformation of its cities and human societies.

Keywords

Plastic pollution · Global South · Africa · Inorganic wastes · United Nations · Sustainable development · Geospatial technology · Global plastic revolution

1 Introduction

Plastic pollution of the marine system has arguably widened the entire spectrum of environmental science research. With a global estimate of up to eight million tons of plastic waste entering the world's oceans each year (Hardesty & Chris, 2015), the economic, environmental, social, and health challenges of plastic pollution are complex and multi-dimensional, but also a major political and research priority area. Eriksen et al. (2014) reported the result of 24 expeditions (2007–2013), in which they found over 5 trillion plastic wastes, exceeding 250 thousand tons in weight, floating on major seas across five sub-tropical gyres, coastal Australia, Bay of Bengal, and the Mediterranean Sea. Not only does this situation threaten the broad aquatic ecosystem, but empirical evidence from recent studies has also established a complex nexus between plastic pollution, food chain, and food security (Seltenrich, 2015; Smith et al., 2018; Picchio et al., 2018). The aggregate of the global plastic pollution arises from mismanaged plastic wastes—either littered or inadequately disposed of—from individuals, communities, countries, and regions across the globe (Ritchie & Roser, 2018). Four-fifths of these plastic wastes come from land-based sources, while the remaining fifth is from marine-based sources. Of all the land-based

U. C. Nkwunonwo (✉) · E. S. Ebinne
Department of Geoinformatics and Surveying, University of Nigeria Enugu Campus, Enugu, Nigeria
e-mail: ugonna.nkwunonwo@unn.edu.ng

Z. A. Ergüler et al. (eds.), *Selected Studies in Geotechnics, Geo-informatics and Remote Sensing*, Advances in Science, Technology & Innovation, https://doi.org/10.1007/978-3-031-43759-5_20

plastic waste sources, packaging is the most pervasive and has increased the concern in many countries regarding the management of shopping bag carriers. While the threats of plastic pollution exemplify an ongoing global concern, it is more critical for the Global South—comprising mainly of the middle- and low-income countries—because of the general poor waste management system, along with poor knowledge of plastic pollution.

This paper presents ongoing research into plastic pollution of the marine ecosystem and the sustainable transition of cities in the Global South. The research aims to use geospatial infrastructure to analyze and visualize the current state of five African countries—South Africa, Kenya, Nigeria, Egypt, and Cameroun—in terms of plastic waste and management. We set to achieve this aim using a quartet of objectives. Firstly, we review existing literature to highlight the status of knowledge of plastic pollution in Africa. Then, we collect relevant data from agencies and organizations having to do with plastic pollution in Africa and various other pertinent environmental issues. Third, in a geospatial environment, we undertake cluster analysis and mapping of these datasets to present the current state of Africa in terms of plastic pollution. Finally, we propose recommendations based on effective waste management strategies to be adopted for the countries in the Global South. We devote this paper to the first objective.

2 Method and Data

The aim of this mini-review is to present the current knowledge regarding plastic pollution in Africa, identify gaps, and spotlight directions for further research. To achieve this aim, we conducted a structured search process in Google Scholar, Thomson Reuters' Web of Science, and PubMed academic search engines to identify the relevant literature. Our scope of literature covers from 2015 to date, and we mainly considered research articles published in highly reputed journals (indexed by Scopus, DOAJ, Biology and Environmental Sciences, Scimago, and ranked in Thompson Reuter). We used the key terms "plastic pollution" and a combination of terms such as "plastic pollution in Africa", "plastic pollution of the marine environment in Africa", "plastic pollution in the Less developed countries", and "plastic wastes in marine environments in Africa". We ensured four quality control criteria in selecting our literature: (1) literature must focus on plastic pollution, (2) literature must have been published after a rigorous peer review, (3) language expressed in the article must be English, and finally, (4) literature must not be an abstract with extended perspective, short communications, letters, or slide/poster presentations.

Based on our selection criteria and the overall population of published literature, few studies have been carried out within the context of Africa's plastic pollution. However, studies that emerged overall underscored plastic wastes in Africa's marine environment. Few others highlighted the human, social, economic, and environmental impacts of plastic pollution within the generality of the continent. Akindele et al. (2019) conducted the first empirical study of freshwater microplasts in West Africa using gastropods from Nigeria as bio-indicators. Nel & Froneman (2015) undertook quantitative analyses of microplasts pollution along the South-East coastline of South Africa. Jambeck et al. (2018) looked at the challenges and emerging solutions to land-based plastic waste, while Adam et al. (2020) reviewed policies to reduce single-use plastic in marine pollution. South Africa seems to be receiving the most focus of the discussion, partly because the country has had a history of studying plastics in the past. Finally, the literature research shows that, despite the wide-ranging discussions on plastic pollution and research on the more scientific approaches to mitigating the impacts of plastic pollution, the application of geospatial technology research has developed little.

3 Results and Discussion

Available literature shows that the severe threat of plastic pollution is significant in Africa's marine environment. To understand the characteristic nature of this threat, Jambeck et al. (2015) in a series of studies that spanned many years have come up with indices and metrics that reveal the status of Africa in terms of mismanaged waste for the years 2010 and 2025. According to the studies of the total global mismanaged plastic waste presently and forecast to be generated by 2025, places in Africa (particularly South Africa, Nigeria, and Egypt) contribute about 5%. This is no wonder many studies have focused on establishing the significant presence of plastic wastes in Africa's marine system: Extensive anthropogenic activities, high population density, and increasing demand for food security plus packaging as essential for everyday life. Unfortunately, the lack of adequate waste management is a major impasse, for which many of the human population resort to littering and indiscriminate dumping of plastic materials. Bulk domestic and industrial wastes are dumped in landfills that are close to water bodies, thus making the leaking of microplasts possible through open channels and poorly managed city drainage systems.

In addition to establishing marine plastic pollution in Africa, literature also presents attributions, characteristics, challenges, local perceptions, and policy solutions to marine plastic pollution in Africa. But discussions in these

areas are not fully developed to stimulate a realistic action toward mitigating the crises. However, looking at the whole stretch of literature on marine plastic pollution in Africa, there is an asymmetry regarding the areas forming the case for studies. Although nearly every aspect of Africa is covered at the regional scale, most discussions in the literature relate to South Africa, which offers some insights into the knowledge profile of marine plastic pollution in the area. One major gap in the literature is the lack of pertinent discussions that relate to countries which will enable us to gain a clearer insight into the level of perception of the plastic pollution crisis in the whole of Africa. One question the literature is yet to address is the management of plastic waste and pollution in the marine systems. Of course, a lot of studies exist on waste management in Africa, but it also appears that little attention has been given to the management of plastic wastes. This is an overriding need that highlights the importance of the present study in line with using geospatial technology to curate complex analyses and use the outcome to stimulate community participation toward developing smarter ways of plastic waste management in the African region.

4 Conclusions

Plastic pollution of the marine environment is a real problem that has severe economic, social, environmental, and human health impacts. There is a strong global outlook on this issue, although it seems too close to danger for the Global South (mostly the medium- and low-income countries) due to the high level of mismanaged plastic wastes that originate from there and, eventually, end up in the marine systems. This calls for strong political and research actions and remedies, especially with the high stakes of the global sustainability goals.

This paper presents an important part of ongoing research on plastic pollution and the sustainability transition of cities in the Global South. The study aims to assess the level of plastic pollution awareness in the Global South, using Africa as a case in point. The first objective, which is the focus of this paper, is to provide a brief overview of the literature on marine plastic pollution in Africa. Literature is still developing on marine plastic pollution in Africa. This shows little awareness of the overall global profile of marine plastic pollution. However, a major part of current literature of the literature established the obvious presence of plastic wastes in the African marine system, characterized the plastics wastes, and linked them to human activities and the high population density which makes packaging (for food and other necessities) an essential part of the African daily life, routine, and culture. As of now, the missing link in the literature is the management of plastic wastes, although some studies shared their views on policy and polity issues.

Going forward, to mitigate marine plastic pollution within a global context, it is important to understand the sources, pathways, and complex processes by which plastic wastes leak from their sources into the marine system. This understanding should also entail finding solutions that would not undermine the usefulness of plastics within human society. In extreme cases, alternatives to plastic might come into the picture, but scientists should remember that the sustainability of cities must reckon with assisting the human population with their daily needs and increasing their knowledge of environmental issues through methods able to enhance visualization, communication, and engage communities and the wider population in deciding for their well-being. At the very least, the ongoing research proposes a geospatial approach believed to have strategies that align well with these objectives.

References

Adam, I., Walker, T. R., Bezerra, J. C., & Clayton, A. (2020). Policies to reduce single-use plastic marine pollution in West Africa. *Marine Policy, 116*, 103928.

Akindele, E. O., Ehlers, S. M., & Koop, J. H. (2019). First empirical study of freshwater microplastics in West Africa using gastropods from Nigeria as bioindicators. *Limnologica, 78*, 125708.

Eriksen, M., Lebreton, L. C., Carson, H. S., Thiel, M., Moore, C. J., Borerro, J. C., Galgain, F., Ryan, P. G., & Reisser, J. (2014). Plastic pollution in the world's oceans: More than 5 trillion plastic pieces weighing over 250,000 tons afloat at sea. *PLoS ONE, 9*(12), e111913.

Hardesty, B. D., & Chris, W. (2015). *Eight million tons of plastic are going into the ocean each year*. Retrieved from The Conversation: https://theconversation.com/uk/topics/plastic-pollution-52714

Jambeck, J., Hardesty, B. D., Brooks, A. L., Friend, T., Teleki, K., Fabres, J., Beaudoin, Y., Bamba, A., Francis, J., Ribbink, A. J., & Baleta, T. (2018). Challenges and emerging solutions to the land-based plastic waste issue in Africa. *Marine Policy, 96*, 256–263.

Jambeck, J. R., Geyer, R., Wilcox, C., Siegler, T. R., Perryman, M., Andrady, A., Narayan, R., & Law, K. L. (2015). Plastic waste inputs from land into the ocean. *Science, 347*(6223), 768–771.

Nel, H. A., & Froneman, P. W. (2015). A quantitative analysis of microplastic pollution along the south-eastern coastline of South Africa. *Marine Pollution Bulletin, 101*(1), 274–279.

Picchio, M. L., Linck, Y. G., Monti, G. A., Gugliotta, L. M., Minari, R. J., & Igarzabal, C. I. A. (2018). Casein films crosslinked by tannic acid for food packaging applications. *Food Hydrocolloids, 84*, 424–434.

Ritchie, H., & Roser, M. (2018). *Plastic pollution*. Our World in Data.

Seltenrich, N. (2015). New link in the food chain? Marine plastic pollution and seafood safety. *Environmental Health Perspectives, 123*(2), A34–A41. https://doi.org/10.1289/ehp.123-A34

Smith, M., Love, D. C., Rochman, C. M., & Neff, R. A. (2018). Microplastics in seafood and the implications for human health. *Current Environmental Health Reports, 5*(3), 375–386.

Evaluation of Permanent Preservation Area (PPA) Registered in the Rural Environmental Registry (CAR) and Obtained by UAV

Emanuelle Zordan de Melo and Claudionor Ribeiro da Silva

Abstract

The Rural Environmental Registry (CAR) constitutes a public electronic registration system in Brazil, which aims to integrate environmental information from rural properties and possessions. Unfortunately, despite their importance, the measurements of the features recorded in the CAR are not accurate. This study aims to compare the Preservation Permanent Area (PPA) of a watercourse as determined from an orthophotograph obtained by unmanned aerial vehicle (UAV) with the delimitation registered in the CAR. To accomplish this, the methodology proposed by Melo e Silva (Melo, E. Z., & Silva, C. R. (2019). Calculation of the objective width of regular riverbed of a watercourse using unmanned aerial vehicles. In: Brazilian Journal of Environmental Sciences, 79–94. (Rio de Janeiro, RJ, Brazil).) was used in an effort to eliminate current subjectivities in regulatory legislation. Although CAR comprises an important environmental control and monitoring mechanism, the low cartographic accuracy of the system stands out. This research provides subsidies for the management bodies to mitigate the existing weaknesses in the process of monitoring and inspection of properties regarding the correct delimitation of PPA.

Keywords

Digital image processing · GIS · Environmental laws · Rural properties · Vegetation

1 Introduction

The Rural Environmental Registry (CAR) is a declaratory and permanent electronic record, corresponding to the official environmental instrument for forest regularization of rural properties and possessions in Brazil. Its absence may result in restrictions on access for various benefits, such as obtaining agricultural credit; insurance contracting better conditions; possibility of regularizing the Preservation Permanent Area (PPA) and/or Legal Reserve, and suppressed or altered natural vegetation until 07/22/2008, without assessment for administrative infraction or environmental crime; among others (Brazil. Law, 2012; Brazilian Forest Service, 2016).

The main objective of CAR is to monitor and preserve riparian vegetation. This is part of the broader ecosystem conservation, water resources protection, and preservation of water quality. The PPA boundaries are defined in the guidelines of the Brazilian Forest Code, established by Law no. 12.651/2012. The width of the PPA is calculated based on the width of the river, measured from its regular riverbed channel (Brazil. Law, 2012).

Studies that guarantee the correct delimitation, as well as the preservation of these environments, should be prioritized, so that the regulations expressed in the form of law have their effectiveness and efficiency duly ensured. Therefore, this study aims to delimit PPA using the method proposed by Melo e Silva (2019), in line with the current Forest Code, and to compare it with data recorded under the CAR.

2 Materials and Methods

Located in Uberlândia, Minas Gerais/Brazil, the study area comprises part of the stretch of the Uberabinha River (Lat: 18°59′18.00″S Long: 48°12′35.00″W). The analysis section is approximately of 1.000 m and is located near on BR-050.

E. Z. de Melo (✉) · C. R. da Silva
Federal University of Uberlândia, PPGEO, Uberlândia, MG, Brazil
e-mail: emanuellezm@gmail.com

Z. A. Ergüler et al. (eds.), *Selected Studies in Geotechnics, Geo-Informatics and Remote Sensing*,
Advances in Science, Technology & Innovation, https://doi.org/10.1007/978-3-031-43759-5_21

In this research, photographs obtained by Phantom 3 Standard, manufactured by DJI, unmanned aerial vehicle (UAV) were used. A 291 photographs were collected in this configuration, distributed over four flight lines. The programmed flight speed was 15 m/s. It generated an orthophotograph (3.79 cm), using Agisoft software version 3.2, and the processing was performed in ArcGIS® version 10.3 developed by ESRI. The methodology comprises three sequential steps: (1) Definition of the regular riverbed trough of the watercourse (Melo & Silva, 2019); (2) Delimitation of the PPA related to the stretch of river under study, following the guidelines expressed in the legislation and the obtained regular riverbed trough in the previous step; and (3) Comparison of the PPA obtained in this research with the data registered in the CAR.

3 Results

The proposed method was also effective for the rainy season, since it was possible to segment the orthophotograph, and to extract, in vector format (polygon), the studied riverbed. After obtaining the riverbed polygonal, the feature was converted to a linear vector, representing the right and left margins of the course of water. Subsequently, points equidistant 3 m from each other were extracted. The validity Query ID="Q2" Text="Please check and confirm if the inserted citation of 'Fig. 1' is correct. If not, please suggest an alternate citation. Please note that figures and tables should be cited sequentially in the text." of this distance has been demonstrated in Melo and Silva (2019) (Fig. 1).

On the 2.036 equidistant points, the Thiessen Polygons tool, implemented in ArcGIS 10.3, was applied to extract the central axis and perform the descriptive statistical measures (maximum, minimum, average, mode, and median) related to the width of the watercourse. The values, obtained in meters, were: 70 (max), 0.80 (min), 12 (mean), 8 (mode), and 10 (median).

The statistical measure of central tendency "mean" was considered the most representative to standardize the width of the river, as it shows best the reality of the regular riverbed of the water body (Melo & Silva, 2019).

Following the guidelines expressed in the Forest Code regarding the delimitation of PPA from the width identified for regular riverbed of watercourse (Table 1), the standardization obtained of 12 m, for the mean, in the studied river section determines a PPA of 50 m in width.

To compare the delimitation of the PPA obtained in the present study with the data recorded in the CAR, the illustration presented in Fig. 2 was elaborated, demonstrating inconsistency and divergence in the system data.

4 Discussion

While analyzing the inconsistencies observed in the CAR data, it is important to note that the studied part of the river includes two rural properties, consequently generating two registers in the system, which are based on interpretation of each owner regarding the provided information. Verifying the integration between CAR compared to other online regularization systems (such as SIGEF/INCRA used for land regularization), it is clearly demonstrated that CAR data entry does not provide the data visualization of the neighbors for confrontation, not guaranteeing a geometric confidence in the definition of limits, being able to generate inconsistent data with distinct geometric figures on the same object (Oliveira & Oliveira, 2019).

Table 1 PPA values according to the width of the watercourse delimitation, in meters

Width of the watercourse (m)	PPA buffer values (m)
< 10	30
> 10 < 50	50
> 50 < 200	100
> 200 < 600	200
> 600	500

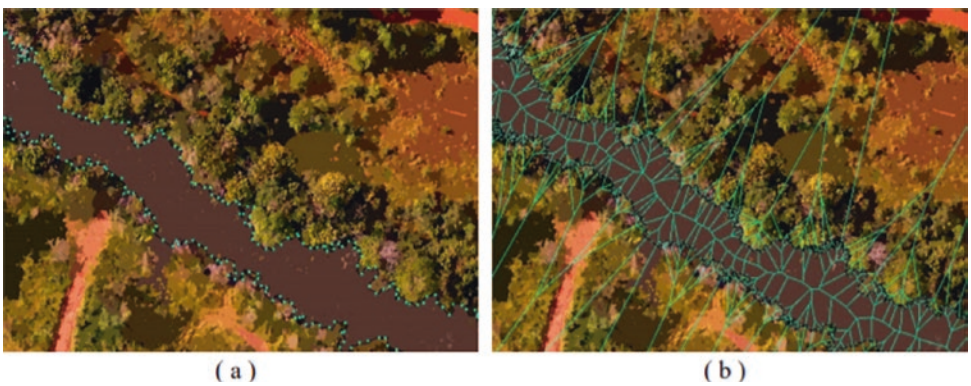

Fig. 1 Extraction of equidistant points of 3.00 m (**a**); Result of Thiessen Polygons (**b**)

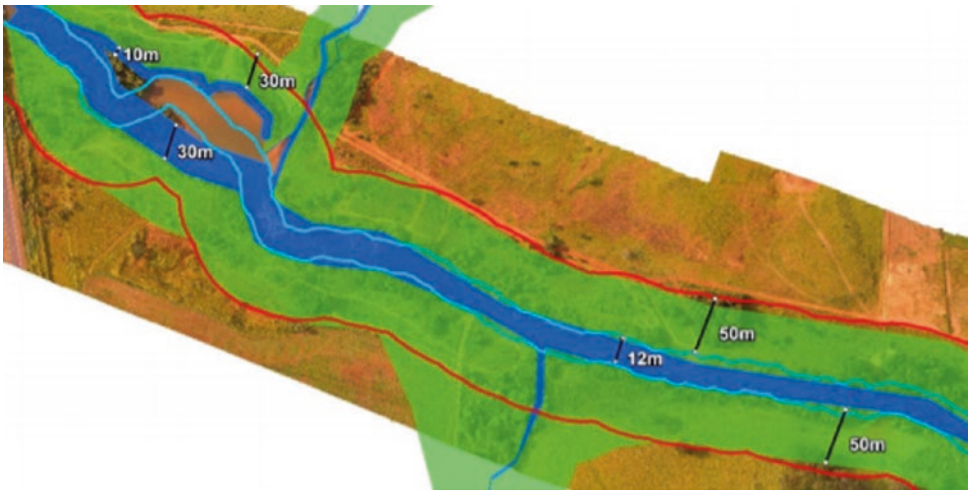

Fig. 2 Comparative between PPA and hydrography data obtained in the present study and those registered in the CAR. Red: PPA (50 m); Light blue: Standardized hydrography by mean (12 m); both proposed in the study. Green: PPA; Dark blue: hydrography; both registered in the CAR

The methods to perform the registration of environmental information in the CAR are manual vectoring in the system or importing geo-referenced files. Geo-referencing, carried out directly at the CAR basis, is promoted from RapidEye satellite images, provided by the Ministry of the Environment, which have 5 m-pixels. Experts point out that the area vectorization method, made available by the system itself, comprises the least accurate option among the available, given that the scale of RapidEye images is 1:50.000, differing significantly from the visualization potential in the CAR registration module which can reach a scale of 1: 5.000 (Scolforo, 2014).

The owners or rural holders can carry out the registration of rural properties in the CAR, and professionals are not required to be responsible for data generation and registration. In addition to this flexibility, CAR, unlike other platforms and registration procedures, does not require pre-defined positional precision for files imported into the system. Such factors corroborate the idea that repetitive inconsistencies are identified such as overlaps and topological errors in the data registered in the CAR.

5 Conclusions

Despite the occasional negative evidence addressed in this study, the CAR comprises an important control and control mechanism of environmental monitoring, which promotes the regularization of rural properties and possessions, gathering in a single database relevant information for environmental management.

UAVs comprise powerful tools for the analysis of the CAR, associating the convenience of techniques with better results in cartographic quality and precision.

This research provides subsidies for the management of the government entities, responsible for accompaniment and monitoring of environmental aspects, mitigate the existing weaknesses in the process of monitoring and inspecting, promoting environmental education, and inspection measures in legally protected areas to enable the application of environmental legislation.

References

Brazil. Law n° 12.651/2012. Brasília, DF, Brazil. (2012). In: http://www.planalto.gov.br/ccivil_03/_Ato2011-2014/2012/Lei/L12651.htm. Last Access December 20, 2019.

Brazilian Forest Service. (2016). *Manual rural environmental registry—CAR*. Brasília, DF, Brazil.

Melo, E. Z., & Silva, C. R. (2019). Calculation of the objective width of regular riverbed of a watercourse using unmanned aerial vehicles. In: *Brazilian Journal of Environmental Sciences*, 79–94. (Rio de Janeiro, RJ, Brazil).

Oliveira, L., & Oliveira, F. H. (2019). Verification of the integration between the rural environmental register (CAR) and the national register of rural properties (CNIR) from the perspective of the multifinalitarian territorial register. *Geosul*, 339–357. (Florianópolis, SC, Brazil).

Scolforo, J. R., et al. (2014). In: *Notions of geotechnologies. Distance extension course. Training course for the rural environmental registry*. Lavras, MG, Brazil.

Estimation of Soil Moisture and Evapotranspiration Products from Global Land Data Assimilation Systems for Nigeria

Adeyemi Oludapo Olusola and Samuel Adelabu

Abstract

The ability to cope with the present population and also cater for those unborn is the central theme of sustainable development campaigns. However, in the light of climate change, the realities being faced by governments in tropical countries such as Nigeria is that of persistent food insecurity amplified by the imprints of climate change on our ecosystem. In most tropical countries, annual rate crop productivity continues to decline due to various factors, largely as a result of land-atmospheric variables anomalies. Unfortunately, the ability to monitor changes in land-atmospheric variables such as soil moisture and evapotranspiration is hampered due to the scarcity of data and inadequate instrumentations. Therefore, this study aims at using Earth Observation products to show the variation in soil moisture and evapotranspiration across Nigeria. Soil moisture is one of the basic requirements for crop growth, likewise evapotranspiration. The issue has always been with their measurements, especially in situ over non-homogeneous surfaces. In data-scarce countries such as Nigeria, sustainable agricultural planning becomes a burden in light of inadequate data. The Global Land Data Assimilation System (GLDAS) is a satellite- and ground-based observational data product, using advanced land surface modelling and data assimilation techniques to generate optimal fields of land surface states and fluxes. Monthly soil moisture and evapotranspiration with 0.25° resolution were retrieved from GLDAS between 2000 and 2019 across the country. The result shows an inverse relationship between soil moisture and evapotranspiration, with the largest increase in SM and ET in the southern part of the country.

Keywords

GLDAS · Soil moisture · Evapotranspiration · Crop · Nigeria

1 Introduction

Challenges in food security are some of the main issues affecting global south countries the world over. The ability to cope with the present population and also cater for those unborn is the central theme of sustainable development campaigns. However, in the light of climate change, the realities being faced by governments, especially in Sub-Saharan Africa, SSA, is that of persistent food insecurity amplified by the imprints of climate change on our ecosystem. Across SSA, there is increased population growth with a large portion of these populations depending on agricultural products for their daily livelihood. Unfortunately, the continued impact of climate change across this region, SSA, puts a lot of pressure on crop production and yield. The fallout from climate change impact as seen in the form of recurrent drought, extensive desertification, and water stress challenges human survival, especially infants within Sub-Saharan Africa.

To be able to tackle the issue posed by climate change on agriculture/crop production, there is the need to optimize yield from available agricultural fields by embracing emerging geo-computational technologies in the form of Earth Observations, EOs, especially in data-scarce countries in SSA. EOs will greatly assist in understanding the regimes of various components of the hydrological cycle and other important variables needed for crop growth such as evapotranspiration (ET) and soil moisture (θ). Exact information

A. O. Olusola (✉)
Faculty of Environmental and Urban Change, York University, Toronto, Canada
e-mail: olusolaadeyemi.ao@gmail.com

S. Adelabu
University of the Free State, Bloemfontein, South Africa

Z. A. Ergüler et al. (eds.), *Selected Studies in Geotechnics, Geo-Informatics and Remote Sensing*, Advances in Science, Technology & Innovation, https://doi.org/10.1007/978-3-031-43759-5_22

on the spatio-temporal variation of these parameters, *ET* and θ, is of key significance as they exert a strong control on the Earth's water, carbon cycles, and ecosystem functioning (Petropoulos et al., 2018). Soil moisture impacts evapotranspiration and also constitutes the water that is directly available to plants (Olusola et al., 2017). This study, therefore, aims to understand the variation in soil moisture and evapotranspiration across Nigeria.

2 Setting and Methods

2.1 Setting

Nigeria is located in the Western part of Africa between latitude 4° and 14° N of the equator and between 2° and 15° E of the Greenwich Meridian (Olusola et al., 2017). It has a landmass of 923,769 km^2, and it is the most populous country in Africa with a population of about 200 million people. The country is primarily influenced by two air masses: the maritime which brings the rainy season (April to October) and the tropical continental which brings the dry season (November to March).

2.2 Methods

The Global Land Data Assimilation System (GLDAS) is a satellite- and ground-based observational data product, using advanced land surface modelling and data assimilation techniques, to generate optimal fields of land surface states and fluxes. GLDAS is unique that it is an uncoupled land surface modelling system that drives multiple models, integrates a huge quantity of observation-based data, runs globally at high resolution (0.25°), and produces results in near real-time. Monthly, soil moisture and evapotranspiration products with 0.25° resolution GLDAS NOAH 2.1 were downloaded from (https://giovanni.gsfc.nasa.gov/) (Beaudoing & Rodell, 2020) from 2000 to 2019 across the country. Plots of θ and *ET* were performed in *R*.

3 Results

3.1 Soil Moisture (θ) and Evapotranspiration (ET)

Figure 1 shows the seasonal variation in soil moisture and evapotranspiration across the country. The figure suggests that during rainfall peak (JJA), we have the highest values for θ and *ET*. The graph (Fig. 1) shows that, as we move into the rainy season, both θ and *ET* increase.

3.2 Relationship Between θ and ET Across Nigeria

From Table 1, an inverse relationship ($p<0.05$) is observed between MAM|DJF, JJA|DJF, JJA|JJA, and SON|JJA. Hence, as evapotranspiration increases, soil moisture decreases significantly. The highest rate of decrease in soil moisture is during DJF (Table 1). The highest amount between 2000 and 2020 across the entire country on average is in the southern part of the country (Fig. 2).

4 Discussion

The relationship between soil moisture and evapotranspiration is very mutual (Fig. 2). Essentially during the peak of the dry season, DJF, in Nigeria, the value of both soil moisture and *ET* across the country is low. For soil moisture, this is the result of little or no precipitation, while for *ET*, it is a result of a relative reduction in vegetation greenness across

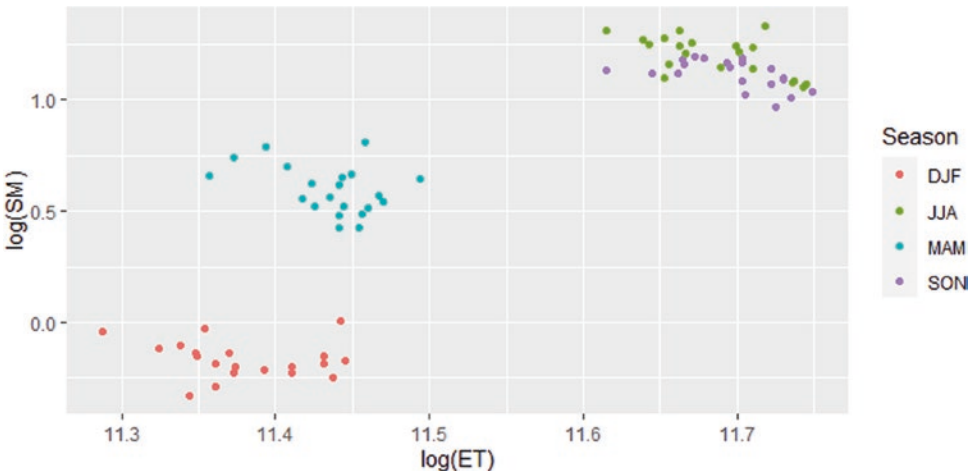

Fig. 1 Scatterplots showing the distribution of θ and *ET* across the country from 2000 to 2020

Table 1 θ and *ET* across Nigeria

	θ_DJF	***ET_DJF***	***θ _MAM***	***ET_MAM***	***θ _JJA***	***ET_JJA***
θ _DJF	1					
ET_DJF	− 0.145	1				
θ _MAM	**0.980**	− 0.163	1			
ET_MAM	− **0.550**	0.171	− 0.367	1		
θ _JJA	**0.935**	− 0.185	**0.959**	− **0.484**	1	
ET_JJA	− **0.538**	**0.634**	− **0.548**	0.165	− **0.595**	1
θ _SON	0.384	0.072	0.347	− 0.075	0.378	− **0.512**
ET_SON	− 0.345	0.330	− 0.284	0.213	− 0.310	**0.501**
Significant						

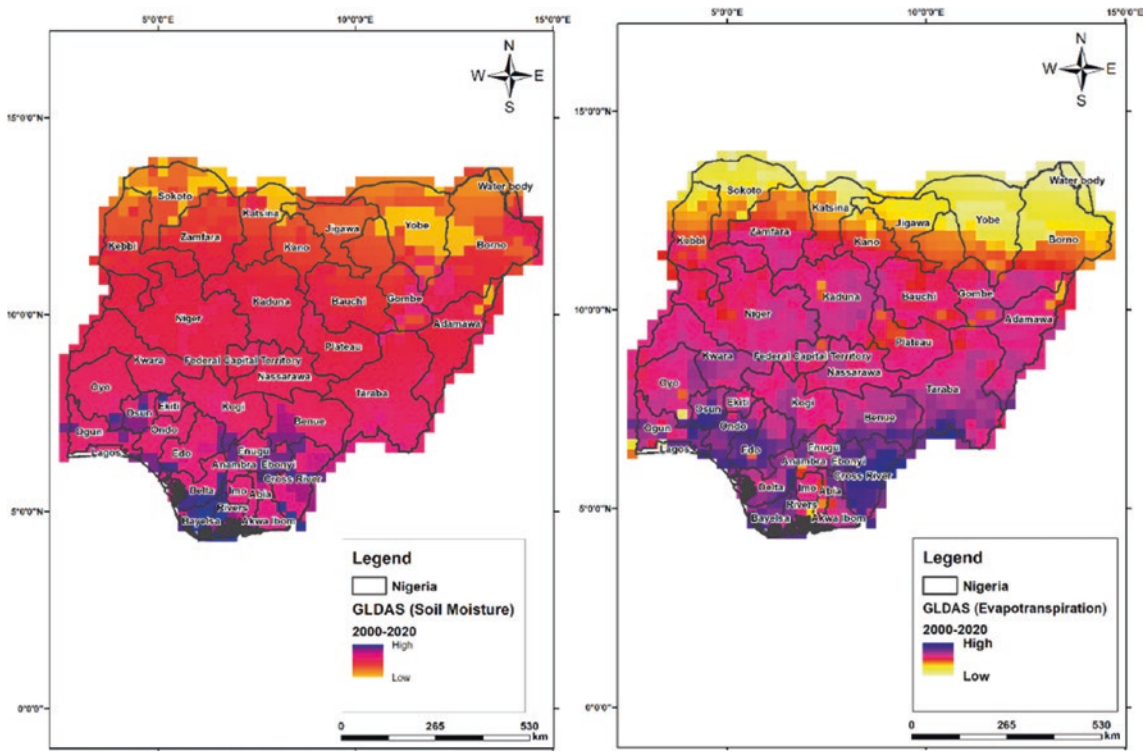

Fig. 2 Spatial distribution of soil moisture and evapotranspiration across Nigeria

the country. As earlier posited, these two parameters are very important for the optimal functioning of plants and crop productivity. Hence, there is a need to adequately monitor and project their spatio-temporal pattern for growing seasons. Unfortunately, in situ monitoring of soil moisture and *ET* is scarce (Olusola et al., 2017), and in most countries in SSA, such as Nigeria, data on soil moisture and *ET* are largely unavailable (Olusola et al., 2017). This in a way affects effective and precise agricultural practices across the country.

Earth Observation products such as the Global Land Data Assimilation provide a rapid and more efficient way to not only monitor but also give an avenue to project the pattern of spread of these variables across various scenarios, especially in the light of climate change. These help in driving an effective monitoring system for a well-balanced agricultural production in regions where livelihood is tied to agricultural products.

5 Conclusions

This study has shown the possibility of the use of Earth Observations to monitor changes in soil moisture and evapotranspiration. This becomes imperative owing to the scarcity of data in most SSA countries, especially Nigeria. Therefore, there is the need to embrace open data sources to enhance crop monitoring to ensure food security even in data scare regions.

References

Beaudoing, H., & Rodell, M. (2020). NASA/GSFC/HSL GLDAS Noah Land Surface Model L4 monthly 0.25 x 0.25 degree V2.1, Greenbelt, Maryland, USA, Goddard Earth Sciences Data and Information Services Center (GES DISC).

Olusola, A. O., Durowoju, O. S., & Adedeji, O. (2017). Interactions between topography, soil moisture and solar radiation: A model approach. *Uniosun Journal of Science, 2*(1), 66–73.

Petropoulos, G. P., Srivastava, P. K., Piles, M., & Pearson, S. (2018). Earth observation-based operational estimation of soil moisture and evapotranspiration for agricultural crops in support of sustainable water management. *Sustainability, 10*(1), 181.

Selection of Optimal Mathematical Models for Simulating and Forecasting Vertical Movements

Nhung Le, Benjamin Männel, Chinh Thai Nguyen, Quang Van Nguyen and Harald Schuh

Abstract

Deformation monitoring is increasingly concerned, especially for large-scale constructions or areas with a high risk of landslides and unstable Earth's crust. The important purpose of deformation monitoring is to determine the real state of the deformation, as well as the movement trend, then to provide the necessary information for forecasting. In this study, hypothesis and statistics are applied to filter observations involving gross errors, test the stability of reference stations, and to select the optimal mathematical models to simulate and forecast movements. Model parameters are determined by regression algorithms and the least-squares principle. Base on the approach of machine learning techniques and the least-squares principle, we built the optimal mathematical models for construction deformation monitoring at the Central Nursing and Rehabilitation Hospital, Thanh-Hoa province, Vietnam. The data collected by the cyclic sampling method includes 19 observation epochs from June 2009 to April 2012, in which 15 epochs are used to train forecast models and four epochs are used to test and validate these models. The accuracy of the forecast models ranges from 0.4 to 0.7 mm (equivalent to the root-mean-squares errors of observations that vary from 0.3 to 0.7 mm) while the average subsidence of the monitoring stations is around 9.5 mm with a velocity of 0.8 mm per month. Therefore, these mathematical models can be applied to simulate and predict movements of the monitoring stations.

Keywords

Deformation monitoring · Optimal mathematical models · Hypothesis and statistics · Least-squares principle

1 Introduction

In deformation analysis, the construction loads on the foundation are one of factors causing movements, and these movements can be predicted based on mathematical models. If movements are equal and have the same directions, deformations are often trivial and can be ignored. However, deformations will occur when motions are large enough and in different directions. Besides natural hazards, factors like heterogeneous soil composition, harsh climate, and groundwater extraction are also the leading causes of various motions such as subsidence, heaving, and rebound (Dang & Liu, 2013; Gugnin et al., 1999). These distortions can lead to serious consequences for constructions, such as cracking, warping, and twisting. Thus, detecting deformations is necessary to propose early warnings.

Detecting deformations is often based on changes in the positions of monitoring stations over time. However, because of errors in monitoring, these changes do not always reflect real states of deformations. This causes inaccurate results and misrepresents the nature of movements. Thus, statistical hypothesis testing plays an important role to remove gross and systematic errors. Statistical testing methods have been developed by Newcomb and Stigler

N. Le (✉) · B. Männel · C. T. Nguyen · H. Schuh
GFZ German Research Centre for Geosciences, Potsdam, Germany
e-mail: nhung@gfz-potsdam.de

N. Le · C. T. Nguyen · H. Schuh
Technische Universität Berlin, Berlin, Germany

N. Le · Q. Van Nguyen
Hanoi University of Natural Resources and Environment, Hanoi, Vietnam

C. T. Nguyen
Hanoi University of Mining and Geology, Hanoi, Vietnam

Z. A. Ergüler et al. (eds.), *Selected Studies in Geotechnics, Geo-Informatics and Remote Sensing*, Advances in Science, Technology & Innovation, https://doi.org/10.1007/978-3-031-43759-5_23

(1973), Tukey (2016), Maronna and Martin (2019), and Hampel (2014) via a range of proven studies. Maronna and Martin (2019) suggested a standard procedure for statistical hypothesis testing including three requirements: efficiency for optimal hypothetical models, stability for strong resistance to small errors of models, and mutation for acceptable large errors in models (Peter & Ronchetti, 2012). Computation adjustments to remove gross errors are based on Baarda's outlier test (Ogundare, 2019) and Peter Huber's robust estimation theory (Newcomb & Stigler, 1973; Zaman & Alakuş, 2015). Nowadays, machine learning is efficiently applied to build these forecast models (Liu et al., 2019). However, to avoid bias of conclusions, preprocessing techniques should be applied to clean data. Besides, it is not likely to immediately define what optimal mathematical models will be appropriate.

Therefore, in this study, we apply the theory of hypothesis and statistics to filter gross errors, and test the stability of reference stations. Then, we select the optimal mathematical models for vertical movement predictions. Regression algorithms and the least-squares principle are used to determine the coefficients of the mathematical functions. These models simulate and forecast the vertical movements of the monitoring stations over time.

2 Data and Methods

2.1 Data

We use data from the project of deformation monitoring at the Central Nursing and Rehabilitation Hospital, Thanh-Hoa province, Vietnam. Data of 19 epochs were observed from June 2009 to April 2012. The monitoring network system has four control stations (as reference stations) and 49 monitoring sites. These control stations have to ensure strict conditions about the accuracy, stability, distance, and the depth to the basement rock (TCVN) (2012). The monitoring process also complies with the criteria of construction standards (TCXDVN) (2002).

2.2 Methods

2.2.1 Test the Quality of Input Data

We apply statistic tests to filtered outliers in raw data, and then, we check the stability of the control stations using Fisher (F) test. Observations with an error greater than twice the root mean square error (RMSE), corresponding to probability 95%, will be rejected. These observations can be considered as outliers. Besides, testing the stability of the reference stations is also one of the preconditions (Dams & Structures; Setan & Singh, 2001) because the unstable control stations can lead to movements of monitoring stations. These movements are considered as systematic errors and will be discarded. We analyze the stability of the control stations based on Pelzer's method via three main steps. The first step is to determine the variance S^2 of datasets. The second is to compute the variance ratio between two consecutive epochs. Finally, Fisher (F) test is used to determine whether the reference variances of two sample datasets are statistically equal (Navratil, 2011). Applying statistical hypothesis to test the confidence interval for the ratio of variances $\frac{\sigma_1^2}{\sigma_2^2}$ (Ogundare, 2019):

$$P\left(\frac{1}{F_{\alpha/2,v_1,,v_2}}\frac{S_1^2}{S_2^2} < \frac{\sigma_1^2}{\sigma_2^2} < \frac{S_1^2}{S_2^2}\frac{1}{F_{1-\alpha/2,v_1,,v_2}}\right) = 1-\alpha$$

where S_1^2, S_2^2 are the variances of two consecutive monitoring epochs; α is the percentage point.

If the variance ratio is within the confidence interval, the control stations are stable. The control stations can be used for the next steps. If this value exceeds the confidence interval, there is at least one unstable station in the control network. Thus, we need to carry out the third step, which is to identify the unstable stations in the control network. The control stations are separated into two groups: N and M, in which group M involves unstable stations. Loops are performed to select unstable stations from group N to group M using F test.

2.2.2 Select the Optimal Mathematical Models

Movements of the monitoring stations will reflect deformations of observed objects in space. We use the mathematical models to simulate these movements. Depending on the movement trajectory, we select the appropriate mathematical models. Then, we test whether the selected models fit the actual movements of the monitoring stations or not.

We apply regression algorithms and the least-squares principle to determine the coefficients of mathematical functions (Amiri-Simkooei et al., 2017; Navratil, 2011; Nowel, 2016; Ogundare, 2019). We investigate three main mathematical functions (exponents, polynomials, and the combined harmonics) which characterize the construction movements in general. Input data to train models are the subsidence values of the monitoring stations over 19 epochs. We build subsidence functions with variables of time. The coefficients of these subsidence functions are unknown. Solutions of normal equations are the coefficient

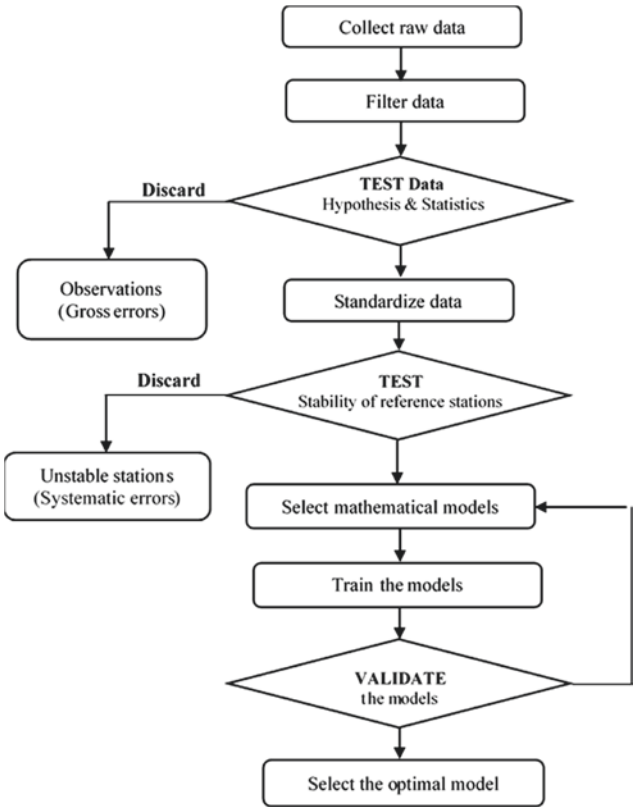

Fig. 1 Flowchart of establishing the optimal forecast models

vectors of the mathematical functions. The accuracy of mathematical models are as follows (r—redundant observations, V—the residual vector):

$$m_{\text{md}} = \pm\sqrt{\frac{[VV]}{r}} \tag{1}$$

The best suited model is used to simulate and forecast movements of monitoring sites. F test is used to check whether the accuracy of the forecast models (m_{md}) is equivalent to the accuracy of measurements (m_{o}) or not. The variance ratio as follows:

$$F = \frac{m_{\text{md}}^2}{m_{\text{o}}^2} \tag{2}$$

The difference between validation and test values is the basis to select the optimal model. Figure 1 presents the main steps of establishing the optimal forecast models.

3 Results and Discussions

After filtering outliers and removing unstable control stations, standardized data will be used to build mathematical models. We use 15 epochs to train, two epochs to validate, and two last epochs to test forecast models.

The mathematical functions of polynomial combined harmonics, exponents, and polynomials are considered to simulate deformation movements (Fig. 2). Five monitoring stations (M5, M28, M30, M47, and M48) are discarded because the program detects gross errors (corresponding to a probability of 95%).

For station M15, the accuracies of the mathematical models are 0.59 mm, 0.52 mm, and 0.63 mm corresponding to polynomial, exponential, and polynomial combined harmonic functions. The differences between the calculated values on these models and the measurement values are 0.70 mm, 1.03 mm, and 0.71 mm, respectively. These differences are equivalent to the required accuracy in construction subsidence monitoring (TCXDVN). The accuracy of the polynomial models for station M49 is 0.45 mm, whereas that of the exponential and harmonic models reach up to 3.18 mm. These values are beyond the confidence interval of Fisher (F) test. Similarly, investigations on all monitoring stations show that polynomial functions are best suited to model vertical movements of the construction. Here, α (the percentage point) is equal to 0.05 corresponding to probability 95% for the F test.

Figure 3 shows the movements of the eight monitoring stations simulated by polynomial functions. The accuracy of these mathematical models ranges from 0.36 to 0.65 mm, equivalent to the RMSE values of observations (0.30 ÷ 0.67 mm). The average subsidence of the building is equal to 9.47 mm with a velocity of ~ 0.84 mm/month. The subsidence of station M15 remains at least (~7.70 mm), while station M49 is at the highest (~13.50 mm). The accuracy of these mathematical models is less than 10% of the subsidence values. The differences between the calculation values and observations range from 0.70 mm to 6.27 mm (Table 1), in which the average value remains about 2.3 mm. Therefore, polynomial functions can be applied to simulate and predict movements of the monitoring stations.

For stations M12 and M20, the difference between the calculation values and observations exceed three times the threshold of the measurement errors (under 1.0 mm)

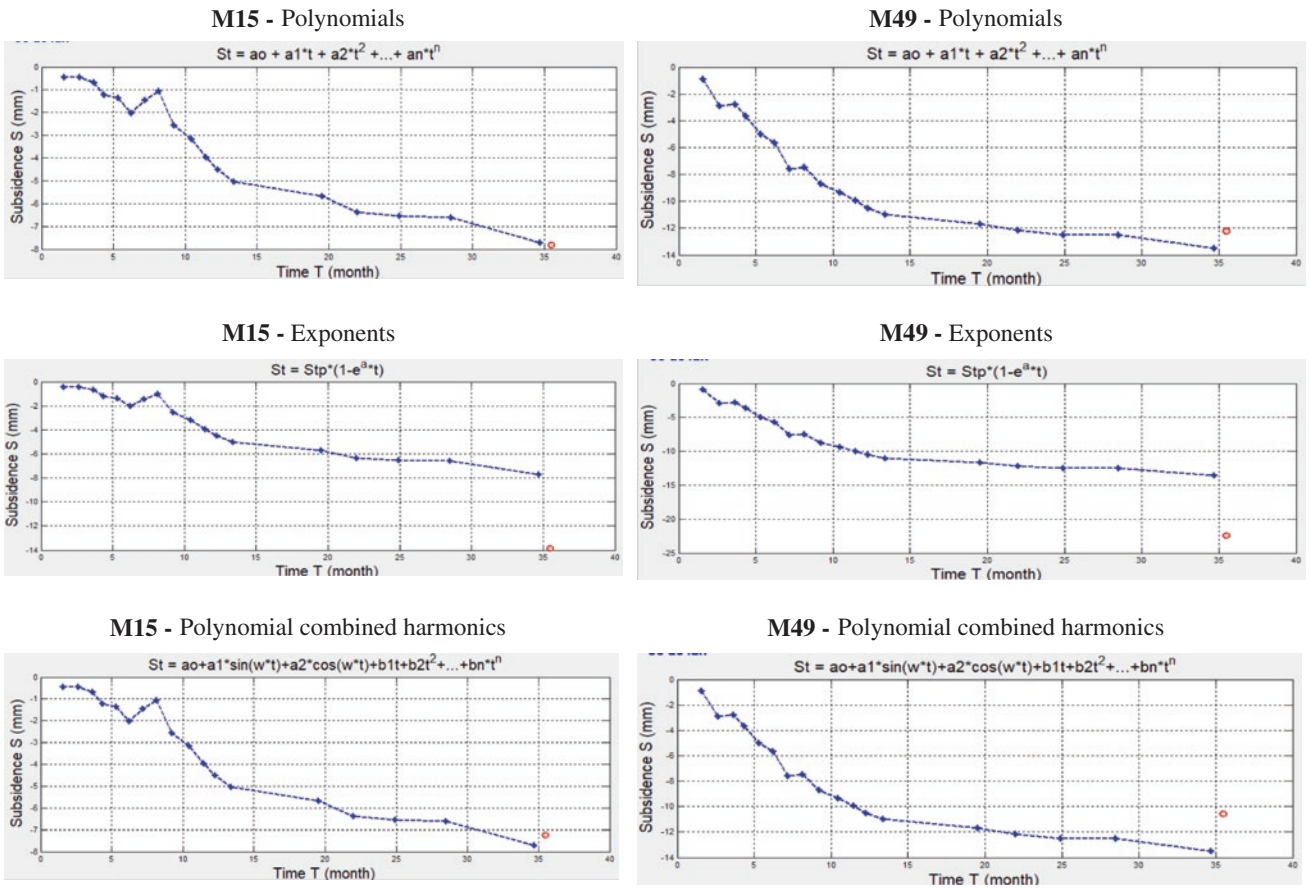

Fig. 2 Movements of monitoring stations M15 and M49 corresponding to the mathematical functions

(TCVN 9360:2012, 2013). The solution is to monitor more observations until time series show all characteristics of movements.

4 Conclusions

The theory of hypothesis and statistics is applied effectively to filter outliers, analyzes the stability of control stations, and is also the basis to select the most appropriate mathematical model in movement monitoring. The polynomial functions are best suited to simulate movements of monitoring stations. These mathematical models can be also applied to forecast the trends of construction movements in general. In case the difference between the calculation values and observations is beyond thresholds, it is necessary to observe more data or adjust the weights of the correlation coefficients in the mathematical functions for better forecast performance.

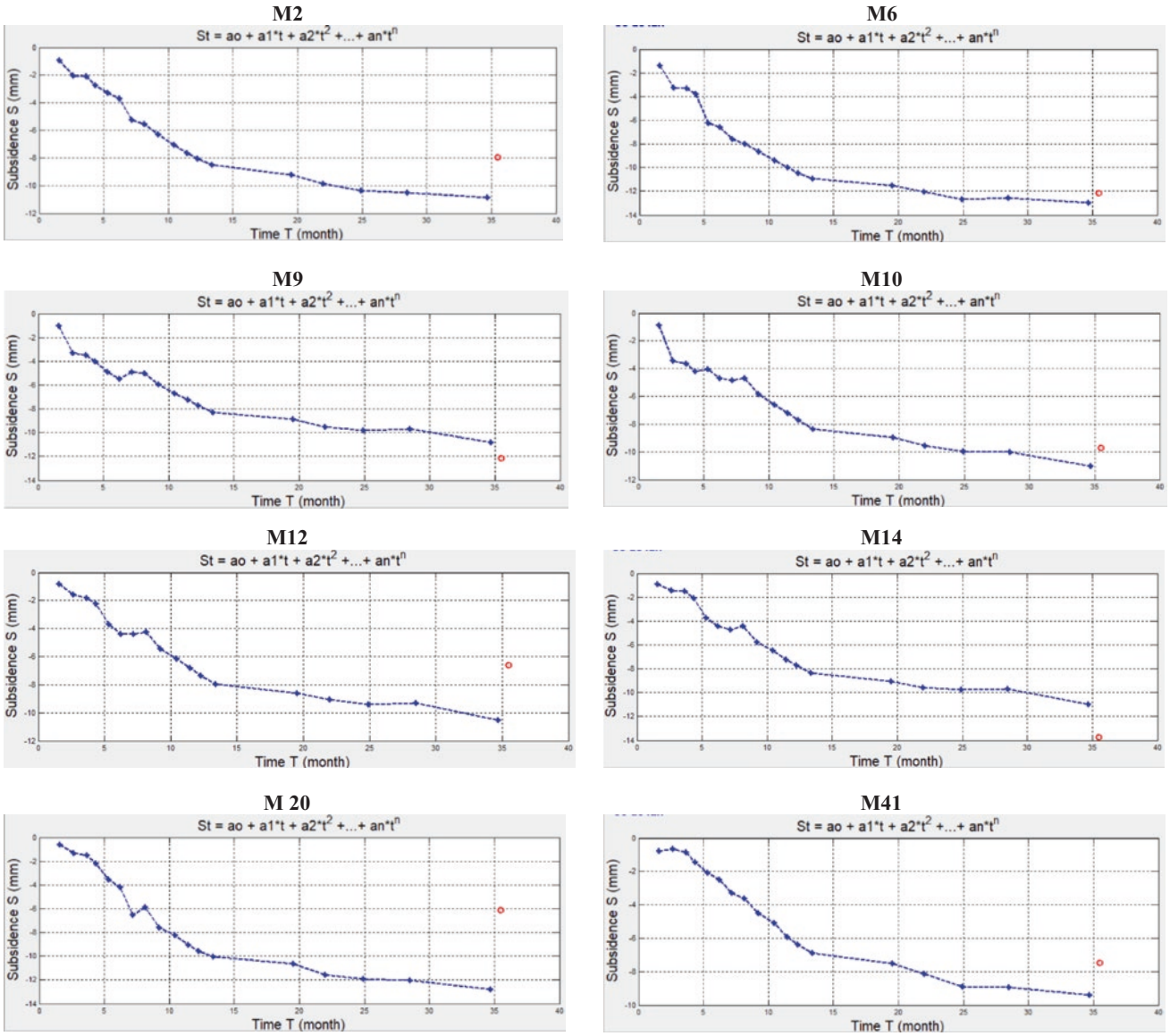

Fig. 3 Movements of monitoring stations (M2, M6, M9, M10, M12, M14, M20, and M41), simulated by polynomial functions

Table 1 Accuracy of optimal mathematical models and the difference between calculation values and observations

Stations	Accuracy of		Difference of
	Measurements (mm)	Models (mm)	Predicted values and observations (mm)
M2	0.42	0.40	2.78
M6	0.63	0.43	1.34
M9	0.67	0.52	1.28
M10	0.66	0.60	1.26
M12	**0.62**	**0.40**	**3.63**
M14	0.61	0.47	2.77
M15	0.59	0.59	0.70
M20	**0.41**	**0.62**	**6.28**
M41	0.40	0.45	1.74
M49	0.61	0.45	1.42

Acknowledgements The authors would like to thank colleagues at the University of Transport Technology in Vietnam for providing data. This work is also supported by the projects of construction deformation monitoring carried out from 2013 to 2017 at Hanoi University of Natural Resources and Environment in Vietnam.

References

Amiri-Simkooei, A. R., Alaei-Tabatabaei, S. M., Zangeneh-Nejad, F., & Voosoghi, B. (2017). Stability analysis of deformation-monitoring network points using simultaneous observation adjustment of two epochs. *Journal of Surveying Engineering, 143*(1), 1–12. https://doi.org/10.1061/(ASCE)SU.1943-5428.0000195

Krawczyk, K. (2023). Influence of reference stations on the stability of the geodetic control network during deformation determination in the area of Kadzielnia in Kielce. *Reports on Geodesy Geoinformatics, 115*(1), 19–26. https://doi.org/10.2478/rgg-2023-0003

Dang, Y., & Liu, Y. K. (2013). Deformation of overlong isolated buildings caused by thermal and concrete shrinkage. *Mathematical Problems in Engineering*. https://doi.org/10.1155/2013/139159.

Gugnin, V. P. K., Charushin, A. L., & Malakhov, V. E. (1999). Causes of structural deformations of an apartment building on weak foundation in Verkhnekamsk. *Soil Mechanics and Foundation Engineering, 36*(5), 19–20. https://doi.org/10.1007/bf02469106.

Hampel, F. R. (1974). The influence curve and its role in robust estimation. *Journal of the American Statistical Association*, *69*(346), 383–393. http://dx.doi.org/10.1080/01621459.1974.10482962

Liu, H., et al. (2019). A nonlinear regression application via machine learning techniques for geomagnetic data reconstruction processing. *IEEE Transactions on Geoscience and Remote Sensing, 57*(1), 128–140. https://doi.org/10.1109/TGRS.2018.2852632

Maronna, R.A., & Martin, R. D. (2019). Linear Regression 1. In *Robust Statistics: Theory and Methods* (pp. 87–114). John Wiley & Sons, Ltd. https://doi.org/10.1002/9781119214656.ch4

Navratil, G. (2011). *Adjustment computations: Spatial data analysis* (Vol. 25, No. 2). Hoboken, New Jersey: John Wiley & Sons, Inc.

Nowel, K. (2016). Application of Monte Carlo method to statistical testing in deformation analysis based on robust M-estimation. *Survey Review, 48*(348), 212–223. https://doi.org/10.1179/1752270615Y.0000000026

Ogundare, J. O. (2019). *Understanding least squares estimation and geomatics data analysis* (Vol. 3, No. 2). Hoboken, New Jersey: John Wiley & Sons, Inc.

Peter, H. J., & Ronchetti, E. M. (2012). *Robust statistics* (2nd ed.). Hoboken, New Jersey: John Wiley & Sons, Inc.

Setan, H., & Singh, R. (2001). Deformation analysis of a geodetic monitoring network. *Geomatica, 55*(3), 333–346.

Stigler, S. M. (1973). *Simon Newcomb, Percy Daniell, and the History of Robust Estimation 1885–1920*, *68*(344), 872–879. https://doi.org/10.2307/2284515

TCVN 9360:2012. (2013). *Technical process of settlement monitoring of civil and industrial building by geometrical levelling*.

TCXDVN 271–2002. (2002). *Technical process of settlement monitoring of civil and industrial building by geometrical levelling* (p. 56).

Tukey, J. W. (1962). The future of data analysis. *Institute of Mathematical Statistics Stable, 33*(1), 1–67 [Online]. Available: http://www.jstor.org/stable/2237638

Zaman, T., & Alakuş, K. (2015). Some robust estimation methods and their applications. *Alphanumeric Journal, 3*(2). https://doi.org/10.17093/aj.2015.3.2.5000152703.

Building Pattern Typification

Nardjes Hamini and Mohamed Bachir Yagoubi

Abstract

Cartographic generalization is a cartographic process that allows the production of maps at smaller scale from larger scale maps because when we reduce the space where the cartographic objects are, problems can appear such as the superimposition, imperceptibility, coalescence, and the clutter of the map. It is necessary to select the information that is to be represented on the maps. The typification of buildings is a cartographic generalization operation. It consists of simplifying a group of buildings by removing a number of its units but keeping the specifics of the group such as the shape of the cluster, the area, and the characteristics of the buildings. In this work, we are interested in particular groupings which are the patterns of buildings. We suggest a new way of typifying them. Our method goes through several stages including pattern detection, characterization of dispersion, and selection according to a cost function. The buildings are then simplified by applying a simplification of contour, a transformation, or amplification according to the size of the building. Finally, we induce a displacement operation. The method was implemented under PyQGIS programming language. Sample maps were taken from the state of Laghouat, Algeria. The obtained results display the same characteristics as large scale maps, respect the land extent, and are readable.

Keywords

Cartographic-generalization · Typification · Building · Pattern · Clustering

N. Hamini (✉) · M. B. Yagoubi
Laghouat University, PB 37 Ghardaia Road, Laghouat, Algeria
e-mail: 1et1font10@gmail.com

1 Introduction

Map navigation has come to an astonishing level of accuracy in the recent years. Cartographic generalization has allowed any device which enjoys a map software to visualize small scales maps which are produced from large scale maps (that were obtained from aerial and satellite images).

Generalization automation is quite a recent field, and the perfect solution does not yet exist on the market. However, the latter's tools can be grouped into four main categories: Cartographic measurements; they provide information to the generalization process to guide its operations such as area, length, orientation, etc. Geometric algorithms; such as Voronoi diagram, Delaunay triangulation, and convex hull. Generalization algorithms; like simplification, displacement, typification, selection, aggregation, etc. Lastly, the generalization process which is the conductor who manages the set of tools mentioned above to carry out the generalization. We are able to find a set of works from the model (list of established steps) to the intelligent process (neural networks, genetic algorithm, agent-based system, etc.).

The issues raised within the field of generalization are the lack of generalization algorithms and their availability to researchers. There are only a few simplification and aggregation tools. It is this observation that promoted an interest in building a typification operation.

The typification makes it possible to replace a set of buildings with another set with a lesser number of items but which renders it more readable, while retaining the characteristics of the original group (with regard to the extent and general shape of the buildings). However, certain sets of buildings can have particular dispersions (pattern) that should not be disturbed such as an alignment along a road, a grid arrangement, in circle, in star, in alphabet letter (Z, H, …), indescribable shapes but which to the eye say something, or just any buildings facing each other; there are

Z. A. Ergüler et al. (eds.), *Selected Studies in Geotechnics, Geo-Informatics and Remote Sensing*,
Advances in Science, Technology & Innovation, https://doi.org/10.1007/978-3-031-43759-5_24

also hierarchies of patterns (patterns arranged in patterns). This research is concerned with the latter, but the method is applicable to all building patterns.

2 Methods

The method starts with the preprocessing and clustering of buildings which is based on a division of the zone into blocks, followed by a neighborhood search based on a Delaunay triangulation. Then, we have a pattern search based on our method described in a previous document (Hamini, 2019). These are replaced by an enclosing shape to be treated as a single object; we have chosen the concave envelope.

For the detection of the distribution: to detect a linear arrangement along a road, a projection on the section of the nearest road is calculated, and this also allows the ordering of objects (buildings/concave envelopes).

For the grid: we first extract the centroids of the objects (buildings/concave envelopes). We then calculate the bounding rectangle oriented of the set of points. Then, we vary the parameter of a buffer applied to this rectangle negatively. We thus obtain a rectangle which collapses gradually on itself, offering us a sweep of the centroids from the outside to the inside. A two-dimensional array is created and filled as things progress, representing the shape of the grid.

For the selection and the positioning: for the alignment, we were inspired by the work of Hangouët (1998). Let n be the number of objects in the group, and m the number of target objects. We then calculate m positions, and the buildings closest to these locations remain and are placed there, the others are eliminated. The positions are given by: The m positions ($c_{r,i}$) are computers using original positions ($c_{o,\,P(i)}$).

$$c_{r,i} = c_{o,P(i)} + \lambda(i) \times c_{o,P(i)}c_{o,Q(i)}$$
$$R = (i-1) \times (n-1)/(m-1)$$
$$P(i) = 1 + E(R)(E(R) \text{ greatest integer less than or equal } R)$$
$$\lambda(i) = R - E(R). \text{ if } \lambda(i) = 0, \text{ then}$$
$$Q(i) = P(i). \text{else}, Q(i) = P(i) + 1.$$

For the grid: the deletion is done according to the elongation of the shape of the grid (therefore, we extract the orientation and the elongation from the oriented bounding rectangle), the deletion is done by whole row and whole column.

For the unstructured pattern: the selection is based on a cost function, based on the work of Hamini (2019). Buildings that have a high cost value are eliminated. This method has no distribution function, so we rely on a displacement algorithm:

$$\text{Cost} = [\left(\frac{\text{MaxSurf} - \text{Surf}}{\text{MaxSurf}}\right)^{\frac{1}{2}} + \left(\frac{\text{NbrSpaces} - \text{FreeSpaces}}{\text{NbrSpaces}}\right)^{\frac{1}{2}} + \left(\frac{\sum \text{CluteringQuantity}}{\text{NbreSpaces}}\right)^{\frac{1}{2}} + \left(\frac{\text{NbrBuildingsLinks}}{\text{NbrLinks}}\right)^{\frac{1}{2}}$$

For the displacement: the objects are moved as follows:

- If an object does not have an eliminated neighbor, then its position remains the same.
- If an object has eliminated neighbors, its position is then an average between the positions of its eliminated neighbors and its own position.
- A second displacement is performed if there are overlays, in the direction of centroids, by repulsion.

For the simplification of the buildings: we used as needed: an amplification (buffer), the convex hull, the oriented bounding rectangle, the simplification of Douglas and Peucker, and the simplification of Visvalingam. Object number is equal to the ratio of surfaces multiplied by n.

3 Results

The method was tested on samples from the City of Laghouat (Algeria), the City of Dubai, and samples produced in the laboratory. The data comes from "OpenStreetMap" and "GoogleMap." The method was implemented under QGIS (mapping software) which supports PyQGIS (python augmented by QGIS spatial libraries). Here are some of the results (Figs. 1 and 2).

4 Discussion

The values between the original groups and the resulting groups were compared. We first have the land extent calculated by the surface of the convex hull; the value given is the ratio between the original value and the resulting value. We notice that the values are close since they are all close to 1, the extent is therefore preserved. The shape is obtained

Fig. 1 Linear and grid pattern typification

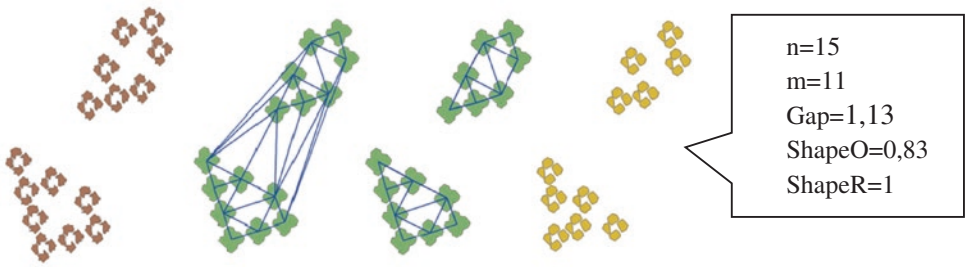

Fig. 2 Unstructured cluster typification

by the ratio of the area of a building and its convex hull, and we notice that the value of this ratio between the two compared is approximately the same.

The results obtained on the other samples are also conclusive. However, the typification is tested alone. It would be interesting to test it in a generalization process.

5 Conclusions

We have seen in this paper that automatic generalization is a young field. It was observed that building typification is a generalization operation. We saw that there were different types of building groups called patterns, and that each required a particular typification. The obtained results were conclusive.

However, most of the tools are not available in the accessible GIS tools. The implementation took up a large part of the project. Thus, we had to limit the application to certain patterns. For future applications, we intend to add other types of patterns (circle, star, Z, H, E…) and eventually the introduction of a shape-recognition method.

References

Hamini, N. (2019). Building pattern identification for map generalization. In *Proceedings of the 2nd Springer Conference of the Arabian Journal of Geosciences (CAJG-2)*, Tunisia.

Hangouët J. F. (1998). Approche et méthodes pour l'automatisation de la généralisation cartographique; application en bord de ville. Ph.D. thesis, University of Marne-LaVallée France1

Fire-Event Management Insights Through Social Media

Stathis G. Arapostathis

Abstract

The main motivation of the current article is to provide evolutions on previously presented methods related to the utilization of social network data for disaster management (DM) purposes of fire events. The evolutions include the extension of the applicability of the approach in different geographic regions, the directive of integrating posted photographs in the classification procedure, the manipulation of more than one social network source, and automation. As case studies, the author selected the deadly wildfires of East Attica (2018, Greece) and the forest fire of Castrocontrigo (2012, Spain). Those fire events are different in terms of epoch of occurrence, geography, and native local language. The approach is divided into four main parts. The first part was related to data collection: 15,132 and 14,698 tweets were scrapped for each fire event, respectively, while a dataset of 14,000 photographs scraped previously from Instagram for the wildfires of East Attica was used as well. The second part was related to classification and included the definition of a structure, and the classification of the collected data to defined classes by using machine learning techniques. The third part was related to geo-referencing of the classified information. The applied automated process was based on conventional list-based geoparsing techniques. Finally, a subset of a processed dataset was used for developing two maps, presenting information about identifying the fire for both geographic regions. Apart from automation and evolved classification, the initial results provide empiric evidence regarding the applicability of the approach in different geographic regions.

Keywords

Social networks · Disaster management · Volunteered geographic information (VGI) · Fire event management

1 Introduction

Innovations in disaster management (DM) are emerging. One of them is related to the use of social networks. There are numerous related researches, specifically for fire events (De Longueville et al., 2009; Sosko & Dalyot, 2015; Spinsanti & Ostermann, 2011). The author has presented related work as well (Arapostathis, 2019; Arapostathis & Karatzia, 2019). The main motivation of the current research is to present evolution, by extending the applicability in different geographic regions and manipulating more than one social media source, and performing automation. As case studies, the author chose two fire events with different characteristics: the forest fire of Castrocontrigo (Spain, August–September 2012) and the wildfires of East Attica (Greece, 2018).

2 Data, Materials, and Methods

The author used a total of 15,132 tweets and about 14,000 Instagram posts for the East Attica fire event. The Instagram dataset was collected previously (Arapostathis, 2019), while a total of 14,698 tweets were collected for the Castrocontrigo fire. Twitter data collection was performed through the use of a related crawler (source: www.github.com/twitterscraper/taspinar/twitterscraper) written in Python. The main used hashtags included: #castrocontrigo, #fuego, #mati, #prayforathens. The fire of Castrocontrigo, occurred within the same year of Instagram launching, and therefore, the author did not seek data. Data processing

S. G. Arapostathis (✉)
Harokopio University, 17671 Kallithea, Athens, Greece
e-mail: e.arapostathis@gmail.com

Z. A. Ergüler et al. (eds.), *Selected Studies in Geotechnics, Geo-Informatics and Remote Sensing*,
Advances in Science, Technology & Innovation, https://doi.org/10.1007/978-3-031-43759-5_25

was mainly performed in R, version 3.6.3. The main packages used were the mxnet R package, the really trustworthy RTextTools even its deployment is stopped, and the Rgdal for spatial data operations. Maps were created in open-source GIS software. Script approaches can be found at the author's Github: www.github.com/stathisar/.

Figure 1 describes the basic parts of the approach. The Twitter dataset consisted of a .json file and included Twitter texts and related metadata, including timestamps. The structure of the Instagram dataset which was collected previously (Arapostathis, 2019) included, apart from the photographs, a .json as well, with metadata, including corresponding captions and timestamps.

The classes defined for both Instagram captions and tweets were: (i) fire identification, (ii) disaster management, (iii) event tracking, and (iv) consequences. The author had used support vector machines (SVM) for text classification and convolutional neural networks (CNN) for photograph classification. Despite the number of social network sources, one model was used for each case study. Photograph classification in the current stage was limited to the creation of a training dataset consisting of some photographs (i) irrelevant or (ii) relevant to fire, along with the creation of an initial CNN model that will be further enriched and calibrated. Upon completion of the classification, the processed output aspires to be fully integrated within the defined classification structure. Georeferencing method applied was based on conventional list-based geoparsing that has been used previously (Arapostathis & Karantzia, 2019). Finally, a processed dataset was used for creating two maps.

3 Results and Discussion

Figure 2 is a map with proportional symbols that represent the frequency of the extracted information related to fire identification of the Castrocontrigo fire event. The output is based on the initial processing of the complete dataset, while the geolocations list that was used for geoparsing was very limited in the current stage of research. Moreover, Fig. 3 displays information extracted through tweets posted within 4 h and Instagram posts, regarding the identification of the East Attica fire event. The representation is based on spatial clustering of the georeferenced content. The displayed information is based on the initial processing of the entire Twitter text corpus, within the related time period and a part of the Instagram dataset.

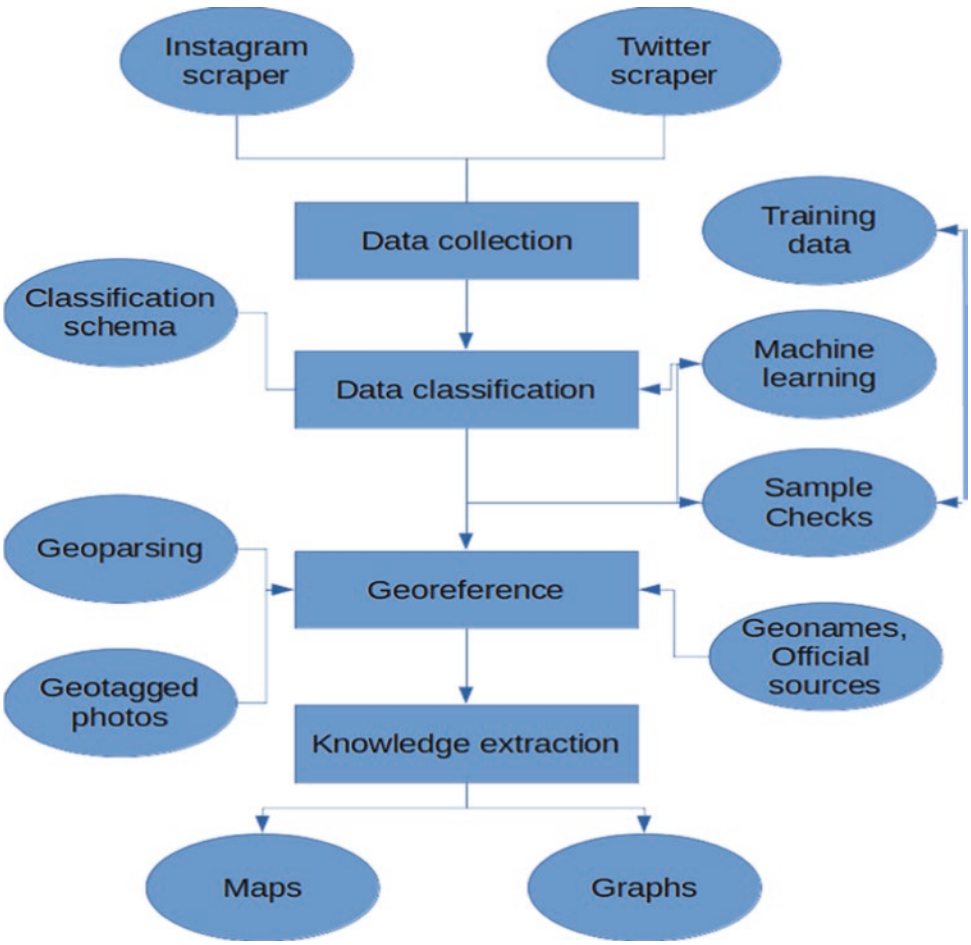

Fig. 1 Schema of the applied methodology for analyzing social network data

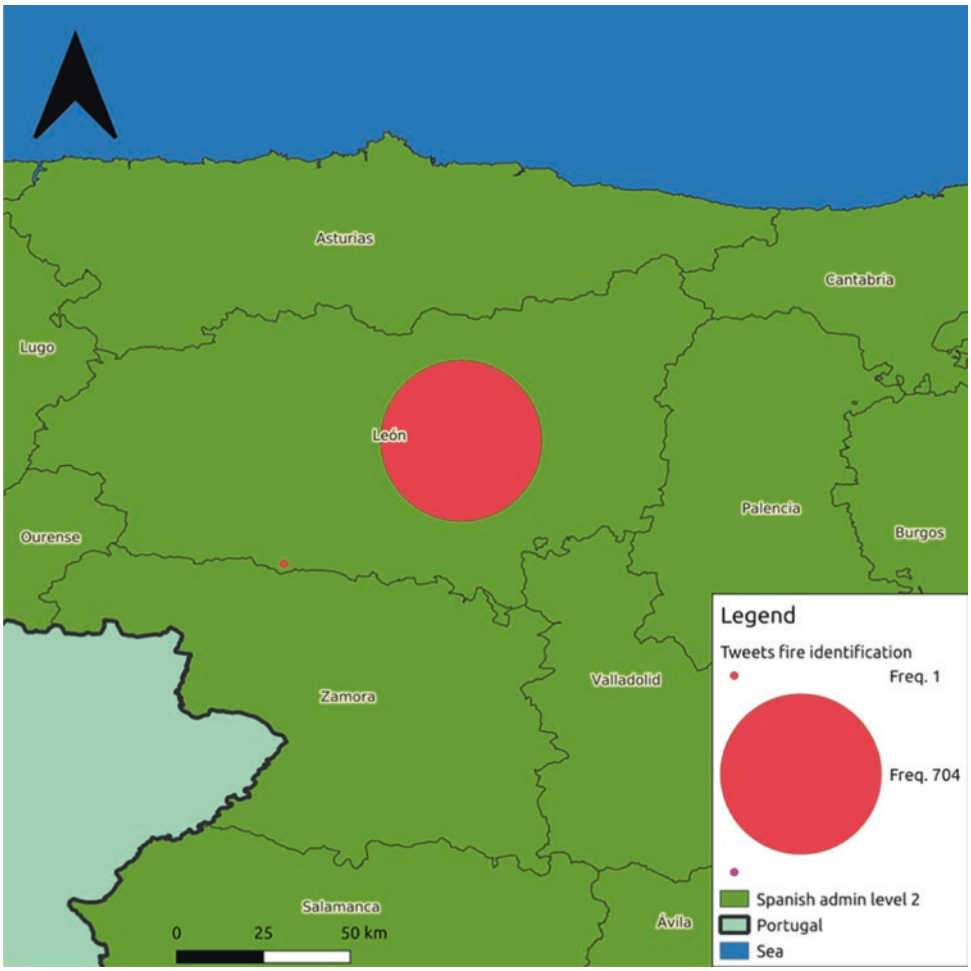

Fig. 2 Proportional map representing quantity of tweets related to fire identification in Leon prefecture (Castrocontrigo fire, Spain, August–September 2012)

Even though the current research is at an initial stage, there is a clear assumption of a presence of a plethora of social network posts related to fire event management information in both case studies. Machine learning and automatic approaches can significantly contribute to providing accurate results. The latter assumption is compliant with published international research regarding social networks and disaster/crisis management (Feng & Sester, 2018; Nguyen et al. 2017). Moreover, the geoparsing method provides impressive results considering the general lack of tweets with x y coordinates (Morstatter et al., 2013). Geographic precision is, however, limited mostly to the city level and in some cases up to hamlet or neighborhood.

4 Conclusion and Future Work

Current work presents a structured automatic methodology which reduces the time needed for efficient data processing. Moreover, the results provide empiric evidence that the whole approach can be applied to different geographic regions and that multiple social media sources and data types can be integrated into the main methodology. Future work includes the full integration of posted photographs to the approach, the completion of data processing, along with the assessment of various machine learning algorithms for extracting information from social network posts and photographs regarding fire event management.

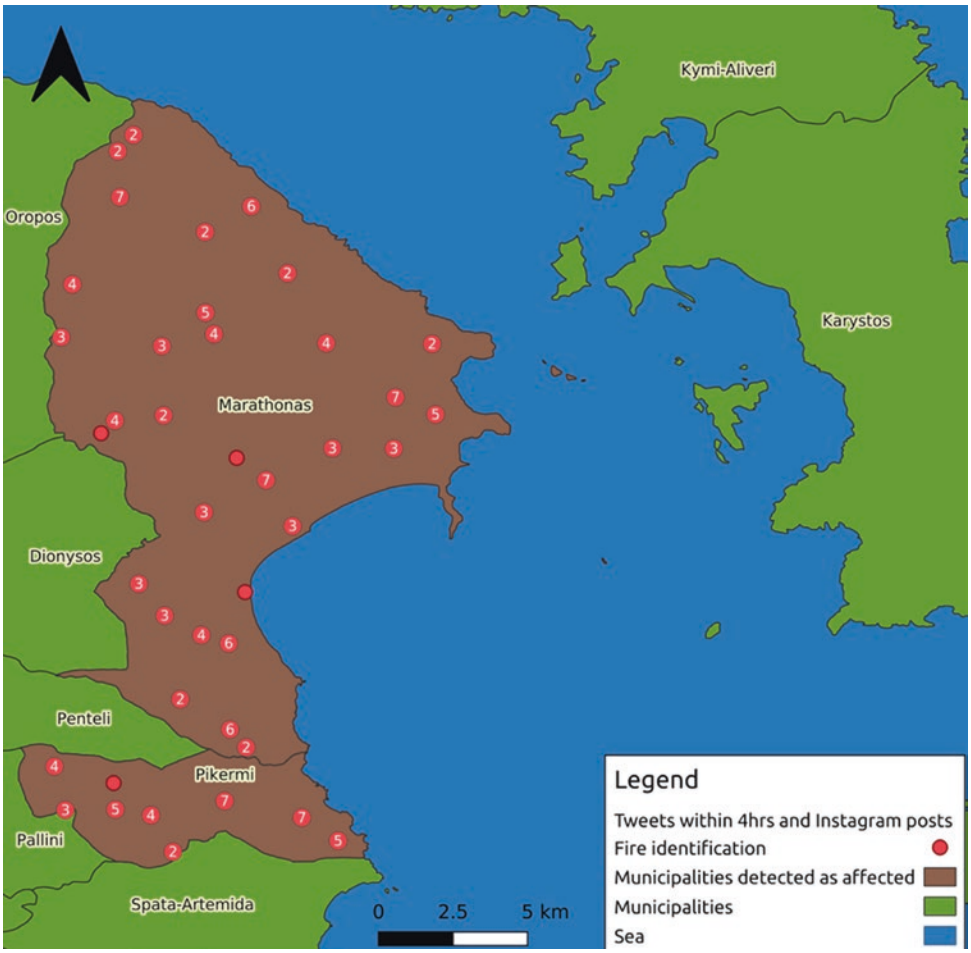

Fig. 3 Clusters of georeferenced tweets related to the fire of East Attica (Greece, 2018)

References

Arapostathis, S. G. (2019). Instagrammers report about the deadly wildfires of East Attica, 2018, Greece: an introductory analytic assessment for disaster management purposes. In *ISCRAM*, Valencia, Spain, 19–22 May 2019.

Arapostathis, S. G., & Karantzia, M. (2019). Mapping information of fire events, from VGI source (Twitter), for effective disaster management (in Greece); the fire of North-East Attica, August 2017, (Greece) case study. In *Advances in remote sensing and geo informatics applications* (pp. 257–260). Springer.

De Longueville, B., Smith, R. S., & Luraschi, G. (2009). Omg, from here, i can see the flames!: A use case of mining location based social networks to acquire spatio-temporal data on forest fires. In *Proceedings of the 2009 International Workshop on Location Based Social Networks* (pp. 73–80). ACM.

Feng, Y., & Sester, M. (2018). Extraction of pluvial flood relevant volunteered geographic information (VGI) by deep learning from user generated texts and photos. *ISPRS International Journal of Geo-Information, 7*(2), 39.

Morstatter, F., Pfeffer, J., Liu, H., & Carley, K. (2013, June). Is the sample good enough? Comparing data from twitter's streaming API with twitter's firehose. In *Proceedings of the International AAAI Conference on Web and Social Media* (Vol. 7, No. 1).

Nguyen, D., Al Mannai, K. A., Joty, S., Sajjad, H., Imran, M., & Mitra, P. (2017, May). Robust classification of crisis-related data on social networks using convolutional neural networks. In *Proceedings of the International AAAI Conference on Web and Social Media* (Vol. 11, No. 1).

Sosko, S., & Dalyot, S. (2015). Towards the use of crowdsourced volunteered meteorological data for forest fire monitoring. *Proceedings of GEOProcessing, 15*, 127–132.

Spinsanti, L., & Ostermann, F. O. (2011). Retrieve volunteered geographic information for forest fire. In *Proceedings of the 2nd Italian Information Retrieval Workshop 2011* (Vol. 704, No. 4). Milano, Italy.

Land Use Land Cover Assessment and Flood Hazard Mapping in Lagos State (Nigeria) Using Optical Remote Sensing Data

Dorcas Idowu and Wendy Zhou

Abstract

Lagos State, the smallest in the area but conceivably the most economically important among the 36 states in Nigeria, is rapidly developing. The Lagos Metropolitan Area is quickly becoming a megacity. This urban expansion accompanied by incessant flooding calls for an assessment of Land Use/Land Cover (LULC) changes and flood hazard mapping. Previous LULC analysis and flood hazard studies mostly focused on a portion of the entire area of Lagos State. Here, we measure LULC change for Lagos State between 1999 and 2019. First, an ISO clustered unsupervised classification is performed on two temporally different satellite images, the Landsat 7 Enhanced Thematic Mapper Plus and the Landsat 8 Operational Land Imager, to identify and classify land covers of interest. A new approach is presented for calculating the actual LULC change between the classified images for each land cover type. In addition, a flood hazard map is produced by combining different identified contributing factors to flooding in the study area by using the weighted overlay method. Areas of very high, high, moderate, and low flood hazards are mapped and identified with this method. Results show that urban development mostly occurs in very high, high, and moderate flood hazards. This study further buttresses the usefulness of remote sensing data for LULC and flood hazard studies. Local governing bodies could use the developed flood hazard map for flood mitigation preparedness, early evacuation plans, and insurance organizations for property insurance.

Keywords

Lagos flooding · LULC change detection · Flood hazard mapping · Urbanization

1 Introduction

Several studies have linked urban expansion in Lagos, Nigeria, to flooding (Adelekan, 2010; Adeloye & Rustum, 2011; Nkwunonwo et al., 2016). Monitoring urban development and identifying both the pace and pattern of that spread have long been a concern of urban planners and policymakers because this growth is taking place in many flood-prone areas.

Given the global rise in flood events recently, the need for accurate flood hazard assessment to be a part of flood mitigation in urban areas cannot be overemphasized (Rincón et al., 2018). Over the years, remote sensing and Geographical Information System (GIS) techniques have been utilized for flood hazard, zonation, risk, and vulnerability mapping (Ajin et al., 2013; Bishaw, 2012; Emmanuel et al., 2015; Idowu & Zhou, 2019, Idowu & Zhou, 2021; Idowu, 2021; Zhou, 2021). Flood hazard mapping is a crucial component for appropriate land use planning in areas prone to flooding. Delineating areas prone to flooding requires specific quantitative measurements from flood monitoring systems such as stream gauges. In developing countries, such records are largely insufficient or absent. As a result, flood hazard studies based on direct measurements may be impossible because there is no basis to determine the specific flood levels and recurrence intervals for any given flood event. Hazard assessments relying on remote sensing data and damage reports can be a substitute when quantitative data are scarce. Here, we determined

D. Idowu · W. Zhou (✉)
Colorado School of Mines, Golden, USA
e-mail: wzhou@mines.edu

Z. A. Ergüler et al. (eds.), *Selected Studies in Geotechnics, Geo-Informatics and Remote Sensing*,
Advances in Science, Technology & Innovation, https://doi.org/10.1007/978-3-031-43759-5_26

and combined some factors responsible for flooding using the weighted overlay method (Ozkan & Tarhan, 2016) and compared them to changes in LULC.

2 Materials and Methods

2.1 Description of Study Area

Lagos is a low-lying area (Fig. 1) bordered to the south by the Atlantic Ocean. Its total area is 3671 km^2, which encompasses land and all inland waters. The topography of Lagos is dominated by a system of islands, sandbars, and lagoons that empty water into the Atlantic Ocean.

2.2 Land Use/Land Cover Analysis (LULC)

We used the Landsat 7 ETM+ (Enhance Thematic Mapper), and Landsat 8 OLI (Operational Land Imager) downloaded from the United States Geological Survey (USGS) Global Visualization Viewer (Glovis) page. Landsat 7 (ETM+) and Landsat 8 (OLI) for 1999 and 2019 were used. The images which have a spatial resolution of 30 m were further classified and analyzed in ArcMap in order to measure LULC changes. The multi-temporal scenes were classified using the unsupervised image classification method. Since we are interested in changes in the developed landcover, images were classified into three classes: water, vegetation, and developed. Table 1 presents the land cover types of explanation.

Change Detection Analysis

For assessing the LULC changes from 1999 to 2019, we performed a two-step analysis of the raster maps. First, a raster multiplication was performed on the LULC maps of 1999 and 2019; and then a raster addition was conducted between the raster multiplication output and the 2019 map. The resulting map from the above calculations quantitatively depicts the changes for the different land covers from 1999 to 2019. Equations (1) and (2) explain the above process mathematically.

$$Y_t = Y_{t1} * Y_{t2} \tag{1}$$

$$\mathrm{CD} = Y_t + Y_{t2} \tag{2}$$

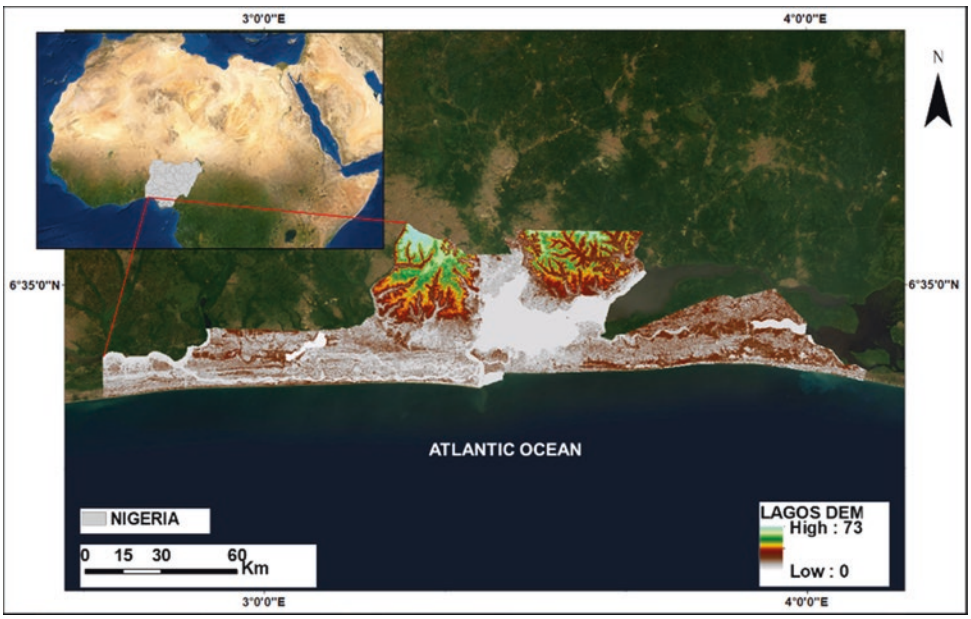

Fig. 1 Location of Lagos State, Nigeria

Table 1 Description of land covers of interest used for the LULC classification

Land cover	Description
Water	Rivers, lagoon, streams, and swamps
Undeveloped	Areas with vegetation, cropland, or areas of agriculture, wetlands, and bare ground (areas stripped of vegetation)
Developed	The built-up area showing buildings, roads, and other human-made structures. Residential, commercial, and industrial areas

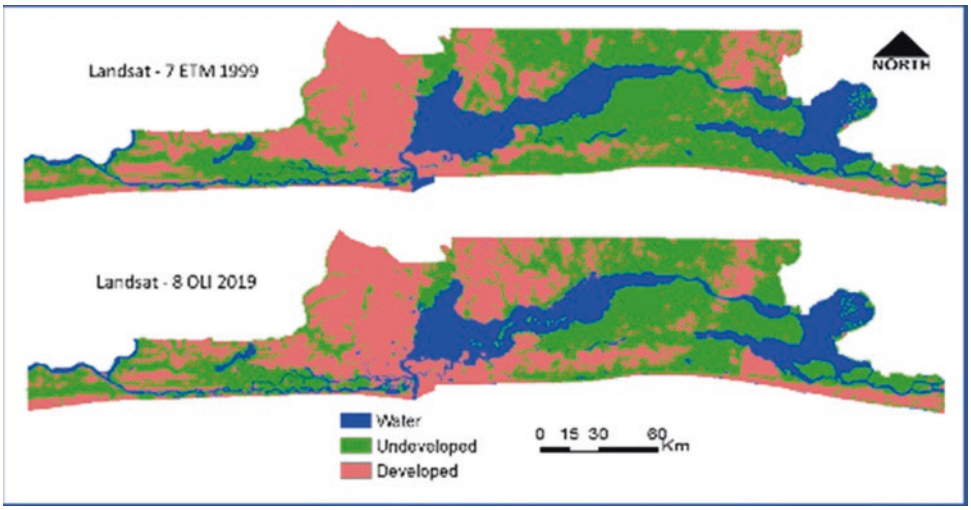

Fig. 2 LULC classes for 1999 and 2019

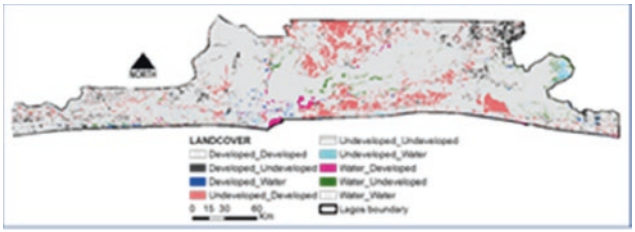

Fig. 3 LULC change detection map

Table 2 Land cover changes in the area and percentage changes

Land-cover types	Area (km^2)		
	1999-Landsat 7	2019-Landsat 8	Percentage change (%)
Water	757	737	− 2.7
Undeveloped	1633	1455	− 11
Developed	1229	1427	16.1

where Y_{t1} is the LULC map for the previous year, Y_{t2} is the LULC for the subsequent year, Y_t is the product of the LULC images, and CD is the detected change.

The map matrix result (Fig. 3) uses Eqs. (1) and (2), where values depict changes for different land covers over time. This analysis quantifies how much change a land cover has undergone between the time steps and for assessing the transformation of one land cover type to another.

For accuracy assessment, the classified images are compared with images from Google Earth and actual ground reference points. These were used to generate error matrixes, which is a table comparing land cover classes found in the validation data to those in the classified images at a given location.

3 Results

Two multi-temporal LULC maps were produced (Fig. 2). Water and undeveloped land covers experienced an estimated 3% and 11% reduction in their total area, respectively (Table 2). However, developed land cover experienced a 16% growth (Table 2).

The outcome of the land cover change detection analysis, calculated using Eqs. (1) and (2) shows approximate changes each land cover experienced between 1999 and 2019. Furthermore, the method allows the quantitative examination and estimation of how land cover types have changed over the years (Figs. 3 and 4). For instance, the area of water that turned into developed land approximately corresponds to the validation data.

Figure 5a is a validation of the flood hazard map using the point location of past flood events from the year 1968 to 2019. Five percent of locations have values corresponding to low flood hazard areas; 80% have values corresponding

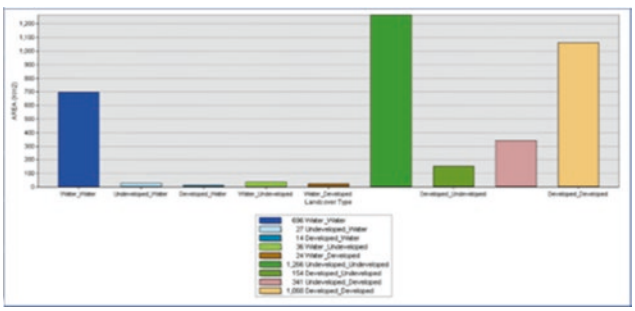

Fig. 4 LULC change detection graph

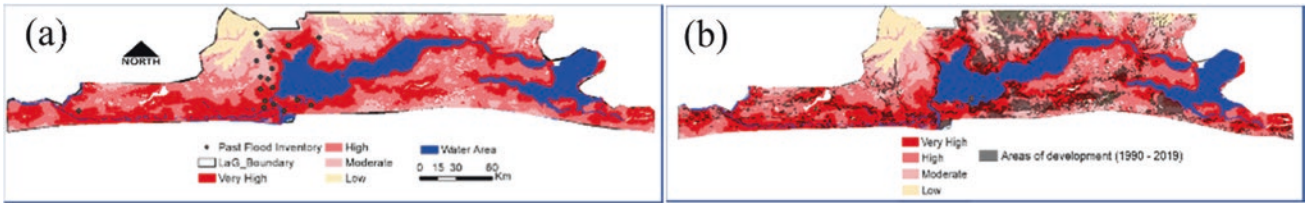

Fig. 5 **a** Displays the flood hazard map with areas of very high to low hazard and location of past flood events; **b** is an overlay of areas of development between 1999 and 2019 on the flood hazard map

to very high to high flood hazard areas, while 15% of locations have values corresponding to moderate flood hazard areas. The past flood inventory points show some agreement with our flood hazard map. Since part of our analysis is linking urbanization to the ongoing flooding in Lagos State, the LULC map of developed areas from 1999 to 2019 is overlaid onto the flood hazard map to aid visual interpretation. The LULC raster map is also converted to points and extracted values of the flood hazard map to each of the locations. The result in Fig. 5b reveals that approximately 90% of the points correspond to very high to moderate flood hazard areas, which may indicate urban development in areas prone to flooding.

4 Conclusions

The method of change detection presented in this study using the map matrix approach proves helpful in estimating changes in land cover in the study area. Furthermore, this study has shown that urbanization has been happening in areas of very high to moderately high hazard zones over the years. However, in recent times, exceptionally high flood hazard areas seem to be experiencing more flooding than other areas. This phenomenon could be a result of their very close proximity to wetlands, floodplains, and lagoons. Additionally, the study shows that urban development into areas close to water bodies and wetlands could be one of the causes of ongoing flooding in Lagos State.

Lagos State is already a megacity, and most developments are already in flood hazard zones. Therefore, stakeholders such as individuals and corporate entities need to be aware of the flood risk and plan accordingly regarding asset insurance, as is the case in developed countries. Furthermore, structural and non-structural flood mitigation measures can be implemented for existing and new developments.

References

Adelekan, I. O. (2010). Vulnerability of poor urban coastal communities to flooding in Lagos, Nigeria. *Environment and Urbanization, 22*, 433–450. https://doi.org/10.1177/0956247810380141

Adeloye, A., & Rustum, R. (2011). Lagos (Nigeria) flooding and influence of urban planning. *Proceedings of the Institution of Civil Engineers- Urban Design and Planning, 164*(3), 175–187. https://doi.org/10.1680/udap.1000014

Ajin, R. S., Krishnamurthy, R. R., Jayaprakash, M., & Vinod, P. G. (2013). Flood hazard assessment of Vamanapuram River Basin, Kerala, India: An approach using Remote Sensing & GIS techniques. *Advances in Applied Science Research, 4*(3), 263–274.

Bishaw, K. (2012). Application of GIS and remote sensing techniques for flood hazard and risk assessment: The case of Dugeda Bora Woreda of Oromiya Regional State, Ethiopia. In *Conference on the Human Dimensions of Global Environmental Change*. Berlin, Germany.

Emmanuel, U. A., Baywood, C. N., Gift, U. A., & OJinnaka, O. C. (2015, May). Flood hazard analysis and damage assessment of 2012 flood in Anambra state using GIS and remote sensing approach. In *FIG working week 2015 from the wisdom of the ages to the challenges of the modern world*. Sofia, Bulgaria.

Idowu, D., & Zhou, W. (2019). Performance evaluation of a potential component of an early flood warning system—A case study of the 2012 flood, lower Niger River Basin, Nigeria. *Remote Sensing, 11*, 1970. https://doi.org/10.3390/rs11171970

Idowu, D., & Zhou, W. (2021). Spatiotemporal evaluation of flood potential indices for watershed flood prediction in the mississippi river basin, USA. *Environmental & Engineering Geoscience, 27*(3): 319–330. https://doi.org/10.2113/EEG-D-20-00056

Idowu, D. (2021). *Assessing the utilization of remote sensing and GIS techniques for flood studies and land use/land cover analysis through case studies in nigeria and the USA*. Colorado School of Mines.

Nkwunonwo, U. C., Whitworth, M., & Baily, B. (2016). Review article: A review and critical analysis of the efforts towards urban flood risk management in the Lagos region of Nigeria. *Natural Hazards and Earth Systems Sciences, 16*, 349–369. https://doi.org/10.5194/nhess-16-349-2016

Ozkan, S. P., & Tarhan, C. (2016). Detection of flood hazard in urban areas using GIS: Izmir case. *Procedia Technology, 2016*(22), 373–381.

Rincón, D., Khan, U., & Armenakis, C. (2018). Flood risk mapping using GIS and multi-criteria analysis: A greater Toronto area case study. *Geosciences, 2018*(8), 275.

Zhou, W. (2021). GIS for earth sciences. In D. Alderton & S. A. Elias (Eds.), *Encyclopedia of geology* (2nd edn., Vol. 6, pp. 281–293). Academic Press.

Robust Face Verification Using Deep Learning in Uncontrolled Environment

Hana Ben Fredj, Rim Ghozzi and Chokri Souani

Abstract

Face recognition in an unconstrained environment has progressively become prevalent in various applications, such as intelligent visual surveillance and identity verification. Recently, convolutional neural networks (CNNs) have been widely used in the field of face recognition. One of the basic elements for the success of deep learning methods is the accessibility of a huge amount of data. In fact, CNNs were able to learn robust face embedding from training data on several subjects. In this paper, we propose a CNN framework to learn faces in an uncontrolled environment based on data augmentation. We use different data augmentation methods such as flipping, noisy, and occluded faces, which use significant variations in facial appearance. The experimental results on the LFW (Labeled Faces in the Wild) dataset demonstrate the effectiveness of the suggested approach in wild face verification tasks with an accuracy of 99.3%. Thus, the accuracy increases by 4.8%, compared to the model without data augmentation. In fact, compared to existing face recognition systems, the proposed model attains important results in face recognition tasks.

Keywords

Deep learning · Convolutional neural networks · Face recognition · CNN · Data augmentation

1 Introduction

Face recognition has become one of the most active research topics in the field of computer vision. It is also useful in various applications such as human–machine interactions, virtual reality, indexing, and multimedia. Recently, CNNs have been very effective in several classification systems, in particular face recognition (Li & Deng, 2020; Lv et al., 2016; Munasinghe et al., 2018; Schroff et al., 2015; Wang et al., 2019; Wen et al., 2018; Zhang et al., 2018).

Learning based on convolutional neural networks (CNNs) is well-developed in the applications of face recognition. Among the architectures which have attained excellent results in face recognition, we have Facenet (Schroff et al., 2015), DeepFace (Taigman et al., 2014), and ArcFace (Deng et al., 2019). Also, many efforts are made on addressing face recognition problems in an uncontrolled environment and real-world scenarios caused by lighting conditions, different poses, expressions, occlusion, and so on (Yang et al., 2019).

Despite all the progress made in the field of face recognition, the systems are often limited by changes in the environment, such as lighting changes, as well as by face-specific variations, such as facial expressions. This variability has made the automation of facial recognition a highly complex task. Among the solutions, we have the data augmentation (DA) method that allows us to work in more difficult environments and complex situations such as noisy and occluded faces.

H. B. Fredj (✉) · R. Ghozzi · C. Souani
Laboratoire de Microélectronique et Instrumentation, Faculté des Sciences de Monastir, Université de Monastir, 5000 Monastir, Tunisia
e-mail: ben.fredj.hanaa@gmail.com

R. Ghozzi
Ecole Nationale d'Ingénieurs de Sousse, Université de Sousse, 4023 Sousse, Tunisia

C. Souani
Institut Supérieur des Sciences Appliquées et de Technologie de Sousse, Université de Sousse, 4003 Sousse, Tunisia

Z. A. Ergüler et al. (eds.), *Selected Studies in Geotechnics, Geo-Informatics and Remote Sensing*, Advances in Science, Technology & Innovation, https://doi.org/10.1007/978-3-031-43759-5_27

Fig. 1 Example of face image alignment using MTCNN method

Fig. 2 Examples images from CASIA-WebFace and LFW datasets

In this work, our goal is to improve the performance of our deep learning-based network by increasing the number of training images and increasing the variance of the presentation of the main features. The training data space should contain a large number of different examples in an uncontrolled environment. Thus, we collected a wide variety of training images using different data augmentation methods. This allows improving the learning scope of our model and predicting new data. According to the results of the experimental analysis, our model performs well in the LFW (Labeled Faces in the Wild) dataset.

The rest of this paper is organized as follows. Section 2 describes the architecture network and details implementations. The experimental results are described in Sect. 3. Section 4 concludes this paper.

2 Network Architecture and Details Implementation

Many of CNNs' architectures are developed for face verification in the literature. In this work, we chose a typical network named Inception v2 (Ioffe & Szegedy, 2015) which recorded very important performances. Inception v2 is a deeper CNN architecture which is a commonly used image recognition model.

Preprocessing. We use MTCNN (Zhang et al., 2016)-based framework for joint face detection and alignment. The proposed method consists of three stages. In the first stage, it produces candidate windows quickly through a shallow CNN. After that, it refines the windows to reject a large number of non-faces windows through a more complex CNN. Finally, it utilizes a more powerful CNN to refine the result and to output facial landmarks positions. Figure 1 presents an example of the face image alignment from using this method.

Training. We use a large training dataset CASIA-WebFace to improve face recognition in an unconstrained environment during training. We train the framework with Root Mean Square Propagation (RMSProp) optimizer. Furthermore, to control a loss function regulation, we utilize the weight decay parameter, which is fixed to $5e^{-4}$ for both fully connected and convolutional layers. Also, we apply the momentum parameter to 0.9, and we adapt the model using a dropout function.

Testing. For testing, we determined the similarity score with the cosine distance. The results are performed on the LFW (Labeled Faces in the Wild) dataset following the standard protocol of restricted, labeled outside data.

3 Results

This section describes the details of the datasets and the experimental results of our work. Our model is trained on the GPU GeForce GTX 1080 Ti using the open-source deep learning framework, Tensorflow.

Datasets

To verify the effectiveness of our face verification model, we used typical and famous datasets, CASIA-WebFace, and the labeled faces in the wild (LFW) datasets.

CASIA-WebFace: CASIA-WebFace is a typical dataset of unconstrained face recognition that contains a variety of celebrity images. It contains 453,453 images of more than 10,575 identities.

LFW: It is a public benchmark for face verification, containing 13,233 images of 5749 people. This dataset contains different images of faces in an uncontrolled environment with face variations, such as illuminations, expressions, and occlusions.

Figure 2 presents the images from CASIA-WebFace and LFW datasets.

Fig. 3 Examples of different data augmentation methods. **a** Original image, **b** flipping, **c** blurring, **d** noise, **e** occlusion

Table 1 Classification accuracy (%) on LFW dataset

Method	Accuracy (%)
Model_1	94.5 ± 0.005
Model_2	99.3 ± 0.004

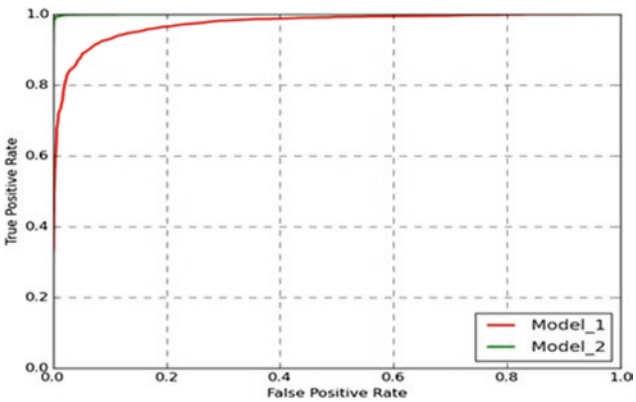

Fig. 4 Influence of a combination of different data augmentation methods on LFW dataset. Model_1: without data augmentation, Method_2: with data augmentation

Table 2 Performance comparison on LFW dataset accuracy (%)

Method	Accuracy (%)
Light CNN 9 (Wu et al., 2018)	98.37
Joint-Res (Zhang et al., 2018)	93.12 ± 0.43
DeepID2+ (Sun et al., 2015)	93.20 ± 0.2
VGG (Chatfeld et al., 2014)	97.30
Facenet (Schroff et al., 2015)	96.63 ± 0.16
Our model	99.3 ± 0.004

3.1 Data Augmentation

Having a large number of training images is often a prerequisite for a successful deep learning model. So, we apply appropriate data augmentation techniques to present the model with as many variations as possible of the main features. This allows the deep learning model to achieve significant performance. In this section, we present the different data augmentation methods used in our work; blurring, noise, flipping, occlusion, etc. Some examples are presented in Fig. 3. We mixed the different methods and we trained our network.

3.2 Performances on LFW Dataset

To further demonstrate the effectiveness of our model, we conduct the experiments on the LFW dataset. First, we train the network without data augmentation (model_1). Then, we retrain the network using the augmented dataset CASIA-WebFace with the different augmentation data methods (model_2) and we test the models on the LFW dataset. The results are provided in Table 1. We can observe that when the model is trained with data augmentation, the accuracy on LFW increases by 4.8%, compared to without data augmentation. Figure 4 also shows the ROC curves for each method tested on the LFW dataset. As shown, the training model without DA fails to achieve good results (red curve). The suggested method (green curve) attains better performance. Thereafter, these results demonstrate the importance of the different methods of data augmentation during classification on the LFW dataset.

Table 2 presents a comparison with the most recent state-of-the-art on the LFW dataset. Our model attains 99.3 ± 0.004% accuracy. As shown, the results of our proposed method surpass the performance of Light CNN 9 (Wu et al., 2018), Joint-Res (Zhang et al., 2018), DeepID2+ (Sun et al., 2015), and VGG (Chatfeld et al., 2014). However, Facenet achieved a very good result (99.63 ± 0.16%) considering the huge dataset used during the training which contains almost 200 million photographs of eight million persons. Moreover, this method uses a very efficient technique called the triplet loss function which has a clearly important capability during classification.

4 Conclusion

In this paper, we propose an effective CNN framework to improve face verification. Indeed, we implement the Inception v2 network which is a deeper CNN architecture and is commonly used in image recognition models. During training, we use different methods of data augmentation, including flipping, blurring, and occluded faces, which significantly enlarge the training set. The data augmentation techniques allow learning faces samples in an uncontrolled environment with different and difficult situations. We achieve significant performance on the LFW dataset with an accuracy of 99.3%. The results demonstrate the effectiveness of our method compared with other state-of-the-art methods.

References

Chatfeld, K., Simonyan, K., Vedaldi, A., & Zisserman, A. (2014). *Return of the devil in the details: Delving deep into convolutional nets*. arXiv:1405.3531

Deng, J., Guo, J., Xue, N., & Zafeiriou, S. (2019). Arcface: Additive angular margin loss for deep face recognition. In *Proceedings of the IEEE Conference on Computer Vision and Pattern Recognition* (pp. 4690–4699).

Ioffe, S., & Szegedy, C. (2015). *Batch normalization: Accelerating deep network training by reducing internal covariate shift*. arXiv preprint arXiv:1502.03167

Li, S., & Deng, W. (2020). Deep facial expression recognition: A survey. *IEEE Transactions on Affective Computing*.

Lv, J. J., Cheng, C., Tian, G. D., Zhou, X. D., & Zhou, X. (2016). Landmark perturbation-based data augmentation for unconstrained face recognition. *Signal Processing: Image Communication, 47*, 465–475.

Munasinghe, S., Fookes, C., & Sridharan, S. (2018). Human-level face verification with intra-personal factor analysis and deep face representation. *IET Biometrics, 7*(5), 467–473.

Schroff, F., Kalenichenko, D., & Philbin, J. (2015). Facenet: A unified embedding for face recognition and clustering. In *Proceedings of the IEEE Conference on Computer Vision and Pattern Recognition* (pp. 815–823).

Sun, Y., Wang, X., & Tang, X.: Deeply learned face representations are sparse, selective, and robust. In *IEEE Conference on Computer Vision and Pattern Recognition* (pp. 2892–2900). Boston, MA, USA.

Taigman, Y., Yang, M., Ranzato, M. A., & Wolf, L. (2014). Deepface: Closing the gap to human-level performance in face verification. In *Proceedings of the IEEE Conference on Computer Vision and Pattern Recognition* (pp. 1701–1708).

Wang, P., Su, F., Zhao, Z., Guo, Y., Zhao, Y., & Zhuang, B. (2019). Deep class-skewed learning for face recognition. *Neurocomputing, 363*, 35–45.

Wen, G., Chen, H., Cai, D., & He, X. (2018). Improving face recognition with domain adaptation. *Neurocomputing, 287*, 45–51.

Wu, X., He, R., Sun, Z., & Tan, T. (2018). A light CNN for deep face representation with noisy labels. *IEEE Transactions on Information Forensics and Security, 13*(11), 2884–2896.

Yang, M., Huang, F., & Lv, X. (2019). A feature learning approach for face recognition with robustness to noisy label based on top-*N* prediction. *Neurocomputing, 330*, 48–55.

Zhang, K., Zhang, Z., Li, Z., & Qiao, Y. (2016). Joint face detection and alignment using multitask cascaded convolutional networks. *IEEE Signal Processing Letters, 23*(10), 1499–1503.

Zhang, Y., Shang, K., Wang, J., Li, N., & Zhang, M. M. (2018). Patch strategy for deep face recognition. *IET Image Processing, 12*(5), 819–825.

Evaluation of Combined Intelligent and Box Jenkins Models for NDVI Temporal Profiles Forecasting via Classical and Temporally Varying Weights

Oumayma Bounouh, Ana Maria Tarquis, Houcine Essid and Imed Riadh Farah

Abstract

Remote sensing platforms provide timely and objective data from local to global coverage. These sensors allow the tracking of several biophysical parameters of plants without direct contact. For this reason, various applications in the benefits of vegetation cover have been addressed such as crop monitoring, plant health forecasting, and drought forecasting. Meanwhile, several forecasting models are proposed by the scientific community in various fields. Indeed, some researchers are satisfied by employing well-known models such as Box Jenkins and Neural network models. On the other hand, others are proposing innovative tools based on enhancing the previously mentioned ones. However, few researchers claim that the multi-models approach remains an effective way to have more accurate and more reliable forecasting results. Herein, we evaluate various multi-models approaches to forecast the NDVI time series of Northwestern Tunisian forest cover derived from MOD13Q1 images. These approaches are employed in two ways: fixed weights based on overall measures and temporally varying weights over the seasons. Interestingly, to enhance the forecasting results, the combination of both models has to well-suit the statistical properties of the NDVI profiles. The classical used combination models generated lower performance than the individual model, e.g., RMSE of 0.052 for the neural network versus 0.056 for the fixed RMSE weights. However, the combination models with temporally varying weights lead to better accuracies than all the used models, especially 0.027 obtained by the seasonally normal weights.

Keywords

NDVI time series · Forecasting · Combination models · Neural networks · Box Jenkins · Weights

1 Introduction

Vegetation land cover is crucial for ecosystem sustainability (biodiversity, carbon cycles, food security, and socio-economic impacts). Therefore, scientists try consistently to raise the conscience about its importance. Meanwhile, remote sensing platforms provide timely and objective data from local to global coverage. These sensors allow the tracking of several biophysical parameters of plants without direct contact. Satellite constellations (e.g., NOAA, TERRA, etc.) provide long-term records of vegetation indices (Jong et al., 2013) such as the normalized difference vegetation index (NDVI) which reflects the vegetation greenness through pursuing the photosynthetic activity (Tomasella et al., 2018). For this reason, various applications in the benefits of vegetation cover have been addressed such as crop monitoring, plant health forecasting, drought forecasting, among others.

Several forecasting models are proposed by the scientific community in various fields. Indeed, some researchers are satisfied by employing well-known models such as Box Jenkins (Tian et al., 2016) and neural network models (Fieuzal et al., 2017). On the other hand, others are proposing innovative tools based on enhancing the previously mentioned ones (Huang et al., 2017). However, few others claim that the multi-models approach remains an effective

O. Bounouh (✉) · H. Essid · I. R. Farah
Laboratoire RIADI, Ecole Nationale des Sciences de l'Informatique, 2010 La Manouba, Tunisia
e-mail: oumayma.bounouh@ensi-uma.tn

A. M. Tarquis
CEIGRAM, ETSI Agrónomos, Universidad Politécnica de Madrid (UPM), Madrid, Spain

I. R. Farah
Laboratoire ITI Department, IMT Atlantique, 29238 Brest, Iroise, France

Z. A. Ergüler et al. (eds.), *Selected Studies in Geotechnics, Geo-Informatics and Remote Sensing*, Advances in Science, Technology & Innovation, https://doi.org/10.1007/978-3-031-43759-5_28

way to have more accurate and more reliable forecasting results (Atiya, 2020).

Herein, we propose the assessment of two different forecasting models for the NDVI time series (SARIMA statistical model and NAR artificial intelligent model) over a forest cover in Northwestern Tunisia. Furthermore, we investigate the accuracy of combining them using classical fixed weights and seasonally varying weights.

2 Study Area and Methods

2.1 Data and Study Area

An NDVI series of 18 years and their data quality series are extracted from bi-monthly MOD13Q1 images. This time series belongs to the north-western part of Tunisia, an African country. They describe a forest area named Lahirech in the Jendouba region. This forest is composed of mixed trees. The area is characterized by a dry-summer Mediterranean climate.

2.2 Methods

The adopted methodology is divided into three parts. The first one aims to preprocess the NDVI time series using data quality layers and the Savitsky Golay filter to minimize noise. The second step is the forecasting of one-year-ahead variations using two different models: the Seasonal AutoRegressive Integrated Moving Average (SARIMA) model and the Nonlinear AutoRegressive neural networks (NAR) model.

Afterward, the forecasted time series are decomposed into seasons (Fig. 2) for each of which the specific distances are calculated before determining the corresponding weights.

Several combination methods are tested through two visions: fixed weights and seasonally varying weights. One of these tools tests combining weight based on normal distribution fitted over the whole season versus varying weights through normal distribution fitted for each season (see Figs. 1 and 2).

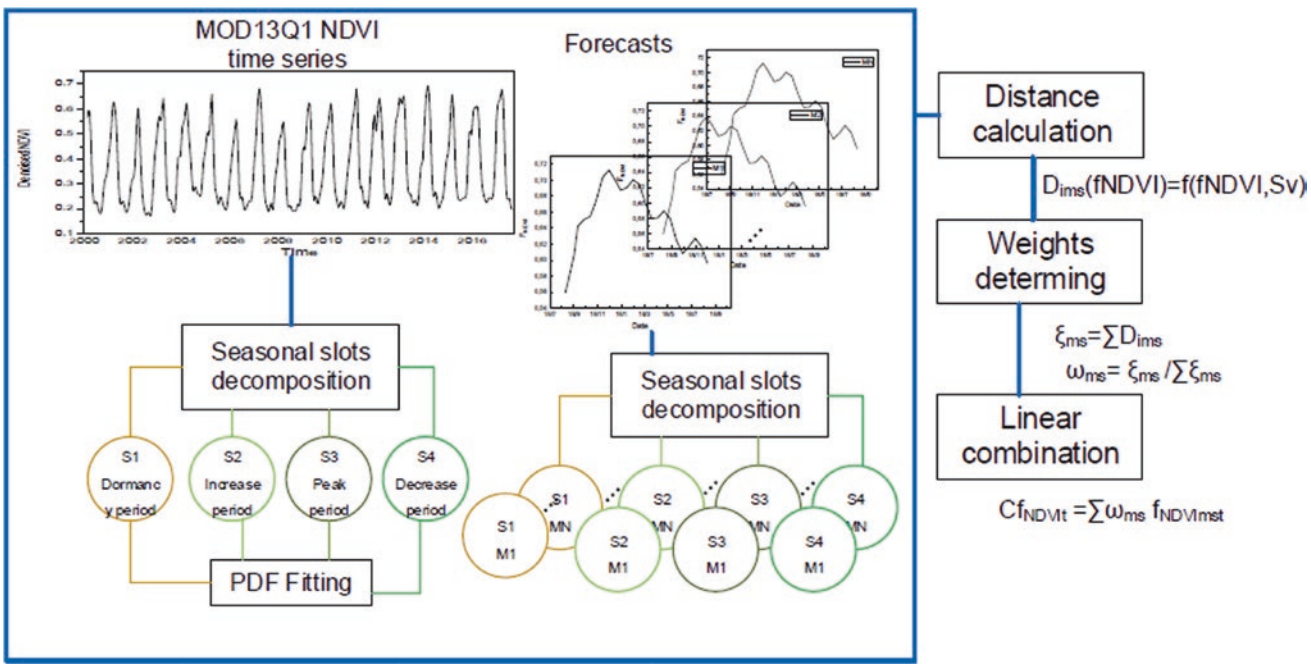

Fig. 1 Combination methodology based on normal distribution fitting

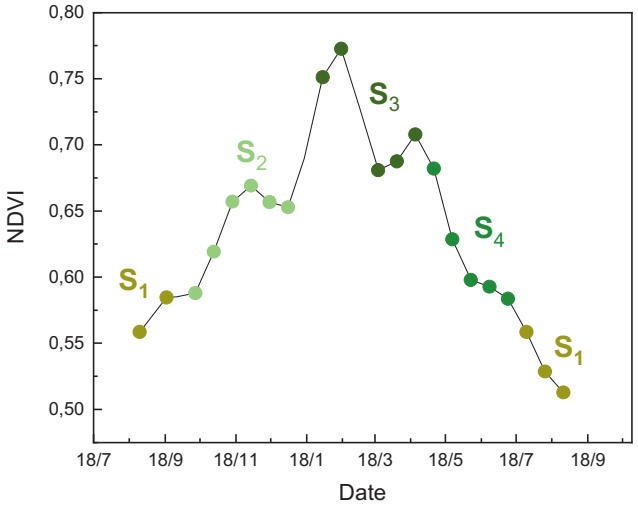

Fig. 2 Seasonal observations

3 Results

Firstly, the parameters of both forecasting models are determined: SARIMA (2, 0, 0) (0, 1, 0) 23+m using auto.arima R package and NAR (4, 23) after multiple tests. Afterward, we determined the combination weights (see example Table 1). Finally, the root mean square error (RMSE) value is calculated for each forecasting model (see Table 2).

Table 1 Seasonally normal weights

	S1	S2	S3	S4
SARIMA	0.53	0.52	0.71	0.48
NAR	0.46	0.47	0.28	0.51

As presented in Table 2, combined models based on fixed weights fail to compete with individual models, in particular the NAR model. However, seasonally varying weights outperform both fixed weights and individual models, particularly the Tnormal method where we tried to fit a normal distribution for each season apart.

4 Discussion and Conclusions

Despite the superiority of intelligent models over statistical models, recent studies still choose the Box Jenkins model with satisfactory results. The black-box nature of neural networks is still questionable. Therefore, some researchers claim that it is better to combine linear and nonlinear models.

Based on Table 1, the performance of both the SARIMA model and the NAR model is temporally varying. This is due to the variability of the statistical properties of the NDVI time series through the seasons. This may explain the good performance of the temporally varying weights and, especially, the Tnormal model. This study proves that the good forecasting model is the one that fits onto the data singularities.

To evaluate the combining methods of forecasts, we tested a few ones over the NDVI time series derived from MODIS data that describe forest areas in Tunisia. As future work, we aim to adopt the evidence theory for the combination step. Furthermore, based on earlier work where we proved that the probability density function (PDF) may be not normal, we study the use of different PDFs for the mass calculation.

Table 2 Accuracy assessment of forecasting models

	SARIMA	NAR	Average	RMSE	sMAPE	Normal	Trmse	Tsmape	Tnormal
RMSE	0.068	0.052	0.054	0.056	0.056	0.055	0.046	0.045	0.031

References

Atiya, A. F. (2020). Why does forecast combination work so well? *International Journal of Forecasting, 36*(1), 197–200.

de Jong, R., Verbesselt, J., Zeileis, A., et al. (2013). Shifts in global vegetation activity trends. *Remote Sensing, 5*(3), 1117–1133.

Fieuzal, R., Sicre, C. M., & Baup, F. (2017). Estimation of corn yield using multi-temporal optical and radar satellite data and artificial neural networks. *International Journal of Applied Earth Observation and Geoinformation, 57*, 14–23.

Huang, S., Ming, B., Huang, Q., Leng, G., & Hou, B. (2017). A case study on a combination NDVI forecasting model based on the entropy weight method. *Water Resources Management, 31*(11), 3667–3681.

Tian, M., Wang, P., & Khan, J. (2016). Drought forecasting with vegetation temperature condition index using ARIMA models in the Guanzhong plain. *Remote Sensing, 8*(9), 690.

Tomasella, J., Vieira, R. M. S. P., Barbosa, A. A., Rodriguez, D. A., de Oliveira Santana, M., & Sestini, M. F. (2018). Desertification trends in the Northeast of Brazil over the period 2000–2016. *International Journal of Applied Earth Observation and Geoinformation, 73*, 197–206.

A Multi-layered Convolutional Neural Network for Soil Variables Estimation with the Combination of Open Access Data

Konstantinos Karyotis, Nikolaos Tziolas, Nikolaos Tsakiridis, Periklis Chatzimisios, Charalambos Kontoes and George Zalidis

Abstract

Soil properties assessment through space-borne derived imagery has attracted vast research interest over the last decades. Predictions become more accurate as spectral sensing technology is evolving and available operational sensors are steadily increasing. Evidently, the combination of products derived from different space missions can produce a significant amount of information that can be used to assess the soils' health. However, heterogeneous imagery fusion comprises many limitations regarding sensor specifications or satellites' orbits; thus, many parts of it remain unexplored. To that end, Deep Learning can be employed for the derivation of robust modeling. The overarching objective of this effort is to propose a multi-input model, based on open access Earth Observation data from various sources for the prediction of clay content. Hence, two iterations of Convolutional Neural Network (CNN) modeling were performed. The first iteration was trained over a composition of the optical and radar data of Sentinel-1 and Sentinel-2. On a second phase, the CNN was trained over an extension of this dataset with fused topsoil data from the SoilGrids map collection and topographical parameters containing Digital Elevation Model mined from the Google Earth Engine. The well-distributed and representative dataset of the GEO-CRADLE initiative was used as an independent set, over which the CNN performed its estimations. The latter iteration demonstrated improvement in overall accuracy compared to the R^2 using the optical and radar composite. The proposed methodology, which is based on the utilization of open access data, can support the creation of various spatial explicit soil indicators in areas with well-reported gaps in soil data and support soil mapping initiatives on a national scale.

Keywords

Earth observation · Deep learning · Machine learning · Open access data · CNN · Vis–NIR · VNIR–SWIR · Google earth engine

1 Introduction

Soil is the most important carbon sink after oceans, playing a crucial role in decelerating climate change (Paustian et al., 2016) and an essential component of the planet's biodiversity. Its functionality is dependent on a variety of organisms that are part of the soil, constituting it a complex system. Overpopulation strongly affects soil resources' sustainability, stimulating awareness for their finiteness (Hartemink & McBratney, 2008) leading to strong concerns about Earth's carrying capacity and soil viability through human exploitation. Moreover, the Mediterranean countries are frequently exposed to the whole mosaic of natural disasters like floods and erosion that affect agricultural resources. They also face the first signs of climate change like droughts and extreme events that are expected to amplify in the forthcoming decades. There is an increasing global concern about soil conservation according to (Hartemink & McBratney, 2008) that

K. Karyotis (✉) · P. Chatzimisios
Department of Science and Technology, International Hellenic University, Thessaloniki, Greece
e-mail: kbkaryotis@gmail.com

N. Tziolas · G. Zalidis
Faculty of Agriculture, Forestry, and Natural Environment, School of Agriculture, Aristotle University of Thessaloniki, 54123 Thessaloniki, Greece

N. Tsakiridis
Automation and Robotics Lab, Department of Electrical Engineering and Computer Science, Faculty of Engineering, Aristotle University of Thessaloniki, Thessaloniki, Greece

C. Kontoes
National Observatory of Athens (NOA), Institute for Astronomy, Astrophysics, Space Applications and Remote Sensing (IAASARS), Athens, Greece

Z. A. Ergüler et al. (eds.), *Selected Studies in Geotechnics, Geo-Informatics and Remote Sensing*, Advances in Science, Technology & Innovation, https://doi.org/10.1007/978-3-031-43759-5_29

brings soils back to the global agenda. This rising concern has led to the introduction of a constantly expanding set of regulations about soil preservation and restoration around the world regarding the constant soil degradation and decrease of organic carbon and clay in topsoils (Ramesh et al., 2019). These ranges from European policies, such as the European Green Deal and the Common Agricultural Policy (CAP), to international policies like the United Nations' Sendai Framework for Disaster Risk Reduction 2015–2030 or the Paris Agreement that have been set to mitigate climate change, adapt to its effects, and set the roadmap for a harmonized global effort (Montanarella & Panagos, 2021).

Unfortunately, high-resolution soil property maps are critically low and where improved management options could be most effective are scarce. Recent soil property maps at regional to global scale consist of rather coarse grid cells and are based on legacy data that are generally not up-to-date. This leads to different approaches per country or region in search of an effective and efficient approach.

On top of these frameworks, the Copernicus program, serving as a data and services broker, supports the efforts made by launching an Open Access Hub for providing free and open access information to increase the knowledge related to land management, monitoring, and reporting. Among others, the Copernicus Open Access Hub offers high-quality Earth Observation (EO) data through Sentinel-1 and Sentinel-2 constellations. The spatial resolution of Copernicus program products reach even 10 m and are openly available, providing a solid substructure for the development of services for supporting policies for natural resources management (Sitokonstantinou et al., 2018). In the same vein, the Group on Earth Observation (GEO) via the development of the GEOSS portal offers the EO-based community a groundbreaking capacity of exploiting a wealth of heterogeneous collections of databases and other spatial explicit indicators related to soil ecosystem monitoring. These range from simple soil data archives (Hengl et al., 2014) to regional soil spectral libraries (Orgiazzi et al., 2018) as well as portals offering coarse resolution soil thematic products.

The abundance of the offered in situ and space-borne EO data, that are accumulatively handled on the scale of big data, signify the imperativeness of introducing novel methods of modeling data of such magnitude. However, the combination of multispectral data from diverse sources creates prospects for utilizing new analysis techniques that require "big data" to optimize their performance. Together with the vast development of computer science, Deep Learning techniques have recently become an efficient method of spectral data analysis in a variety of disciplines. Various studies have shown that Machine Learning algorithms can be more accurate than traditional statistical methods, especially in complex ecosystems (Guo et al., 2015). The utilization of Machine Learning for the prediction of the evolution of a system is suggested in cases that statistical uncertainty in the dataset exists, there is a large amount of data, especially in real-time sampling and in cases where the main objective is to describe a future scenario of the system, without focusing on a single variable. Up to now, integrated surveys based on tree-based techniques such as Boosted Regression Tree (BRT) or Random Forest (RF) have been conducted (Mouazen et al., 2007) while Convolutional Neural Networks (CNNs) can produce accurate approximations for significantly large datasets (Everingham et al., 2015).

Recently, a novel 1D CNN (Tsakiridis et al., 2020) was applied to all the available physicochemical properties of large spectroscopic databases and was statistically compared with the current state-of-the-art where it was shown to statistically outperform its counterparts, as well as with other CNNs where it exhibited the best performance (Padarian et al., 2019). In addition, several studies demonstrated the successful application of spectral modeling chemometrics techniques to predict soil properties from satellite multispectral imagery data such as Sentinel-2, although the spectral resolution was lower compared to imaging spectroscopy (Gholizadeh et al., 2018), while technical challenges were revealed (Gholizadeh et al., 2020; Tziolas et al., 2020).

This paper introduces a novel methodological framework for soil monitoring, building upon prior knowledge, and open access EO data. The proposed approach is considered the development of a multivariate dataset, containing open access SAR and multispectral optical images, topographical data, and observations from coarse resolution EO products, for the assessment of its modeling capacity with the use of CNNs. This study intends to propose new methods for the capitalization of existing global or regional soil spectral libraries (SSLs) and soil-related datasets and to minimize the need for cost-demanding field campaigns and wet-chemistry analysis.

2 Materials and Methods

The main objective of the elaborated work was to capitalize existing EO data and propose a methodology for the assessment of soil health indices through modeling a multitemporal dataset based on open access data. The overall procedure is shown in Fig. 1 and is elaborated below.

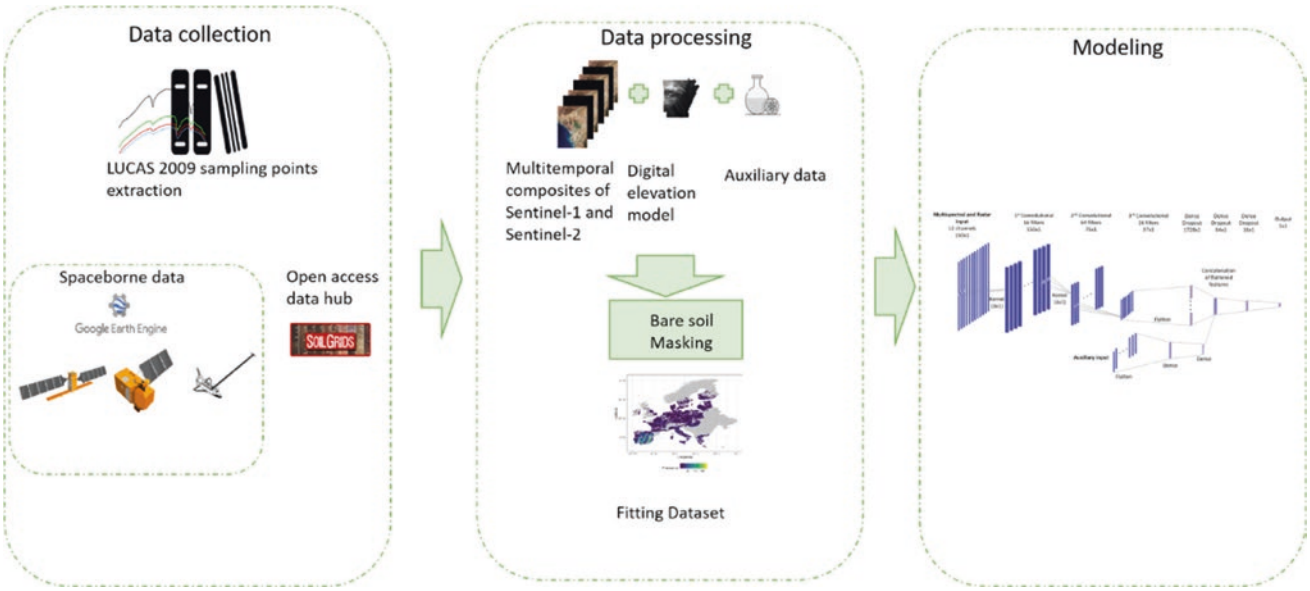

Fig. 1 Methodology sketch: The left-tier contains the data acquisition tier through Google Earth Engine and SoilGrids hub. The mid-tier depicts the fusion of heterogeneous data and the development of the final dataset. The architecture of the Convolutional Neural Network used for modeling is shown in the right-tier

2.1 Earth Observation Data Sources

Sentinel-2 imagery reflectance values have shown great potential in soil attributes assessment (Vaudour et al., 2019), and if combined with complementary Earth Observation measurements, high prediction accuracy can be derived (Tziolas et al., 2020). Along with Sentinel-2 multispectral observations, Sentinel-1 can play an important role in soil monitoring and sustainable soil resources management since radar bands can unobstructedly operate under all weather conditions and amount of available sunlight. Sentinel-1 can also provide valuable information regarding soil structure and moisture which are parameters that can strongly affect Sentinel-2 optical data.

Over the Land Use and Cover Area Frame Survey 2009 (LUCAS 2009) sampling locations, a 5-year-long time-series containing point observations of Sentinel-1 (with spatial resolution of 5 m) and Sentinel-2 (with corresponding spatial resolution ranging from 10 to 60 m) data was shaped, constituted from 822 unique day-stamps and more than 1 million instances. LUCAS 2009 contains topsoil physicochemical properties covering all the territory of the European Union, with stratified sampling points distributed along a 2×2 km orthogonal grid. The above-described data were filtered to retain only images with less than 10% cloud coverage and then masked for bare soil field recognition through NDVI and NBR-2 filtering, with upper boundaries of 0.25 and 0.075, respectively (Demattê et al., 2018). These datasets were conjugated according to the samples' unique IDs and the nearest Sentinel-1 and Sentinel-2 acquisition dates (in terms of absolute distance), with a margin of 1 day. These observations formed the conclusive optical multispectral and radar input, derived from spaceborne data sources, and constitute the dataset used in the first approach.

The above-mentioned dataset was then expanded with auxiliary input containing point observations of topographical and coarse resolution EO products, to form the dataset for the second approach. These products were regarded as time-invariant over the time-series length and are obtained from two sources: Shuttle Radar Topography Mission (SRTM) and International Soil Reference Information Centre (ISRIC) SoilGrids. The SRTM data contain Digital Elevation Model (DEM) point measurements and analyzed in three components (slope, aspect, and altitude) with a spatial resolution of 30 m. It must be noted that both the DEM information and the Sentinel data were mined through the Google Earth Engine (Gorelick et al., 2017). The set of auxiliary variables sourced from SoilGrids is a collection of topsoil physicochemical measurements, namely soil organic carbon, pH, sand, silt, clay, bulk density, and total nitrogen that are provided at a spatial resolution of 250 m.

The well-distributed and representative dataset of the GEO-CRADLE initiative was used as the independent dataset over which the model that was developed performed clay content estimations. GEO-CRADLE's overarching objective was to establish a basic foundation for using SSLs for EO means by establishing an open SSL for North Africa, the Middle East, and the Balkans. The SSL created contains 1754 samples accompanied by spectral

measurements over the VNIR–SWIR region and laboratory analyses concerning their chemical and granulometric composition. The geographical distribution of the soil samples is shown in Fig. 2. Over the set of the GEO-CRADLE sampling points, the analogous to the training dataset was constructed, following the above-mentioned methodology.

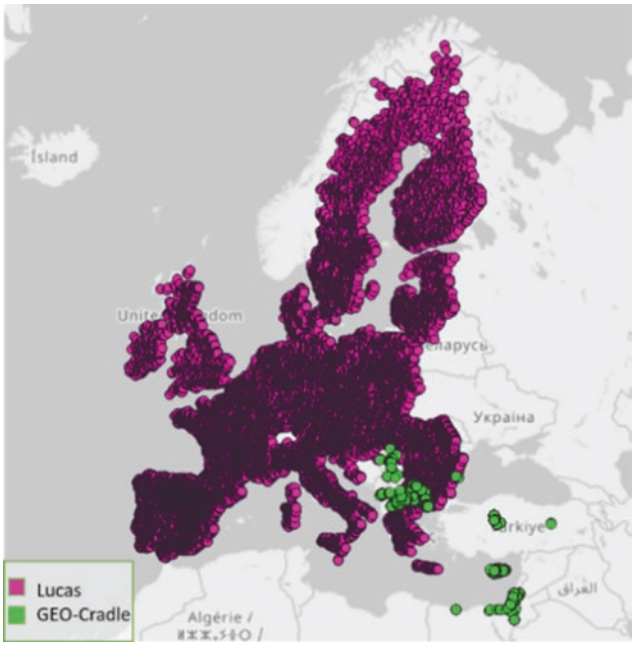

Fig. 2 Spatial distribution of Lucas and GEO-CRADLE sampling locations

2.2 Modeling

A multi-layered CNN was developed (Tziolas et al., 2020). It has as the main input the multispectral and radar datasets that are convolved to produce higher-level features. These are supported through the auxiliary variables that are concatenated with the filtered inputs through a dense layer in order to infer the output.

The aforementioned network, depicted in Fig. 3, was trained over the multi-sourced dataset which is based on open access data formed over the LUCAS sampling positions.

The proposed multi-input CNN combines the aforementioned heterogeneous inputs for the estimation of the topsoil clay fraction. The well-distributed and representative dataset's sampling points were randomly split at a 4 to 1 ratio for the calibration and validation of the CNN. The partition to calibration and validation subsets was performed with the Kennard–Stone algorithm (Kennard & Stone, 1969), to reassure that the calibrating procedure will be conducted over representative samples. The described procedure was performed five consecutive times, without the replacement of Kennard–Stone selected samples. For each iteration, a distinct model was trained, and predictions were made over the independent set. The final outcome of the model was the averaged prediction for each testing instance. Two iterations were performed initially over optical and radar composite responses of Sentinel-1 and Sentinel-2, and on a second phase over the extended dataset containing topsoil

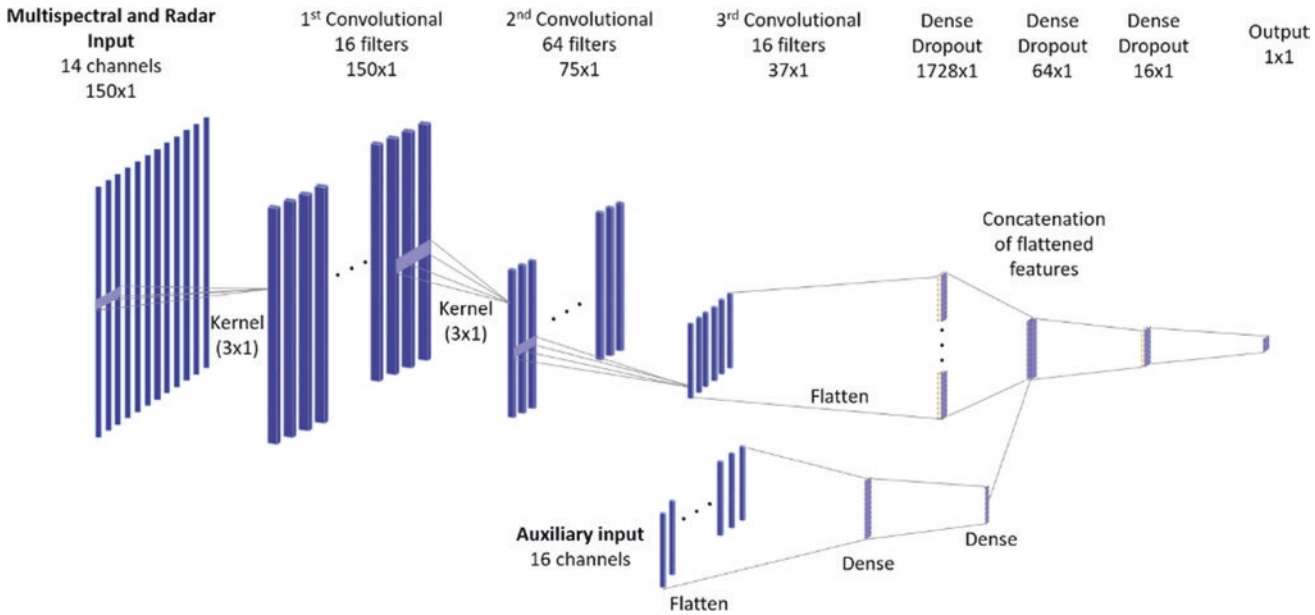

Fig. 3 Architecture of multi-input CNN for clay estimation having as primal input the optical and radar composite and as auxiliary input the SRTM and SoilGrids observations

SoilGrids and topographical covariates. These models were eventually fed with the GEO-CRADLE initiative soil data archive for performing estimations regarding clay content.

The fitted model evaluation was assessed through the calculation of standard measures such as the coefficient of determination, ratio of performance to interquartile distance (Bellon-Maurel et al., 2010), root mean squared error, and ratio of performance to deviation.

3 Results

Two paired iterations of the model fitting were performed, aiming to estimate clay content, under different training dataset selection. The initial iteration's training dataset contained the 5-year time-series containing Sentinel-1 synthetic aperture radar (SAR) measurements and the Sentinel-2 spectral bands. The second iteration's dataset is an expansion to the first, by concatenating topographical parameters containing SRTM's Digital Elevation Model parameters and topsoil SoilGrids measurements. The fitting metrics for the validation dataset of each iteration are presented in Table 1.

A noticeable difference in the accuracy metrics reported in Table 1 may be observed. The value of R^2 which is 80% combined with RPD greater than two signifies very well-fitting of the model to the data, when all available sources of information are used as input for the model. As shown in the scatterplot of Fig. 4, the majority of points are distributed near the main diagonal. It can be concluded that the model's performance is compelling for observations placed in the bottom left region, while it is significantly decreased for higher values of clay content. This is due to the low presence of samples with high clay content inside the training dataset.

The overall estimations for the GEO-CRADLE dataset are depicted in four soil classes as shown in Fig. 5.

The specific GEO-CRADLE sub-area of Greece, which is part of the Eastern Macedonia and Thrace region, extends to soils that are mainly shaped from the Nestos River soil deposits. The area is characterized by light mechanical texture and contains mainly sandy and sandy loam soils with reduced fertility if combined with low soil organic carbon concentration. As shown in Fig. 6, the subarea can be divided into three distinguishable classes. A high concentration of clay can be observed in the southern part, and while moving to the north, one can observe that clay is gradually decreasing.

Table 1 Accuracy metrics for the fitted models over validation dataset

Dataset	Target variable	R^2	RMSE	RPD	RPIQ
Sentinel 1 and 2	Clay	0.55	9.08	1.45	1.86
Sentinel 1 and 2, SRTM's DEM and SoilGrids	Clay	0.80	6.25	2.14	2.73

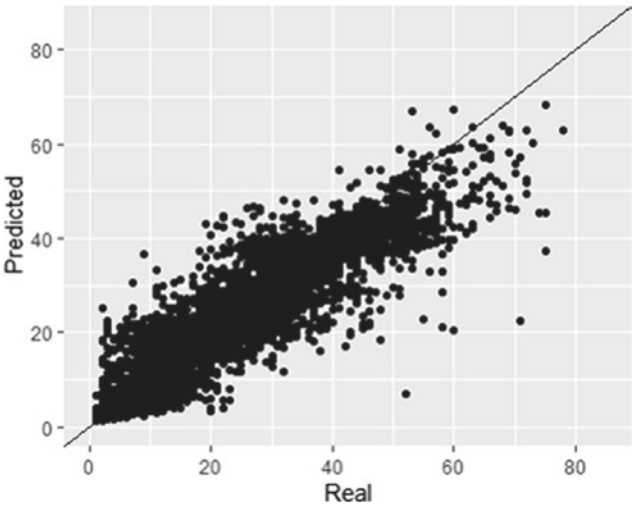

Fig. 4 Scatterplot of fitted (vertical axis) against actual values (horizontal axis)

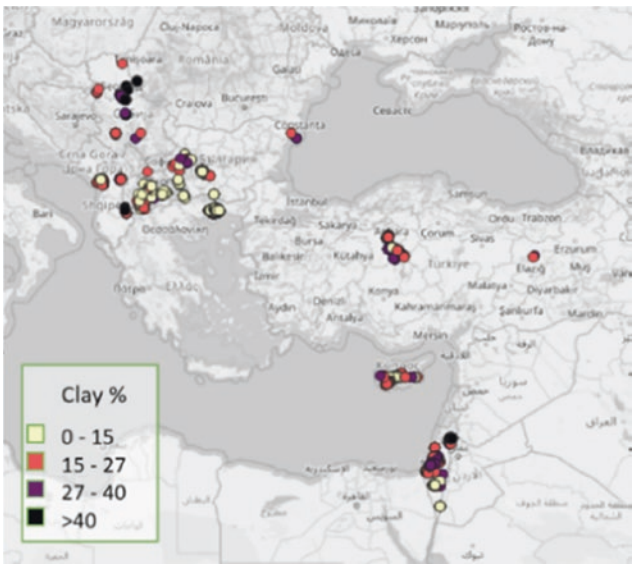

Fig. 5 CNN's clay content predictions for GEO-CRADLE sampling points

4 Discussion

In the current study, some first insights toward the development of an EO-based monitoring system are provided focusing on the direct prediction for exposed soils through Deep Learning techniques, supported by EO information, auxiliary variables, and in situ soil data. In that regard, modern modeling tools were introduced here to handle EO

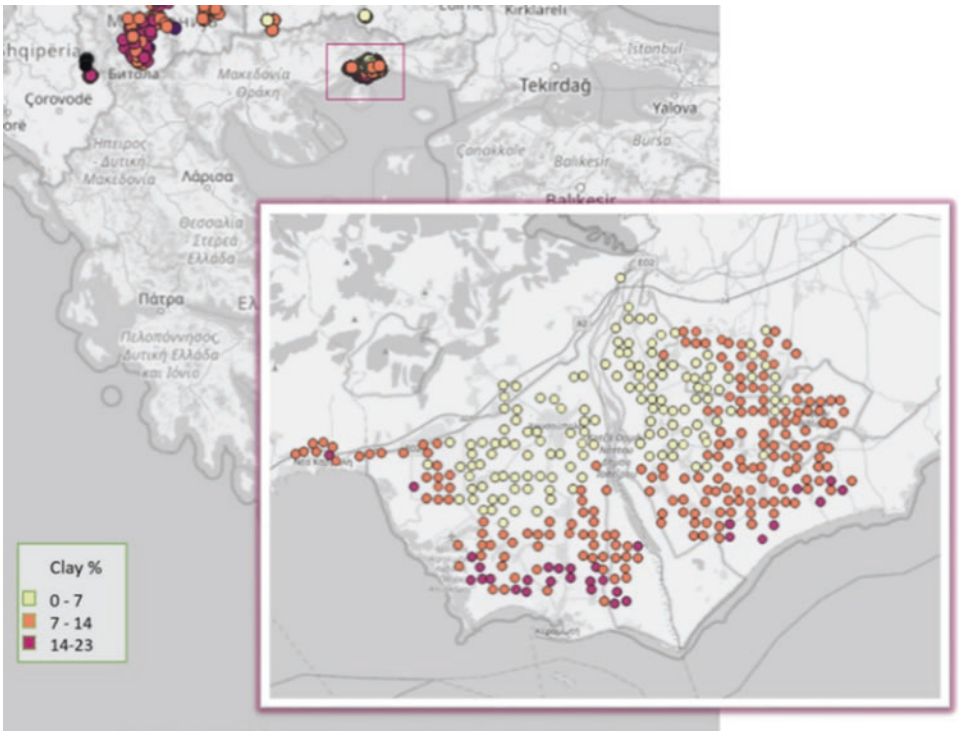

Fig. 6 CNN's clay content predictions for Greek subset of GEO-CRADLE sampling points

data in order to facilitate the production of upscaled and increased resolution digital soil maps, based on updated measurements that are handled in the scale of Big EO Data. More specifically, a multi-input Deep Learning algorithm served this necessity through its capacity to process big datasets with high computational complexity and resulting in a moderate prediction accuracy ($R^2 = 0.55$, RMSE = 9.08). Subsequently, the conjunction of auxiliary variables has shown a compelling accuracy increase in the model's predictive capacity ($R^2 = 0.80$, RMSE = 6.25). The CNN trained over both Sentinel and auxiliary variables demonstrated high performance, taking into consideration that the training dataset contains solely remote sensing data derived from open-sourcing datahubs.

On the doorstep of ESA's CHIME launch, the production rate of hyperspectral earth observations will be significantly higher than their deployments. Given the rapid developments in sensor specifications and in processing capacities, as well as the release of LUCAS 2015 SSL, we will be able to evolve in the quality of clay predictions and accommodate other soil properties in the future.

The GEO-CRADLE and Lucas 2009 synergy paves the way for a new contemporary reality in the need for in situ measurements and wet-chemistry analysis. The traditional techniques are now invited to take the role of reference ground-truth values for the calibration of space-borne EO data sources. The abundancy of existing data highlights the necessity of establishing a universal scheme for producing new SSLs and a reliable framework for transferring knowledge induced from existing ones to future efforts. The effortful coverage of these gaps is intended to be accomplished from the IEEE-P4005 standards and protocols working group for soil spectroscopy by establishing a standard protocol to measure reflectance spectroscopy of soil material in the VNIR–SWIR region. On top of this initiative, the Global Soil Laboratory Network (GLOSOLAN), which is a collaborative effort to enhance the capacity of laboratories and provide a modern solution to the need for soil spectral data harmonization, and which is coordinated by the Food and Agriculture Organization of the United Nations (FAO), has scheduled the development of a global and representative Soil Spectral Library (SSL) over MIR spectra, accompanied with conventional soil property data that will be measured in one gold standard laboratory. Both efforts will leverage agricultural productivity and mitigate land degradation through providing information regarding soil health.

5 Conclusions

The proposed methodology, which is based on the utilization of open access data, can be used to support the creation of various spatial explicit soil indicators in areas with well-reported gaps in soil data, for supporting soil mapping initiatives on a national or broader scale. In order to undertake the challenges that are set by Paris Agreement and Sustainable Development Goals, the described

methodology can offer the tools for exploiting existing GEOSS and external datasets and build upon prior knowledge, with minimal new data collection activities.

Acknowledgements The European Union will be formally mentioned and fully acknowledged in, but not limited to, reports, articles, publications, and presentations of work resulting from the use of the LUCAS_SOIL data as follows: "The LUCAS topsoil dataset used in this work was made available by the European Commission through the European Soil Data Centre managed by the Joint Research Centre (JRC), http://esdac.jrc.ec.europa.eu/".

The GEO-CRADLE regional SSL was retrieved from the official project's portal, http://datahub.geocradle.eu/.

References

Bellon-Maurel, V., et al. (2010). Critical review of chemometric indicators commonly used for assessing the quality of the prediction of soil attributes by NIR spectroscopy. *TrAC—Trends in Analytical Chemistry*. https://doi.org/10.1016/j.trac.2010.05.006

Demattê, J. A. M., et al. (2018). Geospatial soil sensing system (GEOS3): A powerful data mining procedure to retrieve soil spectral reflectance from satellite images. *Remote Sensing of Environment*, *212*, 161–175. https://doi.org/10.1016/j.rse.2018.04.047

Everingham, Y., et al. (2015). A dual ensemble agroclimate modelling procedure to assess climate change impacts on sugarcane production in Australia. *Agricultural Sciences*. https://doi.org/10.4236/as.2015.68084

Gholizadeh, A., Neumann, C., et al. (2020). *Soil organic carbon estimation using VIS–NIR–SWIR spectroscopy: The effect of multiple sensors and scanning conditions*. https://doi.org/10.31219/osf.io/z7htf

Gholizadeh, A., Žižala, D., et al. (2018). Soil organic carbon and texture retrieving and mapping using proximal, airborne and Sentinel-2 spectral imaging. *Remote Sensing of Environment*. https://doi.org/10.1016/j.rse.2018.09.015

Gorelick, N., et al. (2017). Google earth engine: Planetary-scale geospatial analysis for everyone. *Remote Sensing of Environment*. https://doi.org/10.1016/j.rse.2017.06.031

Guo, X. H., et al. (2015). Air-sea CO_2 fluxes in the East China Sea based on multiple-year underway observations. *Biogeosciences*. https://doi.org/10.5194/bg-12-5495-2015

Hartemink, A. E., & McBratney, A. (2008). A soil science renaissance. *Geoderma*. https://doi.org/10.1016/j.geoderma.2008.10.006

Hengl, T., et al. (2014). SoilGrids 1 km—Global soil information based on automated mapping. *PLoS ONE*. https://doi.org/10.1371/journal.pone.0105992

Kennard, R. W., & Stone, L. A. (1969). Computer aided design of experiments. *Technometrics*. https://doi.org/10.1080/00401706.1969.10490666

Montanarella, L., & Panagos, P. (2021). The relevance of sustainable soil management within the European Green Deal. *Land Use Policy*. https://doi.org/10.1016/j.landusepol.2020.104950

Mouazen, A. M., et al. (2007). On-line measurement of some selected soil properties using a VIS-NIR sensor. *Soil and Tillage Research*. https://doi.org/10.1016/j.still.2006.03.009

Orgiazzi, A., et al. (2018). LUCAS soil, the largest expandable soil dataset for Europe: A review. *European Journal of Soil Science*. https://doi.org/10.1111/ejss.12499

Padarian, J., et al. (2019). Using deep learning for digital soil mapping. *The Soil*. https://doi.org/10.5194/soil-5-79-2019

Paustian, K., et al. (2016). Climate-smart soils. *Nature*. https://doi.org/10.1038/nature17174

Ramesh, T., et al. (2019). Soil organic carbon dynamics: Impact of land use changes and management practices: A review. *Advances in Agronomy*. https://doi.org/10.1016/bs.agron.2019.02.001

Sitokonstantinou, V., et al. (2018). Scalable parcel-based crop identification scheme using Sentinel-2 data time-series for the monitoring of the common agricultural policy. *Remote Sensing*. https://doi.org/10.3390/rs10060911

Tsakiridis, N. L., et al. (2020). Simultaneous prediction of soil properties from VNIR-SWIR spectra using a localized multi-channel 1-D convolutional neural network. *Geoderma*. https://doi.org/10.1016/j.geoderma.2020.114208

Tziolas, N., et al. (2020). An integrated methodology using open soil spectral libraries and earth observation data for soil organic carbon estimations in support of soil-related SDGs. *Remote Sensing of Environment*. https://doi.org/10.1016/j.rse.2020.111793

Vaudour, E., et al. (2019). Sentinel-2 image capacities to predict common topsoil properties of temperate and mediterranean agroecosystems. *Remote Sensing of Environment*. https://doi.org/10.1016/j.rse.2019.01.006

Forecasting of Soil Moisture: An ANN Model Integrated with Empirical Mode Decomposition

Chandni Thakur, M. Aadhityaa, S. Vijayalakshmanan, K. S. Kasiviswanathan, B. Soundharajan, Subhamoy Sen and Narsa Reddy Tummuru

Abstract

Soil moisture (SM) plays a crucial role in agriculture planning, especially controlling irrigation and crop growth. While the application of physics-based models requires detailed information of the complex land-atmospheric interaction and high heterogeneity in soil characteristics, the machine learning-based modeling approaches have been proved to produce promising results in SM simulation. This paper aims at developing an Artificial Neural Network (ANN) model integrated with Empirical Mode Decomposition (EMD) named ANN-EMD to forecast the seven-day ahead SM. For this analysis, observed SM at 30 cm depth collected for nine years (i.e., 2008–2016) from the R. J. Cook Agronomy Farm, located in a Mediterranean climate, USA, was utilized. To demonstrate the improved performance of ANN-EMD modeling approach, the results from ANN-EMD were compared with conventional ANN. Overall, it was found that the ANN-EMD models produced consistently high performance both in the calibration and validation phase as EMD extracted the detailed information present in the SM dynamics.

Keywords

Agriculture planning · Artificial neural network · Empirical mode decomposition · Soil moisture

1 Introduction

Accurate estimation of soil moisture is crucial for managing crop growth and the irrigation water requirement. Often, lack of precise soil moisture information leads to excessive or less irrigation water supply and low agricultural productivity (Campbell & Campbell, 1982). Recent advancements in sensor development, the Internet of Things (IoT), and cloud computing have made the close monitoring of SM relatively simple (Gasch et al., 2017). Effective use of these observed SM data in the modeling mainly to forecast the future values would be useful to farmers. Accordingly, efficient irrigation management practices can be achieved for improving the sustainability and productivity of agriculture systems.

Several modeling approaches that include physics-based, conceptual, and machine learning (ML) have been explored to simulate/forecast SM at different spatial and temporal scales. Among these models, ML-based modeling approaches have been widely applied due to the nature of relatively lesser data requirements, and further, these models produce reasonable accurate estimations compared to their counterparts (Maraseni, 2018). However, as these models are data-centric, the overall generalization across different datasets is quite challenging. Thus, further research to enhance the current understanding of the processes through improved modeling approaches for accurate SM forecasts is still highly active. Recently, delineating the embedded frequency information in the SM time series has proved to be efficient in improving the accuracy of SM forecasting. For this endeavor, Empirical Mode Decomposition (EMD), which decodes high frequency in the data series into lower frequency-resolved parts, can be

C. Thakur · K. S. Kasiviswanathan (✉)
Department of Water Resources Development and Management, Indian Institute of Technology Roorkee, Roorkee 247667, India
e-mail: k.kasiviswanathan@wr.iitr.ac.in

M. Aadhityaa · B. Soundharajan
Department of Civil Engineering, Amrita Vishwa Vidyapeetham, Coimbatore 641112, India

S. Vijayalakshmanan · S. Sen
School of Engineering, Indian Institute of Technology Mandi, Mandi 175005, India

N. R. Tummuru
School of Computing and Electrical Engineering, Indian Institute of Technology Mandi, Mandi 175005, India

Z. A. Ergüler et al. (eds.), *Selected Studies in Geotechnics, Geo-Informatics and Remote Sensing*, Advances in Science, Technology & Innovation, https://doi.org/10.1007/978-3-031-43759-5_30

effectively used to extract useful information from the input variables for improving the forecast accuracy of SM models (Maraseni, 2018). Very few studies have explored the EMD for improving SM forecast limited to either a monthly time scale (Maraseni, 2018) or a short-range hourly forecast (Liu et al., 2014).

In this paper, an ANN-EMD model to forecast the seven-day ahead SM at a depth of 30 cm (below ground level) was explored. The performance of ANN-EMD models was compared with conventional ANN models to demonstrate the improved accuracy in the forecasted SM.

2 Methods and Material

2.1 Details of Data and Study Area

A sensor-based daily soil moisture data collected at 30 cm depth for the period 2007–2016 from R. J. Cook Agronomy Farm, USA, were used to develop the models (Gasch et al., 2017). Out of the data available from 42 sensors located throughout the study area, only nine datasets were selected considering the continuity and minimal missing values throughout the period.

2.2 ANN-EMD

An ANN model processes the information in a massively parallel interconnection of simple neurons through a non-linear activation function. Several training algorithms have been proposed to optimize the parameters, such as weights and biases of the ANN model. The multi-layer perceptron (MLP) is the most popular ANN architecture. Detailed information about ANN is not presented here as several literatures are available.

EMD is developed for analyzing nonlinear and nonstationary signals (Huang et al., 1998). EMD decomposes the original signal into a finite number of intrinsic mode functions (IMFs), and each IMF is independent of the others. The signal $x(t)$ can be presented in terms of IMFs as:

$$x(t) = \sum_{m=1}^{M} (\mathrm{imf}_m(t) + r_m(t)) \quad (1)$$

where M is the number of IMFs, $\mathrm{imf}_m(t)$ is the m-th IMF, and the $r_m(\mathrm{t})$ is the final residue.

3 Results and Discussion

In the ANN model, identifying significant input variables is the first step. To account for the effect of the antecedent moisture condition of the field, previous SM values lagged up to 3 days were found out for all the selected nine datasets from the autocorrelation analysis. The forecast lead time was fixed to be seven days as farmers require at least a week ahead of soil moisture information for planning the irrigation effectively. The data lengths of the nine locations ranged from 5 to 9 years. So, the calibration and validation phase was generalized with percentage datapoints. The calibration data consisted of 85% of the total data, and the remaining had been kept for validation. The cross-validation to avoid overfitting was also performed and for which 15% of calibration data were used. Please note that only the calibration and validation results are presented here. To train the model, the Bayesian regularization algorithm was used. The model inputs were processed using EMD, and accordingly, the IMF and residuals were estimated. Please note that the number of IMF signals was different for different locations as it was completely based on the complexity of the dataset. The next step is to fix the number of hidden layers and hidden nodes. In this paper, a single hidden layer was fixed, and the hidden nodes were identified through the trial and error approach. With the initiation of two hidden nodes, it was allowed to increase up to ten hidden nodes adding one at a time. Finally, four hidden nodes were found to be yielding better results both in calibration and validation of ANN and ANN-EMD models. The hidden layer used a sigmoidal activation function, whereas the output layer used a linear activation function.

The model ANN-EMD and ANN produced the SM forecast for seven days lead time and compared it with observed SM. The model performance was assessed mainly using Nash–Sutcliffe efficiency (NSE) and Root Mean Square Error (RMSE). It is evident from Fig. 1 that the ANN-EMD consistently outperformed both in calibration and validation. In specific, the 25 and 75 percentiles of NSE were 84 and 94% in ANN-EMD. However, only in a few locations the ANN model yielded good performance.

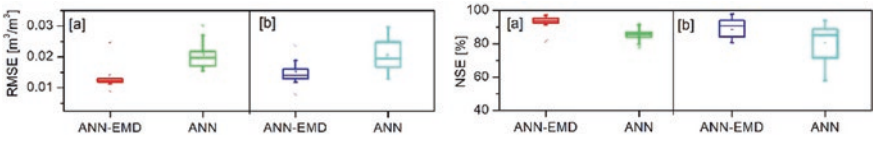

Fig. 1 Box plot showing the variance in model performance across different locations **a** calibration and **b** validation

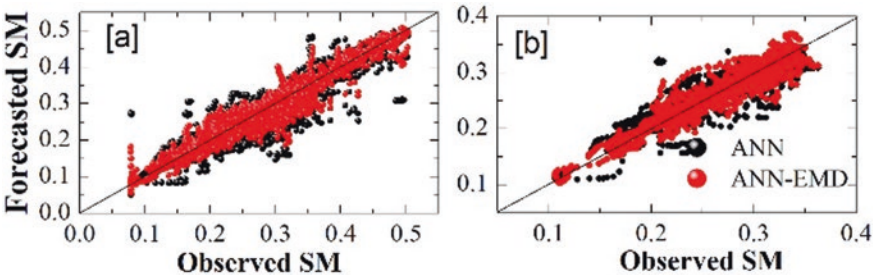

Fig. 2 Scatter plots of ANN-EMD and ANN **a** calibration and **b** validation

The scatter plot was prepared to show the closeness of the model forecast with observation (Fig. 2). Please note that the individual model forecast for different locations along with observed SM was combined to produce the single scatter plot for calibration and validation. The 45° line in Fig. 2 shows the perfect fit of the model. It is very evident that the forecasts made by ANN-EMD were close as compared to ANN in calibration across the entire range of the simulation. However, in the validation, both models produced very similar results in high-range soil moisture forecasts. For the lower and medium range of SM, the forecast of ANN-EMD was comparably better as the ANN model yielded much wider dispersion in this region.

4 Conclusions

An ANN model integrated with EMD has been developed to forecast the SM up to 7 days lead time. EMD extracts the detailed information present in the input variables, and the ANN model learned the underlined process well to capture the dynamics of SM. Subsequently, the comparison with the conventional ANN model demonstrated that the proposed ANN-EMD forecasted the SM well, yielding high NSE and less RMSE in calibration and validation.

Acknowledgements The work presented in this paper has been funded by the Science and Engineering Research Board (SERB) of India under Impacting Research Innovation and Technology (IMPRINT-2) initiative (IMP/2018/002012).

References

Campbell, G., & Campbell, M. (1982) Irrigation scheduling using soil moisture measurements: theory and practice. *Advances in Irrigation*, 25–42.

Gasch, C. K., Brown, D. J., Brooks, E. S., Yourek, M., Poggio, M., Cobos, D. R., & Campbell, C. S. (2017). A pragmatic, automated approach for retroactive calibration of soil moisture sensors using a two-step, soil specific correction. *Computers and Electronics in Agriculture, 137*, 29–40.

Huang, N. E., Shen, Z., Long, S. R., Wu, M. C., Shih, H. H., Zheng, Q., Yen, N.-C., Tung, C. C., & Liu, H. H. (1998). The empirical mode decomposition and the Hilbert spectrum for nonlinear and nonstationary time series analysis. *Proceedings of Royal Society A, 454*, 903–995.

Liu, Y., Mei, L., & Ooe, S. K. (2014). Prediction of soil moisture based on extreme learning machine for an apple orchard. In *Conference on Computational Interdisciplinary Science* (pp. 400–404). IEEE.

Maraseni. (2018) Soil moisture forecasting by a hybrid machine learning technique: ELM integrated with ensemble empirical mode decomposition. *Geoderma*, *330*, 136–161.

Soil Characterization Using Machine Learning Based on Remote Sensing Data

Raja Inoubli, Lilia Bennaceur, Ali Ben Abbes and Imed Riadh Farah

Abstract

Remote sensing (RS) techniques have lately seen a huge advancement which led to the availability of enormous amounts of data. Data with spectral, temporal, and spatial characterizations constitute the basis of soil characterization. The soil parameters provide a database that serves in several applications such as prediction and monitoring. For a variety of soil parameters, several studies use inverse backscattering models (i.e., physical, empirical, and semi-empirical). However, some of the most used backscattering models are not easy to invert due to their complexity. Therefore, a wide range of studies relies on the capacity of Machine Learning (ML) to characterize the soil. The major advantage of ML is the ability to define the nonlinear relationship between soil parameters and the backscatter coefficient, which is considered a challenge for backscattering models. The main objective of this study is to explore the recent studies in the field of soil characterization in particular the retrieval of soil parameters such as soil moisture/ roughness based on backscattering models and ML using RS data.

Keywords

Remote sensing · Soil parameters · Backscattering models · Machine learning

R. Inoubli (✉) · A. B. Abbes · I. R. Farah
RIADI, National School of Computer Sciences, Manouba, Tunisia
e-mail: raja.inoubli@ensi.u-manouba.tn

A. B. Abbes
e-mail: ali.benabbes@yahoo.fr

I. R. Farah
e-mail: imedriadh.farah@mse.uma.tn

L. Bennaceur
LTSIRS (Laboratoire de Télédétection et Systèmes d'Information à Référence Spatial) ENIT, Manar University, Tunis, Tunisia
e-mail: lilia.bennaceur@ipeiem.utm.tn

1 Introduction

Remote sensing (RS) techniques have an advantage for several applications such as land use mapping, weather forecasting, environmental management, natural hazards, and soil science. Without physical contact, RS interacts with objects through emitted radiation where the objects reflect it back (backscatter). The backscatter signal depends on the soil parameters. Synthetic Aperture Radar (SAR) is an active microwave sensor used by several studies to retrieve soil properties due to its independence of weather conditions, time periods, and cloud coverage. Properties such as soil moisture (SM) and roughness are considered as relevant knowledge that serves in different fields such as agricultural activity, water management, weather forecasting, precipitation estimation, drought monitoring, crop yield management, and geology activities. The estimation of SM is realized by inverting the SAR signal using backscattering models. The retrieving process depends on the radar observation (i.e., wavelength, incidence angle, and polarization) and soil parameters (i.e., moisture and roughness). The backscattering models can be categorized into three groups, theoretical (Fung et al., 1992), empirical (Attema & Ulaby, 1978; Sahebi et al., 2003; Shi et al., 1997), and semi-empirical (Dubois et al., 1995; Oh et al., 1992) models, which vary in the degree of complexity, precision, and validity. The most frequently used models are the integral equation model (IEM) (Fung et al., 1992), Dubois et al. (1995), and Oh et al. (1992) models. In the literature, there are two methods to invert backscattering models. The first technique is inverting the model directly. However, the high complexity of a model implies some difficulties in the inverting process. The model's performance is also affected by the natural variability of the soil properties, vegetation, and climate. This soil variability implies major difficulties to retrieve the soil roughness. Other limitations were recorded on describing the nonlinear relationship between soil parameters and the backscattering coefficient.

Z. A. Ergüler et al. (eds.), *Selected Studies in Geotechnics, Geo-Informatics and Remote Sensing*, Advances in Science, Technology & Innovation, https://doi.org/10.1007/978-3-031-43759-5_31

Therefore, a wide range of studies counts on the second technique which is the use of Machine Learning (ML). Therefore, this study aims to highlight the role of ML in retrieving soil parameters based on SAR data.

2 Backscattering Models

The Oh model was introduced by Oh et al. (1992) as a semi-empirical model. It relates backscattering coefficients with the soil parameters (moisture and roughness). Another semi-empirical model was presented by Dubois et al. (1995). This model is only co-polarized backscattering which records more accurate results than cross-polarized backscattering. The model is characterized by an easy calibration process and high sensitivity to noise. A new model was developed by Baghdadi, et al. (2016) as a Modified Dubois Model (MDM). This model is considered the most adaptable model since it provides regulated parameters. On the other hand, (Fung et al., 1992) developed a physical model with no specific site calibration named IEM. However, the model has difficulties in roughness estimation, especially on larger scales. The IEM performance is affected by the use of correlation length (L). Then, (Baghdadi et al., 2006) offered a calibrated version of the model named CIEM. This model replaces L with a calibrated parameter called Lopt.

3 Soil Moisture Retrieving Using Machine Learning (ML)

Recently, several studies count on the high performance of ML and its various capacities. In fact, this study relies on the capacity of ML in presenting the complexity and all relations of the model based on the network's training stage which constitutes a huge advantage in the field of soil characterization. Through the literature, several works explored ML in retrieving soil parameters. The collected works use different data, such as RS, field measurement, and other data (e.g., meteorological information). Li et al. (2020) used the neural network (NN) based on its good performance in both fitting and prediction (Li et al., 2020). This network is able to map the arbitrarily complex nonlinear relationship. Thereby, this study investigates the performance of NN in comparison with the Modified Dubois Model (MDM) and Multiple Linear Regression (MLR). The study records higher coefficient of determination (R^2) values with inversing SM at multi-polarization than at the single polarization. The results assert that MLR gives more correlated SM estimation to the in situ data. The study also proves the NN ability in retrieving SM. According to the authors, to improve NN inversion results, the network should be fitted by the backscattering coefficient at the different polarization. However, Ezzahar et al. (2020) aimed to investigate the support vector machine (SVM) results with semi-empirical and theoretical backscatter models (Ezzahar et al., 2020). SVM techniques are known for their efficiency in both classification and regression problems. It is characterized by ease of implementation and high flexibility. In this study, the results of backscattering coefficients at vertical vertical (VV) are more correlated to SM than the vertical horizontal (VH) polarizations. The comparison between IEM and Oh revealed the efficiency of the Oh model compared to IEM. However, to increase the model's performance, the authors used Lopt for IEM. Concerning the inversion results of SVM at a large scale, they were 0.28 vol.% for bias and 2.77 vol.% for root mean square error (RMSE) where IEM got − 0.13 vol.% for bias and 2.71 vol.% for RMSE. Based on these closed results, the authors approved using SVM to retrieve SM at a large scale. In Mirsoleimani et al. (2019), the authors suggested combining NN with calibrated IEM (CIEM) CIEM and MDB (Mirsoleimani et al., 2019). The results highlight the outperformance of CIEM with RMSE equal to 0.78 dB over MDB with RMSE equal to 1.45 dB. The study used NN based on estimated SM using the two backscattering models, from single-polarization S1 images. The RMSE values of inversion revealed an equal performance between NN and MLR analysis. In addition, the inversion results recorded a high performance in SM retrieving by using single polarization. In particular, the VV polarization improved the accuracy of the model's results with 3.0 vol.% for the CIEM and 3.3 vol.% for the MDB.

4 Discussion

Getting through those works revealed that in order to estimate SM, authors have widely and primarily use the C- and X-bands of SAR data. As for the backscattering model's choice, IEM is the most commonly used physical model to invert the radar signal. However, ML methods are used to surmount the backscattering models' limit. The involvement of ML establishes the nonlinear relationship between soil parameters and the backscatter coefficient. It ensures the estimation of the SM and especially the soil roughness. The studies were divided into two groups. The first group explores works that compare the ML results to those received by backscattering models. The results show a higher performance in retrieving SM by NN and SVM model compared to the selected backscattering model results. The second group recommends the use of backscattering models to generate a synthetic database that uses simulated backscattering coefficients as input for network training. However, even with getting the kind of satisfying

results, this proposition is still insufficient due to inaccurate results between the theoretical values and the measured ones. As for the overall results, more correlation is recorded between backscattering coefficients and SM through the use of single polarization, especially at the VV polarization.

5 Conclusions

This study aimed to discuss the role of backscattering models and ML in retrieving soil parameters. We have detected efficient results through the use of ML over backscattering models. The reviewed papers highlighted the importance of RS data in the retrieval mission. The importance of RS is due to its role in allowing long-term soil parameters monitoring over large areas. Recently, the RS technologies saw an important advancement that serves in soil characterization by providing bigger and heterogeneous data. However, that amount of data implies a serious challenge for traditional ML methods. Therefore, we can go further by discovering other solutions such as deep learning methods to surmount any challenging factors that we may face.

References

Attema, E. P. W., & Ulaby, F. T. (1978). Vegetation modeled as a water cloud. *Radio Science, 13*(2), 357–364. https://doi.org/10.1029/rs013i002p00357

Baghdadi, N., et al. (2016). A new empirical model for radar scattering from bare soil surfaces. *Remote Sensing*, *8*, 920.

Baghdadi, N., Holah, N., & Zribi, M. (2006). Calibration of the integral equation model for SAR data in C-band and HH and VV polarizations. *International Journal of Remote Sensing, 27*, 805–816.

Dubois, P. C., VanZyl, J., & Engman, T. (1995). Corrections to "Measuring soil moisture with imaging radars". *IEEE Transactions on Geoscience and Remote Sensing, 33*(6), 1340.

Ezzahar, J., Ouaadi, N., Zribi, M., Elfarkh, J., Aouade, G., Khabba, S., Er-Raki, S., Chehbouni, A., & Jarlan, L. (2020). Evaluation of backscattering models and support vector machine for the retrieval of bare soil moisture from Sentinel-1 data. *Remote Sensing, 12*(1), 72.

Fung, A., Li, Z., & Chen, K. (1992). Backscattering from a randomly rough dielectric surface. *IEEE Transactions on Geoscience and Remote Sensing, 30*, 356–369.

Li, Y., Yan, S., Chen, N., & Gong, J. (2020). Performance evaluation of a NN model and two empirical models for estimating soil moisture based on Sentinel-1 SAR data. *Progress in Electromagnetics Research, 105*, 85–99.

Mirsoleimani, H. R., Sahebi, M. R., Baghdadi, N., & El Hajj, M. (2019). Bare soil surface moisture retrieval from sentinel-1 SAR data based on the calibrated IEM and Dubois models using NN. *Sensors, 19*(14), 3209.

Oh, Y., Sarabandi, K., & Ulaby, F. T. (1992). An empirical model and an inversion technique for radar scattering from bare soil surfaces. *IEEE Transactions on Geoscience and Remote Sensing, 30*(2), 370–381. https://doi.org/10.1109/36.134086

Sahebi, M. R., Bonn, F., & Gwyn, Q. H. J. (2003). Estimation of the moisture content of bare soil from RADARSAT-1 SAR using simple empirical models. *International Journal of Remote Sensing, 24*(12), 2575–2582. https://doi.org/10.1080/0143116031000072948

Shi, J., Wang, J., Hsu, A. Y., O'Neill, P. E., & Engman, E. T. (1997). Estimation of bare surface soil moisture and surface roughness parameter using L-band SAR image data. *IEEE Transactions on Geoscience and Remote Sensing, 35*(5), 1254–1266. https://doi.org/10.1109/36.628792

New Insights of Design, Development, and Implementation of Digital Petroleum Ecosystems and Technologies in Oil and Gas Industries

Shastri L. Nimmagadda, Andrew Ochan, Neel Mani and Torsten Reiners

Abstract

Heterogeneity and multidimensionality are significant challenges of petroleum data management, precluding the data integration process. Data integration is crucial in the upstream digital petroleum ecosystem development process that unifies multiple domains and systems. To sustain the process, we adopt various Information System (IS) artefacts that can bring and unify diverse petroleum systems into a single ecosystem. In addition, interrelated IT applications are in good demand for integrated exploration project management and decision support systems. One such application that emerges with the design science research method is to build an integrated framework articulated with diverse multidimensional modelling artefacts to drive multiple domain applications of upstream businesses. We articulate IS artefacts related to multiple sedimentary basin settings, linked different petroleum systems and oil and gas fields. Besides, we design petroleum ontology artefacts connectable to diverse petroleum systems of a basin or groups of basins. Petroleum ontologies are extendable to large-scale Big Data systems, which are characteristic of Total Petroleum Systems (TPS) in the Middle Eastern contexts. Metadata cubes are computed to visualize, interpret and analyse the data views for meta-knowledge. We implement the artefacts in an oil and gas exploration project to ascertain the efficacy of digital petroleum ecosystems and technologies in the oil and gas industries.

Keywords

Digital ecosystems · Design science · Big data · Upstream business

1 Introduction

Petroleum data management is a shared domain application, but the existing articulations have constraints in the petroleum digital ecosystem development process. Oil and gas data acquired from various ecosystem sources need better logical and physical data organizations to motivate the integration process. The practice is acceptable by data warehouse designers to achieve development criteria and analysis requirements. To promote the integration process to larger contexts of Big Data systems representing Total Petroleum Systems (TPS), we move one step forward to develop design science guided constructs, models, and methods. They are in demand in the digital petroleum ecosystem projects (Nimmagadda & Dreher, 2012; Roozbahani et al., 2018). In the Big Data era, the knowledge-based ontology models, data warehouse schemas, and advanced data mining procedures are added motivations to build digital oil field solutions. Data views extracted from Big Metadata using data mining algorithms and visualization artefacts are additional cognitive drives for interpreting various exploration and production data trends, patterns, and correlations. Statistical regression models are added predictive tools for forecasting resources needed in upstream-integrated project management. The cost–benefit analysis is a corroborative and decisive commitment through improved knowledge of petroleum discoveries and production attributes. Existing performance indicators of the resources industry can too substantiate future forecast analytics. Total Petroleum Systems are digital ecosystems (Lin, 2014; Nimmagadda & Dreher, 2012; Yerli, 2019), for which multiple conceptualized and contextualized attribute dimensions are construed. They are interpretable between known

S. L. Nimmagadda (✉) · T. Reiners
School of Management, Curtin University, Perth, WA 6151, Australia
e-mail: shastri.nimmagadda@curtin.edu.au

A. Ochan
Petroleum Authority of Uganda, Entebbe, Uganda

N. Mani
Institute of AI, DSVV, Haridwar, Uttarakhand, India

Z. A. Ergüler et al. (eds.), *Selected Studies in Geotechnics, Geo-informatics and Remote Sensing*, Advances in Science, Technology & Innovation, https://doi.org/10.1007/978-3-031-43759-5_32

or unexplored attributes in a variety of geographic contexts. The authors narrate the systems as embedded because of spatial–temporal dimensions with which longitudinal and lateral research solutions are plausible (Nimmagadda & Dreher, 2012). The conceptualization can interpret data relationships between upstream business attributes that evolve during the ontology building process (Bravo et al., 2008; Soma et al., 2008). Longitudinal and latitude research approaches are feasible in both cases as in Nimmagadda and Dreher (2012) and Roozbahani et al. (2018).

2 Research Objectives and Methodologies

Design Science Information System (DSIS) framework is a generic Design Science Research approach, adopted with design, development, and implementation strategies (Nimmagadda & Dreher, 2012; Peffers et al., 2007). The Big Data hype, in recent years, has motivated us to develop DSIS and collaborate with Digital Ecosystems and Technologies (DEST).

As shown in Fig. 1a, two stages of framework development are described, one with a big data paradigm (1) and the other with a research framework with various constructs and artefacts (2). Petroleum ecosystem data sources mapping and modelling are described in a schematic view (Fig. 1b). As itemized (1)–(7) in Fig. 1b, several modelling stages are presented, from data acquisition to data interpretation and knowledge extraction, including prospect evaluation.

Cloud computing and Big Data analytics, their collaborations with DSIS are upcoming exploration industry technologies. The DSIS framework caters the data modelling, data warehousing, and mining artefacts that use volumes and varieties of data sources, with various data mining and visualization tools, as necessitated in Big Data-driven upstream businesses. Longitudinal and lateral research case studies in the current contexts motivate the implementation of design science in Exploration and Production (E&P) contexts. We construe various constructs, models, and methods (Nimmagadda & Dreher, 2012; Rusu, 2012). Business Management Information Systems (BMIS) can add new opportunities to Big Data in industry scenarios. In multiple domains and systems, logical and physical data models are interpreted as artefacts. The conceptual models represent ontologies, descriptive for volumes and various data sources (Nimmagadda & Dreher, 2012; Peffers et al., 2007; Soma et al., 2008; Yerli, 2019). Data Warehouse is a backend application of e-business activities with several data views deliverable for interpretation. Empirical research with the qualitative and quantitative interpretation of data views is added support to the DSIS methodology. Data views mined from oil and gas multidimensional repositories can be useful to trade between different operational centres. Cross-sectional data collection from various oil companies located in other parts of the world may provide a better picture of global economic and technological performance indicators with just-in-time and spatial dimensions. Analysis and Discussions.

In Arabian Gulf Basin contexts, we interpret digital petroleum ecosystems and their embedded systems linked with Middle Eastern onshore and offshore basins (Nimmagadda & Dreher, 2012; Rusu, 2012; Yerli, 2019). The ecosystem concept demonstrates the necessity of ontology models appearing in integrated workflows and implementable in large geographic G&G contexts (Bravo et al., 2008; Soma et al., 2008). The scope of conceptualization and contextualization is explored to unify the multidimensional data sources in repository systems. Total Petroleum Ecosystem cannot isolate overall ecology without petroleum and geomorphic ecosystems. To understand the phenomena of "ecosystem", we collaborate interconnected diverse digital systems with DSIS and communion of petroleum systems. In this context, we present various applications needed to operate remotely to unify multidimensional data in spatial–temporal attribute dimensions. The web interfaces can connect high-speed data warehouses for fast accessing the data and information in remote and distant places. Big Data ecosystem solutions are feasible and applicable in resolving the design science information system design and development issues. Data storage and control, unstructured data processing, and Big Data analysis are manageable for large sedimentary basins settings. A couple of E&P is extracted from the storage-cuboid data structure as cube slices, interpretable as data views, as shown in Fig. 2. A couple of reservoir slices are presented in bubble plots with favourable areas of E&P.

Hadoop ecosystem is synonymous with Big Data technologies (Lin, 2014; Ramiz & Yadigar, 2017) articulated for data storage in clusters and MapReduce parallel processing. Apache Spark ML software is developed for statistical processing, machine learning, and predictive analysis in upstream petroleum businesses. Fine-grained multidimensional data views extracted from metadata in geographic locations can add value to data mining, visualization, and interpretation (Bravo et al., 2008; Nimmagadda & Dreher, 2012).

3 Conclusions and Future Vision

Big Data is an alternative technology to manage data explosion in petroleum digital ecosystem scenarios. The DSIS framework drives multiple digital ecosystems, offering innovative modelling and upstream-integrated solutions with improved petroleum systems' connectivity and meta-knowledge of design and models. Artefacts developed in

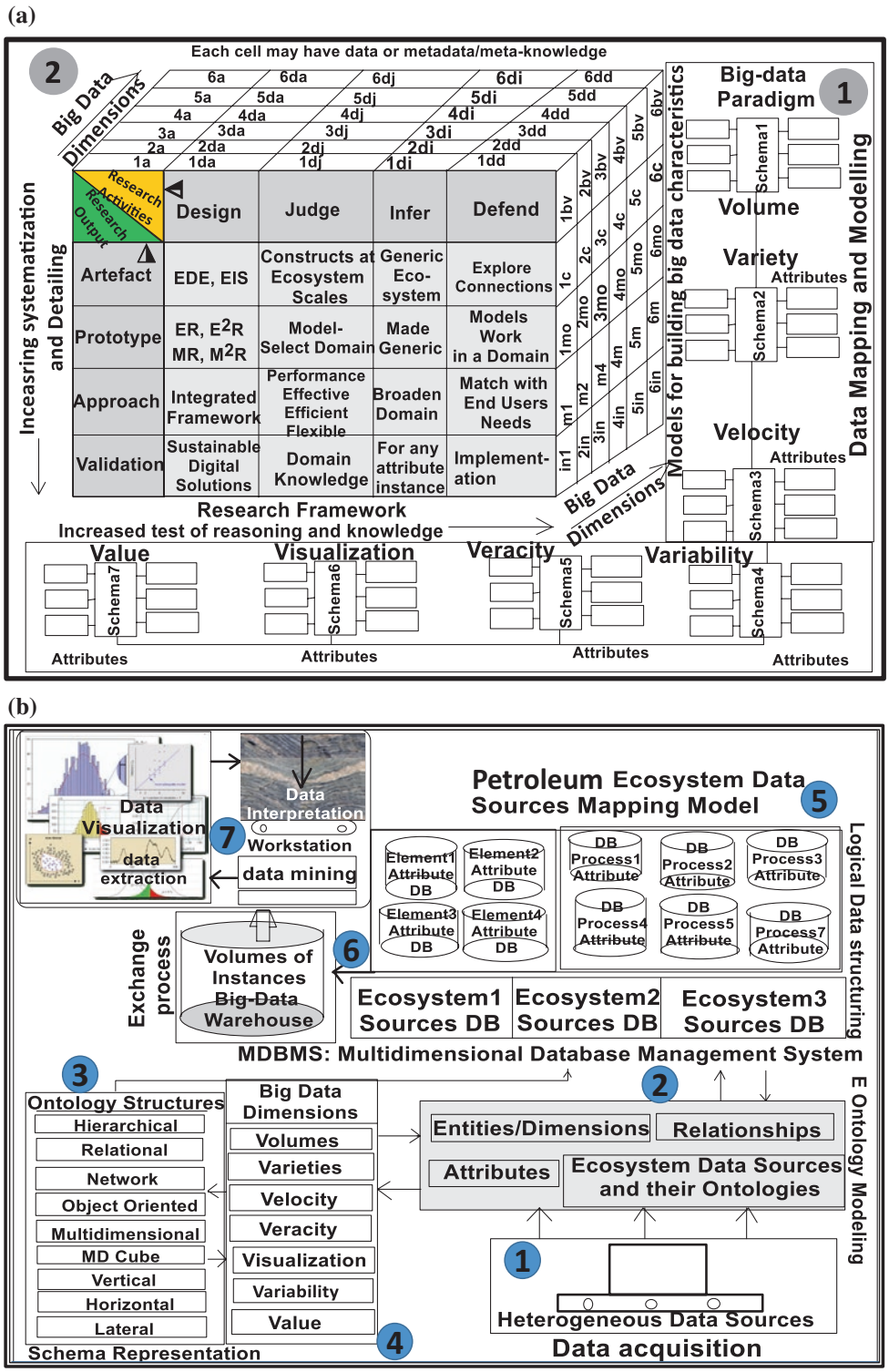

Fig. 1 **a** Big data guided DSIS framework development. **b** Petroleum ecosystem data source mapping and modelling

the framework are data mining, visualization, data analysis and interpretation, which can add values to BMIS and its associated integrated project management. In addition, Big Data tools facilitate global scale generalization to specialization with local-scale events to conceivable digital ecosystem scenarios. Big Data has the power of connecting various business ecosystems, in addition to data and business analytics. The technologies have an enormous impact on minimizing the risk of exploration, appraisal and field development activities in oil and gas industries. We reiterate

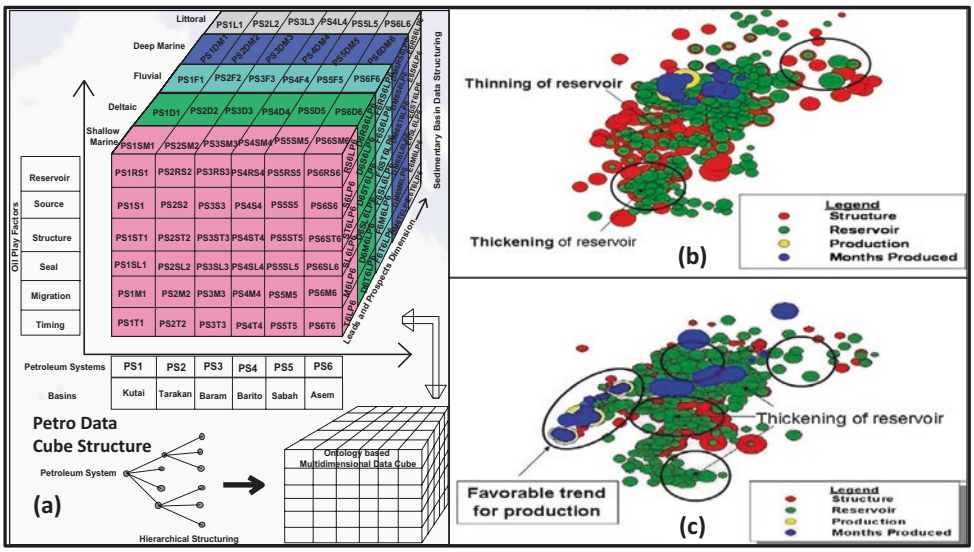

Fig. 2 Cuboid data structure **a** cube **b** reservoir slice1 and **c** reservoir slice2

that DSIS is a methodological approach articulated for oil and gas exploration and production activities in Arabian Gulf contexts.

References

Bravo, C., Aguilar, J., Ríos-Bolívar, A., Aguilar-Martin, J., & Rivas-Echeverría, F. (2008). A generalized data meta-model for production companies ontology definition. *International Journal of Systems Applications, Engineering & Development, 2*(4).

Lin, A. (2014). Principles of big data algorithms and application for unconventional oil and gas resources. In *Proceedings of the SPE Large Scale Computing and Big Data Challenges in Reservoir Simulation Conference and Exhibition* (pp. 87–95).

Nimmagadda, S. L., & Dreher, H. (2012). On new emerging concepts of Petroleum Digital Ecosystem (PDE). *Journal WIREs Data Mining Knowledge Discovery, 2*, 457–475 (2011). https://doi.org/10.1002/widm.1070

Peffers, K., Tuunanen, T., Rothenberger, M. A., & Chatterjee, S. (2007). A design science research methodology for information systems research. *Journal of Management Information Systems, 24*(3), 45–78.

Ramiz, A., & Yadigar, I. (2017). Conceptual big data architecture for the oil and gas industry. *Problems of Information Technology, 08*, 3–13. https://doi.org/10.25045/jpit.v08.i1.01

Roozbahani, F. S., Barjouei, R. S., & Hojjati, S. N. (2018). Identifying an appropriate model for information systems integration in the oil and gas industry. *International Journal of Advanced Networking and Applications, 10*(01), 3687–3691.

Rusu, L. I. (2012). *Survey several approaches to XML data mining, XML data mining, part 1*. https://www.ibm.com/developerworks/xml/library/x-datamine1/

Soma, R., Bakshi, A., Prasanna, V., DaSie, W. J., & Bourgeois, B. (2008). *Semantic web technologies for smart oil field applications*. IECE. https://doi.org/10.2118/112267-MS (SPE-112267-MS).

Yerli, G. (2019). *Capturing and loading oil and gas well site information via Witsml*. https://Community.Snowflake.Com/S/Article/Capturing-And-Loading-Oil-And-Gas-Well-Site-Information-Via-Witsml

Machine Learning for Visualization and Prediction of Spatiotemporal Spread of COVID-19 in India

Rifaat Abdalla

Abstract

The application of GIS for disaster management and emergency response has provided the ease of producing meaningful information products that can otherwise be time and resource-intensive. Modeling, simulation, and visualization of GIS data provides disaster management decision-makers with the ease of using embedded information in effective knowledge generation and decision support processes, based on modeling geospatial data. Data science has emerged as a very promising interdisciplinary science that integrates various components that are related to data through a cycle that starts with problem definition, data acquisition, data processing, data exploration, and model selection and ends with product deployment. This data science life cycle is essentially the GIS modeling life cycle, which makes the process of using machine learning in GIS modeling a step forward. Artificial intelligence techniques, such as machine learning where the user applies a specific algorithm, allow the machine to learn from examples and experience to perform such complicated tasks. This makes the process of data exploration and product delivery worthwhile. This paper will provide a general overview of how supervised learning, unsupervised learning, as well as reinforced learning can be effective for disaster and emergency management applications, highlighting the autoregression integrated moving average (ARIMA) model for the prediction.

Keywords

Machine learning · Disaster management · Natural hazards · Data science · GIS-based modeling · Pandemic modeling

R. Abdalla (✉)
Department of Earth Sciences, College of Science, Sultan Qaboos University, Al Khodh, P.O. Box 36, Oman
e-mail: rabdalla@squ.edu.om

1 Introduction

Machine learning is a branch of computer science branching out of artificial intelligence, part of it studies giving machines and computers the ability to learn without being explicitly programmed by exploring algorithms that can self-teach and make predictions about data. These algorithms work by building models of inputs to help make decisions, rather than following machine-bound, static, and code-defined instructions and codes (Aljaaf et al., 2016).

Machine learning is defined as a set of methods that can detect hidden patterns in data automatically without explicitly programming them and then use these hidden models to predict future data or assist in making decisions. Machine learning is closely related to the fields of statistics, pattern recognition, and data mining, a field of study that gives computers the ability to learn without being explicitly programmed (Brynjolfsson & Mitchell, 2017; Utkin & Zhuk, 2017).

Machine learning is one of the ways in which software is trained to learn and evolve automatically through experimentation, even without being explicitly programmed or altered by its programmers. Sample data is used in training (training data), that is, data used by algorithms to generate mathematical models.

Machine learning relies on the analysis of a huge amount of data in record time, and then the resulting output can be linked to the decision-making processes. It is used to predict the future. Indeed, the computer analyzes a huge amount of data related to human failure in normal ways to analyze and study the patterns and trends of data known as predictive analysis. Apart from the precise technical aspects of machine learning or learning derived from information systems, the uses and applications of these technologies are enormous and extremely useful in various fields. Machine learning contributes significantly to decision-making processes and saves effort and time with a mechanism of accuracy (Khan et al., 2016).

Z. A. Ergüler et al. (eds.), *Selected Studies in Geotechnics, Geo-Informatics and Remote Sensing*, Advances in Science, Technology & Innovation, https://doi.org/10.1007/978-3-031-43759-5_33

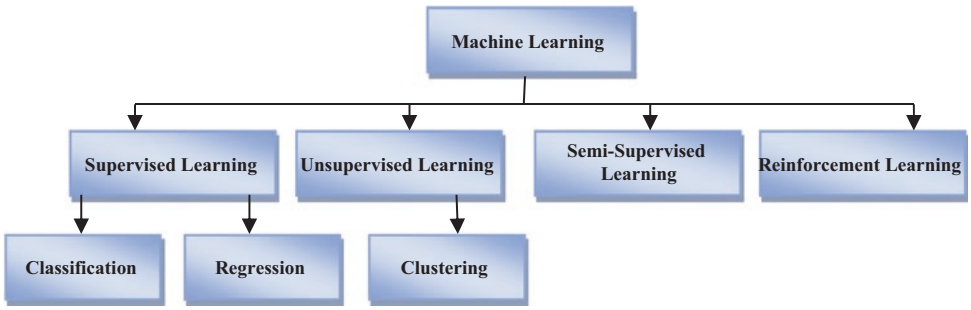

Fig. 1 Classification of machine learning approaches

Machine learning algorithms can be categorized into (Polese et al., 2018) supervised learning, unsupervised learning, semi-supervised learning, and reinforcement learning as shown in Fig. 1.

Its applications are used in the fourth generation of industry and communication, agriculture, irrigation, roads, mines, health care, and in the fields of marketing, insurance, banking, and translation. For example, in agriculture, these techniques are used in crop management in so-called precision agriculture (Nijeweme-d'Hollosy et al., 2018). Machine learning has been utilized extensively most recently during the COVID-19 pandemic (Italian Civil Protection Department et al., 2020; Xie et al., 2020; Zhou et al., 2020).

2 Methods

The application of machine learning for visualization and prediction is growing. Through Python Programming Language (Fig. 2) and a number of dedicated libraries, it is possible to achieve advanced visualization using Matplotlib which is a comprehensive library for creating static, animated, and interactive visualizations in Python "Matplotlib". "Seaborn" is a Python data visualization library based on "Matplotlib". It provides a high-level interface for drawing attractive and informative statistical graphics. Folium library provides mapping functions that build on the data wrangling strengths of Python and allow for mapping capabilities.

```
# importing the required libraries
import pandas as pd

# Visualisation libraries
import matplotlib.pyplot as plt
%matplotlib inline
import seaborn as sns
import plotly.express as px
import plotly.graph_objects as go
import folium
from folium import plugins
```

Fig. 2 Visualization libraries that are useable in Python

Autoregressive integrated moving average (ARIMA) is a class of models that is dealing with time series, based on the past values of the model. ARIMA model is by the order of the autoregression, and the moving average MA, and the number of differences required to make the time series stationary. It relies on the model lags and the lagged forecasting errors, in order to predict future values.

3 Results and Discussion

This section provides an overview of the steps taken in this research. It shows the visualization of demographics distribution in India and how the spread of COVID-19 provides some trends and indicators of the impact, as well as modeling and prediction of geospatial trends as it relates to India. The fifth part shows global modes of the spread of the COVID-19. Figure 3 provides further demographic distribution of the cases reported based on the demographics, where it was found that the majority of the reported cases are for the age group between 20 and 29 years old, which represents the highest fraction of the total population, with 24.9% of the total reported sick cases. The second-largest group of reported cases is for the age group between 30 and 39 years, with a total of 21% of all reported cases. It was observed that elderly reported cases were in the fifth category for the age group between 60 and 69 with a total of 12.9% only, surpassing the age group of 50–59 with 11.9% of the total population. *The demographics distribution figures* confirm that the age group < 40 is the most affected which is against the trend which says elderly people are at a higher risk of being affected. Only 17% of people > 60 are

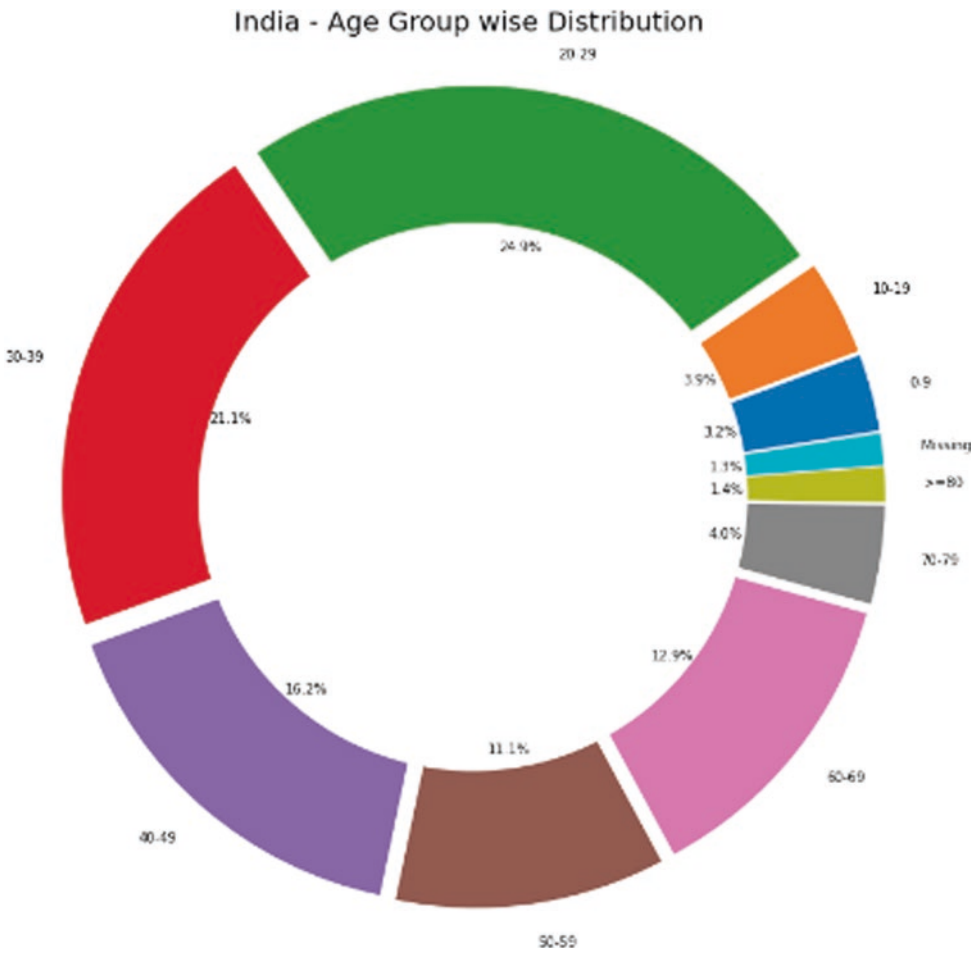

Fig. 3 Age-based demographic distribution of India's population

affected. Figure 4 shows a GIS Folium-produced map of the hotspots of COVID-19 and Fig. 5 shows the ARIMA prediction for 15 days.

4 Conclusions

Visualization of complex and big data for delineating spatiotemporal patterns for disaster management and emergency response has been considered widely during the recent spread of COVID-19. Visualizing invisible patterns of data and spatially enabling decision-makers with information contributes to the strength of knowledge that is mostly needed in extreme situations. Sharing data and allowing various contributing domains free and interoperable access to big data of COVID-19 provide added value for medical resources optimization, planning, and responding, as well as pattern recognition and the overall situational awareness that is highly demanded at the planning, operational, and decision-making levels during pandemic outbreaks. Using ARIMA made it was possible to predict 15 days in advance the spread of COVID-19, with high accuracy.

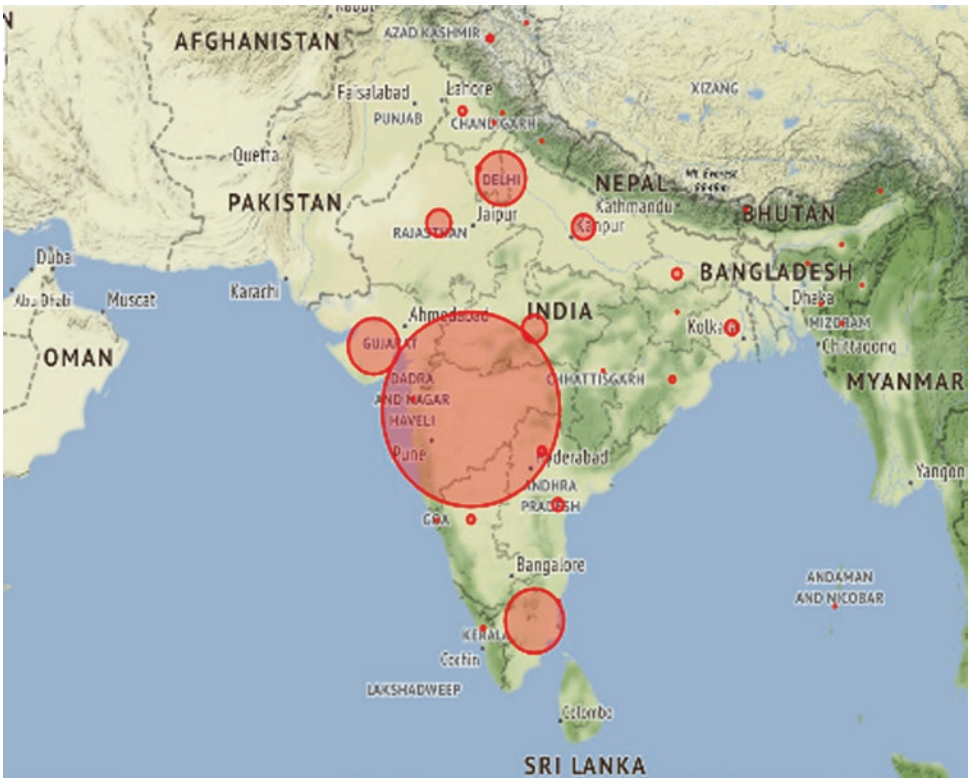

Fig. 4 Geospatial visualization of hotspots of the spread in India as of May 24, 2020

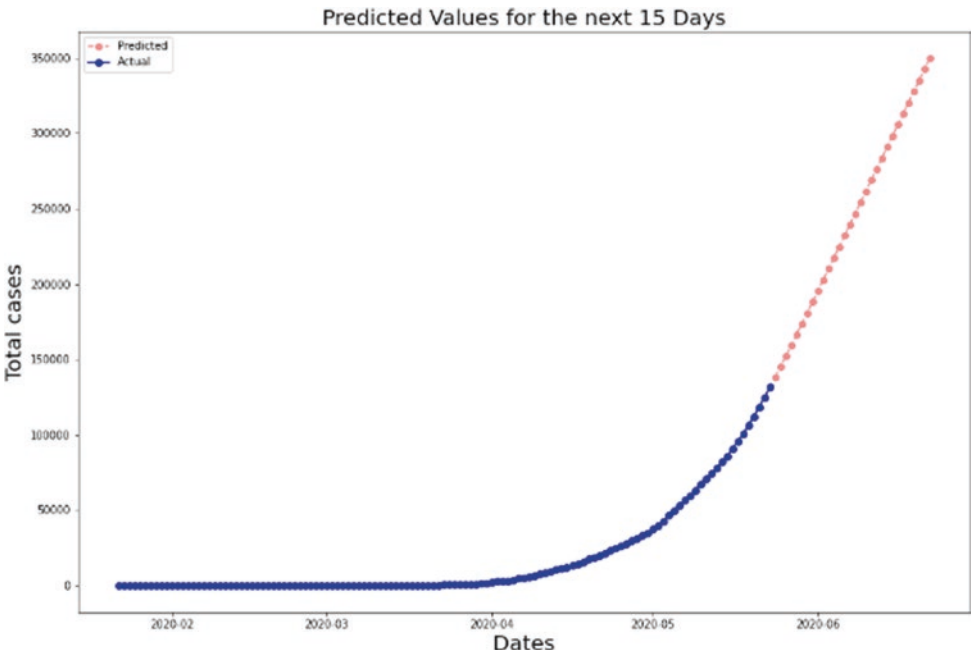

Fig. 5 15 days, ARIMA prediction of the total cases starting from May 24, 2020

References

Aljaaf, A. J., Hussain, A. J., Fergus, P., Przybyla, A., & Barton, G. J. (2016). Evaluation of machine learning methods to predict knee loading from the movement of body segments. In *IEEE International Joint Conference on Neural Networks (IJCNN)*. Cited May 03, 2018.

Brynjolfsson, E., & Mitchell, T. (2017). What can machine learning do? Workforce implications. *Science, 358*(6370), 1530–1534.

Italian Civil Protection Department, Morettini, M., Sbrollini, A., Marcantoni, I., & Burattini, L. (2020). COVID-19 in Italy: Dataset of the Italian Civil Protection Department. *Data in Brief, 30*. https://doi.org/10.1016/j.dib.2020.105526

Khan, F. N., Zhong, K., Al-Arashi, W. H., Yu, C., Lu, C., & Lau, A. P. T. (2016). Modulation format identification in coherent receivers

using deep machine learning. *IEEE Photonics Technology Letters, 28*(17), 1886–1889.

Nijeweme-d'Hollosy, W. O., van Velsen, L. S., Poel, M., Groothuis-Oudshoorn, C. G., Soer, R., & Hermens, H. (2018). Evaluation of three machine learning models for self-referral decision support on low back pain in primary care. *International Journal of Medical Informatics, 110*, 31–41.

Polese, M., Jana, R., Kounev, V., Zhang, K., Deb, S., & Zorzi, M. (2018). Machine learning at the edge: A data-driven architecture with applications to 5G cellular networks. ArXiv e-prints, August 2018.

Utkin, V., & Zhuk, Y. A. (2017). An one-class classification support vector machine model by interval-valued training data. *Knowledge-Based Systems, 120*, 43–56.

Xie, Z., Qin, Y., Li, Y., Shen, W., Zheng, Z., & Liu, S. (2020). Spatial and temporal differentiation of COVID-19 epidemic spread in mainland China and its influencing factors. *Science of the Total Environment, 744*, 140929. https://doi.org/10.1016/j.scitotenv.2020.140929

Zhou, C., Su, F., Pei, T., Zhang, A., Du, Y., Luo, B., Cao, Z., Wang, J., Yuan, W., Zhu, Y., Song, C., Chen, J., Xu, J., Li, F., Ma, T., Jiang, L., Yan, F., Yi, J., Hu, Y., … Xiao, H. (2020). COVID-19: Challenges to GIS with big data. *Geography and Sustainability, 1*(1), 77–87. https://doi.org/10.1016/j.geosus.2020.03.005

Use of Construction Waste in Soil Stabilization

Mustapha Tekkouk, Riad Benzaid, Douniamey Rebiai and Siham Boubeghel

Abstract

In the context of the reuse of plastic soils in the realization of road embankments and in order to preserve geo-resources, the present work consists of an experimental study of the relevant parameters and factors which govern the behavior in the laboratory of some plastic soils extracted from the Jijel region (North-East of Algeria) treated with construction waste. Our experimental study was carried out on two types of soils (clay and marl) stabilized according to various dosages of red brick and plaster waste. The obtained results show that the incidence of treatment with these two types of waste makes the mixture less sensitive to water, hence the flattening of the Proctor curve with a slight increase in the optimal water content.

Keywords

Construction waste · Clays · Marls · Stabilization · Compaction characteristics

1 Introduction

The search for deposit and borrow areas at economically profitable distances and preserving the natural harmony of the landscapes is becoming more and more problematic for earthworks. These difficulties, associated with the optimization of land movement and the respect of implementation deadlines (climatic hazards), have favored the technique of soil treatment over the past two decades (Akinwumi & Aidomojie, 2015; Bereterbide & Puiatti, 1990; CRR, 2010; Gandhi, 2012; Jayashree & YaminiRoja, 2019; Rossi et al., 2008; Singh et al., 2017). Several researchers have been interested in reusing waste from the building sector to stabilize clay soils. The interest of this kind of additions is to preserve the environment of this waste while reusing it to improve the geotechnical characteristics of clay soils (Ali Ashraf & Shazeebur Rahman, 2018; Cabalar et al., 2016; Neeladharan & Vinitha, 2017; Pathania & Soni, 2017; Safiuddin & Jumaat, 2010). In this work, we are interested in the treatment of plastic soil with bricks and plaster waste.

2 Experimental Program

In this study, two types of soil were used from two different places in the Wilaya of Jijel (North-East of Algeria). The geotechnical characteristics of the studied soils are presented in Table 1.

From these results, it is found that the clay soil is moist dense to moderately dense, while the marl soil is slightly moist dense to moderately dense soil.

The preparation of the soil samples and the performance of the compaction tests of the different series of tests were vigorously in accordance with standard NF P 94-093. In order to achieve our objectives and respond to the problem of the behavior of plastic soil treated with some inert waste from the buildings and public works sector, the experimental program carried out is detailed in Table 2.

3 Analysis and Discussion of the Obtained Results

3.1 Effect of Treatment with Brick Waste on Proctor Characteristics

From the experimental results presented in the Proctor curves of Figs. 1 and 2, we note that the red brick waste

M. Tekkouk · R. Benzaid (✉) · D. Rebiai · S. Boubeghel
Geological Engineering Laboratory (LGG), Jijel University, Jijel, Algeria
e-mail: r_benzaid@univ-jijel.dz

Z. A. Ergüler et al. (eds.), *Selected Studies in Geotechnics, Geo-informatics and Remote Sensing*, Advances in Science, Technology & Innovation, https://doi.org/10.1007/978-3-031-43759-5_34

Table 1 Geotechnical characteristics of the studied soils

	Clay soil	Marly soil
Wet density γ_h (kg/m^3)	21.76	22.20
Dry density γ_d (kg/m^3)	20.00	18.77
Water content W (%)	29.00	19.00
Plastic limit W_P (%)	23.56	18.99
Liquid limit W_L (%)	64.70	30.96
Plasticity index I_p	41.14	11.97
Consistency index I_c	0.87	0.99

does not have a notable effect on the mechanical behavior of the two studied soils (clays and marls) with respect to the values of the characteristics of compaction (γ_{dmax}, w_{opt}). The Proctor curves of both studied soils are slightly shifted to the right; they have a flattened shape which reflects the low sensitivity of these mixtures to water (Figs. 1 and 2). This improvement vis-à-vis the sensitivity of the mixture to water is interesting for the treatment of this type of plastic soil in road construction sites. On the other hand, the inert aspect and the lack of cohesion of this type of waste is at the origin of this type of behavior which makes the compaction of the treated soil similar to that of a non-cohesive soil.

3.2 Effect of Treatment with Waste Plaster on Proctor Characteristics

After treatment with the plaster waste by adding for each test sample 2, 4, 6, and 25%, the Proctor curves of the treated soils are shifted to the right; they have a flattened shape which reflects the low sensitivity of these mixtures to water (Figs. 3 and 4). With the exception of samples treated with 25% of plaster waste where the curves have an accentuated shape (this indicates the existence of a saturation threshold). In Fig. 3, treatment with waste plaster with

Table 2 Details of the experimental program

Series of tests carried out	Soil type	Atterberg's limits' tests	Observations
Series No. 01 Effect of soil treatment with red brick waste on compaction characteristics	Clay soil	Reference soil	Without treatment
		Soil treated with brick waste	2, 4, 6, and 25%
	Marly soil	Reference soil	Without treatment
		Soil treated with brick waste	2, 4, 6, and 25%
Series of tests carried out	Soil type	Soil compaction tests	Observations
Series No. 02 Effect of soil treatment with plaster waste on compaction characteristics	Clay soil	Reference soil	Without treatment
		Soil treated with plaster waste	2, 4, 6, and 25%
	Marly soil	Reference soil	Without treatment
		Soil treated with plaster waste	2, 4, 6, and 25%

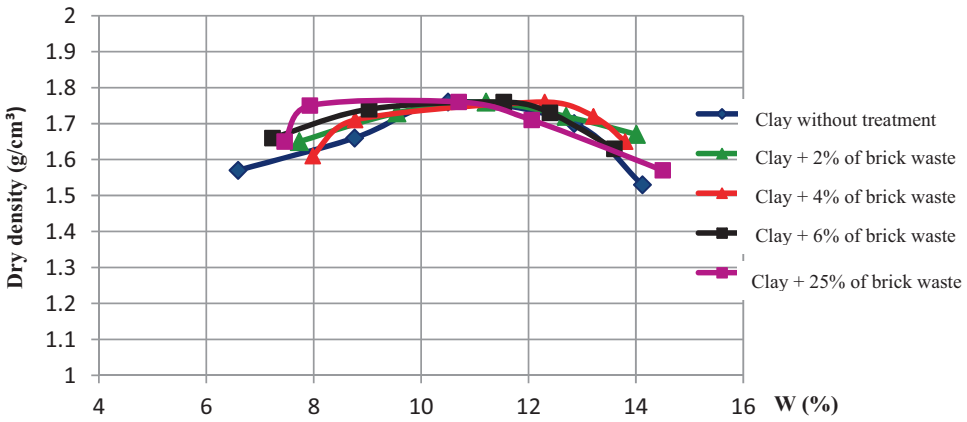

Fig. 1 Influence of treatment with brick waste on the Proctor curves of clays

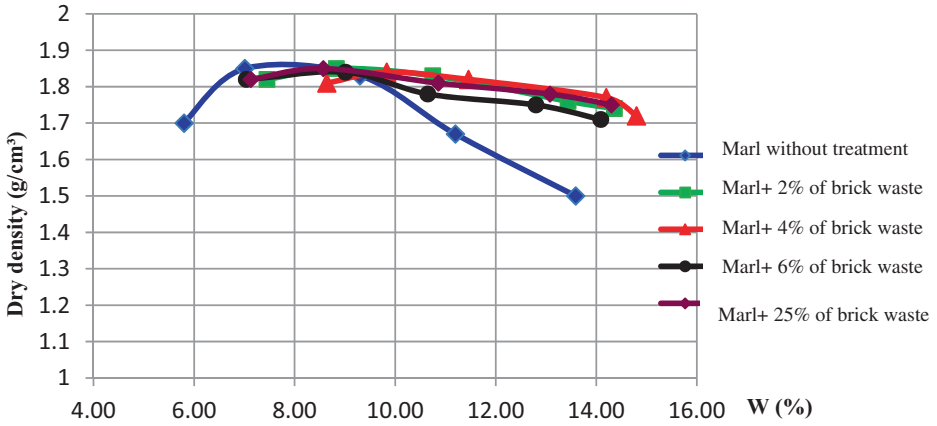

Fig. 2 Influence of treatment with bricks waste on the Proctor curves of marls

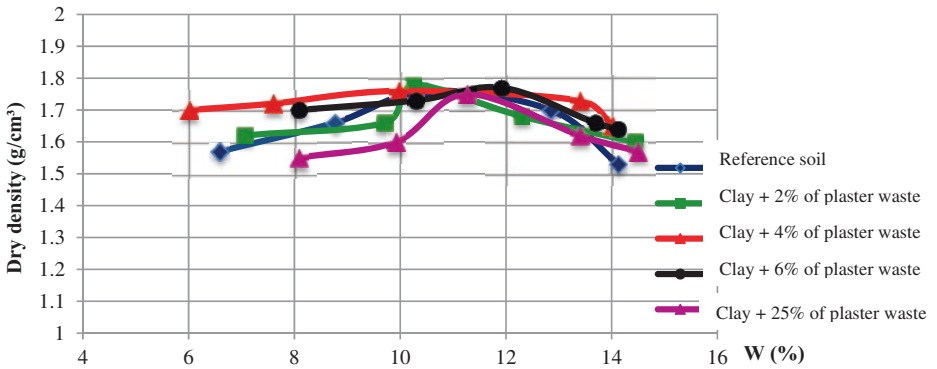

Fig. 3 Influence of treatment with plaster waste on Proctor curves of clays

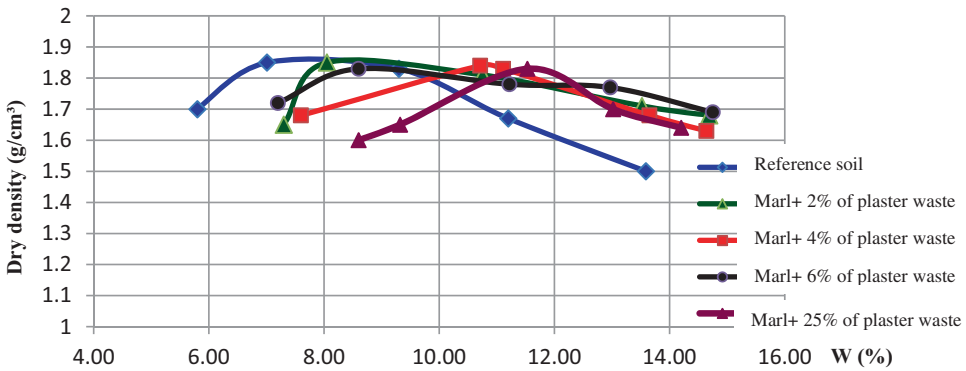

Fig. 4 Influence of treatment with plaster waste on the Proctor curves of marls

additions of 2, 4, and 6% slightly improved the density of the optimum Proctor with a slight consumption of water above the optimum (about 1% increase).

4 Conclusions

From the experimental results presented in this work, we noted that the red brick waste does not have a notable effect on the mechanical behavior of the two soils studied (clays and marls) with respect to the values of the characteristics of compaction (γ_{dmax}, w_{opt}). On the other hand, the Proctor curves of the two studied soils are slightly shifted to the right; they have a flattened shape which reflects the low sensitivity of these mixtures to water. This improvement in the sensitivity of the mixture to water is interesting for the treatment of this type of plastic soil in road construction sites. The inert aspect and the lack of cohesion of this waste is at the origin of this type of behavior which makes the compaction of treated soils similar to that of powdery soil following the substitution of fine soil particles by inert particles of red brick.

On the other hand, after adding the plaster waste (2, 4, 6, and 25%) to the studied soil, the Proctor curves are shifted

to the right with the exception of the samples treated with 25%, where the curves presented an accentuated shape. This indicates the existence of a saturation threshold.

The rest of our work will be oriented toward the study of the bearing capacity, the compressibility, and the shear characteristics of the treated soil.

References

Akinwumi, I. I., & Aidomojie, O. I. (2015). Effect of corn cob ash on the geotechnical properties of lateritic soil stabilized with Portland cement. *International Journal of Geomatics and Geosciences, 5*(3), 375–392.

Ali Ashraf, M., & Shazeebur Rahman, S. M. (2018). Determination of optimum cement content for stabilization of soft soil and durability analysis of soil stabilized with cement. *American Journal of Civil Engineering, 6*(1), 39–43.

Bereterbide, J., & Puiatti, D. (1990). Traitement des sols à la chaux et (ou) aux ciments. *Note d'information, 59*(DTCES6CETE Sud-ouest), 1–4.

Cabalar, A. F., Abdulnafaa, M. D., & Karabash, Z. (2016). Influences of various construction and demolition materials on the behavior of a clay. *Environmental Earth Sciences, 75*, 841. https://doi.org/10.1007/s12665-016-5631-4

CRR. (2010). *Code de bonne pratique pour le traitement des sols à la chaux et/ou aux liants hydrauliques, R81/10* (22 pp.). Centre de recherches routières.

Gandhi, K. S. (2012). Expansive soil stabilization using bagasse ash. *International Journal of Engineering Research and Technology, 1*(5), 1–3.

Jayashree, J., & YaminiRoja, S. (2019). Stabilization of expansive soil using rice husk ash and lime. *International Journal of Recent Technology and Engineering, 8*(3), 2661–2665.

Neeladharan, C., & Vinitha, V. (2017). Stabilisation of soil by using tiles waste with sodium hydroxide as binder. *International Journal of Innovative Research in Science, Engineering and Technology, 6*(4), 1–7.

Pathania, M., & Soni, D. K. (2017). Combined effect of quarry dust and ceramic dust on stabilisation of clay. *International Journal of Advance Research in Science and Engineering, 6*(1), 297–302.

Rossi, P., Gavois, L., & Raoul, G. (2008). *Traitement des matériaux* (C 5 362, 19 pp.). Techniques de l'ingénieur.

Safiuddin, M., & Jumaat, M. Z. (2010). Utilization of solid wastes in construction materials. *International Journal of the Physical Sciences, 5*(13), 1952–1963.

Singh, M., Sharma, R., & Sharma, A. (2017). Soil stabilization using industrial waste (wheat husk and sugarcane straw ash). *International Research Journal of Engineering and Technology, 4*(9), 589–596.

Analysis of Fly Ash and Lime on Stabilization in Clay Soil to Increase Friction Resistance of Pile Foundation

Muhammad Mukhlisin, Muhammad Bintang Kurniaji, R. Hernanda Ade Wibawa, Aiun Hayatu Rabinah, Mochamad Tri Rochadi and Rini Kusumawardani

Abstract

The bearing capacity of the pile foundation is influenced by soil parameters, namely the internal friction angel (φ) and cohesion (c). In this study, a laboratory-scale experiment is conducted to determine the behavior and changes of friction resistance piles in clay soils stabilized with lime and fly ash. Soil samples are taken following 4 scenarios which are soil, and mixtures of 5% lime and 5% fly ash, 5% lime with 10% fly ash, and 5% lime with 15% fly ash. Soil samples will be soaked for one day, and they will be dried at room temperature for 1, 7, and 28 days. The addition of lime and fly ash causes a decrease of soil plasticity. This is because lime and fly ash cause pozzolan reactions that change clay soil material. The highest friction resistance value occurred at drying for 7 days for all scenarios.

Keywords

Soil stabilization · Bearing capacity · Foundation failure

1 Introduction

The foundation is an important part of a building, which serves a basis to withstand the load of a construction. The bearing capacity of the pile foundation influenced by soil parameters, namely the internal friction angel (φ) and cohesion (c).

The amount of fly ash lime needed to increase soil strength effectively varies according to the type of clay mineral (Zumrawi & Hamza, 2014). The stabilization of clay with lime could change and improve the physical and mechanical characteristics of clay due to cation exchange, particle changes, and pozzolanic reactions (Loufi et al., 2015). Research to determine the effect of fly ash and lime stabilization on expansive clay is conducted by Dahale et al. (2016). Generally, the UCS, CBR, and BTS values of stabilized soil increased (Loufi et al., 2015). Research related to the friction resistance of group piles on clay through a laboratory-scale loading test used remolded soil with 4 Ø16 mm pile models. The friction resistance of the pile on remolded soil with treatment was not the same as the initial condition even though the water content was the same or lower (Hamdani & dan Ernawati, 2017).

Many studies have recognized the effectiveness of stabilizing expansive clay with lime and fly ash. Besides, research on increasing the shear strength of clay soil through the stability of lime and fly ash has also been carried out. However, experimental research related to the shear strength behavior of stabilized clay soils has not been widely carried out. Therefore, in this study, laboratory-scale experiments were carried out to determine the behavior and changes in the friction resistance of piles in clay stabilized with lime and fly ash.

2 Method

Soil samples in this study were clay soil taken in the city of Semarang. Soil samples were made in 4 variations and have undergone special treatment (wetting and drying). The treatment consists of soaking the samples for 1 day and drying it at room temperature for 1, 7, and 28 days. The sample scenario can be seen in Table 1.

This research was conducted in laboratory experiments through modeling using four piles with a diameter

M. Mukhlisin (✉) · M. B. Kurniaji · R. Hernanda Ade Wibawa · A. H. Rabinah · M. T. Rochadi
Department of Civil Engineering, Politeknik Negeri Semarang, Semarang, Indonesia
e-mail: mmukhlis@polines.ac.id

R. Kusumawardani
Department of Civil Engineering, Universitas Negeri Semarang, Semarang, Indonesia

Z. A. Ergüler et al. (eds.), *Selected Studies in Geotechnics, Geo-informatics and Remote Sensing*, Advances in Science, Technology & Innovation, https://doi.org/10.1007/978-3-031-43759-5_35

Table 1 Sample testing scenarios

Scenario	Mixture	Treatment			
		Soaked (PR) (day)	Drying (PM) (day)		
		1	1	7	28
1	Soil (S1)	✓	✓	✓	✓
2	5% lime + 5% fly ash (S2)	✓	✓	✓	✓
3	5% lime + 10% fly ash (S3)	✓	✓	✓	✓
4	5% lime + 15% fly ash (S4)	✓	✓	✓	✓

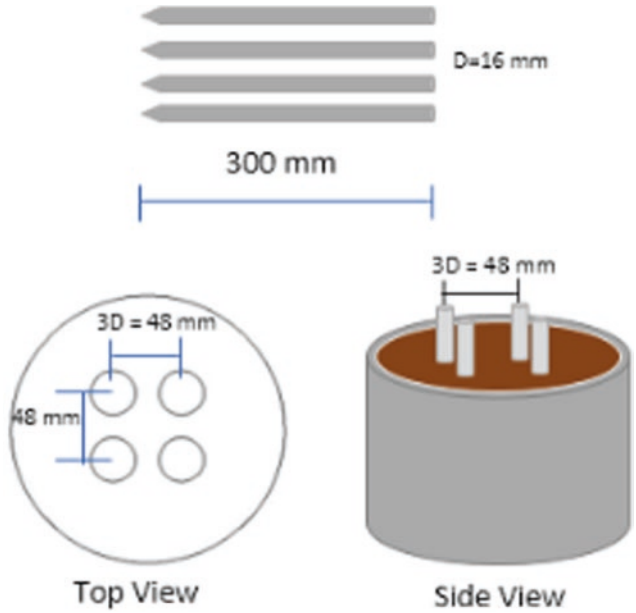

Fig. 1 Illustration of penetration piles model

of 16 mm penetrated inside a mold fabricated from a 3 in. diameter PVC pipe. The pile model for research is made of concrete using mold PVC with a diameter of 16 mm (Fig. 1).

The unconfined compression test in this research is used for loading tests on the pile model. The schematic loading test is shown in Fig. 2.

3 Results and Discussions

3.1 Atterberg Limit

The method to describe the consistency of soil is the Atterberg limit. The results for liquid limit (LL) the Scenarios 1, 2, 3, and 4 are 64%, 37%, 35%, and 36%,

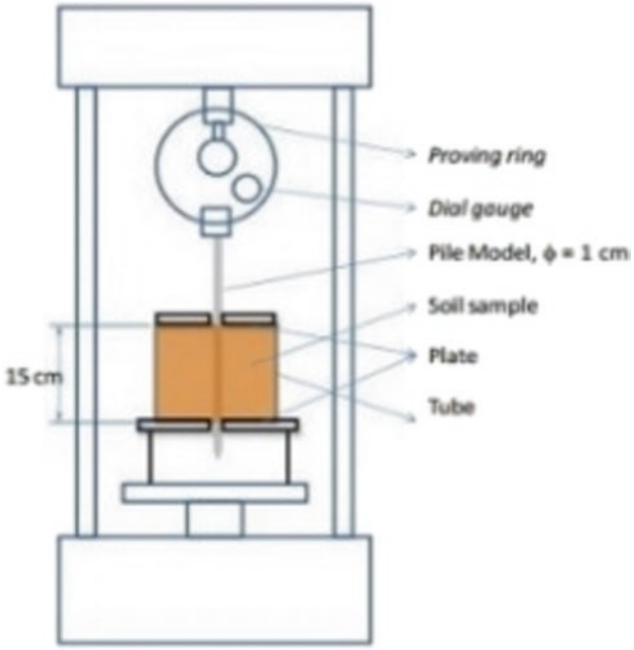

Fig. 2 Schematic of friction resistance testing

respectively. The plastic limit value (PL) for Scenarios 1, 2, 3, and 4 is 43%, 29%, 27%, and 25%, respectively. The plasticity index (PI) value for Scenarios 1, 2, 3, and 4 is 21%, 8%, 8%, and 11%, respectively. The PL value in clay soil decreased after the addition of fly ash and lime (Scenarios 2, 3, and 4). Meanwhile, the LL and PI values decreased until reaching Scenario 3, and increased again in Scenario 4. However, it concluded that with the addition of lime and fly ash, the LL, PL, and PI values decreased from the initial conditions. While the index properties of soil for Scenarios 1, 2, 3, and 4 which include specific gravity (Gs), dry unit weight, void ratio (e), porosity (n), and degree of saturation (Sr) of soil can be seen in Table 2.

3.2 Friction Resistance

The friction resistance value for each scenario can be seen in Fig. 3. Figure 3a shows that the maximum friction value of the sample is soaked for 1 day and dried for 1 day at Scenarios 1, 2, 3, and 4 which are 0.59 kg/cm^2,

Table 2 Index properties

Parameters	Unit	S1	S2	S3	S4
Specific gravity, Gs		2.65	2.56	2.59	2.61
Dry unit weight	g/cc	1.46	1.43	1.49	1.50
Void ratio, e		0.82	0.80	0.74	0.74
Porosity, n		0.45	0.44	0.42	0.43
Degree of saturation, Sr	%	78.56	69.60	84.54	78.14

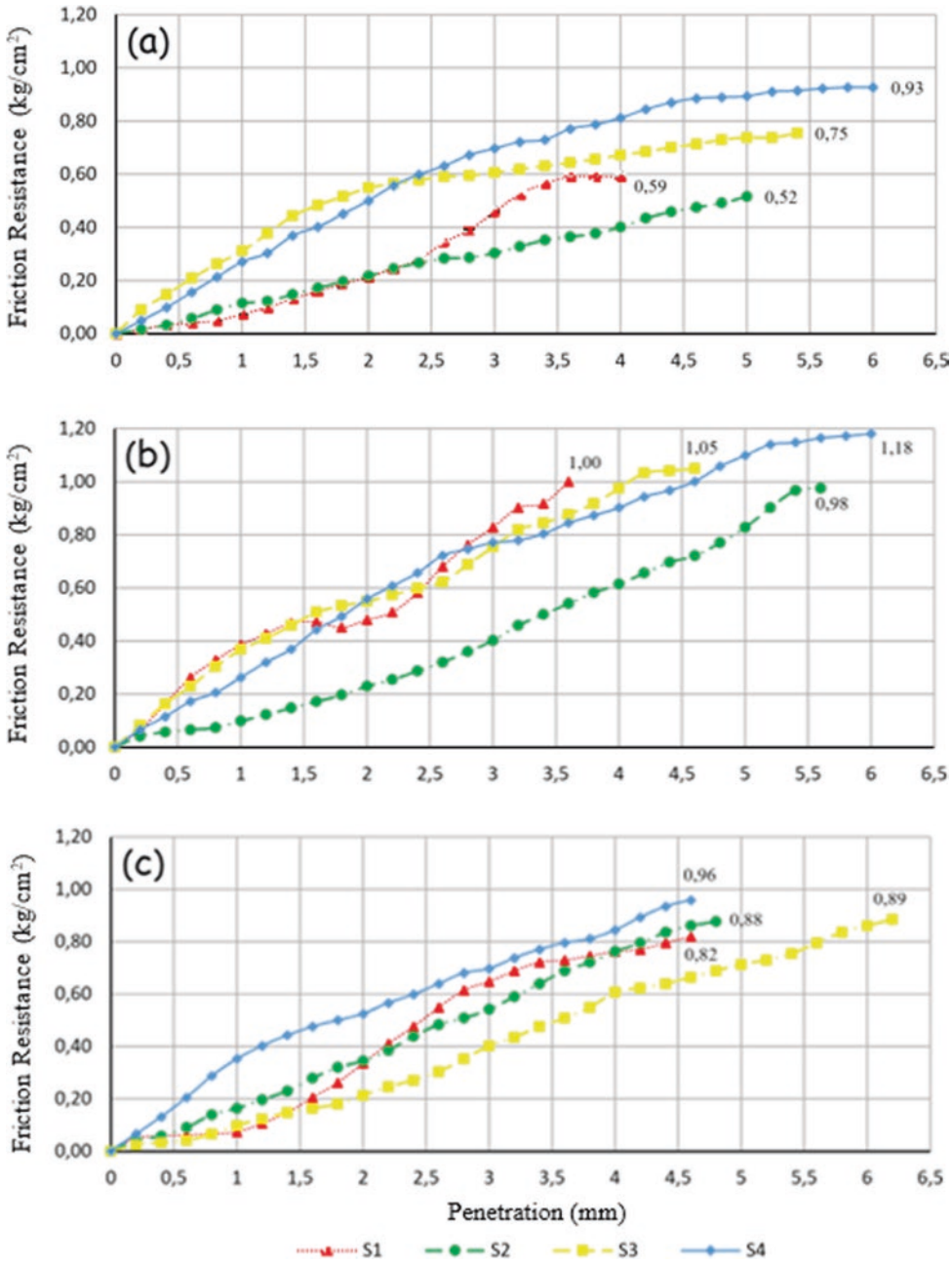

Fig. 3 The relationship of friction resistance against penetration for 1 day soaked. **a** PM 1 day, **b** PM 7 days, **c** PM 28 days

0.52 kg/cm^2, 0.75 kg/cm^2, and 0.93 kg/cm^2, respectively. The results of the samples soaked for 1 day and dried for 7 days can be seen in Fig. 3b, where the maximum friction values of Scenarios 1, 2, 3, and 4 are 1.00 kg/cm^2, 0.98 kg/cm^2, 1.05 kg/cm^2, 1.18 kg/cm^2, respectively. While the results of the samples soaked for 1 day and dried for 28 days can be seen in Fig. 3c, where the maximum friction values of Scenarios 1, 2, 3, and 4 are 0.88 kg/cm^2, 0.82 kg/cm^2, 0.89 kg/cm^2, and 0.96 kg/cm^2, respectively. The value of friction resistance after drying for 1, 7, and 28 days decreased in Scenario 2 then increased in Scenarios 3 and 4. The highest friction resistance value occurred with drying for 7 days for all scenarios.

4 Discussion

The Atterberg Limit (LL, PL, PI) for all conditions has decreased from the initial conditions. It may seem that the addition of lime and fly ash tends to reduce the plasticity

of the soil; this is because the mixture of lime and fly ash causes a pozzolan reaction, which changes the clay material. The value of friction resistance after drying for 1, 7, and 28 days decreased in Scenario 2 then increased in Scenarios 3 and 4. The highest friction resistance value occurred with drying for 7 days for all scenarios.

5 Conclusions

Based on the results of research and testing in the laboratory regarding the effect of adding fly ash and lime on the friction value of clay, it can be concluded that the addition of lime and fly ash causes a decrease in soil plasticity (LL, PL, and PI); this is because lime and fly ash cause a pozzolan reaction, which changes the clay material. The value of friction resistance after drying for 1, 7, and 28 days decreased in Scenario 2 then increased in Scenarios 3 and 4. The highest friction resistance value occurred at drying for 7 days for all scenarios.

References

Dahale, P. P., Nagarnaik, P. B., & Gajbhiye, A. Y. (2016). Effect of flyash and lime on stabilization of expansive soil. *I-Manager's Journal on Civil Engineering, 6*(2), 8–12.

Hamdani, B., & dan Ernawati, W. (2017). *Behavior of pile group friction bearing capacity in clay soil through laboratory scale loading test* (Final report of Bachelor Engineering). Study Program of Road and Bridge Design, Department of Civil Engineering, Politeknik Negeri Semarang, Indonesia.

Loufi, B., Hadef, B., & Bahar, R. (2015). Improvement of geotechnical characteristics of clay soils using lime. *Advance Materials Research, 1105*, 315–319.

Zumrawi, M. M. E., & Hamza, O. S. M. (2014). Improving the characteristics of expansive subgrade soils using lime and fly ash. *International Journal of Science and Research, 3*(12), 1124–1129.

Numerical Analysis of the Dynamical Behavior of Machine Foundations

Gabriel Oliveira Freitas Santos and Celso Romanel

Abstract

This paper analyzes dynamic vertical loadings of machine foundations on embedded structures. Pile raft foundations are analyzed using different approaches. Simplified embedded shallow foundations' solutions by Wolf and by Novak and Beredugo, coupled with Novak and El-Sharnouby's pile foundations (considering both static additional settlement ratios obtained by Poulos and Davis and dynamic additional settlement ratios obtained by Finite Element Method) dynamic analysis, were studied. Settlements obtained on the steady state regime are compared to the values obtained by tri-dimensional finite element method analysis using the software Plaxis 3D, proving the efficiency of dynamic additional settlement ratios.

Keywords

Finite element method · Soil dynamics · Machine foundations · Steady state displacements · Plaxis 3D

1 Introduction

The steady state dynamic vibration problem analysis starts being studied all over the world during the industrialization process. Cyclic loadings, to which industries are typically subjected to due to the motion of their machines, cause additional displacements to the structure on a perpetual state. Therefore, buildings with machinery must be prepared to suffer the displacement on each new loading cycle and designed not to develop any structure harm due to the motion. On this paper, cases of dynamic loadings applied on pile raft foundations are evaluated by numerical and analytical methods.

G. O. F. Santos (✉) · C. Romanel
Pontifícia Universidade Católica do Rio de Janeiro, Rio de Janeiro, Brazil
e-mail: gabriel_olfs@hotmail.com

2 Methods and Materials

Pile raft foundations, which are subjected to dynamic loadings, have contributions from all their elements on their dynamic impedances, considered a sum of the stiffnesses of the shallow foundation (the raft itself) and deep foundation (the pile group) of the structure. Evaluating the problem as a harmonic dynamic case, soil's response to displacement is given by Eqs. 1 and 2:

$$K_d = K_s + i * \omega * C - \omega^2 m, \tag{1}$$

$$\frac{P_0}{K_d} = z_0, \tag{2}$$

with K_d = dynamic stiffness (N/m); K_s = static stiffness (N/m); C = soil's damping coefficient (N s/m); m = foundation mass (kg); ω = vibration's angular frequency (rad/s); i = imaginary number; P_0 = external force module (N); and z_0 = maximum steady state displacement (m).

Regarding shallow foundation's geometry, on this paper, it is considered the case of a circular foundation with mass and an embedment with the same value as the foundation's radius. Dynamic stiffnesses are calculated by two different analytical methods; Novak and Beredugo (1971), as presented on Das and Ramana (2010) and stress propagation 1D cones by Wolf (1994), using double cones with anti-symmetric and symmetric mirror disks to simulate embedment of the foundation.

Dynamic impedance of the pile group is calculated by Novak and El-Sharnouby's (1983) analytical method, quoted on Das and Ramana (2010), which establishes a dynamic coefficient to a singular pile and reduces each pile's stiffness by an interaction factor dependent of each

Z. A. Ergüler et al. (eds.), *Selected Studies in Geotechnics, Geo-Informatics and Remote Sensing*, Advances in Science, Technology & Innovation, https://doi.org/10.1007/978-3-031-43759-5_36

pile's length (L), diameter (d), distances between piles (s), and pile's stiffness. This interaction factor is also known as additional settlement ratio, and an analytical solution to these ratios for the static loading case was obtained by Poulos and Davis (1991).

In order to develop a dynamic solution by numerical analysis, Plaxis 3D and a geotechnical software that models problems through Finite Element Method (FEM) are used to observe displacements of a pile under dynamic loading. Numerical model's boundaries' conditions were set as viscous dynamic boundaries, which dissipate stress waves that reach the boundary, simulating geometrical damping on the soil. The dynamic frequencies evaluated on FEM analysis avoid natural frequencies of the evaluated soils.

A singular pile with an infinite stiffness is subjected to a dynamical loading. Then, two piles on a near distance are subjected to the same loading, in order to evaluate dynamic additional settlement ratios to said distance. The piles had a length–diameter ratio of 10 and 25. Dynamic additional settlement ratios to different elasticity modulus of the media, distances between piles, and frequencies are given on Table 1.

In order to simulate steady state displacement on FEM, 10 dynamic loading cycles are applied on the top of the raft during a dynamic stage, which is followed by a static stage, and then another dynamic loading cycle is applied on the structure.

Two cases of pile raft foundations are modeled. Case 1's structure has a pile group of 4 circular piles, 0.2 m diameter and 5 m. The raft foundation is of 1 m height, circular, with 1 m radius. Raft's dimensions are very large compared to the pile's dimensions in order to guarantee the same distances between the piles to better observe the effects of dynamic interaction factors. Polynomial equations were used in order to better estimate dynamic additional settlement ratios to all s/d.

Case 2's structure has a pile group of 4 circular piles, of 0.1 m diameter and 2.5 m length. The raft foundation is of 1 m height, circular with 1 m radius. Figure 1 illustrates both cases of pile raft foundations analyzed on this paper.

Pile raft foundation's material is concrete, and the elasticity modulus is 21 GPa. Material stiffness is high enough to avoid flexure strains on its edges. The structure's mass is considered on the numerical analysis.

Upper soil layer's elasticity modulus is 5 MPa, and the half-space's elasticity modulus is 10 MPa. The interface of both media is on the lower part of the raft. Soils are modeled as Hardening Soil model, with a specific weight of 18 kN/m^3.

3 Results

3.1 Pile Raft Foundations on Low Compressibility Soil

Dynamic additional settlement ratios led to displacements closer to the ones obtained on Plaxis 3D to all evaluated analytical methods. Figures 2 and 3 compare displacements obtained by Plaxis 3D and by dynamic and static additional settlement ratios with Wolf's method.

3.2 Pile Raft Foundation 2 on a Soil with No Lateral Strain

Wolf's analytical solution led to displacements closer to FEM than Novak and Beredugo's. Figure 4 shows steady state displacements to the analyzed frequencies for all methods used on this paper.

Table 1 Dynamic additional settlement ratios to different soil's elasticity modulus (E), length–diameter ratio (L/d), distance between pile centers–diameter ratio (s/d), and frequencies

α ($L/d=10$; $E=10$ MPa)				α ($L/d=10$; $E=1$ MPa)			
f (Hz)	$s/d=10$	$s/d=5$	$s/d=2$	f (Hz)	$s/d=10$	$s/d=5$	$s/d=2$
0.5	18.21	33.34	59.17	0.5	17.27	32.43	58.34
1	17.68	32.91	58.90	1	17.17	32.36	58.28
2	17.33	32.60	58.73	2	17.33	32.44	58.35
5	17.48	32.73	58.81	5	18.16	33.83	56.69
α ($L/d=25$; $E=10$ MPa)				α ($L/d=25$; $E=1$ MPa)			
f (Hz)	$s/d=10$	$s/d=5$	$s/d=2$	f (Hz)	$s/d=10$	$s/d=5$	$s/d=2$
0.5	41.38	58.70	81.66	0.5	32.48	48.67	73.65
1	40.43	58.03	81.36	1	32.33	48.58	73.62
2	39.86	57.63	81.19	2	32.69	48.82	73.71
5	40.21	57.92	81.32				

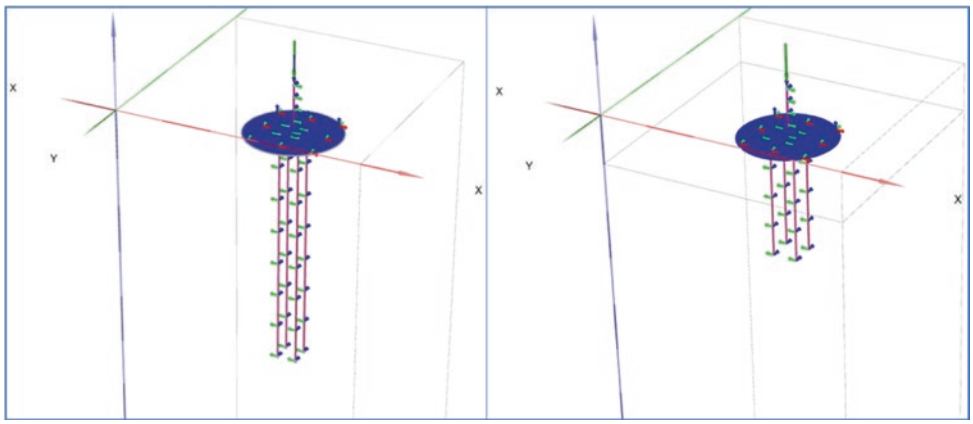

Fig. 1 Pile raft foundations' geometry on Plaxis 3D platform. On the left side, pile raft from case 1; on the right side, pile raft from case 2

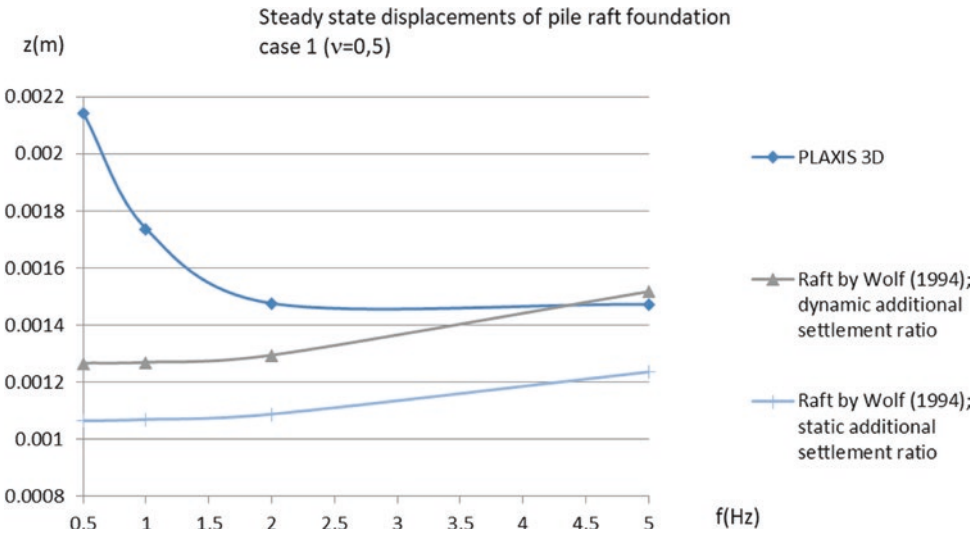

Fig. 2 Steady state displacements obtained by Wolf's 1D stress and FEM to low compressibility soils (case 1)

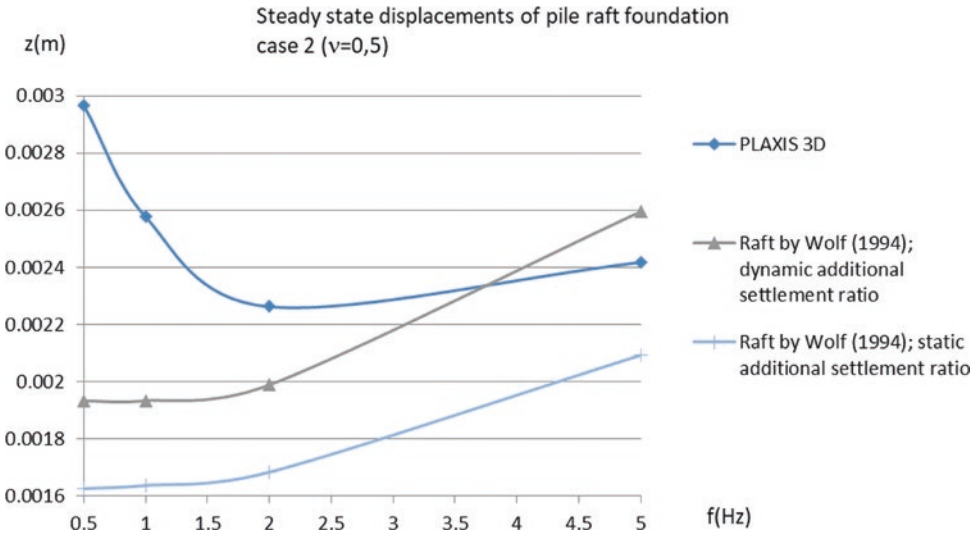

Fig. 3 Steady state displacements obtained by Wolf's 1D stress and FEM to low compressibility soils (case 2)

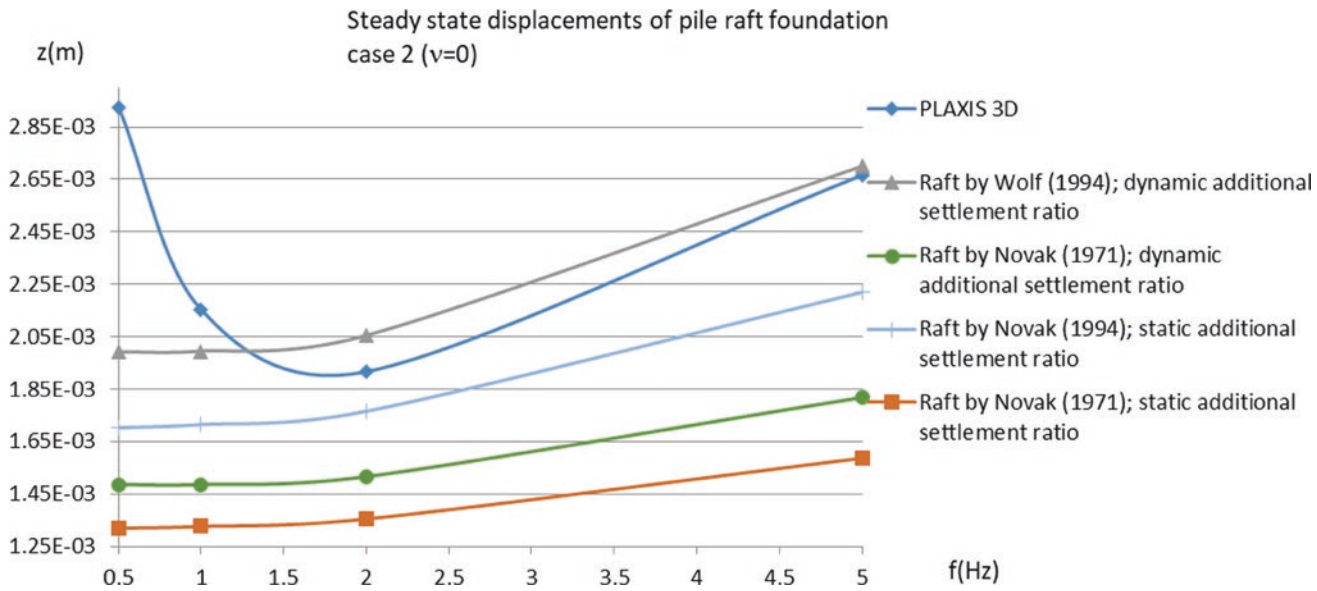

Fig. 4 Steady state displacements obtained by Wolf's 1D stress, Novak and Beredugo, and FEM to pile raft foundation to soils with no lateral strain (case 2)

4 Conclusions

The employed methods obtain displacements closer to FEM displacements when using dynamic additional settlement ratios.

Wolf's analytical method of 1D stress cone has better precision to embedded foundations subjected to dynamic vertical loadings.

References

Das, B. M., & Ramana, G. V. (2010). *Principles of soil dynamics*. Cengage Learning.

Poulos, H. G., & Davis, E. H. (1991). *Elastic solutions for soil and rock mechanics*. University of Sydney.

Wolf, J. P. (1994). *Foundation vibration analysis using simple physical models*. BooksCraft Inc.

Evaluation of Various Modes of Fracture Toughness (Mode I, II, and I + II) in Indian Limestone Based on AE Parameters

Tariq Anwar Ansari, Hemant Kumar Singh, Mohammed Sazid, Hari Om Singh, Trilok Nath Singh, Kumar Hemant Singh and Hui Zhou

Abstract

Limestone acts as a reservoir rock and is being routinely used as building material. It regularly considers the main raw ingredient in the manufacture of Portland cement. The rock fracturing is characterized by fracture toughness and stress intensity factor. Therefore, the determination of fracture toughness in various modes (mode I, mode II, and mixed mode (I + II)) is essential to understand the fracturing process in limestone. In this paper, we investigate the various modes of fracture toughness based on three-point bending test of SCB specimen. A total of 15 SCB specimens with five different notch angles (0°, 15°, 30°, 45°, and 60°) were selected and tested at a constant loading rate (5 kN/min). During the SCB specimen loading, the acoustic emissions are recorded using two transducers to monitor fractures in limestone. The determined fractures' toughness in various modes, fracture length, and fracture orientation from tip of notch are studied with reference to acoustic emission (AE) parameters such as AE counts, cumulative AE counts, and cumulative AE energy. The experimental results indicate that AE counts, cumulative AE counts and AE energy, and cumulative energy show similar trend with time and load, and these undergo with three different stages. The cumulative energy shows gradual decreasing trend with mode I fracture toughness, whereas it shows gradual increasing trend with mode II fracture toughness. The cumulative energy increases with notch angle and crack length. The possible reasons behind obtained results were discussed in detail. This study will enhance the understanding of fracture toughness with reference to AE characteristics.

Keywords

Fracture toughness · AE characteristics · AE energy · Fracture length · Limestone

1 Introduction

Limestone is a vital rock type, and it covers around 10% of total sedimentary rock on the earth crust. It acts as reservoir rock and is also being used as building materials. Moreover, it frequently considers the main raw ingredient in the manufacture of Portland cement. A noteworthy portion of the oil reservoirs fields are frequently placed in limestone (Bombay High oil field, Taranaki Basin oil, and gas, etc.). It is considered as prime bedrock for roadbeds, bridges, and tunnel constructions, slope protection engineering, water conservancy, and hydropower engineering. The use of limestone is mostly common in architect design, especially in Europe and North America. The world's most famous landmarks were built using limestone such as Great Pyramid, many buildings in Kingston, Ontario, Canada; Megalithic Temples of Malta; Riley County Courthouse, Manhattan; Kansas, USA. The limestone is also being used for storage

T. A. Ansari (✉) · H. O. Singh · T. N. Singh · K. H. Singh
Department of Earth Sciences, Indian Institute of Technology Bombay, Mumbai 400076, India
e-mail: 22tariq@gmail.com

H. K. Singh · H. Zhou
State Key Laboratory of Geomechanics and Geotechnical Engineering, Institute of Rock and Soil Mechanics, Chinese Academy of Sciences, Wuhan 430071, China

H. K. Singh · H. Zhou
Department of Earth Sciences, University of Chinese Academy of Sciences, Beijing 100049, China

H. K. Singh
Department of Petroleum Engineering and Geoengineering, Rajiv Gandhi Institute of Petroleum Technology, Jais, Amethi, Uttar Pradesh 229304, India

M. Sazid
King Abdul-Aziz University, Jeddah, Saudi Arabia

Z. A. Ergüler et al. (eds.), *Selected Studies in Geotechnics, Geo-informatics and Remote Sensing*, Advances in Science, Technology & Innovation, https://doi.org/10.1007/978-3-031-43759-5_37

of CO_2 gases and site deep geological repository (storage of heat-emitting nuclear fuel waste). Therefore, a comprehensive understanding of physico-mechanical and fracturing process is important for limestone rock as it directly relate to these projects' stability, and is therefore helpful to forecast risk. During the past decades, many researchers studied physico-mechanical properties of limestones from various parts of the world (Guo et al., 2001; Huang et al., 2016; Zhao & Cao, 2013). A few researchers considered the fracturing behavior of limestone (Kuruppu & Chong, 2012; Zhang et al., 2019). However, fracture toughness of limestone rock using SCB specimen with reference to AE parameters does not seem to get much attention and need a detailed study of the same.

In this study, the various mode of fracture toughness (mode I, II, and I+II) of SCB specimens of limestone was calculated, and the corresponding variations in the AE characteristics, occurs during experimental determination, were determined at different loading angles (0°, 15°, 30°, 45°, and 60°). The fracture initiation angle and fracture process zone from mode I to mode II including mixed mode (I+II) fracture toughness were studied in limestone rock with reference to AE characteristics. The energy release rate, obtained during fracturing process, was determined and correlated with AE count and AE energy for all mode of fracture.

2 Methods

2.1 Specimen Preparation

Limestone block samples were collected from East Jaintia Hill district, in the state of Meghalaya, India (Fig. 1a). Geologically, the limestone belongs to Upper Sylhet/Simsang Formation/Prang Limestone of Shella formation (Jaintia Group) (Department of Mining and Geology, 2020). The limestone is basically exposed along the hill slopes, valley, and flat grounds. It is exposed therein as massive and thinly bedded. In order to determine different modes of fracture toughness, core samples of limestone were prepared in the laboratory and, subsequently, SCB specimens were prepared following the standard protocol described by various researchers (Lim et al., 1993; Zuo et al., 2019). Firstly, core samples were saw cut in 27–30 mm circular cylinder and followed by half cut along the core diameter. The core dimeter of specimen was 60 mm. The '*S*/*R*' and '*a*/*R*' ratios were kept 0.5 for different cracks inclination angle in each rock type such as ($\beta = 0°$, 15°, 30°, 45°, and 60°). The notch length was kept constant for all specimens and it is varied between 12 and 13 mm. It is to note that 1 mm thick saw cut blade was used to prepare the notch into SCB specimen (Fig. 1b).

2.2 Calculation of Fracture Toughness

The fracture toughness of SCB specimens was calculated using following formula suggested by Lim et al. (1993):

$$K_{\mathrm{I}} = \sigma_0 \sqrt{\pi a} Y_{\mathrm{I}} \left(\frac{a}{R}, \frac{S}{R}, \beta \right) \tag{1}$$

$$K_{\mathrm{II}} = \sigma_0 \sqrt{\pi a} Y_{\mathrm{II}} \left(\frac{a}{R}, \frac{S}{R}, \beta \right) \tag{2}$$

where K_{I} and K_{II} represent mode I and mode II's stress intensity factors, respectively; Y_{I} and Y_{II} are non-dimensional stress intensity factors for mode I and mode II, respectively; $\sigma_0 = P/2RB$ (P: maximum applied load, R: radius of SCB specimen, B: thickness of SCB specimen). It

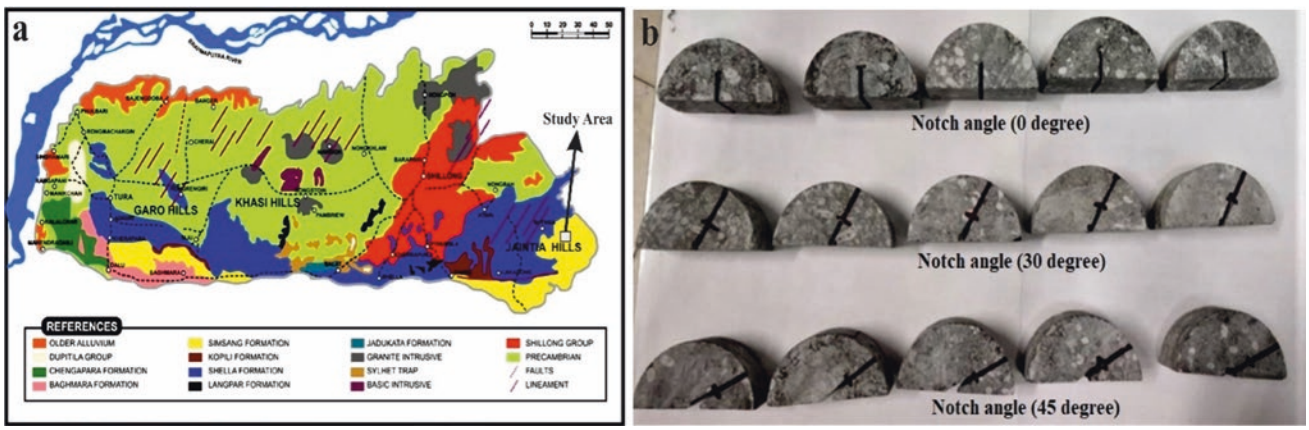

Fig. 1 **a** The detailed geological and tectonic map from where limestone blocks were collected. **b** An overview of prepared SCB specimen at different notch angles

is to note that Y_I and Y_{II} are estimated using the curve demonstrated by Lim et al. (1993) for 'S/D' = 0.50 and different value of 'a/R' and angle notch angle 'β'. The effective stress intensity factor was calculated to represent mixed mode (I + II) fracture toughness using the following Eq. (3):

$$K_{\text{eff}} = \sqrt{K_I^2 + K_{II}^2} \tag{3}$$

3 Results

In order to evaluate various modes of fracture toughness based on AE parameters, a total of 15 SCB specimens were tested at 5 different angles such as 0°, 15°, 30°, 45°, and 60°. Afterward, the load and AE characteristics curves were recorded through data logger. A total of three specimens were tested at individual angle and only average values of obtained results were discussed and plotted. The experimental results of various modes of fracture toughness of SCB specimens with reference to AE events and AE energy are presented in Fig. 2. The AE counts, cumulative AE energy, and load show similar trend as AE energy and cumulative energy (Fig. 2). These curves show that the energy release rate is approximately proportional to the number of AE event rates (Fig. 2). AE events and AE energy progression experience different steps during SCB specimen loading with increasing load and time. In general, a total of three steps were observed: in an early stage, a very few counts and energy released; subsequently, the AE counts and energy are formed. Most of the AE counts and AE energy are generated during development stage in the fracture toughness process, where continuous generation of cracks and expansion are progressively formed; finally, the cumulative counts and cumulative energy curves sharply rises due to unstable crack growth generation in SCB specimen. At this point, the fracture energy is released and AE counts and AE energy are reached at peak values.

In order to comprehend the variation of cumulative AE energy with reference to mode I and mode II fracture toughness, notch angle and crack length curves are plotted against cumulative AE energy versus mode I, mode II, notch angle, and crack length (Fig. 3). Figure 3a, b illustrates the variation of cumulative AE energy with mode I and mode II fracture toughness. The cumulative AE energy continuously decreases with increasing mode I fracture toughness values (calculated at selected notch angles) (Fig. 3a). Whereas, with the increase in mode II's fracture toughness values, the cumulative energy shows a gradually increasing trend (Fig. 3b). This resulting trend is similar to

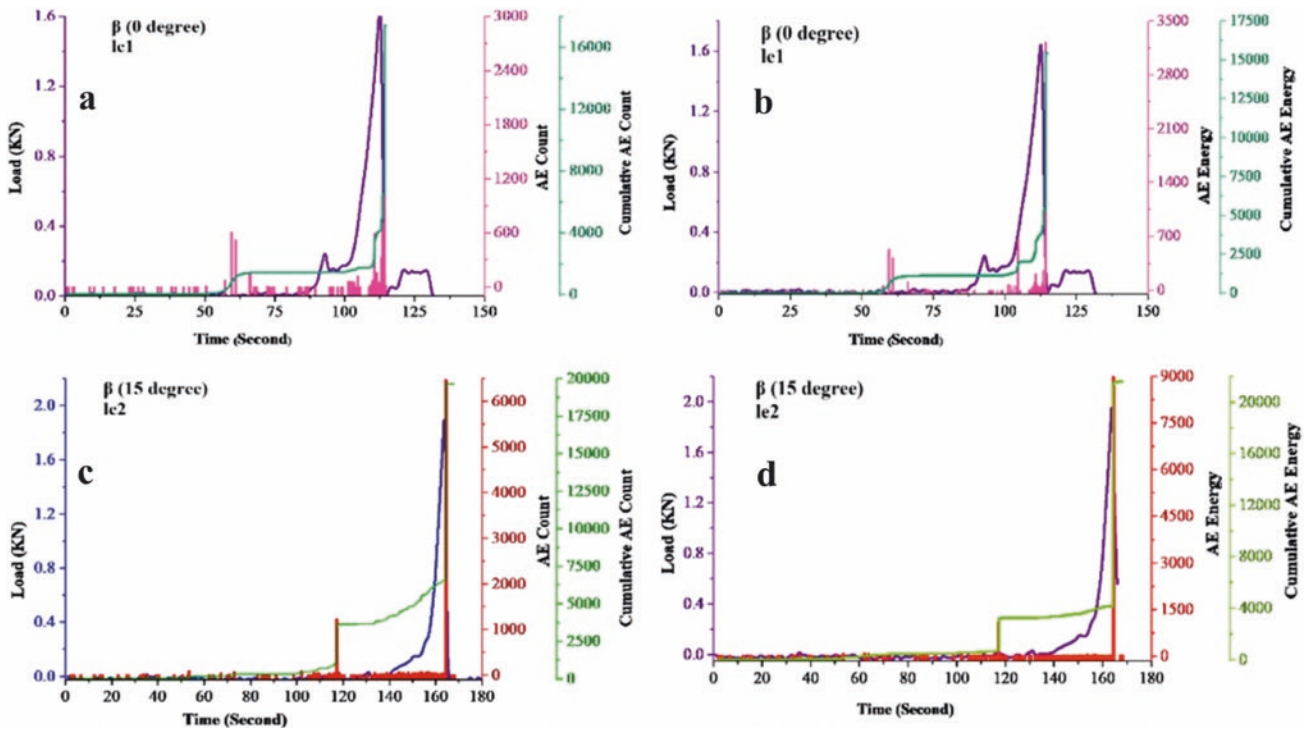

Fig. 2 Variations of load, AE counts, cumulative AE counts, AE energy, and cumulative AE energy against time: **a** time versus load, AE counts and cumulative AE counts for 0°; **b** time versus load, AE energy, and cumulative AE energy for 0°; **c** time versus load, AE counts and cumulative AE counts for 15°; **d** time versus load, AE energy, and cumulative AE energy for 15°. *Note* le1 to le2 represent specimen number

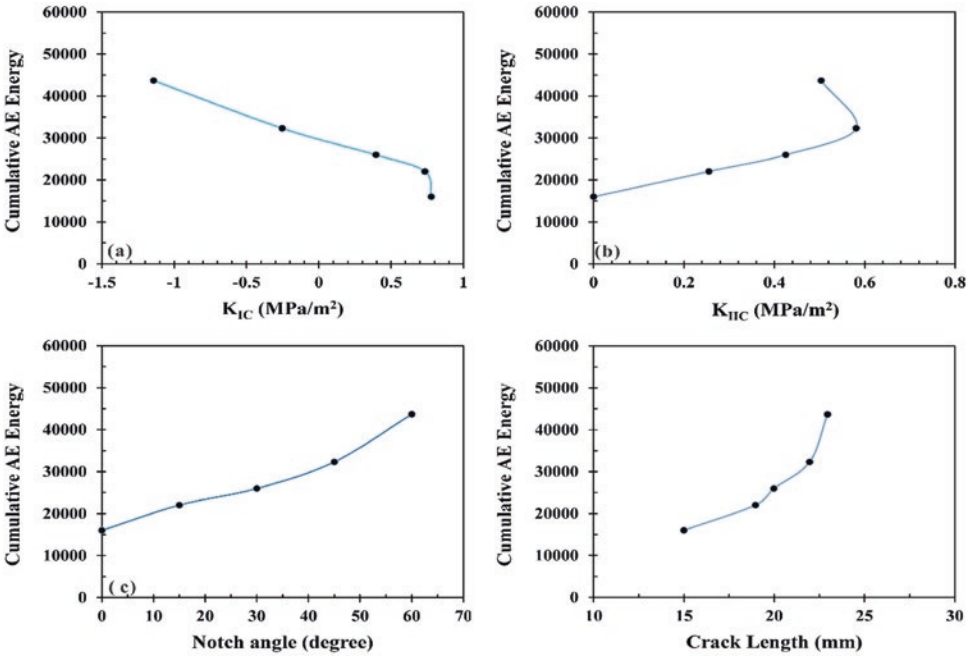

Fig. 3 The variation of cumulative AE energy against mode I, mode II, notch angle, and crack length: **a** cumulative AE energy versus mode I fracture toughness; **b** cumulative AE energy versus mode II fracture toughness; **c** cumulative AE energy versus notch angles; **d** cumulative AE energy versus crack length

results reported by Aliha and Ayatollahi (2009). It should be noted that the mixed mode (I+II) fracture toughness lies between mode I and mode II fracture toughness. Therefore, the variation of cumulative energy will be in between mode I and mode II. The plots of cumulative AE energy against notch angle and fracture length demonstrate that cumulative AE energy significantly increases with the rise in notch orientation and fracture length. This may be possible because an increase in notch angle and crack length indicates changeover of tensile splitting to combination of tensile and shear mode failure, then followed by shear mode splitting failure of specimens. Generally, the tensile mode of splitting is the easiest failure mode as it requires low applied load and energy compared to other failure modes such as shear mode and compression mode (Mahanta et al., 2017).

4 Conclusions

In the present investigation, the various modes of fracture toughness for limestone rock at different notch angles (0°, 15°, 30°, 45°, and 60°) were studied with reference to AE parameters, e.g., AE counts, cumulative AE counts, AE energy, and cumulative AE energy. A total of 15 SCB specimens of limestone rock (collected from Jaintia Hill, Meghalaya, India) with five dissimilar notch angles were tested at a constant load (5 kN/m) and, simultaneously, the load and AE characteristics curve were recorded through data logger. The major findings of this study are the following:

- The AE events, AE energy, and cumulative energy process undergo through three different stages during the SCB specimen loading with increasing load and time such as: early stage (a few AE counts and AE energy released); intermediate stage (gradual increasing trend of AE count and AE energy released due to continuous generation of cracks and expansion); final stage (AE counts and AE energy rises sharply due to unstable crack growth generation).
- The cumulative AE energy continuously decreases with the increase in mode I fracture toughness values calculated at selected notch angles, whereas with the increase in mode II fracture toughness values, the cumulative energy shows a gradually increasing trend.
- The cumulative AE energy against notch angle and fracture length demonstrate that cumulative AE energy significantly increases with the rise in notch orientation and fracture length.

References

Aliha, M. R. M., & Ayatollahi, M. R. (2009). Brittle fracture evaluation of a fine grain cement mortar in combined tensile–shear deformation. *Fatigue & Fracture of Engineering Materials & Structures, 2*, 987–994.

Department of Mining and Geology. (2020). Government of Meghalaya, India. https://megdmg.gov.in/features.html. Accessed November 27, 2020.

Guo, Z. H., Zhu, Z. D., Hua, J. N., Zhang, A. J., & Fang, Z. (2001). Limestone strength characteristics of experimental analysis and mathematical simulation. *Journal of Underground Space, 21*, 280–286.

Huang, Z. P., Zhang, Y., Sun, Y. K., Liu, C. Y., & Wu, W. D. (2016). Mechanical and acoustic characteristics of high temperature limestone with water cooling treatment. *Journal of Central South University, 47*, 4181–4189.

Kuruppu, M. D., & Chong, K. P. (2012). Fracture toughness testing of brittle materials using semi-circular bend (SCB) specimen. *Engineering Fracture Mechanics, 91*, 133–150.

Lim, I. L., Johnston, I. W., & Choi, S. K. (1993). Stress intensity factors for semi-circular specimens under three-point bending. *Engineering Fracture Mechanics, 44*, 363–382.

Mahanta, B., Tripathy, A., Vishal, V., Singh, T. N., & Ranjith, P. G. (2017). Effects of strain rate on fracture toughness and energy release rate of gas shales. *Engineering Geology, 218*, 39–49.

Zhang, S., Wang, L., & Gao, M. (2019). Experimental of the size effect of the mode I static fracture toughness of limestone. *Advance in Civil Engineering*. https://doi.org/10.1155/2019/7921694

Zhao, W., & Cao, P. (2013). *Rock mechanics* (pp. 15–17). Central South University Press.

Zuo, J.-P., Yao, M.-H., Li, Y.-J., Zhao, S. K., Jiang, Y.-Q., & Li, Z.-D. (2019). Investigation on fracture toughness and micro-deformation field of SCB sandstone including different inclination angle cracks. *Engineering Fracture Mechanics, 208*, 27–37.

Comparative Study of Aggregates from Various Moroccan Regions Used to Produce Concrete for the Building Sector

Fadoua Hattani, Wafaa Hamid, Driss Allaoui, Mustapha Mouflih, Abdellah Choukir, Hassan Zanzoun, Hassan Hannache and Bouchaib Manoun

Abstract

Aggregates are defined as grains with dimensions between 0 and 63 mm, which occupy about three-quarters of the volume of concrete and form its skeleton. The different characteristics of aggregates have an impact on those of concrete. Aggregates must, therefore, be the subject of a qualification study before being used in the manufacture of a given concrete. In Morocco, concrete aggregates are subject to the Moroccan standard NM 10.1.271. A large number of tests are required to determine their suitability for the desired use. Our objective is to establish a qualification study of the most used aggregates in the manufacture of concrete for buildings' sector in the following Moroccan cities: Casablanca, El Jadida, Settat, Marrakech and Temara. A panel of chemical and physical tests has been established to achieve this objective; also, the alkali-silica reactivity was studied based on a combination of a mineralogical and petrographic study. Differences in results are found. But the following conclusions can be drawn: The coarse aggregates are of class A. The fine aggregates contain fine elements that can negatively influence the granular skeleton and the distribution of particles, high levels of chlorides, and sulfates have been noticed in some samples. As for the chemical reactivity of the studied aggregates, it is high and remains a subject of further, deeper studies.

Keywords

Aggregates · Chemical study · Physical study · Petrographic study · Alkali-silica reactivity

1 Introduction

Aggregates are not considered anymore as an inert constituent, they strongly contribute to the quality of either fresh or hardened concrete, since they represent the skeleton of the material and constitute about 75% of its volume (Neville, 2011). Several properties of aggregates may have a considerable impact on concrete strength, whether present in the parent rock such as chemical and mineralogical composition, petrographic classification, specific gravity, hardness, strength, physical and chemical stability, and pore structure, or properties absent in the parent rock: particle shape and size, surface texture, and absorption (Meddah et al., 2010). It is assumed that the utilization of aggregates with different properties and the same past and curing conditions may result in different mechanical and long-term concrete properties. Most importantly, concrete compressive strength and damages are caused by internal chemical reactions such as the alkali-silica reaction, which may trigger into concrete if the environment allows it (Hasdemir et al., 2016). According to the NM 10.1.271, the Moroccan standard of concrete aggregates for construction work, four classes of aggregates exist: A, B, C, and D. Class A and class B are of good quality and can be used in structures and works of arts, class C and class D are used for regular concrete. So, the aim of the current study is to classify the aggregates put on sale for the public, and to check their chemical

F. Hattani (✉) · W. Hamid · D. Allaoui · B. Manoun
Faculty of Science and Technology of Settat, RMI, S3M, University Hassan First of Settat, 26000 Settat, Morocco
e-mail: f.hattani@uhp.ac.ma

M. Mouflih · H. Hannache
Faculty of Science Ben M'sik, University of Hassan II Casablanca, Casablanca, Morocco

A. Choukir · H. Zanzoun
Public Laboratory of Tests and Studies, LPEE-CEMGI, Tit Mellil, Casablanca, Morocco

H. Hannache · B. Manoun
Materials Science and Nano-engineering Department, University Mohammed VI Polytechnic, Ben Guerir, Morocco

Z. A. Ergüler et al. (eds.), *Selected Studies in Geotechnics, Geo-informatics and Remote Sensing*, Advances in Science, Technology & Innovation, https://doi.org/10.1007/978-3-031-43759-5_38

reactivity. As the NM 10.1.271 specifies, aggregates of class C are suitable for concrete manufacturing in the building sector (NM 10.1.271, 2008).

2 Materials and Methods

The studied aggregates are coarse and fine natural aggregates, collected from five different areas in Morocco: Tit Mellil-Casablanca, El Jadida, Settat, Marrakech, and Temara. They were purchased from public points of sale and are the most used aggregates in each region.

Chlorides and sulfates are harmful elements that can, in high dosage, trigger chemical reactions harmful to the stability of the concrete, so determining their contents is of importance. The physical parameters such as cleanliness, grain size distribution, shape, density, water absorption, and hardness serve as a basis for classifying the aggregates and designing concrete, and have been studied. Petrographic and mineralogical studies were held to determine the petrographic composition of the aggregates using binocular microscopy, the SiO_2 percentages were defined using X-ray fluorescence. The petrographic and mineralogical studies were executed on each single sample.

Based on the given results, the accelerated autoclave test was done on a combination of coarse and fine aggregates to allow a classification in: non-reactive (NR), potentially reactive (PR), potentially reactive with pessimum effect (RPE), at a specific percentage. The accelerated autoclave test was conducted on the 0.16/5 mm granular fraction. From this fraction and a 4% Na_2O_{eq} cement, two series of three 4 * 4 * 16 cm mortar specimens were made with a cement/aggregate (*C*/*G*) ratio of 0.5 and 1.25. After two days of curing in water at 20 °C, the specimens were autoclaved with steam at 127 °C for 5 h and at a relative pressure of 0.15 MPa, and then were progressively cooled. The elongations exhibited by the specimens following autoclaving are recorded and compared to the qualification criteria of the FD P18-542.

3 Results

3.1 Chemical and Physical Results

The chemical and physical results are presented in Table 1. Each test was performed according to its specific standard test.

Table 1 Chemical and physical aggregates properties' classification

Coarse and fine aggregates test and standard no	Tit Mellil		El Jadida		Settat			Marrakech		Temara	
	C.A	F.A	C.A	F.A	C.A	S.S	R.S	C.A	F.A	C.A	F.A
Maximum size (mm) NM 10.1.700	16	2.5	14	5	16	2.5	4	16	2.5	16	1
Fineness modulus NM 10.1.271	–	NC	–	NC	–	NC	A	–	NC	–	NC
Density (g/cm^3) NM 10.1.273	2.74	2.72	2.73	2.72	2.63	2.75	2.73	2.68	2.71	2.72	2.71
% Water absorption NM 10.1.273	A	A	A	A	A	A	A	A	A	A	A
% Cleanliness NM 10.1.169	A	–	A	–	A	–	–	A	–	A	–
% Sand equivalent NM 10.1.732	–	NC	–	NC	–	A	NC	–	A	–	B
Methylene blue (g/kg) NM 10.1.141	–	A	–	A	–	A	NC	–	A	–	A
% Flattening coefficient NM 10.1. 155	A	–	A	–	A	–	–	A	–	A	–
% L. Angeles coefficient NM 10.1.706	A	–	A	–	A	–	–	A	–	A	–
Organic impurities NM 10.1.144	N	N	N	N	N	N	N	N	N	N	N
% Chlorides NM 10.1.005	H	NH	H	H	H	NH	H	NH	NH	NH	NH
% Sulfates NM 10.1.005	A	A	A	D	D	A	A	A	A	A	A

C.A coarse aggregates; *F.A* fine aggregates; *NC* not conforming; *N* negative; *NH* not harmful; *H* harmful

Table 2 Accelerated autoclave elongations in mm

Ref	Elongations *C*/*G* 0.5 (mm)	Elongations *C*/*G* 1.25 (mm)	Classification
Tit Mellil (62% C.A 38% F.A)	0.08	–	NR
Settat (30% C.A 70% F.A)	0.26	0.53	RPE
El Jadida (46% C.A 54% F.A)	0.35	0.59	RPE
Marrakech (60% C.A 40% F.A)	0.17	0.52	RPE
Temara (67% C.A 33% F.A)	0.24	0.56	RPE

NR non-reactive; *RPE* reactive with pessimum effect

3.2 Alkali-Silica Reactivity Results

The mineralogical results show that the total silica content varies from 4.70 to 63.07%, values that are higher than the 4% limit recommended by FD P18-542 (2004). The petrographic study reveals the presence of sensitive and chemically unstable phases under the basic concrete conditions, hence the need for an autoclave test (FD P18-542, 2017). The accelerated autoclave elongations are summarized in Table 2.

4 Discussion

As illustrated in Table 2, coarse aggregates physical parameters are classified class A. The chlorides content in Tit Mellil, El Jadida, and Settat samples are higher than permitted, and so, the total chloride content in concrete should be verified. Settat's sulfate content is of class D, it may in certain conditions be harmful to concrete stability.

It is obvious from the study of fine aggregates sand equivalent test and fineness modulus results that they contain fine particles. Settat's river sand contains clay, unclean, and containing high content of chlorides.

The mineralogical results and the petrographic study reveal the presence of sensitive and chemically unstable phases. When it comes to the autoclave results, the $C/G = 0.5$ elongations are greater than 0.15 mm for all the samples except for Tit Mellil. According to the FD P18-542 protocol, the granular combination of Tit Mellil is considered non-reactive to alkali reaction. While the other combinations' elongations at $C/G = 1.25$ are more than 10% higher than the elongations at $C/G = 0.5$ and are therefore considered reactive with pessimum effect. However, the autoclave test qualifies with certainty the non-reactivity of an aggregate or a combination, the acceleration imposed by the operating procedure overestimates the real reaction, hence the need to move on to the long-term test.

5 Conclusions

According to the NM 10.1.271, C is the class of aggregates required to produce the studied concrete. The results show that the coarse aggregates are suitable for concrete production. In contrast to the sands, they are unsuitable for construction work as they contain fine elements harmful to the granular skeleton. Also, the levels of chlorides must be verified in concrete samples. As for the chemical reactivity of the studied aggregates, the long-term test must be held in future studies to verify their chemical reactivity.

References

FD P18-542. (2017). *Aggregates—Alkali-reaction qualification criteria for natural aggregates for hydraulic concrete*. AFNOR Editions.

Hasdemir, S., Tugrul, A., & Yılmaz, M. (2016). The effect of natural sand composition on concrete strength. *Construction and Building Materials, 112*, 940–948.

Meddah, M. S., Zitouni, S., & Belâabes, S. (2010). Effect of content and particle size distribution of coarse aggregate on the compressive strength of concrete. *Construction and Building Materials, 24*(4), 505–512.

Neville, A. M. (2011). *Properties of concrete* (5th ed.). Pearson Education Limited.

NM 10.1.271. (2008). *Aggregates for hydraulic concrete—Definitions, specifications, conformity*.

Finite Element Analysis of Rainfall Infiltration Effects on Open-Pit Coal Mines' Slope Stability

Alexandros V. Deliveris, Alexandros I. Theocharis, Ioannis E. Zevgolis and Nikolaos C. Koukouzas

Abstract

The climate crisis lead to the frequent occurrence of extreme weather events, such as rainfalls of great intensity. Rainfall infiltration may adversely influence the stability of pit mining slopes. Pit slope design should take into account the potential of heavy rainfall occurrence. In this work, a finite element analysis framework is utilized for the investigation of rainfall infiltration impact on surface coal mines' slope stability. The influence of pit slope angle as well as the initial groundwater table position, during heavy rainfall events, on the slopes' safety reduction rate is investigated. It is inferred that the effect of the initial groundwater table location on the reduction rate of pit slope safety factor is more pronounced than pit slope angle. However, both play an essential role in overall stability.

Keywords

Atmospheric precipitation · Lignite mines · Rainfall percolation · Unsaturated soil · Numerical simulation

1 Introduction

Global warming and climate change may result in extreme weather events, such as rainfalls of increased intensity (Rahardjo et al., 2019). During heavy rainfalls, slope stability issues and rainfall-induced failures are often encountered (Chatra et al., 2017). Consideration of rain infiltration for slope stability analysis is particularly applicable to the mining context since pit, and dump slopes are for prolonged periods exposed to weather conditions (Koner & Chakravarty, 2016). The large size of the encountered slopes in open-pit mining operations is a significant challenge not yet rigorously confronted and is emphasized in the present work. An open-pit coal mine slope of 50 m height is simulated in Plaxis 2D (Plaxis, 2020). The initial position of groundwater table results from a steady-state flow calculation, via the determination of specific boundary conditions at the vertical boundaries of the numerical model. A coupled flow-deformation computational scheme considers the infiltration process; slope stability is evaluated by the shear strength reduction method during the rainfall event. The influence of the pit slope inclination and the initial groundwater position on the slope's safety factor is examined.

2 Finite Element Analysis Framework

Saturation degree S_w, above the phreatic surface within the slope's unsaturated zone, is associated with the negative pore-water pressures u_w (suction), according to:

$$S_w = S_r + (S_s - S_r) \cdot \left[1 + \left(g_a \cdot \frac{u_w}{\gamma_w}\right)^{g_n}\right]^{\frac{1-g_n}{g_n}} \quad (1)$$

where (S_r) denotes the residual soil saturation degree; (S_s) the saturation degree of the soil in its saturated state; fitting parameters (g_a) and (g_n) comprise material properties of the unsaturated soil's Soil–Water Characteristic Curve (SWCC); (γ_w) represents the unit weight of water, taken equal to 10 kN/m^3. The unsaturated soil permeability (k_w) above the groundwater table reduces from its relevant saturated value k_s as:

A. V. Deliveris · A. I. Theocharis · N. C. Koukouzas
Centre for Research and Technology Hellas, Chemical Process and Energy Resources Institute, Athens, Greece

I. E. Zevgolis (✉)
School of Mining and Metallurgical Engineering, National Technical University of Athens, Athens, Greece
e-mail: izevgolis@metal.ntua.gr

Z. A. Ergüler et al. (eds.), *Selected Studies in Geotechnics, Geo-Informatics and Remote Sensing*, Advances in Science, Technology & Innovation, https://doi.org/10.1007/978-3-031-43759-5_39

$$k_w = k_s \cdot S_e^{g_l} \cdot \left[1 - \left(1 - S_e^{\frac{g_n}{g_n - 1}}\right)^{\frac{g_n - 1}{g_n}}\right]^2 \quad (2)$$

where (g_l) is an additional fitting parameter of the SWCC. Equations (1) and (2) constitute the key elements of the SWCC model and describe the behavior of the unsaturated soil (Van Genuchten, 1980). Furthermore, the effective degree of saturation (S_e) is defined as:

$$S_e = \frac{S_w - S_r}{S_s - S_r} \quad (3)$$

Additionally, soil's shear strength, (s), in the unsaturated zone is written based on Bishop's effective stress (Bishop & Blight, 1963):

$$s = (\sigma + S_e \cdot u_w) \cdot \tan\varphi' + c' \quad (4)$$

where (σ) denotes the total stress of a soil element and φ' and c' express the effective soil shear strength parameters. Finally, slope's safety factor (SF) is defined as the ratio of the average soil shear strength, (s), to the average applied shear stress, (τ), along the slope's slip surface:

$$SF = \frac{s}{\tau} \quad (5)$$

The slope model, as well as the physical, hydraulic, and mechanical properties of the soil, is shown in Fig. 1. Three mild slope angles $a = 14°$, 11°, 9.5°, typical for lignite excavations, were examined, corresponding to vertical-to-horizontal ratios $v{:}h = 1{:}4$, 1:5, 1:6. The influence of groundwater table was also investigated; three groundwater heads were considered, $H_w = 0$, 7.5 and 15, 100 m behind slope's crest. A heavy rainfall event was simulated as a worst-case scenario, by a constant discharge flow velocity equal to 36 mm/h, applied at the outer model boundaries for a time interval of one day. The parameters of the SWCC model, the soil's strength, and permeability represent a fine-grained silty material with medium strength.

3 Results

3.1 Safety Factor with Time for Various Slope Angles and Groundwater Heads

Figure 2a presents the effect of various slope angles on the safety factor (SF) with rainfall time. A groundwater head of $H_w = 0$ is assumed for the various slope inclinations.

SF decreases with the time-lapse of rainfall. In particular, for $\alpha = 9.5°$, SF is reduced from 2.14 to 2.03 after one-day rain, corresponding to a decrease of 5.3%. For the slope of $\alpha = 11°$, the initial safety factor of 1.92 reduces to 1.82, corresponding also to a decrease of 5.3%. Finally, for the steeper slope under consideration ($\alpha = 14°$), the SF decreases from 1.68 to 1.59, corresponding to the same decrease (5.5%). Overall, rainfall infiltration slightly affects the SF of the slope for all inclinations, and the effect of slope inclination on the reduction rate of SF is negligible. This small effect of infiltration is due to the SWCC parameters that dictate a dramatical decrease of the drainage capacity of the soil inside the unsaturated zone.

In Fig. 2b, the variation of pit slope safety factor with rainfall time is displayed for the various groundwater heads. It is noted that the slope angle is kept constant for the various groundwater heads, and equal to $\alpha = 14°$. For high initial groundwater table, $H_w = 0$ at 100 m behind the crest, the SF decreases from 1.68 to 1.60; this corresponds to a 5.5% reduction. For the case of the intermediate initial groundwater table, groundwater head of $H_w = 7.5$ m, the SF reduces from 1.82 to 1.77, showing a variation of 3.2%. Finally, for the case of the low initial groundwater table, groundwater head of $H_w = 15$ m, the safety factor of the pit slope remains practically the same from 1.96 to 1.93, presenting the lower variation percentage, equal to 1.8%. It seems that the initial position of the groundwater table somewhat affects pit slope safety during rainfall infiltration; as the initial groundwater table deepens, this impact becomes less significant.

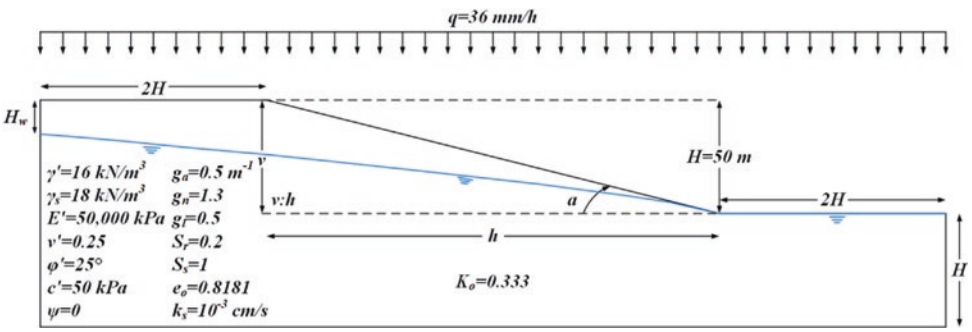

Fig. 1 Pit slope's rainfall infiltration model

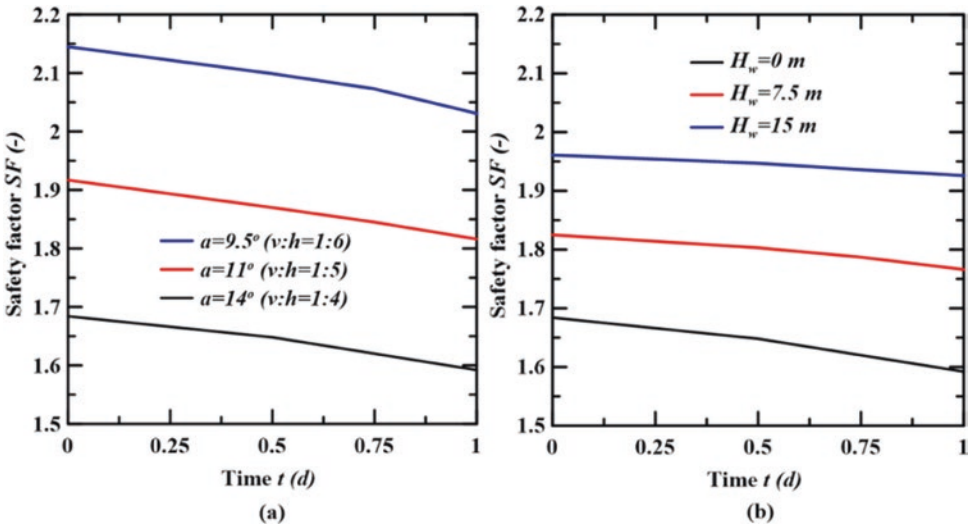

Fig. 2 Safety factor with time for various slope angles (**a**) and groundwater heads (**b**)

As previously mentioned, the negligible effect of infiltration irrespective the groundwater table is due to the decrease of soil's permeability within the unsaturated zone. As the groundwater table deepens, the effective saturation in the unsaturated zone decreases. Thus, the drainage capacity of the soil dramatically decreases, impeding the advancement of the rainfall-induced wetting front.

4 Conclusions

In this work, the impact of an extreme rainfall event on the stability of a high pit slope, equal to 50 m, was examined. Rain infiltration was simulated by a fully coupled flow-deformation analysis scheme, employing the Finite Element Method. Through a series of analyses, the impact of the pit slope angle and the initial groundwater table position on rain infiltration process was investigated. The rise of the pit slope angle and the initial groundwater table result in slightly lower safety factors. In addition, the rate of reduction of the pit slope's SF due to rain infiltration slightly increases with the raise of the initial groundwater table. Nonetheless, the effect of pit slope's angle on the rate of safety reduction is negligible.

Acknowledgements This work has received funding from the European Union's Research Fund for Coal and Steel under the project TEXMIN grant agreement No. 847250.

References

Bishop, A., & Blight, G. (1963). Some aspects of effective stress in saturated and partly saturated soils. *Geotechnique, 13*(3), 177–197.

Chatra, A., Dodagoudar, G., & Maji, V. (2017). Numerical modelling of rainfall effects on stability of soil slopes. *International Journal of Geotechnical Engineering, 13*(5), 425–437.

Koner, R., & Chakravarty, D. (2016). Numerical analysis of rainfall effects in external overburden dump. *International Journal of Mining Science and Technology, 26*(5), 825–831.

Plaxis. (2020). *2D finite element geotechnical analysis software*. Bentley.

Rahardjo, H., Kim, Y., & Satyanaga, A. (2019). Role of unsaturated soil mechanics in geotechnical engineering. *International Journal of Geo-Engineering, 10*(1), 8.

Van Genuchten, M. (1980). A closed-form equation for predicting the hydraulic conductivity of unsaturated soils. *Soil Science Society of America Journal, 44*(5), 892–898.

Validation of Constitutive Models for Spoil Material of Brown Coal Mines

Alexandros I. Theocharis, Ioannis E. Zevgolis and Nikolaos C. Koukouzas

Abstract

During surface lignite mining, vast amounts of waste overburden materials are excavated and then dumped without consideration for future use or valorisation in spoil heaps (also called spoil piles or spoil dumps). The exploitation of these heaps has primarily been limited to low load uses, such as agriculture and public leisure amenities. Nonetheless, due to the large areas they cover, spoil heaps are particularly fitted for larger projects, e.g. renewable energy projects, with imminent social importance. The complex nature of the spoil material is a well-known challenge and has been somehow confronted in the recent years, but the constitutive response of spoil materials is yet unknown. In the present work, results from consolidated undrained triaxial tests for three characteristic samples of a significant Greek spoil heap are employed, and three constitutive models are validated towards them. The three models represent different degrees of sophistication and aim in representing the monotonic constitutive response of this spoil material. This modelling representation is an essential step towards describing and simulating spoil materials that can be used in future works on spoil heaps in an engineering context.

Keywords

Spoil heap · Spoil pile · Surface lignite mine · Constitutive models

A. I. Theocharis · N. C. Koukouzas
Centre for Research and Technology Hellas, Chemical Process and Energy Resources Institute, Athens, Greece

I. E. Zevgolis (✉)
School of Mining and Metallurgical Engineering, National Technical University of Athens, Athens, Greece
e-mail: izevgolis@metal.ntua.gr

1 Introduction

Spoil is the waste produced during coal and brown coal (lignite) extraction at surface mines and is usually dumped in massive heaps (also named spoil piles, spoil dumps, or waste dumps). Spoil presents significant variability in physical and engineering properties, proposing a higher heterogeneity than natural soils (Masoudian et al., 2019). Efforts have been recently made to characterize and categorize the spoil material of an important Greek spoil heap from a geotechnical perspective (Zevgolis et al., 2018, 2020); in particular, a detailed analysis was conducted in that work on the overall characterization of the spoil material and will not be repeated herein. These results reveal significant variability in material properties and propose a high plasticity silt as the characteristic and representative material for the spoil. Additionally, for this characteristic material, a typical response is proposed in Zevgolis et al. (2020) based on the stress–strain response of consolidated undrained triaxial tests and is approximated by three constitutive models in this work.

2 Spoil Material's Stress–Strain Response and Validation of Constitutive Models

Three representative samples from different depths (2–2.5 m sample 1, 16–16.5 m sample 2, and 30–30.5 m sample 3) have been identified and are employed in this work (as also described in Zevgolis et al. (2020)). Their granulometries are presented in Fig. 1, while they were classified as high plasticity silts with PI ≈ 13% and LL ≈ 57%. Stress–strain curves from consolidated undrained triaxial tests are presented in Fig. 2, quantifying the constitutive response for three different mean effective stresses $p = 100$ kPa, $p = 200$ kPa, and $p = 400$ kPa.

It is not assumed that the response of this material is the accurate one of the spoil heap's, but rather that the

Z. A. Ergüler et al. (eds.), *Selected Studies in Geotechnics, Geo-informatics and Remote Sensing*, Advances in Science, Technology & Innovation, https://doi.org/10.1007/978-3-031-43759-5_40

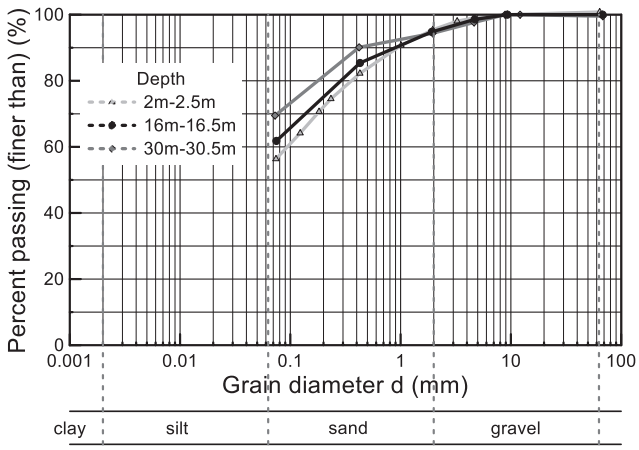

Fig. 1 Grain size distribution curves of the three characteristic spoil samples

"average" behaviour of the spoil heap would follow this response. Overall, triaxial results suggest an apparent behaviour similar to a normally consolidated clay, identifying hardening and tendency for volumetric decrease with the increase of deviatoric stress, pressure dependency, and a vanishingly small elastic region. Various constitutive models that could be implemented for this type of response are available in the literature. However, the heterogeneity of spoil material and the fundamental differences from natural soils prohibit the use of very sophisticated models, usually based on physical aspects of geomaterials and are absent in this case.

Simple and advanced models are employed in this work for the monotonic response of spoil material; the Mohr–Coulomb elastic-perfectly plastic model (MC), the hardening soil model (HS), and the soft soil model (SS) as implemented in Plaxis software have been validated towards the spoil's characteristic response (Plaxis, 2020). The calibrated parameters of the three models are denoted in Table 1: E is the Young modulus for MC model, (E_{50}) is the secant stiffness for HS model, (φ) is the effective friction angle, (c) the cohesion, (ψ) is the dilation angle, (ν) is the Poisson ratio, (m) is an HS model parameter relating stiffness to stress level, (E_{oed}) is the oedometric modulus, (C_c) is the compression index, and (C_r) the recompression index. The three models represent different degrees of sophistication in constitutive modelling and are all presented versus the laboratory results in Fig. 2.

Mohr–Coulomb is a simple choice based on the heterogeneity of the spoils, the uncertainties on its properties and the lack of physical mechanisms. It adequately fits the monotonic behaviour in deviatoric stress, but it cannot accurately follow the pore pressure changes. The hardening soil model follows the pore pressure build-up more closely during the undrained triaxial shear and accurately represents the nonlinear nature of response. However, spoil material builds up pore pressures more rapidly compared to the model. Finally, the soft soil model represents the pore pressure build-up most accurately, but proposes a more rapid deviatoric stress increase than experiments. Overall, it is observed that hardening soil and soft soil are more accurate than the Mohr–Coulomb model.

3 Conclusions

In this work, three constitutive models have been validated and calibrated versus a spoil material. It is the first time of such an effort due to the few published results in spoil characterization, the variability of spoil properties, and the difficulty in representing spoil materials. The three models, Mohr–Coulomb, hardening soil, and soft soil, represent three different degrees of sophistication. Overall, all three follow adequately well the monotonic triaxial response, but significantly differ in the pore pressure build-up. It is observed that hardening soil and soft soil are more accurate than the Mohr–Coulomb model, and it is considered that the higher calculation effort of these models is worth the higher accuracy. The authors consider that the significant heterogeneity of spoil material renders more sophisticated constitutive models redundant.

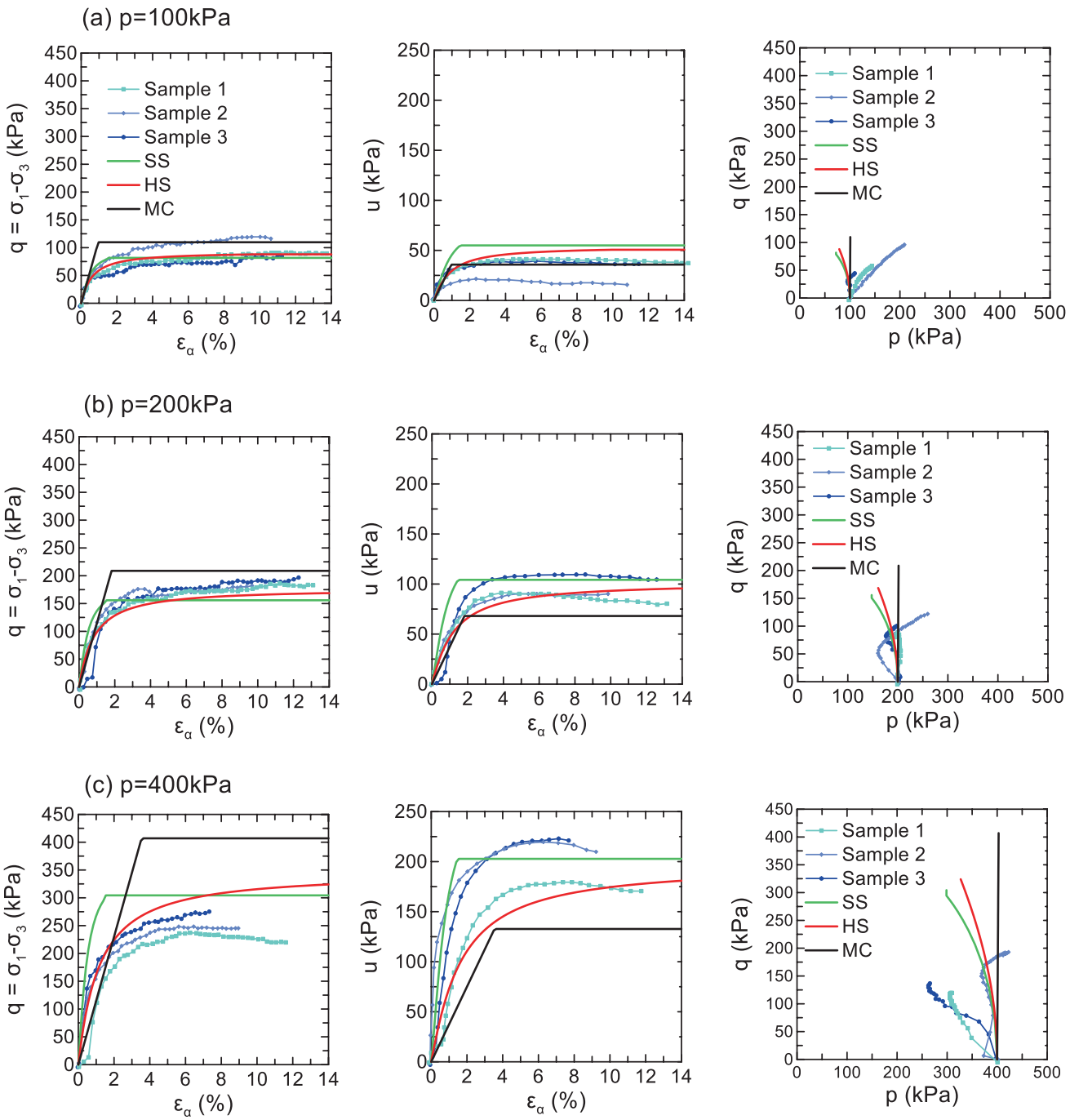

Fig. 2 Consolidated undrained triaxial tests for three characteristic samples, three different initial mean effective stress (p) of spoil materials, and three fits with different constitutive models: Mohr–Coulomb (MC), hardening soil (HS), and soft soil (SS)

Table 1 Constitutive models' parameters

Parameters	Mohr–Coulomb	Hardening soil	Soft soil
E or E_{50} (kPa)	10,000	5000	–
φ (°)	25	25	25
c (kPa)	5	5	5
ψ (°)	0	0	0
v	0.3	–	–
m	–	0.5	–
E_{oed} (kPa)	–	5000	–
C_c	–	–	0.2
C_r	–	–	0.037

Acknowledgements This work has received funding from the European Union's Research Fund for Coal and Steel under the project SUMAD grant agreement No. 847227.

References

Masoudian, M. S., Zevgolis, I. E., Deliveris, A. V., Marshall, A. M., Heron, C. M., & Koukouzas, N. C. (2019). Stability and characterisation of spoil heaps in European surface lignite mines: A state-of-the-art review in light of new data. *Environmental Earth Sciences, 78*(16), 505.

Plaxis. (2020). *2D finite element geotechnical analysis software*. Bentley.

Zevgolis, I. E., Koukouzas, N. C., Roumpos, C., Deliveris, A. V., & Marshall, A. M. (2018). Evaluation of geotechnical property variability: The case of spoil material from surface lignite mines. In *5th International Civil Protection Conference—SafeKozani 2018*. Kozani, Greece.

Zevgolis, I. E., Theocharis, A. I., Deliveris, A. V., Koukouzas, N. C., Roumpos, C., & Marshall, A. M. (2020). Geotechnical characterization of fine-grained spoil material from surface coal mines. Submitted for publication.

Probability Distributions of Geotechnical Parameters of a Silty Spoil Material

Alexandros I. Theocharis, Ioannis E. Zevgolis and Nikolaos C. Koukouzas

Abstract

During coal and lignite mining, vast amounts of overburden sterile materials (particularly in surface operations) are excavated to reach the deposits. These materials are characterised as waste and are dumped inside or outside the mine pit. Nowadays, sustainable waste management is a global priority, and thus, considerable efforts are made to exploit spoil heaps properly. Given that dumps were often not constructed with future valorisation in mind, they consist of randomly dumped mixed soils that result in a challenging construction environment (highly random, variable, and heterogeneous). The authors recently made a systematic analysis in order to quantify the uncertainty of the geotechnical properties of a Greek spoil heap. A database based on laboratory test results was established and statistically analysed; the results revealed and quantified the significant spoil material variability. In the present work, the focus is on the probability distributions of significant physical and engineering parameters. Due to the large variability of spoil materials, a reliability analysis rather than a deterministic one should be considered. For that purpose, the probability distributions of the parameters involved are essential and are thus, presented and analysed herein.

Keywords

Spoil heap · Spoil pile · Waste dump · Geotechnical properties · Probability distributions · Reliability analysis

A. I. Theocharis · N. C. Koukouzas
Centre for Research and Technology Hellas, Chemical Process and Energy Resources Institute, Athens, Greece

I. E. Zevgolis (✉)
School of Mining and Metallurgical Engineering, National Technical University of Athens, Athens, Greece
e-mail: izevgolis@metal.ntua.gr

1 Introduction

Coal and lignite (brown coal) mining has been an enormous industry aiming at extracting coal resources from the ground. During surface mining, the overburden of the lignite (primarily soil rather than rock) is removed and usually dumped as waste in spoil heaps (also referred to as spoil dumps, spoil piles, or waste embankments). Nowadays, significant consideration is given to properly exploiting spoil heaps within the framework of cyclic economy and sustainable management of mines and wastes. In Masoudian et al. (2019), a tentative overview of the geotechnical characteristics of European spoil heaps was presented, while in Zevgolis et al. (2018, 2020), the authors presented an in-depth statistical analysis of an important Greek heap. It was concluded that spoil materials present remarkable variability, significantly larger than natural soils, and a challenging scenario for engineering purposes.

For the efficient exploitation of spoil heaps, it is of utmost importance to understand and quantify the geotechnical properties of the spoil material. The present work refers to a massive spoil heap located in northern Greece, composed of soils from two adjacent surface lignite mines; it measures 5 km in length and more than 150 m in height. A laboratory campaign on the spoil material of this heap led to the creation of an extensive database of geotechnical parameters (Zevgolis et al., 2020). In this work, the distributions of the spoil's physical and engineering properties were analysed to gain an in-depth understanding of the properties' variability and provide input for reliability analysis.

2 Probability Distributions

Physical and engineering parameters were evaluated in terms of their probability distributions. Based on several observations in Zevgolis et al. (2020), a general stratigraphy

Z. A. Ergüler et al. (eds.), *Selected Studies in Geotechnics, Geo-Informatics and Remote Sensing*, Advances in Science, Technology & Innovation, https://doi.org/10.1007/978-3-031-43759-5_41

or even characterisation of layers cannot be identified. Given the disordered structure of the spoil material, a statistical treatment of the heap can be employed considering a single material with significant inherent variability; this approach is used in Zevgolis et al. (2020) and for the following analysis. Herein, only normal and lognormal distributions were examined versus the laboratory results; mean value, standard deviation, and coefficient of variation (COV) are mentioned as calculated in Zevgolis et al. (2020). Finally, the goodness of fit is estimated based on Anderson–Darling statistical test (Stephens, 1974), and *p*-values of each fit are calculated; if $p>5\%$ (as frequently assumed), then the null hypothesis (indicating that the data come from a normal- or lognormal-distribution) is accepted. Only the best out of the two fits (normal or lognormal) is mentioned in each figure.

Liquid limit (LL) and plastic limit (PL) are the two main physical parameters used for fine-grained soil characterisation (Fig. 1). LL (Fig. 1a) presents a high peak at 55–60%, larger than the mean value, and larger relative frequencies for high plasticity materials (LL>50%). Additionally, it presents a significant tail on low plasticity materials (LL<50%); the *p*-value is very low and normal distribution is not accepted as an accurate fit. Furthermore, PL (Fig. 1b) presents two high peaks at 15–25 and 35–45%. The normal distribution, in this case, cannot describe the first peak at 15–25%. However, most of the measurements (approx. 60%) still lie within one standard deviation, and the *p*-value is greater than 5%, denoting an acceptable normal fit.

Further frequently employed physical parameters and indexes are the liquidity index (LI) and the moisture (or water) content (*w*), and Fig. 2 presents their distributions. LI has a relatively normal distribution (with $p>>5\%$) around its mean value—equal to 0.3—and exhibits values from 0 to 0.8, denoting a soil that behaves plastically; most cohesive soil deposits have LI values within this range. Moisture content cannot be accurately represented from a normal or a lognormal distribution as it exhibits two peaks at 20–25 and 40–45% and a large tail on values from 50 to 85%.

The two major investigated engineering parameters are the effective friction angle and the cohesion of the spoil. These two parameters define a failure surface for the material and are characteristic of its strength (Fig. 3). Effective friction angle (Fig. 3a), although having some gaps, can be represented by a normal distribution around its mean value of 25.2° (with $p>5\%$). However, due to the peculiarities

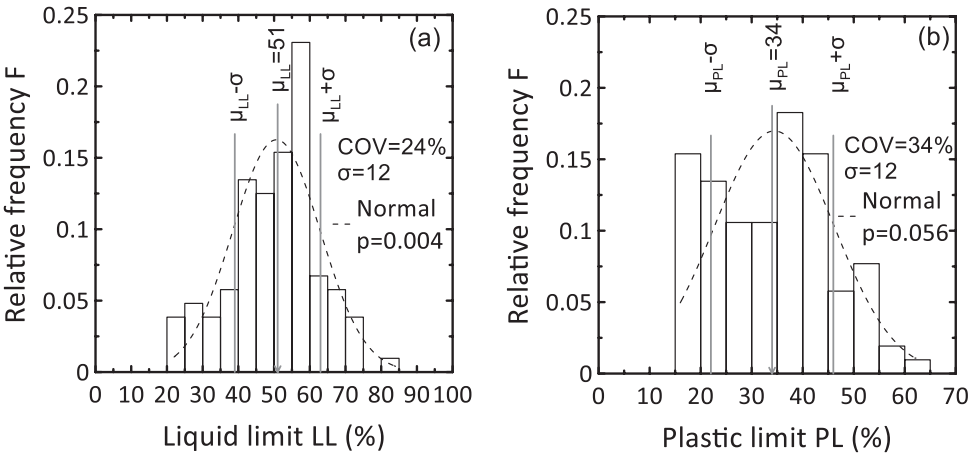

Fig. 1 Probability distributions of **a** liquid limit (LL) and **b** plastic limit (PL)

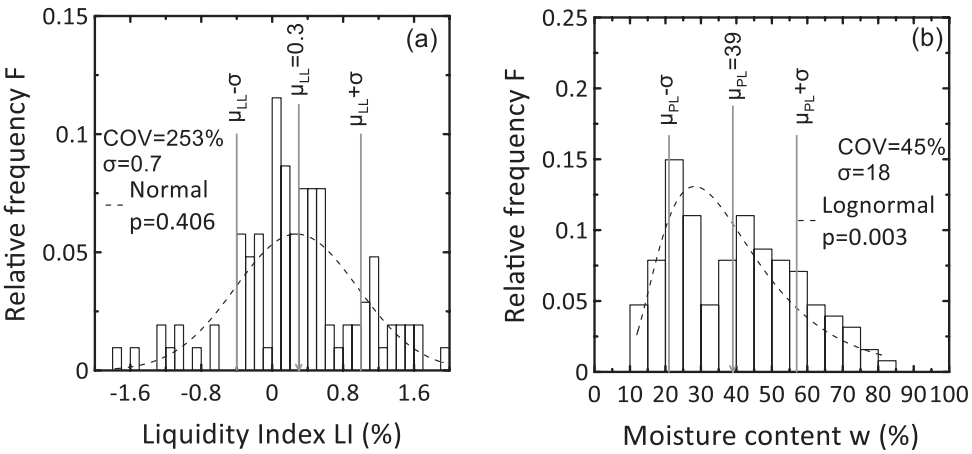

Fig. 2 Probability distributions of **a** liquidity index (LI) and **b** moisture content (*w*)

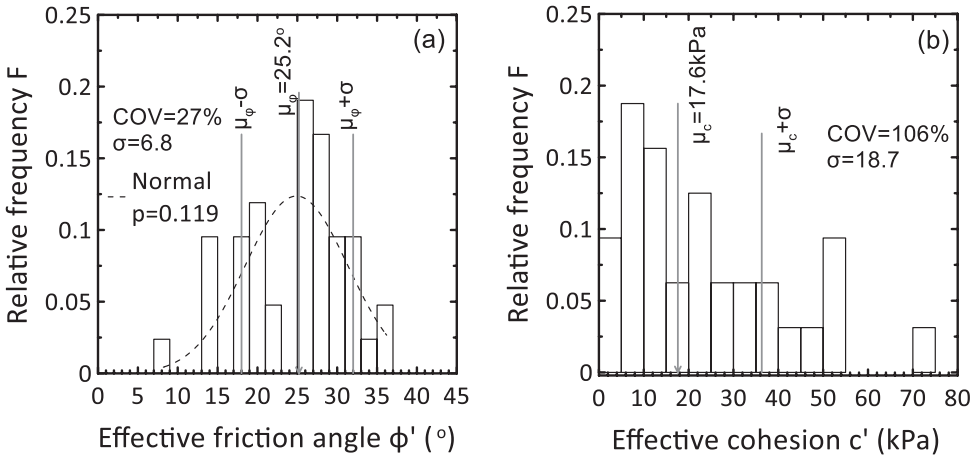

Fig. 3 Probability distributions of **a** effective friction angle (φ) and **b** cohesion (c)

illustrated in Fig. 3a, the normal fit should be applied cautiously. Additionally, 37% of the results lie outside one standard deviation of the mean value. Cohesion presents a distribution challenging to fit, as many samples have low or zero cohesion, and a large tail goes up to 80 kPa. This difficulty is also identified by the COV that is equal to 106%.

3 Conclusions

Geotechnical properties of spoil material from lignite mines generally present large variability. So, when it comes to stability or deformation analysis of spoil heaps, reliability analysis should be considered as an additional tool to the conventional deterministic analysis. For this purpose, the probability distributions of the major geotechnical parameters are essential and have been, herein, presented and analysed. Based on a standard statistical test and by testing the normal and the lognormal distribution for each case, the liquid limit, the liquidity index, and the effective friction angle could be accurately approximated by a normal distribution. Peculiarities in the distribution of the other examined parameters (plastic limit, moisture content, and cohesion), such as gaps, large tails, and two peaks, propose complex distributions that should be further analysed.

Acknowledgements This work has received funding from the European Union's Research Fund for Coal and Steel under the project SUMAD grant agreement No. 847227.

References

Masoudian, M. S., Zevgolis, I. E., Deliveris, A. V., Marshall, A. M., Heron, C. M., & Koukouzas, N. C. (2019). Stability and characterisation of spoil heaps in European surface lignite mines: A state-of-the-art review in light of new data. *Environmental Earth Sciences, 78*(16), 505.

Stephens, M. A. (1974). EDF statistics for goodness of fit and some comparisons. *Journal of the American Statistical Association, 69*(347), 730–737.

Zevgolis, I. E., Koukouzas, N. C., Roumpos, C., Deliveris, A. V., & Marshall, A. M. (2018). Evaluation of geotechnical property variability: The case of spoil material from surface lignite mines. In *5th International Civil Protection Conference—SafeKozani 2018*. Kozani, Greece.

Zevgolis, I. E., Theocharis, A. I., Deliveris, A. V., Koukouzas, N. C., Roumpos, C., & Marshall, A. M. (2020). Geotechnical characterization of fine-grained spoil material from surface coal mines. Submitted for publication.

Experimental Study of the Factors of Variation of Atterberg Limits

Chahra Yellas, Riad Benzaid, Hassiba Kherrouba and Mustapha Tekkouk

Abstract

The Atterberg limits or consistency limits are considered to be the oldest and most widely used geotechnical tests for the identification of cohesive soils. However, these are empirical tests whose results can be strongly influenced by several factors, such as the operator's accuracy, the quality and wear of the material, and the method of sample preparation. The purpose of this work is to show the relative importance of the factors of variation of Atterberg limits. In this kind of tests, the rigorous application of the operating mode is particularly essential if we want to obtain reliable and comparable results from one operator to another.

Keywords

Atterberg limits · Fine soil · Water content · Consistency · Variation factors

1 Introduction

The Atterberg limits are conventional physical constants expressing differences in the mechanical behavior of soils, differences mainly linked to variations in water content. They are, therefore, likely to provide information on the greater or lesser ease of working the soil. They correspond in principle to the thresholds of passage from the solid state to the plastic state (plastic limit W_P) and from the plastic state to the liquid state (liquid limit W_L). The interval between these two limits defines the extent of the plasticity domain which is known as the plasticity index I_P (Combeau, 1964; Proust et al., 2004). The present work consists of an experimental study of the factors of variation of the Atterberg limits.

2 Physical Characteristics of the Studied Soils

Table 1 shows the physical characteristics and classification of both soils used in this study. The preparation of the soil samples and the achievement of the Atterberg limits of the different series of tests were in accordance with standard NF P94-051 (1993).

3 Analysis and Discussion of Experimental Results

3.1 Effect of the Condition of the Base of the Casagrande Apparatus

Standard NF P94-051 (1993) recommends using an ebonite-type material for the bottom, which allows easy resurfacing when the cup manages to dig the bottom where it fell. Furthermore, this base must be made of a material always having the same hardness; the currently marketed devices include bakelized wood bases. This material has a minimum impact resistance of 11 kJ and a maximum of 17 kJ. To verify the influence of the state of the base of the Casagrande device on the results of the liquid limit and consequently the Atterberg limits, we performed the liquid limit test using a hard steel plate between the cup and the base of the device to amplify the shock. Then, a rubber plate was used in order to absorb the shock between the cup and the base of the Casagrande apparatus. The obtained results for the two used soils (clay and marl) show that the condition of the base is important and has an influence on the values of the liquid limit, which consequently affects

C. Yellas · R. Benzaid (✉) · H. Kherrouba · M. Tekkouk
Laboratoire de Génie Géologique, Jijel University, Jijel, Algeria
e-mail: r_benzaid@univ-jijel.dz

Z. A. Ergüler et al. (eds.), *Selected Studies in Geotechnics, Geo-Informatics and Remote Sensing*,
Advances in Science, Technology & Innovation, https://doi.org/10.1007/978-3-031-43759-5_42

Table 1 Physical characteristics of both soils used in this study

Physical properties	Clays	Marls
Wet density γ_h (kg/m^3)	2140.0	2220.0
Dry density γ_d (kg/m^3)	1850.0	1880.0
Water content W (%)	16.35	19.00
Plastic limit W_P (%)	18.85	19.30
Liquid limit W_L (%)	39.36	30.96
Plasticity index I_p	20.51	11.66
Consistency index I_c	1.12	1.02
Blue value (VBS)	5.84	7
GTR[a] classification	A2	A2

[a] GTR: "Guide de Terrassement Routier", French for road earth moving guide

the other soil consistency parameters (Fig. 1). We can see a significant increase in W_L, W_P, and I_P compared to the reference sample as shown in Fig. 1.

3.2 Effect of the Groove Tool

According to standard NF P94-051, the groove tool must produce a groove of 2 ± 0.05 mm, for this reason it recommends the use of the groove tool from Casagrande. As for the ASTM D4318-17e1 (2017) type tool, its use is not recommended by users of the French standard NF P94-051, although it is used in several Anglo-Saxon countries. What interests us here is the influence of the groove tool on the liquid limit results, not to mention the wear effect. For this reason we performed two series of tests, one with the Casagrande groove tool and the other with the ASTM one. We notice that the angle of the lips of the grooves made with these two tools is the same (60°), but the depth is different (8 mm for the Casagrande tool, against 10 mm for the ASTM tool). In addition, the ASTM tool has the disadvantage of producing a groove whose depth is a function of the thickness of the material placed in the cup, whose thickness further elevates by pushing the material sideways. This is not the case with the Casagrande tool which even grinds the thickness of the material and therefore results in a groove of the same depth. This finding becomes more and more interesting when one thinks that the liquid limit test is a ground shear test at certain water content. As a result, the deeper the groove, the lower the shear strength during the liquid limit test, which is shown in the comparative tests, performed using the two grooving tools (Fig. 2). These results indicate the differences on W_L observed using the ASTM and Casagrande groove tools. This is the reason why usually Casagrande's tool is used for clay type soil, but for soil with low plasticity, ASTM tool is recommended.

3.3 Effect of the Drop Height of the Cup

In the Atterberg limits test, the drop height of the cup must always be carefully adjusted (according to standard NF P94-051, it is equal to 10 mm). Table 2 shows the variations of the liquidity limit W_L as a function of the fall height for the two studied soils, namely: clays with a reference value of $W_L = 39.36\%$, and marls with $W_L = 30.96\%$. We note that a deviation of ± 1 mm on the drop height of the cup can lead to an error ranging from 4% (case of clays) to 2% (case of marls) on the value of the liquidity limit W_L, without forgetting the impact of these errors on the other soil consistency parameters in question (Table 2). As a result, the base must be resurfaced as it is hollowed out by the cup over time. Controlling the diameter of the cavity is important because when adjusting the height of the fall, the additional height caused by the hollow made by the cup in the base is not taken into account.

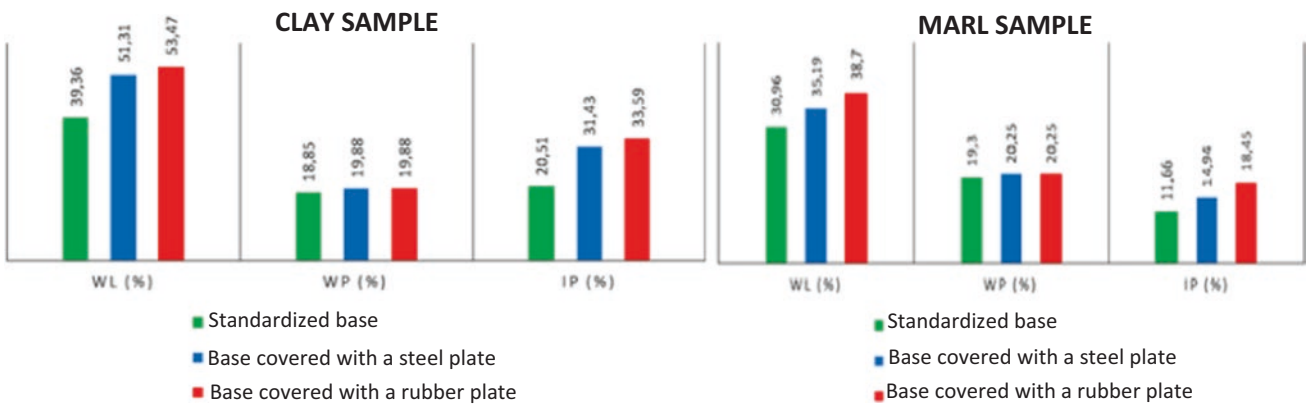

Fig. 1 Effect of basement condition on Atterberg limit results

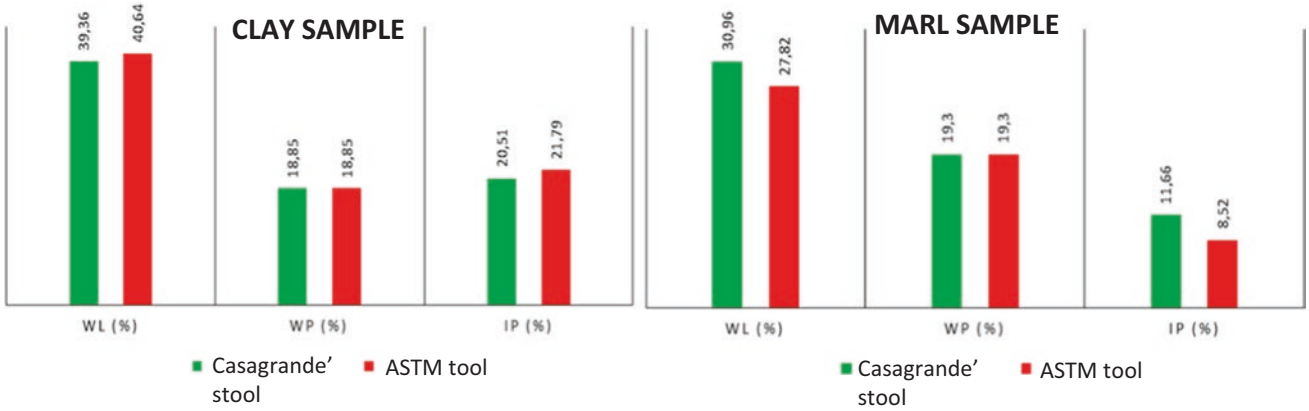

Fig. 2 Effect of groove tool on Atterberg limit results

Table 2 Effect of the drop height of the cup

		10 mm drop height (standard test)	5 mm drop height (non-standardized test)	Observations
Clay	W_L (%)	39.36	60.22	+20.86%
	W_P (%)	18.85	20.71	
	I_P (%)	20.51	39.51	+19.00%
Marl	W_L (%)	30.96	39.79	+8.83%
	W_P (%)	19.30	20.03	
	I_P (%)	11.66	19.76	+8.10%

4 Conclusions

The objective of this work was to show the relative importance of the factors of variation of the Atterberg limits because, in this type of test, the rigorous application of the operating mode is particularly essential if we want to obtain reliable and comparable results from one operator to another. The results obtained in this study led to the following conclusions.

The liquid limits depend on the state of the base of the Casagrande apparatus; they are directly influenced by the state of hardness of the latter which consequently affects the plastic limits as well as the plasticity index.

We have noticed that the angle of the lips of the grooves made with these two tools is the same, but the depth is different (8 mm for the Casagrande tool, against 10 mm for the ASTM tool). In addition, the ASTM tool has the disadvantage of producing a groove whose depth is a function of the thickness of the material placed in the cup, whose thickness further elevates by pushing the material sideways. This is not the case with the Casagrande tool which even grinds the thickness of the material and therefore results in a groove of the same depth. It is for this reason that standard NF P94-051 recommends the Casagrande groove tool.

We have observed that a deviation of ± 1 mm on the drop height of the cup can lead to an error ranging from 2 to 4% on the value of the liquid limit W_L, without forgetting the impact of these errors on the other consistency parameters of the soil in question.

Finally, consistency limit or Atterberg limit test is a major test for cohesive soil. Its determination is not complex, but operator-dependent if the device is not automatic and the technician is not an expert. If factors affecting the determination of these parameters are determined, it will be useful for practicing engineers to see which factor is the most effective on test results. This will help determining the correct limit values.

References

ASTM D4318-17e1. (2017). *Standard test methods for liquid limit, plastic limit, and plasticity index of soils*.

Combeau, A. (1964). Remarques sur les facteurs de variation des limites d'Atterberg. *Cahiers ORSTOM. Serie Pédologie, II*(4), 29–39.

NF P94-051. (1993). *Sols: Reconnaissance et essais—Détermination des limites d'Atterberg—Limite de liquidité à la coupelle—Limite de plasticité au rouleau*.

Proust, Ch., Jullien, A., & Le Forestier, L. (2004). Détermination indirecte des limites d'Atterberg par gravimétrie dynamique. *Comptes Rendus Géoscience,* 1–336.

Improvement of the Engineering Behavior of Plastic Soils Using Lime and Hydraulic Binders

Hassiba Kherrouba, Riad Benzaid, Chahra Yellas and Mustapha Tekkouk

Abstract

Once wet or saturated, clays become soft and have low compressive strengths, which in the presence of loads lead to excessive settlements. This reduction in compressive strength often causes damage to infrastructure. To remedy this problem, soils can be stabilized by adding cement or lime. Such stabilization methods improve the various technical properties of the stabilized soil and generate an improved material. The present work consists of a laboratory study carried out on two types of plastic soils (clay and marl) stabilized according to various doses of lime, cement, and with a mixed lime–cement treatment. The obtained results show that the impact of the lime treatment makes the mixture less sensitive to water, hence flattening the Proctor curve and increasing the optimum water content. Unlike the use of cement where mixed treatment (lime–cement) or the water content of the soil–cement or soil–lime–cement mixture is reduced, on the other hand, there are no significant changes to the Proctor curve.

Keywords

Hydraulic binders · Clays · Marls · Atterberg limits · Compaction characteristics

H. Kherrouba · R. Benzaid (✉) · C. Yellas · M. Tekkouk
Geological Engineering Laboratory (LGG), Jijel University, Jijel, Algeria
e-mail: r_benzaid@univ-jijel.dz

1 Introduction

The concept of stabilization is very old. At the time of the Pharaohs, the Egyptians built roads with stabilized earth, while the Greeks and Romans used lime as a stabilizer in construction projects (McDowell, 1959). In 1915, cement was introduced as a stabilizer to build a street in Sarasota, Florida, and in 1924, lime was used in road embankments to improve load-bearing capacity and respond to the growth in vehicle traffic (Firoozi et al., 2014; Wang, 2002). Nowadays, the stabilization of soils by adding cement or lime is a widely used technique in the world, especially in road projects in order to improve the geotechnical properties of soils (Bouras et al., 2020; Firoozi et al., 2017; Harichane et al., 2012; Mahamedi & Khemissa, 2015; Pourakbar & Huat, 2017). The aim of the experimental work presented in this paper is to evaluate the efficiency of lime and cement additions on the Atterberg limits and the compaction curves of plastic soils.

2 Methods and Materials

Physical characteristics and Atterberg limit test results of both soils used in this study are presented in Tables 1 and 2, respectively.

Based on these results, clay soil is found to be moist dense to moderately dense, while marly soil is slightly moist dense to moderately dense soil.

For clay soil, the plasticity index is equal to 41.14%, which indicates a very plastic soil. Whereas, the consistency index (IC) of 0.87 corresponds to plastic soils. For marly soil, the plasticity index (IP) is equal to 11.97%, which characterizes soil with low plasticity. The consistency index (IC) equal to 0.99 corresponds to plastic soils.

The experimental program carried out in this study is presented in Table 3.

Z. A. Ergüler et al. (eds.), *Selected Studies in Geotechnics, Geo-Informatics and Remote Sensing*, Advances in Science, Technology & Innovation, https://doi.org/10.1007/978-3-031-43759-5_43

Table 1 Physical characteristics of the two soils used in this study

Physical properties	Clay soil	Marly soil
Wet unit weight γ_h (kN/m^3)	21.76	22.20
Dry unit weight γ_d (kN/m^3)	20.00	18.77
Water content w (%)	29.00	19.00

Table 2 Atterberg limit test results

Consistency parameters	Clay soil	Marly soil
Water content w (%)	29.00	19.00
Plastic limit W_P (%)	23.56	18.99
Liquid limit W_L (%)	64.70	30.96
Plasticity index IP	41.14	11.97
Consistency index IC	0.87	0.99

3 Analysis and Discussion of Experimental Results

3.1 Soil Treatment with Addition of Lime

From the obtained results, it can be seen that the addition of lime has a remarkable influence on the Atterberg limits of both studied types of soil. It is clear that an increase in the percentage of lime in the treated soil induces a significant increase in the plastic limit (WP) than for the liquid limit (WL). On the other hand, increasing the percentage of lime in the treated soil considerably reduces the plasticity index (IP). Indeed, with 4% added lime reduced the plasticity index (IP) of clays by 37%, while that of marls was only 22%.

3.2 Soil Treatment with the Addition of Cement

Adding cement to soils gave the same effect as adding lime, with some exceptions for clays. First, treating the marl soil with cement increased both WL and WP with a decrease in the IP. On the other hand, for clay soil, the addition of cement certainly increased the WL and WP. These increases, recorded at rates 2 and 4% of cement, were reduced to 6% of the added product. The 6% represents the saturation value beyond which the cement treatment is no longer effective for clay; we have certainly reached the saturation threshold for clays.

Table 3 Details of the experimental program

Series of tests carried out	Soil type	Atterberg limits' testing	Observations
Series N ° 01: Effect of soil treatment with lime and/or cement on Atterberg limits	Clay soil	Reference soil	Without treatment
		Soil treated with lime	2, 4 and 6%
		Soil treated with cement	2, 4 and 6%
		Soil treated with lime and cement	2, 4 and 6%
	Marly soil	Reference soil	Without treatment
		Soil treated with lime	2, 4 and 6%
		Soil treated with cement	2, 4 and 6%
		Soil treated with lime and cement	2, 4 and 6%
Series N ° 02: Effect of soil treatment with lime and/or cement on compaction characteristics	Clay soil	Reference soil	Without treatment
		Soil treated with lime	2, 4 and 6%
		Soil treated with cement	2, 4 and 6%
		Soil treated with lime and cement	2, 4 and 6%
	Marly soil	Reference soil	Without treatment
		Soil treated with lime	2, 4 and 6%
		Soil treated with cement	2, 4 and 6%
		Soil treated with lime and cement	2, 4 and 6%

3.3 Mixed Treatment with the Addition of Lime and Cement

The mixed treatment of the studied soils (clay and marl) with lime and cement significantly reduced the WL of both soils. On the other hand, for the WP, after an increase with the percentages of the mixed treatment of 2 and 4%, a decrease was recorded at the threshold of 6% for both soils studied. What confirms once again that this value of 6% is a saturation value beyond which the treatment is no longer effective is the saturation threshold. The IP decreased in both cases.

3.4 Effect of Treatment with Lime and/or Cement on Proctor Curves

The sensitivity to water of the tested samples was reflected in the various shapes of the Proctor curves (according to Figs. 1 and 2). We noted that for the natural state of clay and marl soil, the compaction curve has an accentuated shape, which explains the great sensitivity of fine soils to water. After treatment with lime with additions of 2, 4, and 6%, the Proctor curves of the clays shifted to the right; they have a flattened shape which reflects the low sensitivity of these mixtures to water (Fig. 1). In Fig. 2, the lime treatment of marls with additions of 2, 4, and 6% decreases the density of the optimum Proctor than that of clays, but without a considerable increase in optimal water content.

The treatment of soils with cement improves the initial characteristics of the plastic soil. It is mainly used for obtaining rapid development of mechanical resistance. The water content of the mixture decreased due to the addition of dry materials, the consumption of the necessary water for the hydraulic setting of the cement, and the evaporation of water by aeration of the soil during mixing. On the other hand, no significant modification observed on Proctor curve

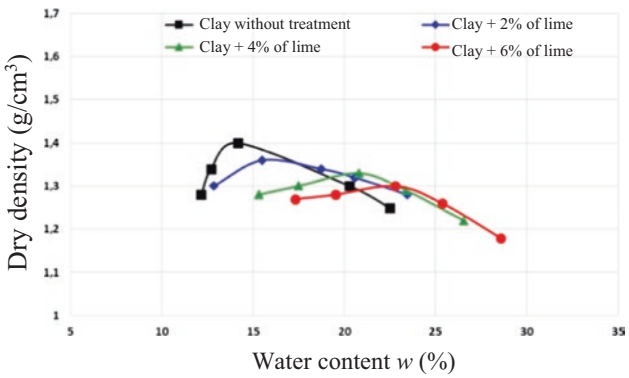

Fig. 1 Lime treatment of clay soil

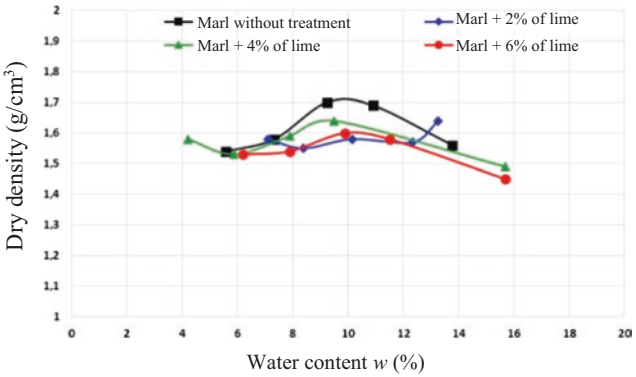

Fig. 2 Lime treatment of marly soil

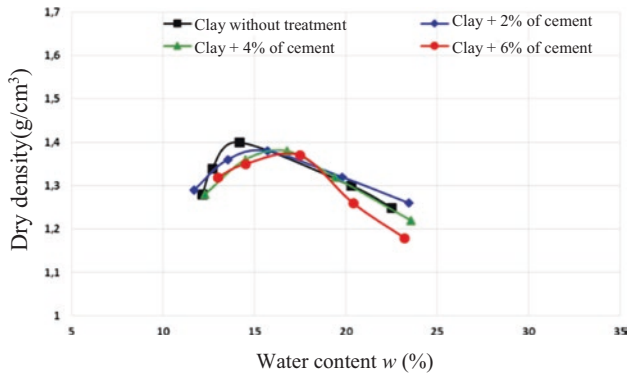

Fig. 3 Cement treatment of clay soil

apart from a moderate flattening which induces a reduction in the water sensitivity of the treated soil (Figs. 3 and 4).

The mixed treatment using lime and then cement is applied to poorly plastic soils, generally intended for subgrade or pavement layer. The action of the lime helps to bring the soil to an optimal state for treatment with cement. The more or less flattened Proctor curves in Figs. 5 and 6 reveal that the mixed treatment makes the soil less sensitive to water with an optimal reduction in water content compared to previous treatments.

4 Conclusions

The decrease in the water content of a lime treated soil is of 1–2% for 1% addition of lime. Adding lime in clay soil develops an agglomeration of fine clay particles into coarser and more friable elements, and this is flocculation. The impacts of these reactions on the soil–lime mixture are a decrease in the IP, a flattening of the Proctor curve with a decrease in density, and an increase in the optimum water content.

The reactions of cement with a soil essentially consist of hydration of anhydrous calcium silicates and aluminates,

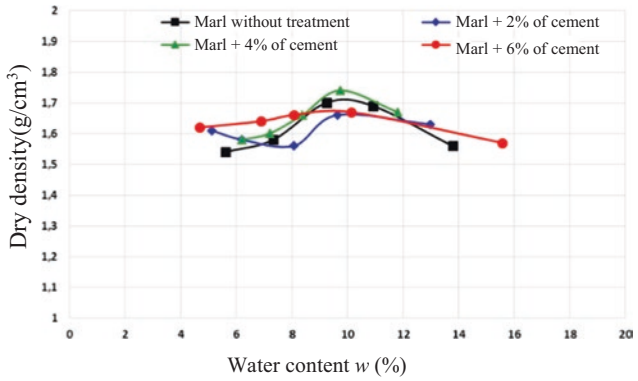

Fig. 4 Cement treatment of marly soil

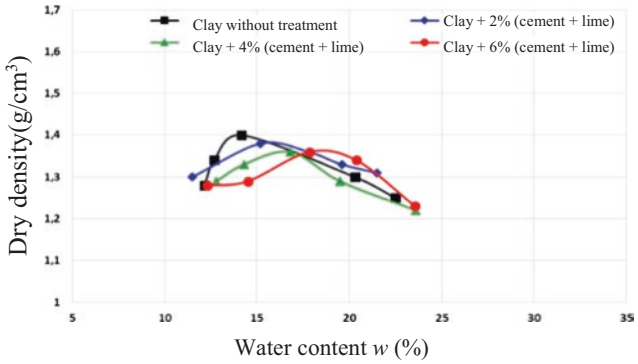

Fig. 5 Mixed treatment (cement and lime) of clay soil

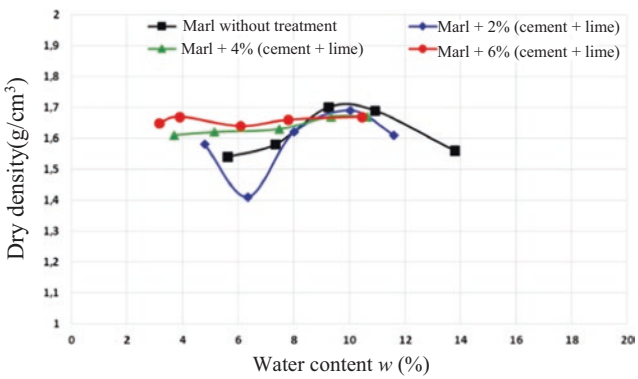

Fig. 6 Mixed treatment (cement and lime) of marly soil

with passage through the solute phase followed by crystallization of the hydrated products, and this is the hydraulic socket. The growth of the formed microcrystals, their entanglement, their progressive felting, coat, and connection of the material's grains to each other form more and more numerous and solid bridges. This quickly leads to the hardening of the mixture, obtaining high mechanical characteristics and its stability to water and frost. The water content of a soil–cement mixture is lowered due to the addition of dry materials; the consumption of water necessary for the hydraulic setting of the cement; evaporation of water by aeration of the soil during mixing. On the other hand, no significant modifications on Proctor curve.

Finally, the mixed treatment (lime and cement) is applied to slightly-to-moderately plastic soils used in sub-layers and, if necessary, in pavement layers. The action of the lime helps to bring the soil to an optimal state for treatment with cement. Thus, a moist clay soil passes almost instantaneously from a plastic state to a solid, friable, non-sticky state and partially loses its sensitivity to water. Its handling on site becomes easy, and its handling behavior and its bearing capacity are improved. The homogeneity that it acquires places it under ideal conditions to undergo the cement treatment.

References

Bouras, F., Tapsoba, N., Martin, M., Sabio, S., Jacquet, A., Beck, K., Belayachi, N., Bouasker, M., Al-Mukhtar., M. (2020). Effect of hydrated lime and cement on the engineering behavior of highly expansive clay. *Athens Journal of Technology and Engineering, 7*(1), 1–14.

Firoozi, A. A., Taha, M. R., Firoozi, A. A., Khan, T. A. (2014). Assessment of nano-zeolite on soil properties. *Australian Journal of Basic and Applied Sciences, 8*(19), 292–295.

Firoozi, A. A., GuneyOlgun, C., Firoozi, A. A. Baghini, M. S. (2017). Fundamentals of soil stabilization. *Geo-Engineering, 8*(26), 1–16.

Harichane, K., Ghrici, M., & Kenai, S. (2012). Effect of the combination of lime and natural pozzolana on the compaction and strength of soft clayey soils: A preliminary study. *Environmental Earth Science, 66*, 2197–2205.

Mahamedi, A., & Khemissa, M. (2015). Stabilization of an expansive overconsolidated clay using hydraulic binders. *HBRC Journal, 11*(1), 82–90.

McDowell, C. (1959) .Stabilization of soils with lime, lime-flyash, and other lime reactive materials. *Highway Research Board Bulletin, 23*, 60–66.

Pourakbar, S., & Huat, B. K. (2017). A review of alternatives traditional cementitious binders for engineering improvement of soils. *International Journal of Geotechnical Engineering, 11*(2), 206–216.

Wang, L. (2002). *Cementitious stabilization of soils in the presence of sulfate* [Doctoral dissertation, Louisiana State University and Agricultural and Mechanical College].

Soil Profile Stratification Based on Cone Penetration Test Results Using *k*-means and Hierarchical Clustering

Ressol Shakir, Jawad Thajeel and Mohammad Al-Umar

Abstract

The design of the foundation for any structure depends mainly on the soil stratigraphic profiling and the characteristics of the soil. Accuracy of the profiling and identification of the boundary of layers help create accurate and cost-effective designs. In recent years, cone penetration test (CPT) is used widely in soil stratigraphic profiling since it produces near-continuous records for both the cone and sleeve resistance. It is used widely for soil profiling and engineering soil characteristics, especially in important projects such as those related to petroleum production projects. This paper applies the *k*-means method of clustering and hierarchical clustering to the soil behavior index obtained from the cone penetration test to identify the soil profile for the soil. These two approaches have been applied to the results obtained from the sound of CPT tested on the soil at the site of Nasiriyah province in Iraq. Applying these two methods is very useful as it can detect the layers and identify the soil layers simply. The analysis shows that the soil at the site can be classified into two main layers with several secondary layers. Collecting the clustering of the soil behavior index with the other engineering properties can give a strong imaginary picture of the soil stratification. The study uses different methods for verifying the results obtained from the hierarchical and *k*-means clustering method such as inconsistency and silhouette graphs. A comparative study has been achieved on the obtained results by the suggested approaches with the adjacent borehole logs showing very good agreement.

Keywords

Site investigation · Cone penetration test · Cluster analysis · Soil profiling · Statistical analysis

1 Introduction

The design of the foundation for any structure, such as shallow foundations, mainly depends on soil characterization (Godoy et al., 2020; Zhang et al., 2019) and soil profiling. There is a significant effect of soil stratification and characterized values of soils on the design, which helps in an accurate and cost-effective method. In recent years, cone penetration test (CPT) has been used widely worldwide in soil stratigraphic profiling since its cost is fair and it produces near-continuous records for both measured components: cone and sleeve resistance. This test is used for essential projects in Iraq since it is relatively expensive. Soil identification contains detecting the type of soil, the number of soil layers, the thickness of each layer, and the soil properties of each layer (Li et al., 2016). Different soil classification charts were produced by several researchers and used widely decades ago, such as those presented by Robertson (Robertson, 1990, 2016). These modes depend on the cone resistance and sleeve friction. Classification charts are empirically developed; therefore, the reference values are uncertain.

Because of uncertainty in the soil classification chart, statistical analysis was applied to identify homogeneous soil as groups of layers (Uzielli et al., 2007). Some topics applied the Bayesian approach (Deng et al., 2020; Wang et al., 2013; Wang, 2020a, 2020b). Cluster analysis is used by Zhang et al. (2019) and Carvalho and Ribeiro (2019). In several methods (Depina et al., 2016; Krogstad et al., 2018), two variables measured through CPT are used in classification. Others functioned the soil behavior type index I_{SBT} to

R. Shakir (✉) · J. Thajeel · M. Al-Umar
Civil Engineering Department, College of Engineering, University of Thi-Qar, Nasiriyah, Iraq
e-mail: rrshakir@utq.edu.iq; rrshakir@yahoo.com

Z. A. Ergüler et al. (eds.), *Selected Studies in Geotechnics, Geo-Informatics and Remote Sensing*, Advances in Science, Technology & Innovation, https://doi.org/10.1007/978-3-031-43759-5_44

identify the soil by using the wavelet transform modulus maxima method, e.g. (Ching et al., 2015).

Several techniques may be used to compute clusters' quality, such as direct and statistical methods (Kassambara, 2017). However, some problematic aspects still exist, such as the number of clusters and the unique clusters. In addition, complex procedures used in some methods, such as Bayesian methods, form non-practical approaches for engineers.

In this paper, two methods of clustering are used, the first is *k*-means of clustering, and the second is hierarchical clustering. The analysis is based on the CPTs results performed on the soil at the project site of a petrol refinery station in the south of Nasseriyah city. First, the CPT and soil behavior type-based classification results are produced, and then, clustering analysis is utilized to test the data. Silhouette graphical technique is used to estimate the number of clusters. The results of cluster techniques are compared with the CPT-based classification results. This method is simple, efficient, and can be practiced and used with the limitation that the type of soil cannot be identified without referring to soil attributes.

2 Methodology

The research methodology comprises computing soil behavior indices developed by Robertson based on CPT results. A clustering method using the *K*-means and hierarchical approach is used to know the number of clusters and identify the thickness of the layers. The number of layers can be obtained based on the following subsections that state the research methodology. An example of the CPT test result is used to apply the clustering method.

2.1 Soil Behavior Type

The soil stratification is obtained based on normalized charts (Robertson, 1990) and non-normalized charts updated by Robertson (2010), where the soils are classified into nine soil behavior types (SBT) instead of non-normalized charts that define 12 SBT zones (Robertson et al., 1986). The non-normalized SBT index (I_{SBT}) updated for nine zones can be defined as

$$I_{SBT} = \sqrt{\left((3.47) - \log\left(q_c / p_a\right)\right)^2 + \left(\log R_f + 1.22\right)^2} \quad (1)$$

It uses the basic CPT measurements (q_c and R_f), where q_c is CPT cone resistance (or corrected cone resistance, q_t), R_f is the friction ratio (f_s/q_c) 100%, and f_s is the sleeve friction. The normalized and non-normalized indices are the same, except when in-situ vertical stress is between 50 and 150 kPa, there is a difference between them (Godoy et al., 2020; Zhang et al., 2019). For simplicity, the updated non-normalized method is used to identify the soil type.

2.2 Clustering Techniques

Many clustering techniques are developed, such as partitional clustering, hierarchical clustering, artificial system clustering, and kernel-based clustering based on the properties of the generated clusters (Olusegun et al., 2012). Partitional clustering directly divides data points into some pre-specified number of clusters without a hierarchical structure. In this paper, partitional and hierarchical clustering are used. Different types of distance methods, such as Euclidean distance, are used to evaluate the similarity between different data sets.

2.3 Applying Clustering Algorithm

Generally, different kinds of partitional clustering methods are used in literature, such as *K*-means and *K*-median. In this paper, the *K*-means method is used for clustering, which is an unsupervised method used to partition the data into clusters (Li et al., 2016). The variable included in the analysis in this paper is the I_{SBT}. The technique has functioned I_{SBT} as a variable using the probabilistic method for clustering purposes (Cao et al., 2019).

Let the variable is $(I_{SBT})_i$ and $i = 1,\ldots,n$ be the set of 1-dimensional points to be clustered into K clusters, $C = \{c_k, k = 1,\ldots K\}$, where I_{SBT} is obtained from CPT test. The squared error between the mean of the cluster $(\mu_{I_{SBT}})_k$ and the points in the cluster is defined as

$$J(c_k) = \sum_{I_{SBT} \in c_k} \left\| (I_{SBT})_i - \left(\mu_{I_{SBT}}\right)_k \right\|^2 \quad (2)$$

2.4 Number of Clusters

Determining the number of clusters (k) is the most challenging problem in data analysis. Trials with a different number of clusters may be performed, and then, the best value of k can be identified. Two groups of methods can be used to obtain the best solution: direct methods (Kassambara, 2017), such as silhouette and elbow technique, and statistical methods, such as gap technique (Li et al., 2016), Dirichlet process, minimum message length criterion MML, Bayes information criterion (BIC), and Akiake information criterion (AIC). Silhouette graph is used in this study in addition to the dendrogram to estimate the number of clusters because of its simplicity. Many

Fig. 1 Geographic map of Nasiriyah city

clusters can be provided depending on the number of data in the set. For the soil classification, the reference number of clusters is often less than eight ($N_c < 8$) (Hegazy & Mayne, 2002). The number of layers in this study is taken as eight layers.

2.5 Site Description

The methodology presented in this research is applied to the CPTs results obtained through site investigation on Nasiriyah soil. It is achieved as part of the site investigation of the soil in the South of Nasiriyah, Iraq, where a petrol refinery station was intended to be constructed (Shakir, 2019). Figure 1 shows the map of Nasiriyah city that demonstrates the project's location. One CPT test among more than 20 test results is presented here to test the approach. CPT No 1, as illustrated in Fig. 2, will be analyzed. More information about the soil in Nasiriyah can be obtained through reference (Shakir, 2018).

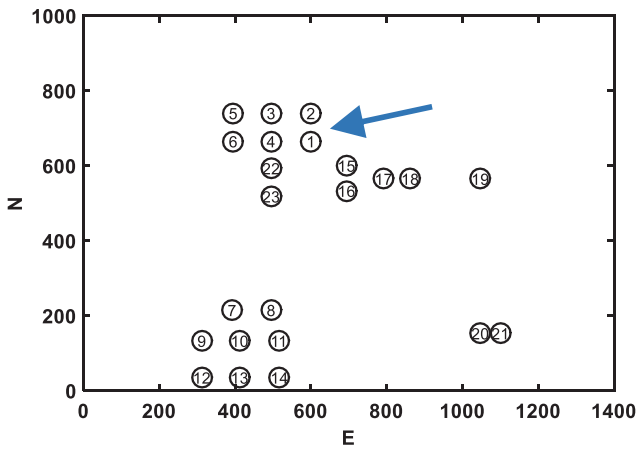

Fig. 2 Layout of vertical CPTs at the oil refinery site at Nasiriyah City

3 Results

Figure 3 shows the components measured through CPT 1 and the quantities computed based on the measured values. Because of the lake of space, only one sound CPT is considered. Figure 3a shows the distribution of cone tip resistance with depth. The values of q_c increase starting from a depth equal to about 11–12 m. The plot considers the values every 0.2 m, where about 100 points are plotted with depth. Figure 3b shows the relation of sleeve friction in kPa with depth. The corrected value of q_c is drawn with depth (see Fig. 3c). The R_f representing the basic quantity f_s/q_t is drawn with depth Fig. 3d. The last two quantities are used to classify the soil based on non-normalized basic quantities q_t and R_f. Using Eq. 1, the SBT can be obtained based on I_{SBT} presented in Fig. 3e. Nine types of soils can be identified based on I_{SBT}. All the calculations and plots are given based on a MATLAB code written for this research. Figure 3f shows the soil profile with depth based on the I_{SBT} of a non-normalized chart. The profile consists mainly of two layers. The depth of 12 m is the split line between them.

By using the *k*-means method, the number of clusters is obtained based on I_{SBT}. It is clearly shown that the clusters approximately reflect the soil stratification but without indicating the type of soil. Figure 4a shows a trial profile by assuming 2 clusters which give an approximate profile among choices from 3 to 7 clusters. For two clusters, as in Fig. 4a, it is obvious that the two layers are separated at 12 m, precisely similar to the soil profile presented in Fig. 3f for the soil profile based on non-normalized charts.

4 Discussion

Validation of the soil classification results based on the *k*-means techniques was performed by comparing the numerical results with the actual classification of soil based on the samples extruded from the boreholes. Figure 4b

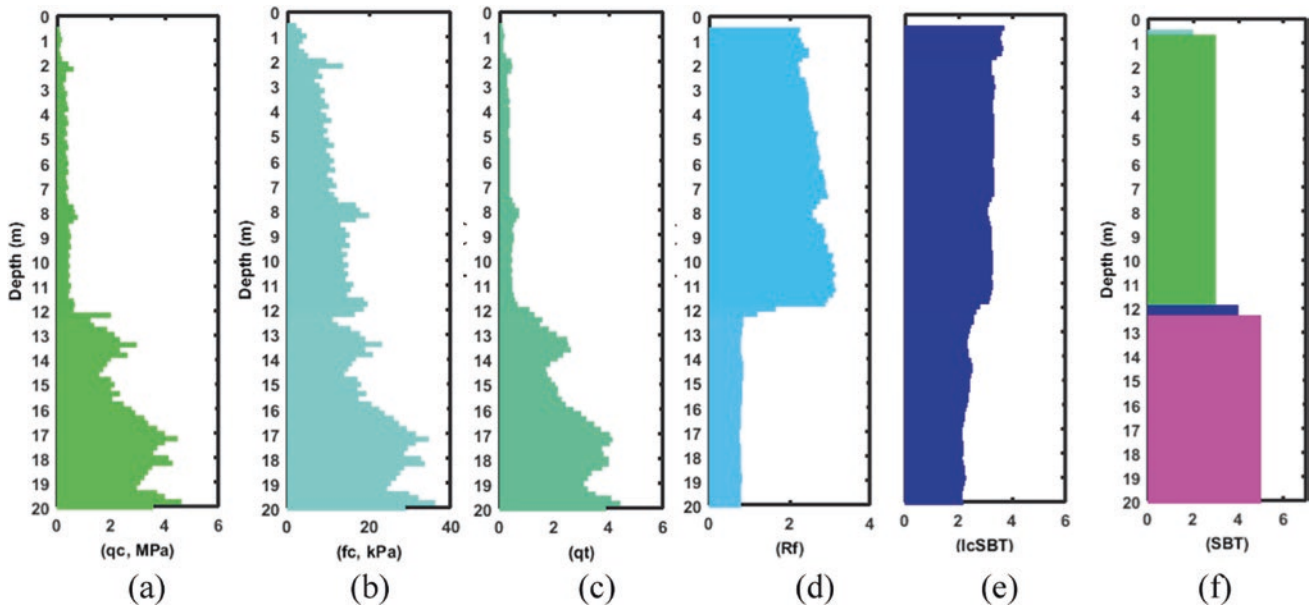

Fig. 3 Cone tip resistance, friction resistance, corrected cone tip resistance, friction ratio, and soil classification

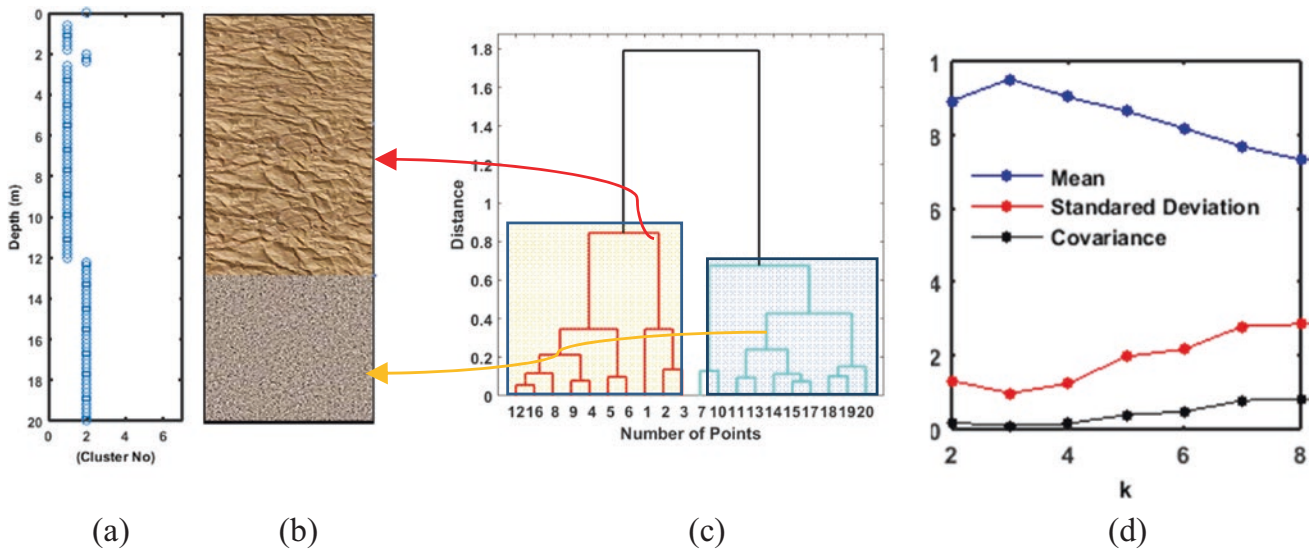

Fig. 4 **a** Soil profile based on two clusters, **b** soil profile based on two boreholes, **c** dendrogram plot, **d** Silhouette values versus the number of clusters

shows the soils at a borehole in the location of the CPTs for comparison. Approximately the soil classification is equal to clusters.

As a result of applying the hierarchical clustering and demonstrating the relationships between the I_{SBT}, a common diagram is used in hierarchical clustering called a dendrogram with the aid of inconsistency. Figure 4a, c shows the hierarchical relationship between the soils. The number of nodes was 20 points. The number of clusters can be obtained based on Silhouette graphics in the *K*-mean algorithm. Figure 4d shows the relationship between the number of clusters and silhouette values. As the silhouette decrease indicates, the number of values is not well clustered. The mean value of the silhouette values for every cluster is drawn (Fig. 4d). The number of clusters that display the greater silhouette value will show the best number of clusters. According to Fig. 4, the two clusters will give the greatest value of the silhouette value.

5 Conclusions

Two clustering methods were used to numerically classify the soils based on the CPT results in Naseriyah, Iraq. The number of clusters and the thickness of every layer were obtained approximately similar to those obtained based on the CPT classification chart. The number of clustering is based on the mean values of silhouette, and it is found to be two layers of soil. Comparing the clustering with the layers obtained based on boreholes gave approximately similar results. The hierarchical method was also used, and it gave roughly the same results. It can classify the soil but without identifying the type of soil.

References

Cao, Z. J., Zheng, S., Li, D. Q., & Phoon, K. K. (2019). Bayesian identification of soil stratigraphy based on soil behaviour type index. *Canadian Geotechnical Journal, 56*, 570–586. https://doi.org/10.1139/cgj-2017-0714

Carvalho, L. O., Ribeiro, D. B. (2019). Soil classification system from cone penetration test data applying distance-based machine learning algorithms. *Soils and Rocks, 42*, 167–178. https://doi.org/10.28927/SR.422167

Ching, J., Wang, J. S., Juang, C. H., & Ku, C. S. (2015). Cone penetration test (CPT)-based stratigraphic profiling using the wavelet transform modulus maxima method. *Canadian Geotechnical Journal, 52*, 1993–2007. https://doi.org/10.1139/cgj-2015-0027

Deng, Z. P., Jiang, S. H., Niu, J. T., Pan, M., & Liu, L. L. (2020). Stratigraphic uncertainty characterization using generalized coupled Markov chain. *Bulletin of Engineering Geology and the Environment*. https://doi.org/10.1007/s10064-020-01883-y

Depina, I., Le, T. M. H., Eiksund, G., & Strøm, P. (2016). Cone penetration data classification with Bayesian mixture analysis. *Georisk, 10*, 27–41. https://doi.org/10.1080/17499518.2015.1072637

Godoy, C., Depina, I., Thakur, V. (2020). Application of machine learning to the identification of quick and highly sensitive clays from cone penetration tests. *Journal of Zhejiang University-Science A, 21*, 445–461. https://doi.org/10.1631/jzus.A1900556

Hegazy, Y. A., & Mayne, P. W. (2002). Objective site characterization using clustering of piezocone data. *Journal of Geotechnical and Geoenvironmental Engineering*. https://doi.org/10.1061/(ASCE)1090-0241(2002)128:12(986)

Kassambara, A. (2017). *Cluster analysis in R—Unsupervised machine learning*. STHDA.

Krogstad, A., Depina, I., Omre, H. (2018). Cone penetration data classification by Bayesian inversion with a Hidden Markov model. *Journal of Physics: Conference Series, 1104*, 012015.

Li, J., Cassidy, M. J., Huang, J., Zhang, L., & Kelly, R. (2016). Probabilistic identification of soil stratification. *Geotechnique*. https://doi.org/10.1680/jgeot.14.P.242

Olusegun, A., Makun, H. A., Ogara, I. M., Edema, M., Idahor, K. O., Oluwabamiwo, B. F., Eshiett, M. E. (2012). We are IntechOpen, the world's leading publisher of Open Access books built by scientists, for scientists TOP 1%. *Intech, 1*, 38. https://doi.org/10.1016/j.colsurfa.2011.12.014

Robertson, P. K. (1990). Soil classification using the cone penetration test. *Canadian Geotechnical Journal, 27*, 151–158. https://doi.org/10.1139/t90-014

Robertson, P. K. (2016). Cone penetration test (CPT)-based soil behaviour type (SBT) classification system—An update. *Canadian Geotechnical Journal, 53*, 1910–1927. https://doi.org/10.1139/cgj-2016-0044

Robertson, P. K. (2010). Soil behaviour type from the CPT: An update. In *2nd International symposium on cone penetration testing* (p. 8).

Robertson, P. K., Campanella, R. G., Gillespie, D., Greig, J. (1986). Use of piezometer cone data.

Shakir, R. R. (2018). Spatial correlation of cone tip resistance for soil in Nasiriyah. *The Open Civil Engineering Journal*. https://doi.org/10.2174/1874149501812010413

Shakir, R. R. (2019). Selecting the probability distribution of cone tip resistance using moment ratio diagram for soil in Nasiriyah. *Geotechnical and Geological Engineering*. https://doi.org/10.1007/s10706-018-0716-3

Uzielli, M., Lacasse, S., Nadim, F., Phoon, K. K. (2007). Soil variability analysis for geotechnical practice. In *Characterisation and engineering properties of natural soils*.

Wang, Y., Huang, K., & Cao, Z. (2013). Probabilistic identification of underground soil stratification using cone penetration tests. *Canadian Geotechnical Journal, 50*, 766–776. https://doi.org/10.1139/cgj-2013-0004

Wang, H. (2020a). Finding patterns in subsurface using Bayesian machine learning approach. *Underground Space, 5*(1), 84–92. https://doi.org/10.1016/j.undsp.2018.10.006

Wang, X. (2020b). Uncertainty quantification and reduction in the characterization of subsurface stratigraphy using limited geotechnical investigation data. *Underground Space, 5*, 125–143. https://doi.org/10.1016/j.undsp.2018.10.008

Zhang, W. G., Zhang, R. H., Han, L., Goh, A. T. C. (2019). Engineering properties of the Bukit Timah Granitic residual soil in Singapore. *Underground Space, 4*(2), 98–108. https://doi.org/10.1016/j.undsp.2018.07.001

Stability Analysis of Shallow Tunnels in Soft Soils Containing Boulders

Javad Shahmoradi, Siavash Norouzi and Pedram Roghanchi

Abstract

In this paper, the stability of a shallow tunnel in an environment with the existence of boulders in a soft soil was studied. A case study of a near-surface subway line crossing heterogeneous alluviums of Tehran plain was carried out. The interaction of the soil environment with the boulders and the influence of the volume of boulders on the stability of the tunnel were investigated using 2D numerical modeling. Numerical modeling and field investigations show that the size and volume of boulders will affect the stability of shallow tunnels, and larger boulders may effectively increase the tunnel stability. Therefore, investigation of the stability of the shallow tunnel should include the effect of the volume of boulders.

Keywords

Boulder · Soil · Shallow Tunnel · TBM · NATM

1 Introduction

Tunnels are important underground structures which find a wide range of applications such as traffic and water transmission (e.g. Li & Yang, 2018; Zhang et al., 2020; Abdollahi et al., 2019). Subway tunnels are among the constructions that are only purposed for urban environments (Qiu et al., 2020; Shahmoradi et al., 2020). Most of large cities are situated on alluviums (Sugai & Honda, 2016; Zalbuin Mase et al., 2020; Elgamal, 2019). This is the case for the city of Tehran, which is located on the mountainsides of the Alborz range, Iran. Tehran is located on alluvial sediments stretching from the Alborz mountainside into the southern desert. The deposits have been created by the rivers and seasonal floodwaters originating from the Alborz range. In the regions closer to the range, the alluvium is mainly consisted of boulders. The tunnel construction in which the TBM and NATM methods are employed, the presence of boulders induces several excavations and stability challenges. This paper provides a case study that investigates the stability of a tunnel constructed in rocky boulders. A statistical study of boulders in terms of volumetric characteristics and positioning is presented. Using numerical modeling, tunnel stability with temporary support is analyzed at different volumes of boulders.

2 Statistical Study of Volumetric Distribution of Boulders at Site

Excavated using the NATM method, the tunnel section belongs to line 1 of Tehran's subway tunnel extending from Pol-e-Rumi Avenue to Emamzadeh Avenue, both intersecting Shariati Street. The boulders existing along the tunnel extension did not follow a regular pattern in terms of volume and positioning. Measurements showed that the maximum encountered rock volume was 48 m^3. On average, every 1m^3 of excavation contained 0.669 m^3 of boulders or at the tunnel profile of 72 m^2 and an advancement depth of 1 m, 5 m^3 of boulders could be extracted.

Figure 1 shows the quantities of boulders extracted at the volumetric intervals of 3 m^3. Based on this analysis, 71% of boulders are smaller than 5 m^3. Therefore, boulders smaller than or equal to this threshold were more likely present at the walls and ceiling.

J. Shahmoradi · S. Norouzi · P. Roghanchi (✉)
New Mexico Institute of Mining and Technology, 801 Leroy Pl, Socorro, NM, USA
e-mail: pedram.roghanchi@nmt.edu

Z. A. Ergüler et al. (eds.), *Selected Studies in Geotechnics, Geo-informatics and Remote Sensing*, Advances in Science, Technology & Innovation, https://doi.org/10.1007/978-3-031-43759-5_45

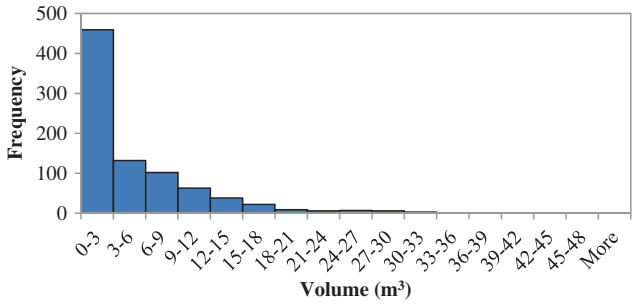

Fig. 1 Number of excavated boulders sorted based on their volume

3 Results

3.1 Numerical Analysis Using UDEC

Featuring discrete element method (DEM) as its framework, UDEC is software for analysis of stability and simulation of deformation at 2-dimensional discontinuous media (Itasca & UDEC, 2004). As DEM considers the interactions and interfaces between the constituents of a solid body (Azarfar et al., 2018), UDEC was selected as the numerical tool to capture the interactions between soil and rock in the stability analysis of the tunnel subject to this study.

3.2 Effect of Surrounding Boulders on Tunnel's Stability

Figures 2 and 3 show displacement vectors for models: (a) no boulders, (b) boulders of 3.0 m^3, (c) boulders of 5.0 m^3, and (d) boulders of 48 m^3.

In all four models, a temporary support with 30 cm thickness composed of shotcrete layer, frame, and meshes have been applied to the walls, ground, and ceiling. In all models except b, reinforcement was installed in discrete steps, each of which involved applying shotcrete for 5 cm and relaxing for the subsequent step such that the real reinforcement process was simulated. Model b, however, received the shotcrete in one step along the entire tunnel extent, which will be discussed more in details in the full paper.

4 Discussion

The numerical model properly captured the effect of the existing boulders on the tunnelling performance. The model was able to simulate some localized collapses after the first shotcrete application as a result of the presence of small boulders, producing mixtures of soil, and small rocky boulders. At some sections, parts of the large boulders outside the tunnel appeared as outcrops and the excavators used in the construction were not able to extract them. However, these blocks were cut by means of other machinery.

The aforementioned statistical analysis of the size distribution of the boulders necessitated a numerical investigation of the stability of the tunnel section with different volumes of rocky boulders. This numerical study will be presented in the full-text paper.

5 Conclusions

The statistical study of the volume distribution of boulders showed that 71% of them were smaller than 5m^3. The numerical analysis reflected a negative correlation between the displacements at the tunnel crown and the volume of boulders therein. It was also shown that the soil

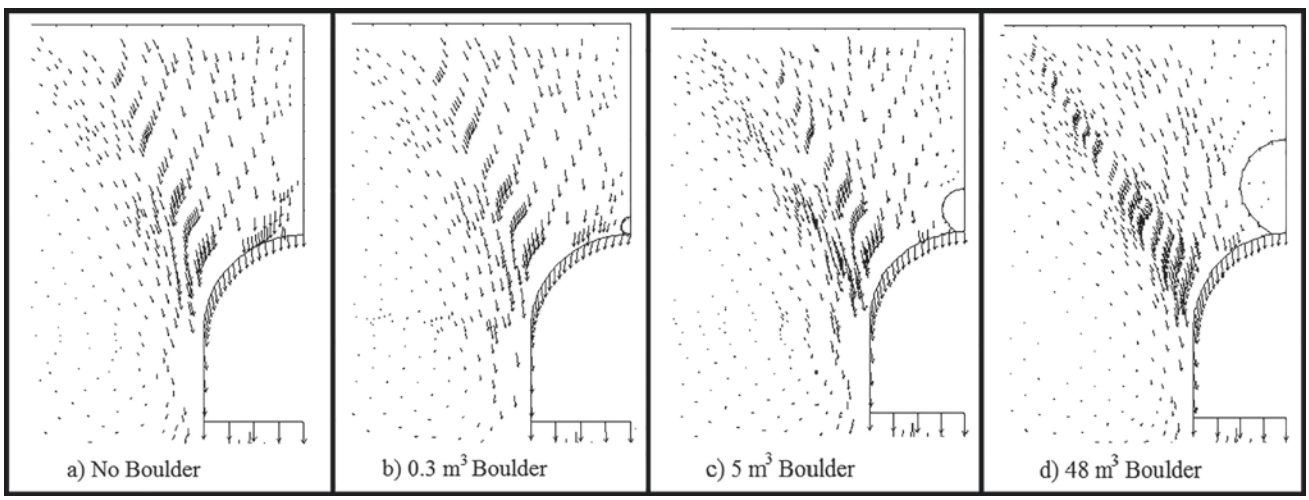

Fig. 2 Displacement vectors in the tunnel section

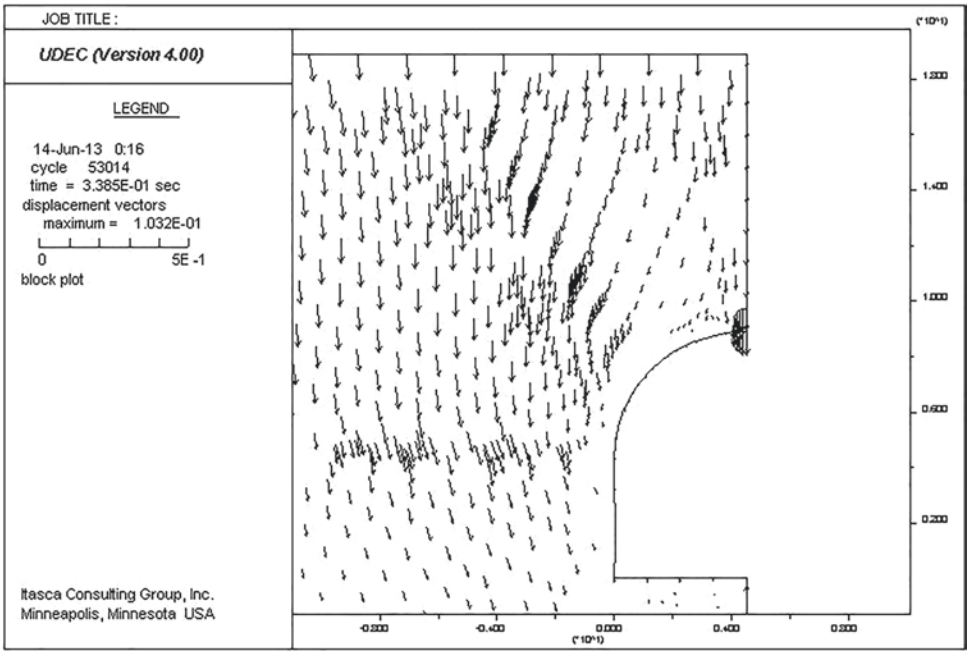

Fig. 3 Displacement vectors for a failure in the top

flows through the boulders toward the inside of the tunnel, with the boulders remaining immobile. Therefore, it can be concluded that any instability would be due to the soil. Obviously, the application of proper supporting systems is critical during tunnel excavations in such environments. In presence of boulders, immediate installation of supporting system is necessary. In such cases, extensive studies on the distribution, size, and other characteristics of boulders should be conducted prior to tunneling. Moreover, higher factors of safety should be considered when smaller boulders exist around the excavation.

References

Abdollahi, M. S., Najafi, M., Bafghi, A. Y., & Marji, M. F. (2019). A 3D numerical model to determine suitable reinforcement strategies for passing TBM through a fault zone, a case study: Safaroud water transmission tunnel, Iran. *Tunnelling and Underground Space Technology, 88*, 186–199. https://doi.org/10.1016/j.tust.2019.03.008

Azarfar, B., Peik, B., Abbasi, B., & Roghanchi, P. (2018). A discussion on numerical modeling of fault for large open pit mines. In *52nd US rock mechanics/geomechanics symposium*. American Rock Mechanics Association.

Elgamal, A. (2019). Using micropile to retrofit of tilting building rested on alluvium deposits: Case study of inclined elven stories building at Egyptian Delta. https://doi.org/10.11159/icgre19.142

Itasca, U. D. E. C., & UDEC. (2004). Version 4.0, Itasca Consulting Group.

Li, T. Z., & Yang, X. L. (2018). Probabilistic stability analysis of subway tunnels combining multiple failure mechanisms and response surface method. *International Journal of Geomechanics, 18*, 04018167. https://doi.org/10.1061/(ASCE)GM.1943-5622.0001315

Qiu, J., Lu, Y., Lai, J., et al. (2020). Experimental study on the effect of water gushing on loess metro tunnel. *Environmental Earth Sciences, 79*, 261. https://doi.org/10.1007/s12665-020-08995-4

Shahmoradi, J., Salari Rad, H., & Roghanchi, P. (2020). Face stability analysis for the earth pressure balance method in nonhomogeneous inclined soil layers: Case study. *International Journal of Geomechanics, 20*, 05020005. https://doi.org/10.1061/(ASCE)GM.1943-5622.0001833

Sugai, T., Honda, K. (2016). Distribution of liquefaction sites and coastal alluvium in Japan. In *Natural disaster and coastal geomorphology* (pp. 93–111). Springer International Publishing.

Zalbuin Mase, L. (2020). Seismic hazard vulnerability of Bengkulu City, Indonesia, based on deterministic seismic hazard analysis. *Geotechnical and Geological Engineering, 38*(5):5433–5455. https://doi.org/10.1007/s10706-020-01375-6

Zhang, C., Li, W., Zhu, W., & Tan, Z. (2020). Face stability analysis of a shallow horseshoe-shaped shield tunnel in clay with a linearly increasing shear strength with depth. *Tunnelling and Underground Space Technology, 97*, 103291. https://doi.org/10.1016/j.tust.2020.103291

Landslides' Analysis Using Geotechnical and Geophysical Survey: A Case Study of Djebahia Area (Bouira, Algeria)

Brahim Meziani, Hamid Gadouri, Abdelkader Bouderbala and Mohammed Hemza Aissa

Abstract

Most of the regions in northern Algeria are highly exposed to several natural hazards such as earthquakes, landslides, and floods, which cause significant material and human losses. Consequently, the main aim of this paper is specifically limited to the study of the landslides observed in Djebahia region (the case of water transfer pipeline from the Acerdoune dam to M'sila town). Accordingly, geophysical and geotechnical results related to the Djebahia landslides have been collected and then analyzed in order to determine the main factors that affect the region. As results, it was found that land steepness, water availability, and soil quality (marl and clay) are the main factors of the induced landslides, where the breaking surface can occur at different depths (from 7 to 20 m). Subsequently, the installation of two series of piles was suggested as an adequate solution in order to reduce the risk of movements in this region where several inclinometers have been installed near these piles to control movements in depth. The inclinometric results, taken over two years, showed admissible displacements at different depths.

Keywords

Natural hazards · Landslides · Geotechnical facts · Geophysical methods · Soil quality

B. Meziani (✉) · H. Gadouri · A. Bouderbala · M. H. Aissa
Earth Sciences Department, University Djillali Bounaama, 44225 Khemis Miliana, Ain Defla, Algeria
e-mail: brahim.meziani@univ-dbkm.dz

H. Gadouri
Geomaterials Laboratory, Chlef University, 02000 Chlef, Algeria

1 Introduction

Landslides constitute the most important problem in the financial system and improvement of the northern location of Algeria, which is characterized by several mountains, critical values of precipitation, and different geological formations (Machane et al., 2008; Meziani et al., 1955, 2017, 2019). Djebahia region is situated in the North-West of Bouira metropolis at 20 km within the South-East of Algeria at 77 km (see Fig. 1). This region is characterized by the aid of reliefs to steep slopes between 15 and 25 levels because it belongs to the location of the Djurdjura Mountains. Due to the more youthful remedy attributable to tectonic moves, excessive slope, and a crucial precipitation rate, the hydrographical community device is incredibly dense. However, landslides frequently have an effect on the primary street section of RN25 connecting Bouira to Tizi-Ouzou and the toll station of the Bouira-Tizi Ouzou penetrating highway.

In this present study, geotechnical facts (center drilling and laboratory analyzes) and two distinct geophysical methods (seismic profile and vertical electrical sounding) were used within the objectives of reading and characterizing the landslide of the toll station in Djebahia, which include lithology (marly clay), soil characteristics, and depth rupture surfaces (7–20 m). So, as to reduce the risk of landslides in this region, a few answers are proposed to protect the road network and the pipeline and mainly to avoid these lands' moves. Whilst for the affected areas, some inclinometers have been hooked up to display ground movements.

2 Materials and Methods

Geotechnical investigations are executed using mechanical boreholes with non-stop coring, which will establish the lithological sequence and determination of the physico-mechanical parameters of soil from extracted samples. Tests of different geotechnical results were carried out by

Z. A. Ergüler et al. (eds.), *Selected Studies in Geotechnics, Geo-Informatics and Remote Sensing*, Advances in Science, Technology & Innovation, https://doi.org/10.1007/978-3-031-43759-5_46

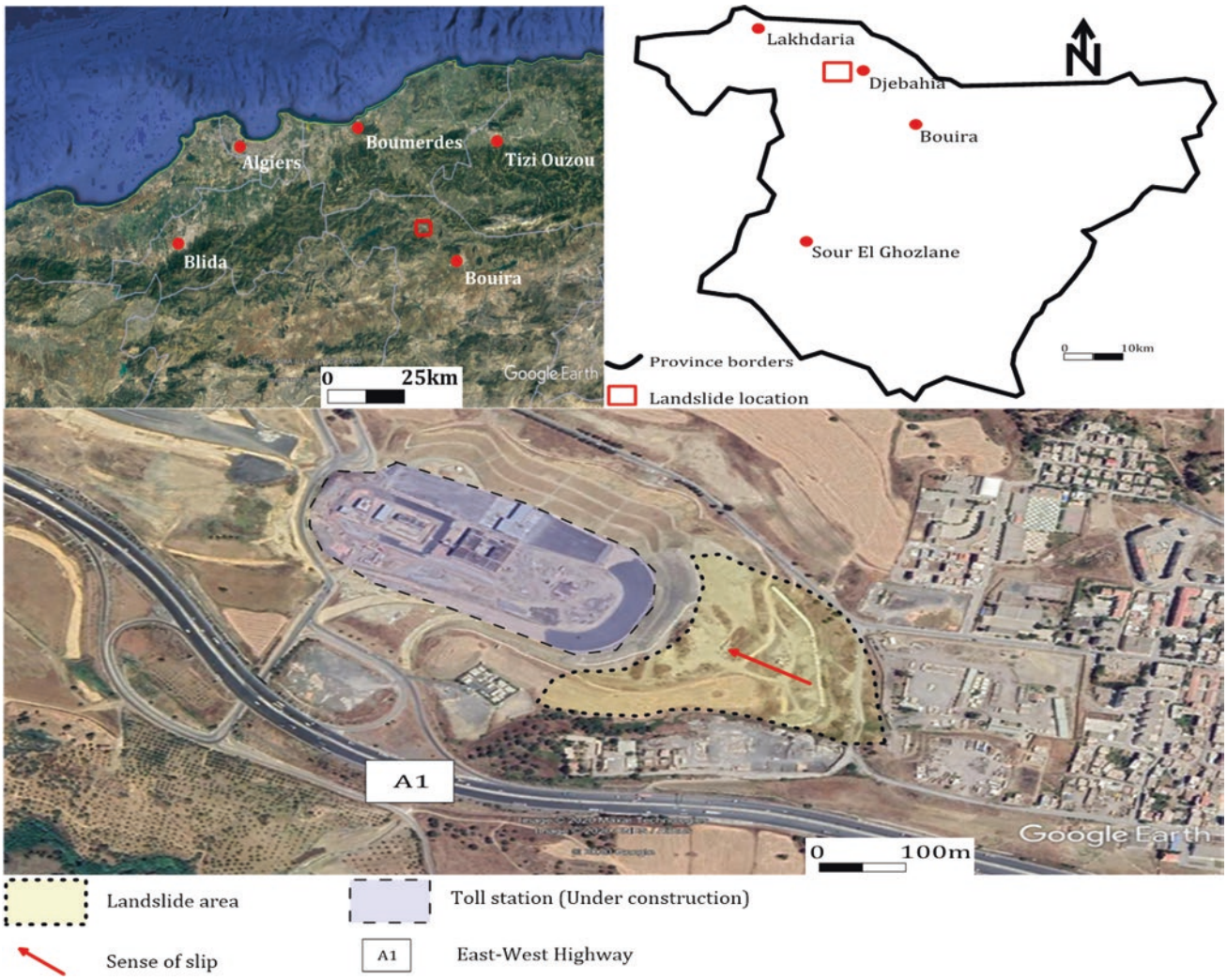

Fig. 1 Landslide of the Toll station in Djebahia. Area of study with its situation in Algeria (*Source* Google Earth). The red rectangular is the localization of the landslide

"Algerian Construction and Public Works Company" and used in this study (KOU.G.C., 2016). Three core drillings noted BHI2, BHI3, and BHI3 were placed by three inclinometers in accordance with NF standard P94-156, where one of these boreholes (BH1) was fitted with PVC pipes to serve as a monitoring well for up to 20 m depth, and three pressiometric tests were implemented to cover the entire surface of the landslide (Fig. 2). Classification tests, shear strength, and compressibility were performed in order to determine the geotechnical properties.

The geophysical methods have become useful in the study of landslides by defining lithological boundaries and their characteristics (Bottari et al., 2018). One seismic profile and one electrical vertical survey are realized in this study, which are the main geophysical methods that are usually used for studying landslides. These surveys were planned to provide detailed reconstruction of the subsoil, highlight stratigraphic succession, and lateral lithological variations, and to evaluate physical properties of the subsurface materials. In the current work, we combine geophysical data and land instability data to provide detailed results of the studied site.

3 Results and Discussions

3.1 Geotechnical Properties

The various observations showed that the lithological succession in this slope is illustrated mainly from top to bottom by embankments, brownish marsh clays, and deep compacted marl interspersed by sandstone banks (Fig. 3). As a result of the pressiometric test, no tests could be performed at the heterogeneous embankment due to the slumping of the drilling walls and due to the fear of a deflation of

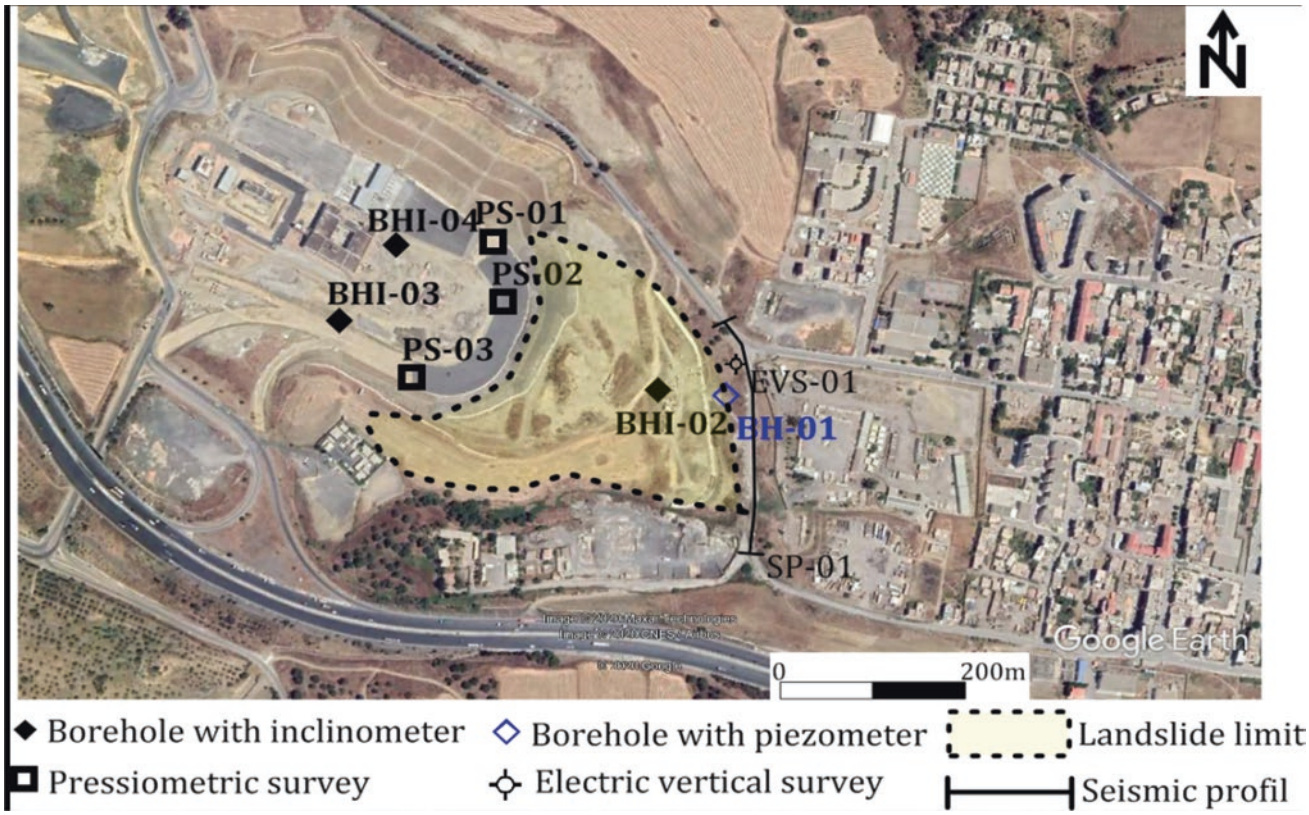

Fig. 2 Localization of deferent in situ tests on the study area

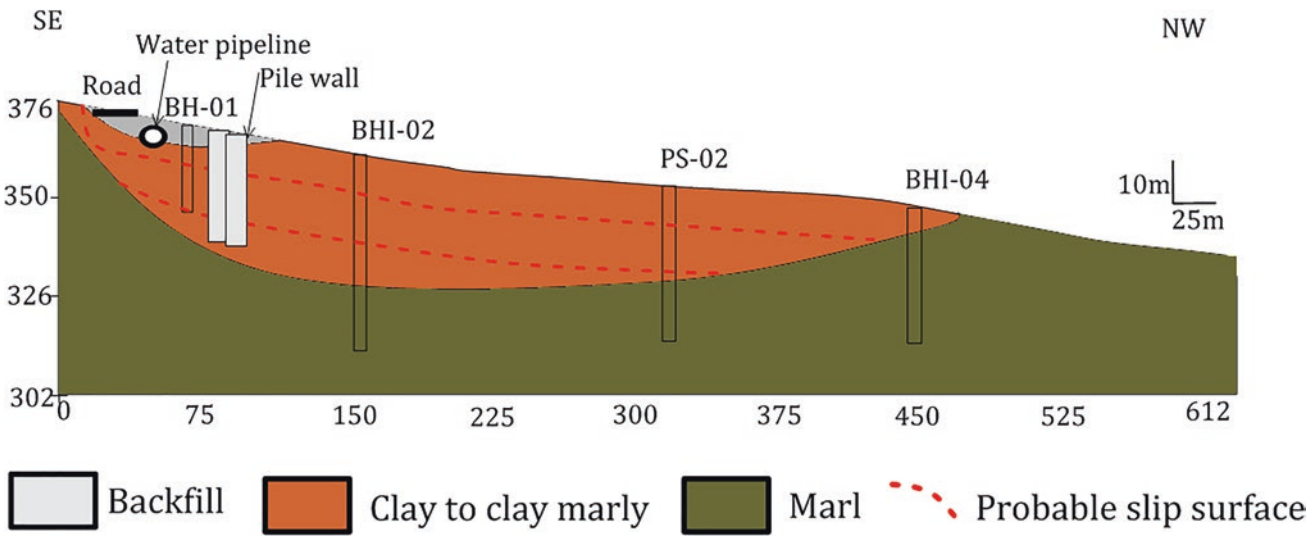

Fig. 3 Synthetic lithological cross section of the Toll station landslide in Djebahia (Bouira)

the pressiometric survey. The pressiometric characteristics obtained at the clay level highlight the moderately compact character of this formation (1.5 < pl < 1.7 MPa) with pressiometric modules ranging from 31 to 35 MPa. For the compact marl, pressiometric characteristics showed that its roof is altered (1.6 < pl < 2.0 MPa) and becomes hard in depth (pl > 2.2Mpa).

Laboratory tests' results of, for example, the marly clays have dry unit weight (γd) ranging between 17.8 and 19.2 kN.m$-^{3}$. Natural water contents (W) range from 14.2

to 18.2%, characterizing relatively wet soils. The plasticity index (PI) varies from 27 to 32%. These results showed that these geological formations are mainly classified as *A*3 materials (plastic clay). In addition, the consistency index (Ic) of the various samples tested showed that the land is more of a humid water state.

3.2 Geophysical Properties

The interpretation of geophysical profiles results indicated that the studied site is composed of two main formations:

- Marly clay surface formation with thickness ranging from 5 to 9 m (North to South) with seismic speeds ranging from 400 to 800 m/s, with highly dispersed resistivity;
- The second field appears relatively compact and represents marl with sandstone passage, characterized by very high seismic speeds (1100–2000 m/s).

3.3 Appropriate Solution and Inclionmetric Monitoring

Based on the above results, two lines of piles were inserted between 40 and 50 m depth, which are connected between them as a solution to strengthen and stabilize the slope. In order to serve the field movements and confirm the reliability of the suggested solution, several inclinometers were installed at the site of the toll station slip, which have showed very low movements. As far as the graphs of the movements are concerned, these are the cumulative movements according to the AA' axis laid in the direction of the slope, so it can be said that there is no movement. The small differences of 1–3 mm in the lead are not significant, and they are of the same order as the "background noise" or imprecision of measurement that can be recorded on some drilling.

4 Conclusions

This landslide has a limited size, about 90 m wide, over a hundred meters upstream downstream extension. Geotechnical (core drillings and pressiometric tests) and geophysics (seismic profile and vertical electrical survey) results, consistent in their results, showed that there is the presence of heterogeneous formation (clay embankments about 3 m thick, heterogeneous clays up to 6–9 m, then hard marl beyond 9 m). The cross-seismic profile at the roadside showed a form of paleotalweg at the roof of the substratum, which could correspond to a larger axis of alteration. A very low movement has been observed due to the installation of two lines of piles.

References

Bottari, C., Albano, M., Capizzi, P., D'Alessandro, A., Doumaz, F., Martorana, R., Moro, M., & Saroli, M. (2018). Recognition of earthquake-induced damage in the Abakainon Necropolis (NE Sicily): Results from geomorphological, geophysical and numerical analyses. *Pure and Applied Geophysics, 175*, 133–148.

KOU.G.C. (2016) études de confortement et de protection des desordes et des glissements de terrain apparus le long du trace de la conduite AEP « wilaya de bouira » rapport interne Unpubl.

Machane, D., Bouhadad, Y., Cheikhlounis, G., Chatelain, J. L., Oubaiche, E. H., Abbes, K., Guillier, B., & Bensalem, R. (2008). Examples of geomorphologic and geological hazards in Algeria. *Natural Hazards, 45*, 295–308.

Meziani, B., Machane, D., Bendaoud, D., CheikhLounis, G., Oubaiche, E., Chabane, S., Bensalem, R., & Moulouel, H. (2017). Geotechnical and geophysical characterization of the Bouira-Algiers Highway (AinTurck, Algeria) landslide. *Arabian Journal of Geosciences, 10*, 117.

Meziani, B., Gadouri, H., Bouderbala, A. E. K., Itatahine, A. E. F., Ouaad, M. (2019). Contribution of geophysical and geotechnical to the evaluation of the landslide appeared along the road of the AEP pipe from Acerdoune in Djebahia (W. Bouira). In *The 1st international congress on advances in geotechnical engineering and construction management (ICAGECM'19)*, université 20 Août 1955 Skikda, Algeria.

Comparative Analysis of Slope Stability Through Empirical and Numerical technique—A Case Study, Uttarakhand, India

Hari Om Singh, Tariq Anwar Ansari, T. N. Singh and K. H. Singh

Abstract

Slope failures and landslides are persistent incidents in the seismically active Indian Himalayan terrain. The National Highway (NH)-7 in Uttarakhand, India, passes through highly fractured rocky slopes and witnessed some of the worst natural disasters in history. The frequent occurrences of slope failures are causing great distress to local residents and commuters and are also affecting the various geotechnical engineering projects in the Himalayan valley. The appraisal of slope stability is somewhat a crucial task in the tectonically deformed and fragile rock masses of the Himalayas, where climatic conditions are uncertain. The present study deals with stability analysis of a cut slope along the NH-7, in Garhwal Himalayan, to check their potential state of instability. Rockmass characteristics of cut slope were performed on the basis of geological strength index and rock mass rating. The critical wedge and other failure types present at field site show a good correlation with kinematic analysis. The unstable condition of slope as estimated by continuous slope mass rating is also validated by newly developed Q_{slope} stability technique. Additionally, factor of safety computed through finite element method indicates that the slope is unstable. The accumulation of stress and strain near the toe region also signifies the instability of slope. In addition, the estimated deformations along the failure surface have been equated with the field observations and are found to be in close association. The comparative stability analysis of slope provides a better strategy to stable design along NH-7 with greater safety and reliability.

Keywords

Slope stability · Rock mass characteristics · Continuous slope mass rating · Q_{slope} stability · Finite element method

1 Introduction

The NH-7 is the busiest road in Uttarakhand, routed through tectonically and seismically active Garhwal Himalaya region. The rocks of Himalaya are highly deformed, fragile, and dissected with numerous unfavorable discrete geological structures, making this region highly vulnerable to landslide and other natural hazards (Valdiya, 1980). Recent development in Alaknanda river valley, Uttarakhand, such as road expansion, urban settlements, hydroelectric project, etc., leads to more unstable cut slope (Pain et al., 2014; Sati et al., 2011; Singh et al., 2020). Furthermore, human-induced landslides generally occur due to odd excavation at vulnerable sites, toe unloading, stress disequilibrium, and inadequate deliberation, causing fatalities and damage of property and economics (Sati et al., 2011). In the past, recurrent slope failures in Garhwal region caused huge interruption in transportation and other communication, exclusively during monsoon period. The present study deals with cut slope along NH-7 (30° 11′ 37.6″ N, 78° 38′ 32.3″ E), near Luneta, Garhwal Himalaya, Uttarakhand, India. Geologically, the study area comes under Garhwal Lesser Himalaya sequence (Valdiya, 1980), where Jaunsar Group of rocks is well exposed along NH-7, which is comprised of Chandpur Phyllites and Nagthat Quartzites. The contact between these two litho-formations is preferably normal aggradational, and sometimes due to more arenaceous character, phyllite shows transition from phyllite to phyllitic quartzite.

The lithological units of Himalayan terrain are quite complex, highly deformed, and fractured/jointed due to geotectonic activity and low grade of metamorphism. In

H. O. Singh (✉) · T. A. Ansari · T. N. Singh · K. H. Singh
Department of Earth Sciences, Indian Institute of Technology Bombay, Mumbai 400076, India
e-mail: hsagl.iitb@gmail.com

Z. A. Ergüler et al. (eds.), *Selected Studies in Geotechnics, Geo-Informatics and Remote Sensing*, Advances in Science, Technology & Innovation, https://doi.org/10.1007/978-3-031-43759-5_47

such terrain, prediction of accurate slope stability is somewhat challenging through different slope stability methods. The present study deals with the rock mass characteristics (GSI and RMR_{basic}), kinematic analysis, and assessment of slope stability through empirical methods (CoSMR and Q_{slope} stability). However, these empirical methods do not provide the appropriate instability and deformation mechanism for preliminary slope design. Therefore, numerical techniques are widely used to incorporate failure, differential stress, and deformation of rock mass. The examined slope was highly jointed, partly disturbed, with multifaceted angular blocks resting on slope in uncertain stress fields. Finite element method (FEM), a numerical technique (continuum model), based on theoretical stress–strain constitutive models, is the best suited to weak or heavily fractured rocks, or soil like rock masses and offers better simulation of slope failure. The FEM is quite flexible to handle material's heterogeneity, nonlinear deformability, in situ stresses, and complex boundary conditions than other continuum methods (Eberhardt, 2003; Jing, 2003). The collective approach of empirical and finite element method has been applied to predict the stability, deformational mechanism, and stress/strain and also to delineate potential vulnerable portions of cut slope.

2 Methodology

This paper demonstrates the stability analysis of a phyllitic quartzite road cut section (Fig. 1a) which was selected based on their susceptibility to failure, typically observed during field survey. The field investigation was carried out to determine the quality of rock masses exposed on slope surfaces, failure type, structural parameters, and slope conditions, along with collection of representative rock samples. Thereafter, the acquired field data was analyzed, and geotechnical strength parameters of the sample were estimated through lab experiment. The stereographic projection of joints and slope face data was investigated through kinematics analysis. It is a pretty convenient and unique technique for the determination of kinematically permissible different modes of failure (planer, wedge, and topple) of jointed rocky slopes (Markland, 1972). The rock mass characteristics of cut slope were accomplished initially on the basis of RMR_{basic} anticipated by Bieniawski in (1979). As the slopes are highly jointed, in such cases, Hoek and Brown (1997) recommended that the assessment of the quality of rock mass may be difficult as RQD in most of the highly jointed (weak) rock mass is zero. Therefore, GSI of Marinos and Hoek () was also acquired for better qualitative assessment of rock mass. To further check the preliminary condition of slope, CoSMR was acquired as per Tomás et al. (2007).

However, the slope mass rating system does not integrate weathering and surface discontinuity conditions (Irigaray et al., 2003), and analytical methods (kinematics, numerical simulations) are pretty much laborious and time consuming. Therefore, Bar and Barton (2017, 2015) introduced Q_{slope} stability (revised version of Q-system) to quickly assess the stability of cut slope/bench in real-time field conditions. The expression to calculate Q_{slope} for its different zones (stable, unstable, and uncertain) and rating of different parameters is well presented in Bar and Barton (2017, 2015). It also facilitates potential adjustments in slope angles ($\beta°$) for different probability of failure (PoF) to make stable slope design. Additionally, to comprehend the deformation and failure mechanism of potential vulnerable section, the slope was simulated using 2D finite element continuum plain strain method using shear strength reduction (SSR) technique. The SSR technique is well appropriate for material specified by Mohr–Coulomb failure criterion. Under SSR, the Mohr–Coulomb strength

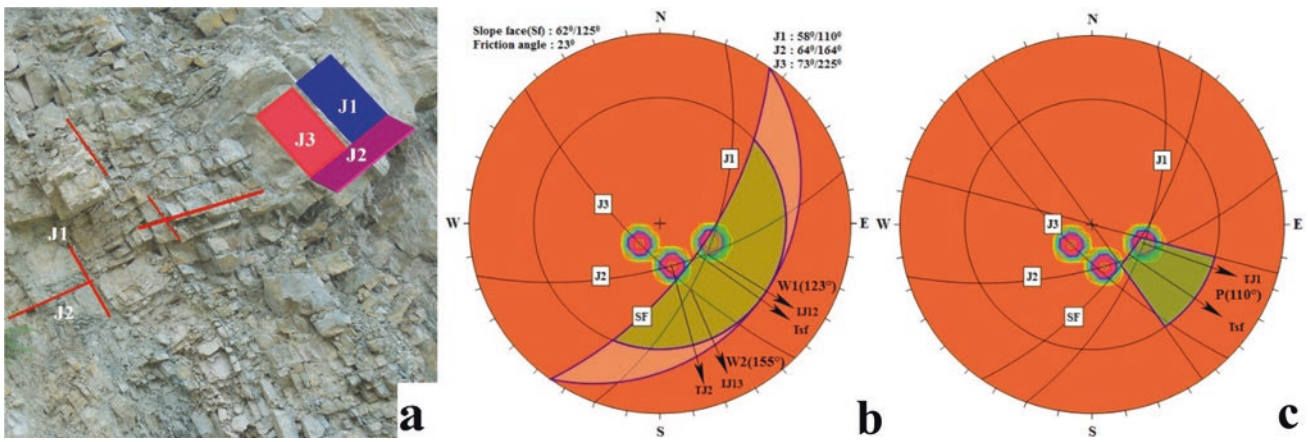

Fig. 1 **a** Generalised view of jointed cut slope face; **b** wedge failure in two directions; and **c** plane failure

parameters (c and φ) were reduced according to equations descripted in Griffiths and Lane (1999), until the slope fails (non-convergence) within definite number of iterations and tolerance, where corresponding SRF is the factor of safety (FoS) of the slope (Wang et al., 2020b).

3 Results

Kinematic analysis was performed using DIPS 6.0 software, a computer programme of Rocscience Inc. (2013), where orientation of joint and slope data and angle of internal friction was used as input parameter. The analysis showed that wedge failures commonly occurred. In Fig. 1b, wedge failure is present in two directions ($W1$ toward 123° and $W2$ toward 155°) and probability of plane failure toward 110° as well (Fig. 1c). Furthermore, rock mass property RMR_{basic} was calculated by adding the ratings of five different parameters, where different parameters with their ratings are presented as uniaxial compressive strength (UCS—4), rock quality designation (RQD—13), the spacing of discontinuities (8), conditions of discontinuities (7), and groundwater condition (15). The obtained value of RMR_{basic} (47) exposed that cut slope encompass 'fair' quality of rock mass. For the geological strength index (GSI) value, surface condition rating (SCR—7) and structural rating (SR—33.5) were plotted on the chart of Sonmez and Ulusay (2002). The quantified GSI (34) value indicates that the cut slope consists of blocky/disturbed structure with almost fair surface condition of rock mass.

The use of quantitative functions (continuous) in CoSMR analytically defines rock mass conditions and probable instability condition, which is substantial pro over RMR system. To calculate the adjustment factor for CoSMR, continuous functions/equations of Tomas et al. (2007) was used. Thereafter, CoSMR was assessed from the equation of SMR as proposed by Romana (1985). CoSMR (23.67) value illustrates that the cut slope is unstable. Substantially, to obtain the Q_{slope} value different parameters, (RQD, J_n, J_r, J_a, J_{wice}, and SRF_{slope}) are augmented. The rating of different parameters for the Q_{slope}were as (RQD%—67.36), (J_n—6), (J_r—3), (J_a—6), (J_{wice}—0.1), and (SRF_{slope}—9.72). The Q_{slope} (0.057) value was plotted on data chart against average slope angle to evaluate the stability condition, which revealed that cut slope is unstable. Furthermore, slope angle was reduced at PoF = 1% ($\beta° = 20 \log 10\ Q_{slope} + 65°$), and plot of $\beta°$ (38.9) versus Q_{slope} indicated the stable condition of slope; therefore, $\beta°$ (38.9) can be applied for potential stable design during excavation process. To comprehend the slope behavior and extreme vulnerability of cut slope, steepest 2D model (FEM) of cut slope was simulated using Phase^2 ~ Rocscience (2011) software, where 6-noded triangular mesh was discretized to diminish geometrical complexities. Different input parameters for numerical simulation as mean value of UCS (41.86 MPa) of intact rock, Young modules (E: 19.33 GPa), Poisson's ratio (0.24), strength parameters (c: 0.157 MPa and $\varphi = 23°$), unit weight (0.027 MN/m^3), material constant (10 ± 3), and slope height (H: 62 m) were utilized to predict the critical stress reduction factor (SRF), stress, and strain behavior. The critical SRF (0.87) resulted from FEM simulation, exposing that cut slope is highly unstable. The result of total displacement contour generated from FEM method and its distribution pattern across the model representing the most deformed portion lies near the toe of the slope section (Fig. 2a). The analysis also pretends maximum value of total displacement (0.024 m) with minimum volumetric strain of − 0.00031 for the cut slope. Subsequently, the maximum shear strain (0.0039) and differential stress (0.605 MPa) was consumed at most deformed section of the cut slope.

4 Discussion

The studied rock slope was highly jointed and moderately weathered with slightly rough surfaces. The joints are closely spaced with low persistence, which may be due to repetitive loading and unloading events during deformation, incorporating variable climatic conditions and seismic events. In such case, discrete geological structures typically control the stability of rock slopes (Bieniawski, 1979). To predict the extreme critical situation of various structures, it is crucial to determine the characteristics of rock mass. The instability mode of failure, as predicted from kinematic analysis, shows a good correlation with field observation. The RMR_{basic} quantified GSI and CoSMR value generally demonstrates that cut slope has fair rock mass with blocky/disturbed and unstable slope structure. The result of CoSMR is also validated from Q_{slope} stability technique, where estimation of $\beta°$ assists to make stable slope design in real time. FE simulation results directly specify that cut slope is unstable in its natural state. Figure 2a of total displacement versus distance plot suggests that nearly equal range of displacement contour is concentrated along the whole length of cut slope. The speculated zone of failure has widespread distribution near the apex and steadily reduced near foot region of the slope, and therefore, slightly deeper failure zone can be anticipated. Based on visual observation in conjunction with FE result, the inspected slope may experience wedge (predicted from kinematics) or probably curvo-plane failure due to heavily jointing nature and reduced block dimension under the influence of gravitational loading.

The variation of total displacement, maximum shear strain, and differential stress with respect to distance along

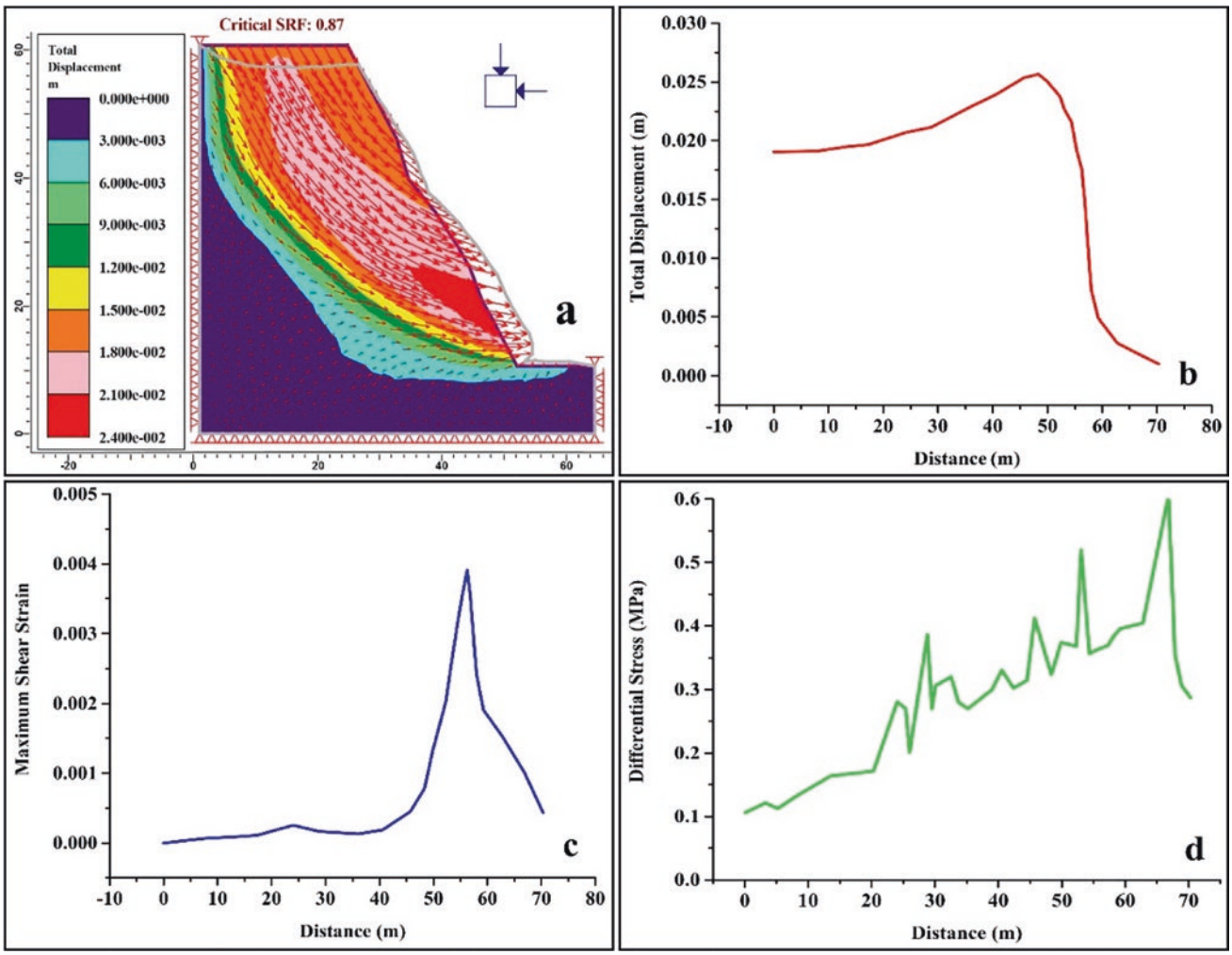

Fig. 2 **a** Total displacement contour pattern extracted from FE analysis, indicating the deformation across the cut slope; **b** total displacement versus distance; **c** maximum shear strain versus distance; and **d** differential stress versus distance

the unrestricted face of slope surfaces has been characterized from apex to toe in zones prone to failure (Fig. 2b–d). Gradual increment and connection of shear strain and deformation near toe determine the sliding path of slope (Zhang et al., 2015). Additionally, the highest value of these constraints was found at the toe of slope section, and it was also being substantiated by field indications, where numerous failed blocks were settled at the slope base. Statistically, total displacement, maximum shear strain, and differential stress had variances of 0.0001, 0.000, and 0.011 and standard errors of 0.001, 0.000, and 0.017, respectively. This depicts the accuracy of data variation of total displacement, maximum shear strain, and differential stress along the unrestricted slope face distance. As the area is seismically active (zone IV) (IS, 1893) and has repetitive rainfall processes, freezing and thawing may cause opening of existing joints, reducing the rock mass strength parameters which make slope more vulnerable toward block failure and rockfall. Application of seismic loading with horizontal seismic coefficient ($k_H = 0.25$ g) alone and both horizontal ($k_H = 0.25$ g) and vertical seismic coefficient ($k_V = -0.16$ g) reduces critical SRF up to 0.6 and 0.56, respectively. Additionally, seismic forces also modify the profile of stress–strain and displacement, where at particular distance these parameters exceed in seismic loading than gravity. Relatively higher deformation with deeper landslide is anticipated during any earth tremor. Further, slope failure induced by toe excavation leads to the stress disequilibrium, and failure begins from foot zone and gradually extends toward slope top (Wang et al., 2020a).

5 Conclusions

In this current study, a road cut slope along NH-7 near Luneta in Uttarakhand has been explored to predict the stability and deformation mechanism. Initially, rock mass characteristics evaluated by RMR_{basic} and GSI system which designate that rockmass has blocky structure with almost fair surface condition. CoSMR techniques also exhibited that slope is unstable and predicted failure mode is well supported by kinematic analysis. To enhance the failure prediction, Q_{slope} stability method was also applied, which also authenticated the result of CoSMR. Subsequently, potential adjustment in slope angle was also computed at PoF = 1% to make stable slope design. The results of empirical methods were also compared with numerical method. FEM analysis also indicates that cut slope is unstable, where the distribution of total displacement contour suggests the possibility of slight deeper failure zone. The highest value of total displacement, shear strain, and differential stress found near the toe of cut slope. The empirical results prompt outstanding correlation with FEM analysis. Furthermore, the application of seismic forces significantly reduces the critical SRF, where it ranges from 31.03 to 35.63%. Therefore, to enhance the stability of slope, toe wall, systematic reinforced shotcrete, and fully grouted rock bolting with appropriate wire mesh is compulsory to avoid any distress due to slope failure.

References

Bar, N., & Barton, N. (2017). The Q-slope method for rock slope engineering. *Rock Mechanics and Rock Engineering, 50*, 3307–3322. https://doi.org/10.1007/s00603-017-1305-0

Barton, N., Bar, N. (2015). Introducing the Q-slope method and its intended use within civil and mining engineering projects. In Schubert & Kluckner (Ed.), *Future development of rock mechanics; Proceedings of ISRM regional symposium—EUROCK 2015 & 64th geomechanics colloquium*, Salzburg, 7–10 Oct 2015 (pp. 157–162).

Bieniawski, Z. T. (1979). The geomechanics classification in rock engineering applications. In *4th ISRM congress*. International Society for Rock Mechanics and Rock Engineering.

Eberhardt, E. (2003). *Rock slope stability analysis–utilization of advanced numerical techniques*. Earth and Ocean sciences at UBC.

Griffiths, D. V., & Lane, P. A. (1999). Slope stability analysis by finite elements. *Geotechnique, 49*(3), 387–403. https://doi.org/10.1680/geot.1999.49.3.387

Hoek, E., & Brown, E. T. (1997). Practical estimates of rock mass strength. *International Journal of Rock Mechanics and Mining Sciences, 34*(8), 1165–1186. https://doi.org/10.1016/S1365-1609(97)80069-X

Irigaray, C., Fernández, T., & Chacón, J. (2003). Preliminary rock-slope-susceptibility assessment using GIS and the SMR classification. *Natural Hazards, 30*(3), 309–324. https://doi.org/10.1023/B:NHAZ.0000007178.44617.c6

IS. (1893). *Part 1, 2002. Criteria for earthquake resistant design of structures*. Bureau of Indian Standards, New Delhi.

Jing, L. (2003). A review of techniques, advances and outstanding issues in numerical modelling for rock mechanics and rock engineering. *International Journal of Rock Mechanics and Mining Sciences, 40*(3), 283–353. https://doi.org/10.1016/S1365-1609(03)00013-3

Marinos, P., Hoek, E. (2000). GSI: A geologically friendly tool for rock mass strength estimation. In *ISRM international symposium*. International Society for Rock Mechanics and Rock Engineering.

Marinos, P., & Hoek, E. (2001). Estimating the geotechnical properties of heterogeneous rock masses such as flysch. *Bulletin of Engineering Geology and the Environment, 60*(2), 85–92. https://doi.org/10.1007/s100640000090

Markland, J. T. (1972). *A useful technique for estimating the stability of rock slopes when the rigid wedge slide type of failure is expected*. Interdepartmental Rock Mechanics Project, Imperial College of Science and Technology.

Pain, A., Kanungo, D. P., & Sarkar, S. (2014). Rock slope stability assessment using finite element based modelling–examples from the Indian Himalayas. *Geomechanics and Geoengineering, 9*(3), 215–230.

Rocscience. (2011). *Phase2 v. 8.005:2D finite element program for calculating stresses and estimating support around underground excavations*. Rocscience Inc.

Rocscience. (2013). *Dips v 6.008: Stereographic projection program for the analysis and presentation of orientation based data*. Rocscience Inc.

Romana, M. (1985). New adjustment ratings for application of Bieniawski classification to slopes. In *Proceedings of the international symposium on role of rock mechanics*, Zacatecas, Mexico (pp. 49–53).

Sati, S. P., Sundriyal, Y. P., Rana, N., & Dangwal, S. (2011). Recent landslides in Uttarakhand: Nature's fury or human folly. *Current Science (bangalore), 100*(11), 1617–1620.

Singh, H. O., Ansari, T. A., Singh, T. N., & Singh, K. H. (2020). Analytical and numerical stability analysis of road cut slopes in Garhwal Himalaya, India. *Geotechnical Geological Engineering*. https://doi.org/10.1007/s10706-020-01329-y(2020)

Sonmez, H., & Ulusay, R. (2002). A discussion on the Hoek-Brown failure criterion and suggested modifications to the criterion verified by slope stability case studies. *Yerbilimleri, 26*(1), 77–99.

Tomás, R., Delgado, J., & SerónGáñez, J. B. (2007). Modification of slope mass rating (SMR) by continuous functions. https://doi.org/10.1016/j.ijrmms.2007.02.004

Valdiya, K. S. (1980). The two intracrustal boundary thrusts of the Himalaya. *Tectonophysics, 66*(4), 323–348.

Wang, Z. Y., Gu, D. M., & Zhang, W. G. (2020a). Influence of excavation schemes on slope stability: A DEM study. *Journal of Mountain Science, 17*(6).

Wang, Z., Zhang, W., Gao, X., Liu, H., & Bohlke, T. (2020b). Stability analysis of soil slopes based on strain information. *Acta Geotechnica, 15*(11), 3121–3134.

Zhang, K., Cao, P., Meng, J., Li, K., & Fan, W. (2015). Modeling the progressive failure of jointed rock slope using fracture mechanics and the strength reduction method. *Rock Mechanics and Rock Engineering, 48*(2), 771–785.

Surface and Internal Erosion in Embankment Dams: A Comparative Review

Nourelhouda Slimani, Mohamed Amine Boukhemacha and Nadir Marouf

Abstract

Earth-made dams are frequently used as water retention structures and are particularly vulnerable to erosion. This phenomenon (inits different forms—surface or internal) is in fact one of the main causes of failure of embankment dams. In this context, an adequate understanding of erosion process is necessary at many levels; from the selection of the sedimentary materials, to the design and damage assessment practices. The present work provides a comparative review of two particular erosion processes: internal and surface erosion in embankment dams. The overview covers the mechanisms, forms, the development stages, and the properties used to assess the susceptibility of a given sedimentary material to erosion and governing equations.

Keywords

Internal/surface erosion · Embankment dams · Soil erodibility

1 Introduction

Erosion in embankment dams takes different forms, namely internal and surface. Dam failure statistics show that the main causes of earthen-dam failure are surface erosion, internal erosion, and slope stability, which, respectively, account for 35.9, 46.1, and 5.5% of all failure cases among 11,192 embankment dams (Foster et al., 2000). Hence, erosion is a major concern for the safety of such hydraulic features. It is defined as the detachment of particles from the soil matrix by the flow pressure (Chang, 2012; Mach, 2010; Wan, 2006). The present work presents a brief comparative literature review that aims to better understand the differences and similarities between surface and internal erosion processes.

2 Phenomenological Description of Internal and Surface Erosion

Internal erosion is the movement (within the hydraulic work) of particles of soil matrix by seeping fluid due to the high hydraulic head from upstream to downstream—where it will be deposed. This kind of erosion depends on the material type, structural properties, and even operational activities (Van Beek et al., 2013; Foster & Fell, 1999; Kang et al., 2020; Mach, 2010; Wan, 2006; Wan & Fell, 2004a; Zhang et al., 2009). Surface erosion (overflow erosion) is due to the water flow over an embankment during overtopping events (also termed overflow erosion).Water overtopping can be caused by high waves, floods, dam settlements, or dam landslide. The soil entertainment is affected by the turbulence of the flow if it imposes a rapid and significant pressure on the bed surface (Briaud et al., 2008; Chang, 2012; Hahn et al., 2000).

The initiation of internal erosion is classified in four processes (Beguin, 2011; Fell & Fry, 2013; Wan, 2006; Zhang et al., 2009): **(1) concentrated leak erosion** (where the concentration of the flow causes the erosion of the sides of the crack and inter-connected voids); **(2) backward erosion** (the soil particles detachment, in or beneath the water retaining structure, creates hollow spaces by seepage flow where high velocity leads to the progression of a pipe from the downstream to the upstream); **(3) soil contact erosion** (occurs at interfaces between coarse and fine layers. The flow through the coarse layer drives the fine particles), and

N. Slimani (✉) · N. Marouf
Larbi Ben M'hidi University, B.P. 358, Route de Constantine, 04000 Oum El Bouaghi, Algeria
e-mail: nour_el_houda.slimani@g.enp.edu.dz

N. Slimani · M. A. Boukhemacha
LMGCE, Ecole Nationale Polytechnique, 10 Rue Frères OUDEK, 16200, El-Harrach, Algeria

Z. A. Ergüler et al. (eds.), *Selected Studies in Geotechnics, Geo-Informatics and Remote Sensing*, Advances in Science, Technology & Innovation, https://doi.org/10.1007/978-3-031-43759-5_48

(4) suffusion (finer soil particles are moved from within the intact soil skeleton by seepage flow).

The initiation of surface erosion due to overtopping (Briaud et al., 2008; Chang, 2012) is mechanically described as the point where the driving forces on soil particles/soil blocs (buoyancy and drag force) of the overflow exceed the resisting forces (weight, friction, etc.).This process can affect soil particles individually, as well as soil blocs.

3 Development Stages

The failure of a dam by internal erosion passes through four phases: **(1)** the initiation and **(2)** continuation of the erosion, **(3)** the progression to form a pipe, and **(4)** the initiation of a breach (Foster & Fell, 1999).

The process of overtopping in embankment dams differs from granular to cohesive soils. For the development of failure by surface erosion over an embankment dam, (Hahn et al., 2000) describes the breaching process (for both types of soils) through six stages: **(1)** flow over the intact embankment; **(2)** initiation of rill and micro-rill erosion on the downstream slope; **(3)** development of a master rill from a network of rills evolving to the main head-cut; **(4)** upstream migration of the head-cut through the downstream slope and formation of a larger head-cutting channel; **(5)**upstream migration of the head-cut to the embankment's and reduction of the crest elevation; and **(6)** the increase of the discharge from the reservoir and full breach.

4 Quantifying Erodibility

Several physically based approaches used to quantify soil erosion are based on the concept of excess hydraulic shear stress by DuBoys (DuBoys, 1879) given in the following form:

$$\dot{\varepsilon} = C_e(\tau_t - \tau_c) \quad (1)$$

where $\dot{\varepsilon}$ is the rate of erosion; C_e is the erodibility coefficient, and τ_t and τ_c are the hydraulic and critical shear stresses (respectively). This model quantifies the erodibility of a soil by defining an initiation threshold (τ_c) and an erosion speed proportional to the excess in stress and to C_e. These soil erodibility properties can be quantified experimentally using laboratory or field tests (see Table 1). Most tests are conducted on small samples in laboratory/or in-situ (e.g. hole erosion test and jet erosion test), or exceptionally using in-situ reduced-scale physical models (e.g. overtopping model (Bonelli et al., 2018)). It must be noted that, to our knowledge, the correlation between surface and internal erosion erodibility properties has never been investigated. Considering the validity of the Duboys erosion model to quantify both surface and internal erosion (more precisely for piping erosion), doing so would assess the validity of the given test to characterize soil erodibility for both processes. It would also be useful to assess the susceptibility of earthen-dam materials to either process (by unifying the scale used to assess the initiation ease, expressed by the critical shear stress, and the evolution speed which is directly proportional to the erodibility coefficient).

Table 1 Examples of internal and surface erosion investigation tests

Erosion process		Test	Type	References
Internal erosion	Piping (concentrated leak erosion)	Hole erosion test (HET)	Laboratory	Wan and Fell (2002)
		Slot erosion test (SET)	Laboratory	Wan and Fell (2002)
		Crack, leakage erosion test	Laboratory	Hjeldnes and Lavania (1980)
		Pinhole test	Laboratory	Sherard et al. (1976)
	Backward erosion	Backward erosion piping	Laboratory	Robbins et al. (2017)
	Contact soil erosion	Parallel erosion test	Laboratory	Ho (2007)
	Suffusion	Triaxial compression test	Laboratory	Aboul Hosn et al. (2018)
		Multi-directional flow in suffusion susceptibility	Laboratory	Marot et al. (2018)
		Laboratory suffusion test	Laboratory	Wan and Fell (2004b)
Surface erosion		The Digue ELITE overflowing simulator	Field	Bonelli et al. (2018)
		The USDA-ARS physical modeling of overflowing erosion and breach formation	Field	Hanson et al. (2005)
		Jet erosion test (JET)	Both	Hanson (1991)
		Flume test/annual flume test/the sediment Erosion rate flume (SERF)	Both	Crowley et al. (2012)
		Rotating erosion cylinder test (RECT)	Laboratory	Kang et al. (2020)

5 Conclusions

This short review describes surface and internal erosion processes in earthen dams from initiation to failure, the main factors influencing them, and how to quantify them. Since such hydraulic structures are particularly vulnerable to these two erosion phenomena (that intervened, according to statistics, in about 95% of earthen dams failures), an adequate understanding of erosion processes and how to quantify them is necessary at many levels—from the selection of construction materials, to the design and damage assessment practices.

References

Aboul Hosn, R., Benhmed, N., Nguyen, C. D., Sibille, L., Philippe, P., Chareyre, B. (2017). Effect of suffusion on the soil's mechanical behavior: Experimental investigations. In S. Bonelli (Ed.), *EWG-IE 2018, LNC 17* (pp. 3–15). Springer.

Beguin, R. (2011). *Etude multi-échelle de l'érosion de contact au sien des ouvrages hydraulique en terre*. Grenoble University.

Bonelli, S., Nicaise, S., Charrier, G., Chaouch, N., Byron, F., Grémeaux, Y. (2018). Quantifying the erosion resistance of dikes with the overflowing simulator. In *3rd International conference on protection against overtopping*, UK (pp. 1–6).

Briaud, J., Chen, H., Govindasamy, A., & Storesund, R. (2008). Levee erosion by overtopping in New Orleans during the Katrina hurricane. *Journal of Geotechnical and Geoenviromental Engineering, 134*(5), 618–632.

Chang, D. (2012). *Internal erosion and overtopping erosion of earth dams and landslide dams*. The Hong Kong University of Science and Technology.

Crowley, R. W., Blomquist, D. B., Shah, F. D., & Holst, C. M. (2012). The sediment erosion rate flume (SERF): A new testing device for measuring soil erosion rate and shear stress. *Geotechnical Testing Journal, 35*(4), 1–11.

DuBoys, M. (1879). Le Rhône et les rivières à lit affouillable. *Annales Des Ponts Et Chaussées, 18*(5), 141–195.

Fell, R., Fry, J. -J. (2013). State of the art on the likelihood of internal erosion of dams and levees by means of testing. In *Erosion in geomechanics applied to dams and levees* (1st ed.). ISTE Ltd and Wiley.

Foster, M. A., Fell, R. (1999). *A framework for estimating the probability of failure of embankment dams by internal erosion and piping using event tree methods.* UNICIV, The University Of New South Wales.

Foster, M., Fell, R., Spannagle, M. (2000). The statistics of embankment dam failure and accident. *Canadian Geotechnical Journal, 37*, 1000–1024.

Hahn, W., Hanson, G. J., Cook, K. R. (2000). Breach morphology observations of embankment overtopping tests. *Water Resources*, 1–10.

Hanson, G. J. (1991). Development of a jet index erosion to characterize erosion resistance of soils in earthen spillways. *ASAE, 34*(5), 2015–2020.

Hanson, G. J., Cook, K. R., & Hunt, S. L. (2005). Physical modeling of overtopping erosion and breach formation of cohesive embankment. *American Society of Agricultural Engineers, 48*(5), 1783–1794.

Hjeldnes, E. I., & Lavania, B. V. K. (1980). Cracking, leakage, and erosion of earth dam materials. *Journal of the Geotechnical Engineering Division, 106*(2), 117–135.

Ho, C. C. (2007). *The erosion behavior of revetment using geotextile*. Joseph-Fourier University.

Kang, G.-O., Do, T. M., Lim, J.-S., & Kim, Y.-S. (2020). Evaluation of erosion resistance capacity on compacted weathered granite soil using non-destructive tests. *Bulletin of Engineering Geology and the Environment, 79*(2), 907–923.

Mach, Q. T. (2010). *A simple model of internal erosion in embankment dams.* Library and Archives Canada.

Marot, D., Bendahmane, F., Le, V. T. (2019). New apparatus for assessing soil suffusion susceptibility under two flow directions. In S. Bonelli (Ed.), *EWG-IE 2018, LNC 17* (pp. 69–80). Springer.

Robbins, B. A., Van Beer, V. M., Lopez-Soto, J. F., Montalvo-Bartolomei, A. M., Murphy, J. (2017). A novel laboratory test for backward erosion piping. *International Journal of Physical Modelling Geotechnics, 18*(5), 266–279.

Sherard, J. L., Decker, R. S., & Dunnigan, L. P. (1976). Identification and nature of dispersive soils. *Journal of the Geotechnical Engineering Division, 102*(4), 287–301.

Van Beek, V., Bezuijen, A., Sellemeijer, H. (2013). Backward erosion piping. In *Erosion in geomechanics applied to dams and levees* (2nd ed.). ISTE Ltd and Wiley.

Wan, C. F. (2006). *Experimental investigation of piping erosion and suffusion of soils in embankment dams and their foundation.* University of New South Wales.

Wan, C. F., Fell, R. (2002) *Investigation of internal erosion and piping of soils in embankment dams by the slot erosion test and hole erosion test*. The University of New South Wales, UNICIV Report No. R-412.

Wan, C. F., & Fell, R. (2004a). Investigation of rate of erosion of soils in embankment dams. *Journal of Geotechnical and Geoenvironmental Engineering, 130*(4), 373–380.

Wan, C. F., & Fell, R. (2004b). Assessing the potential of internal instability and suffusion in embankment dams and their foundations. *Journal of Geotechnical and Geoenvironmntal Engineering, 134*, 401–407.

Zhang, L., Xu, Y., Jia, J. (2009). Analysis of earth dam failures: A database approach. *Georisk: Assessment and Management of Risk for Engineered Systems and Geohazards, 3*(3), 184–189.

Geological Description and Modeling of Djebel Kerdada in Saharan Atlas–Bou Saada, Algeria

Brahim Belahcene, Mohamed Zinelabidine Doghmane and Said Eladj

Abstract

This paper presents stratigraphic and structural descriptions of Djebel Kerdada in the studied areas of Bou Saada in Algeria. The choice of Djebel Kerdada is due to its geological complexity that can provide more detailed information about the regional geology of the area located at the northern limit of the African plate. This region belongs, geologically, to the Saharan Atlas, which is limited by flexures caused by slow dislocations, transgression, alternations, and regressions. The marginal basin in western Mediterranean Sea was generated by an N-NW subduction of the African and Adriatic plates under the European plate. The geological structures created by the subduction are near the city of Bou Saada, which is located 234 km South-East of Algiers. Based on the results of field investigation internship, it has been confirmed that, due to the compressive tectonic phenomenon caused by the sliding of the African plate under the Euro-Asian plate, many geological structures have a N-E/ S-W direction. Thus, this field study allowed us to limit the different litho-stratigraphic series that appeared in the form of outcrops, fossils, measurement of dips, and all structural faults. Moreover, a static modeling of the geological structure, namely Djebel Kerdada, was established based on the isopath maps of the region and data obtained from the internship. In addition to the limits of the litho-stratigraphic series, the results demonstrated the paths of the hydro-geodynamic forces toward the river of Bou Saada.

Keywords

Stratigraphic · Structural · Djebel kerdada · Fossils · Modeling

1 Introduction

At a distance of 234 km South-East of Algiers lies the city of Bou Saada. The city's coordinates are 35 13′ North and 4° 10′ East (Rehault et al., 1984). This historic city belongs geologically to the Saharan Atlas. The structural geological footprint of this region is the effect of the cohesion between the African and Euro-Asian plates caused by tectonic phenomena. Figure 1 shows the map that has been used to locate the geological structures of the region. The internship was scheduled for five days, for which many geological sites have been visited. Because of the massive outcrops of the Cretaceous, different litho-stratigraphic series have been identified for the same sites (Caby, 1970).

2 Stratigraphy of the Region

In the Neocombian of Kerdada, massive bars of primary limestone dolomites are presented in the syncline (Fig. 2a) with a brown color (Ghandriche, 1991). The presence of limestone is ensured by the hot interaction with HCL, and the dip varies from 65 to 1 m (Fig. 2b). This series is limited by an intermediate limestone bar of oolitic nature, which marks the beginning of Barremian formation (Guardia, 1975). Later, we have determined a reverse fault in the South side, so, a loophole is detected, and it goes through the fault (Fig. 2a). The Barremian is characterized by alternating deposits of clayey sandstone, bioclastic

B. Belahcene (✉)
Abou Bekr Belkaid University, 13000 Tlemcen, Algeria
e-mail: Brahim.belahcen@mail.univ-tlemcen.dz; belahcene.brahim@gmail.com

M. Z. Doghmane
Department of Geophysics, FSTGAT, USTHB, Bab Ezzouar, Algeria

S. Eladj
M'hamed Bougara Universityof Boumerdes, 35000 Boumerdes, Algeria

Z. A. Ergüler et al. (eds.), *Selected Studies in Geotechnics, Geo-Informatics and Remote Sensing*,
Advances in Science, Technology & Innovation, https://doi.org/10.1007/978-3-031-43759-5_49

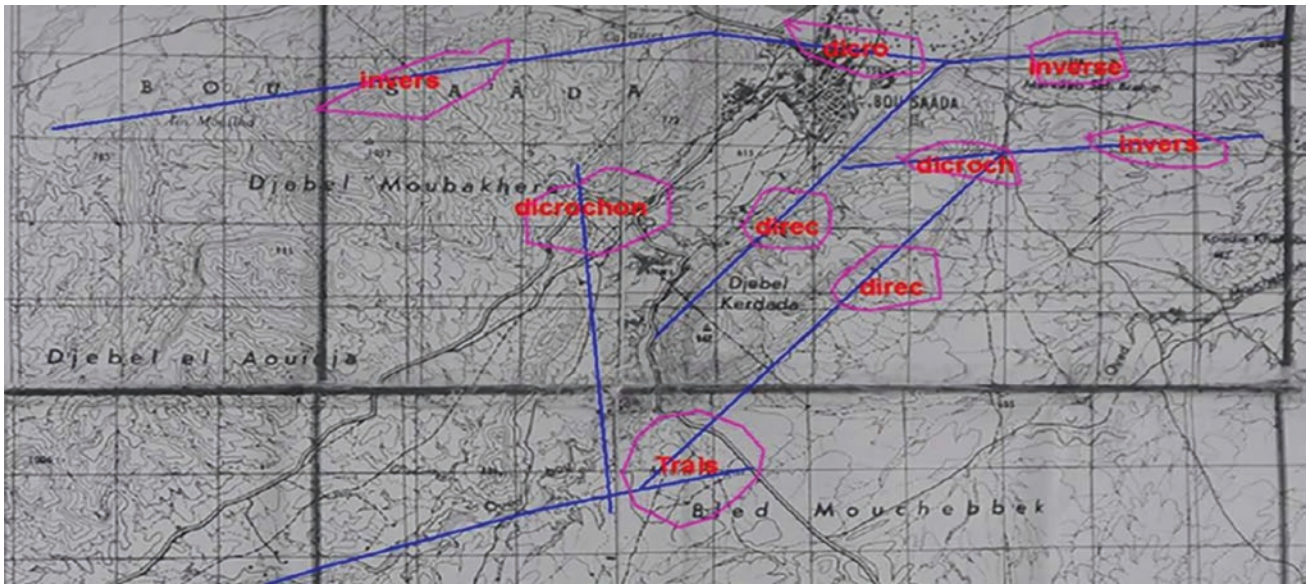

Fig. 1 Used map for the studied regions containing Djebel Kerdada (1 unit = 1 km)

limestones (metric), and the beginning of this series is an oolitic limestone (Caby, 1970; Guardia, 1975). Part of this series has undergone a shear after a folding, so, we noticed the existence of a directional fault. The upper Aptian is characterized by limestone bars without the presence of sandstone formations (Saadallah, 1987). The fossils shown in Fig. 2c confirmed that the formation environment was less deep than in Djebel Freytas and Djebel Dahla (Fig. 1). The limits of this series are stretched to Djebel Luiza and Arrar, and they are characterized by marly limestone beds, gypsum, and the presence of fossils and oyster shells and gastropod (Fig. 2d. The lower Aptian is characterized by clayey sandstone as found in Djebel Luiza, and thus, there is sandstone cement bar with the presence of hollows along the structure (Fig. 2e). At the level of this formation, we found an elementary unit of carbonate (Fig. 2f). The upper Albian is characterized by the presence of massive bars and Strombes (Fig. 2g). The Cenomanian series are characterized by one of the evaporative sedimentations with oyster marl alternations and gastropods, which we noticed in Djebel El-Hamel; the limit of this series is gypsi-ferous green marls (Fig. 2h). The Turonian series is characterized by fossiliferous limestone blocks, which have been found at the synclinal perchis in Djebel El Hamel.

3 Hydro-geological Modeling of Djebel Kardada

From the isopath maps of region, the hydro-geological model of Djebel Kerdada has been obtained (Fig. 3). The Barremian series is located below the contact zone less than 450 m, and all what is the contact higher than 500 m is the Neocombian (Guardia, 1975).

From Fig. 2 and field observations, this region contains undergoing faults. Thus, the southern termination of the structure is different to the one we found in the northern part because of a reverse fault that deformed the latter (Saadallah, 1987). A strong southerly inclination is justified by the presence of a compressive stress at the heart of the due structure of salt dome and clays, which is confirmed after a field survey due to the presence of salty minerals. The hydrodynamic paths distribution of the river or the water-drained regions was represented by arrows in Fig. 3; it is called the hydrodynamic forces of the river.

4 Conclusion

Based on this field study, the geological structures appeared in the form of outcrops which have been characterized by gathered fossils and the types of litho-stratigraphic series. The existence of deferent fault types shows the influence of the degree of tectonic events in this region. The static model allowed us to simulate the morphology of the Djebel Kerdada structure. Furthermore, the litho-stratigraphic series, as well as the paths of the hydro-geodynamic forces toward the river, have been identified and modeled. For future perspective, this study can be expanded by analyzing seismic data of the region to make investigation on hydrocarbons' existence, which will lead us to investigate recent algorithms for water saturation estimation and reservoirs' evaluation (Bacetti & Doghmane, 2020; Doghmane & Belahcene, 2019; Doghmane et al., 2018; Eladj et al., 2019).

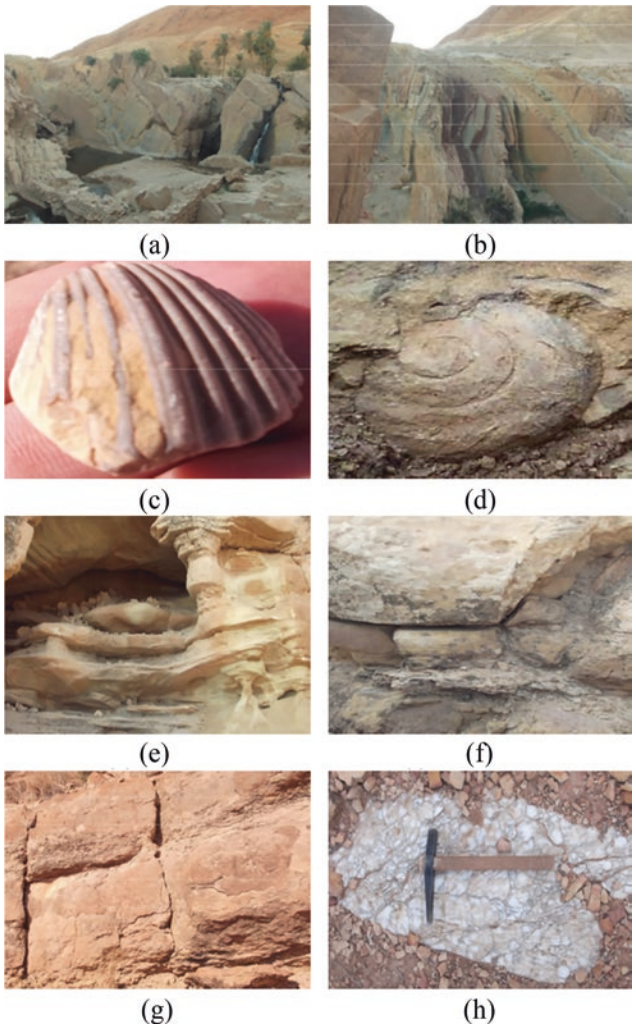

Fig. 2 **a** Bars of primary limestone dolomites of Neocombian, **b** dips of the Barremean, **c** fossils of the upper Aptian, **d** oyster shells and gastropod of the upper Aptian, **e** hollows along the lower Aptian, **f** elementary unit of carbonate, **g** bars and Strombes of the upper Albian, and **h** gypsi-ferous green marls of the Cenomanian

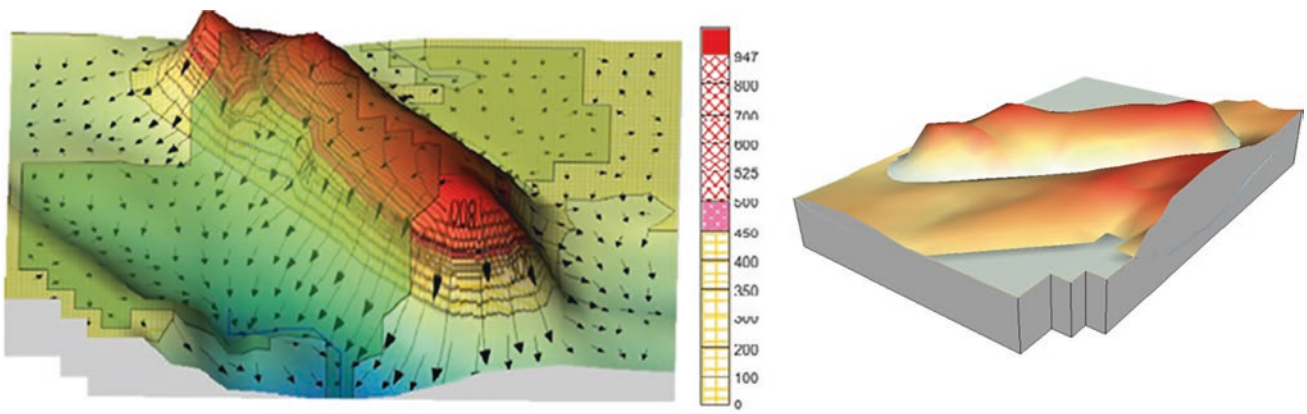

Fig. 3 Hydro-geological and structural models of Djebel Kerdada

References

Bacetti, A., Doghmane, M. Z. (2020). A Practical workflow using seismic attributes to enhance sub seismic geological structures and natural fractures correlation. In *conference proceedings, first EAGE digitalization conference and exhibition* (vol. 2020, pp. 1–5).

Caby, R. (1970). *La Chaîne pharusienne dans le nord-ouest de l'Ahaggar (Sahara central, Algérie): sa place dans l'orogenèse du Précambrien supérieur en Afrique* [Ph.D. Thesis, Montpellier University].

Doghmane, M. Z., Belahcene, B., Kidouche M. (2019). Application of improved artificial neural network algorithm in hydrocarbons' reservoir evaluation. In M. Hatti (Eds.), *Renewable energy for smart and sustainable cities. ICAIRES 2018. Lecture notes in networks and systems* (vol. 62). Springer.

Doghmane, M. Z., & Belahcene, B. (2019). Design of new model (ANNSVM) compensator for saturation calculation based on logging curves for low resistivity phenomenon. *EAGE/ALNAFT Geoscience Workshop, 2019*(1), 1–5.

Eladj, S., Lounissi, T. K., Doghmane, M. Z., & Djeddi, M. (2019). Lithological characterization by simultaneous seismic inversion in Algerian South Eastern field. *Eng. Technol. Appl. Sci. Res., 10*(1), 5251–5258.

Ghandriche, H. (1991). *Modalités de la superposition de structures de plissement-chevauchement d'âge alpin dans les Aurès (Algérie)* [Ph.D. Thesis, University of Sud-Paris].

Guardia, P. (1975). *Géodynamique de la marge alpine du continent africain d'après l'étude de l'Oranie nord-occidentale: relations structurales et paléo-géographiques entre le Rif externe, le Tell et l'avant pays atlasique* [Ph.D. Thesis, Mediterranean Polytechnic Institute of Nice].

Rehault, J.-P., Boillot, G., & Mauffret, A. (1984). The Western Mediterranean basin geological evolution. *Marine Geology, 55*, 447–477.

Saadallah A (1987). *Le massif cristallophyllien d'El-Djazair (Algérie): évaluation d'un charriage à vergence nord* [Ph.D. Thesis, ALgiers University].

Earthquake Induced Settlement of Imphal City

Kumar Pallav, Tekcham Gishan Singh
and Konjengbam Darunkumar Singh

Abstract

The present research article estimates the liquefaction induced settlement of 114 sites present in Imphal city due to the 1869 Cachar earthquake ($Mw = 7.0$). Liquefaction triggering analysis has been performed using the latest revised method. Using the Factor of safety against the liquefaction and relative density (DR) of the soil layer, the sites' settlement is calculated based on procedures given by (Cetin et al., 2009) and (Ishihara and Yoshimine, 1992). A modified method is proposed, which involves considering optimum depth concept, whereas omitted the depth factor consideration for obtaining the liquefaction induced settlement of Imphal city. Contour map has been prepared to show the variation of settlement throughout Imphal city. The results show that the Kangla place area is more prone to settlement than other Imphal cities. The map generated will help the geotechnical engineer as a ready reference map in the design of foundations.

Keywords

Liquefaction induced settlement · Cyclic stress ratio · Cyclic resistance ratio · Factor of safety · Optimum depth

K. Pallav (✉)
Civil Engineering and Geomatics, Cape Peninsula University of Technology, Bellville Campus, Capetown 7530, South Africa
e-mail: kumarp@cput.ac.za; kumarpallav23@gmail.com

T. G. Singh
Indian Institute of Technology Jodhpur, Jodhpur 342030, India

K. D. Singh
Civil Engineering, Indian Institute of Technology Guwahati, Guwahati 781039, India

1 Introduction

The failures of shallow foundations due to liquefaction were observed in Niigata, Japan (1964) Luzon, Philippine (1990), and many recent earthquakes around the world. In Niigata, many buildings slanted up to 60° and sunk up 3.8 m (Ishihara & Koga, 1964). In Dagupan city, due to the 1990 Luzon earthquake, buildings settled as much as 2.5 m (Adachi et al., 1990). Adapazari city in Turkey, where buildings were tilted 30° and rotated about 60° due to earthquake-induced failure of soil during the Kocaeli earthquake (Shahir & Pak, 2010). The Indian code of practice (IS, 1893) is silent on earthquake stimulated settlement. In contrast, the International Building Code (2009) recommends that the geotechnical engineer reports the settlement due to liquefaction and incorporated during the design while site investigating.

As per the author's knowledge, no such procedure has been mentioned in the Indian code of practice to estimate earthquake-induced settlement. Settlements due to earthquake-induced ground motion in sand deposits (saturated or dry) have been initiated. Lee and Albaisa (1974), established by Tatsuoka et al. (1984) and Tokimatsu and Seed (1987). Further, the method was developed by Nagase and Ishihara (1988), Ishihara and Yoshimine (1992), and Cetin et al. (2009) and was advanced by Lee et al. (2012). The present work emphasizes computing earthquake-induced settlement based on the procedure given by Cetin et al. (2009) where the Factor of safety against liquefaction (FOS) is calculated by Idriss and Boulanger (2015). Based on the analysis, the settlement map for Imphal has been prepared for the 1869 Cachar earthquake (M_w 7.5), which occurred on Kopili fault; this may help planners, design engineers, and city administration to know the level of settlement for the 114 sites in Imphal city. Figure 1 shows the study area along with the location of the important places and the boreholes. This method can be expediently applied numerically to any earthquake magnitude by using its peak ground acceleration (PGA).

Z. A. Ergüler et al. (eds.), *Selected Studies in Geotechnics, Geo-Informatics and Remote Sensing*,
Advances in Science, Technology & Innovation, https://doi.org/10.1007/978-3-031-43759-5_50

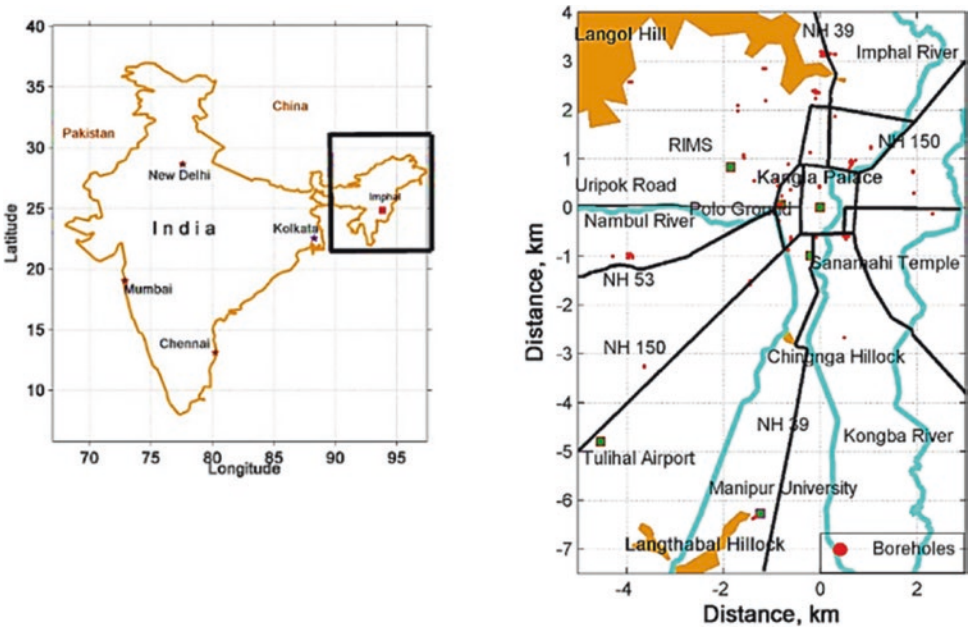

Fig. 1 Location of Imphal city along with 114 boreholes location

2 Seismotectonic Scenario

Quaternary geology map of Manipur state is shown in Fig. 2a. The map is as per geological survey of India, GSI (*GMSR-Miscellaneous Publication No. 30*) shows that most of Imphal city is located on youthful Holocene deposits which are vulnerable to liquefaction (Youd & Hoose, 1977). However, soils are belonging to the Disang group (i.e., from Palaeocene to Eocene) in the Northwest corner of the study area. The Imphal city is situated in the most seismically active region of the world and surrounded with the complex tectonic setup, as shown in Fig. 2b. On the 10th of January1869, Cachar earthquake (Oldham, 1869), which created extensive damage in and around Imphal city, was the earliest documented earthquake recorded by Oldham (1869). For the present study, a rectangular region of Imphal city of size 8.0×11.5 km is considered for estimating the earthquake-induced settlement of Imphal city Fig. 1. Imphal city, as shown in Fig. 1, is situated at the extreme end of Northeastern India (24.8°N 93.9°E). It may be noted that since 1897, this NE region has experienced more than 180 earthquakes of magnitudes ≥ 5.5 (Dasgupta, et al., 2000). Ambraseys (1988) studied worldwide earthquakes and liquefaction data, and concluded that an earthquake of magnitude M_w as low as 5.0 could produce liquefaction.

Oldham (1869) reported the extensive damage to buildings in Imphal, land fissures, liquefaction phenomena, and sand venting due to the 1869 A.D. earthquake. The

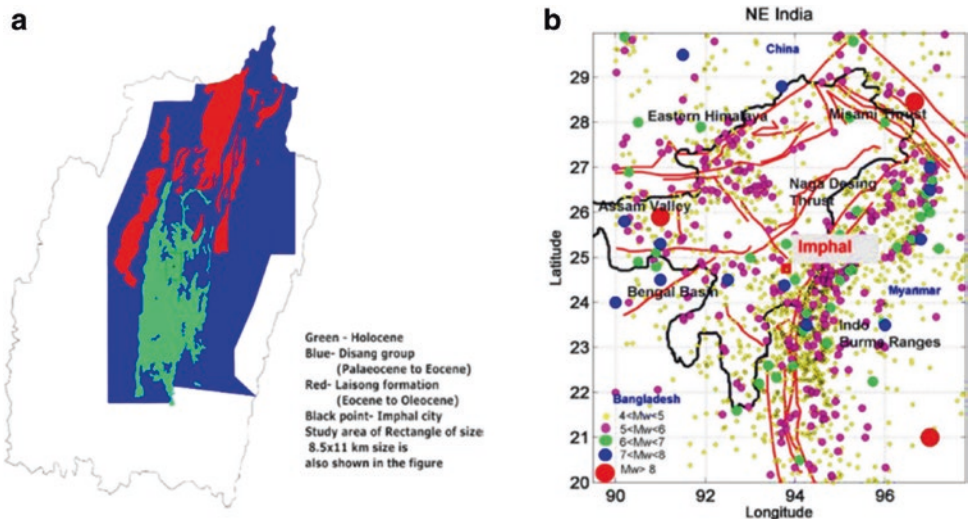

Fig. 2 **a** Geological map of Manipur state (after GSI-GMSR Miscellaneous Pub No. 30), **b** seismotectonic setups around Imphal City (modified from GSI, 2000)

earthquake caused severe damage in Assam, Manipur and West Bengal states. The double-storey Maharaja's Palace collapsed and four people died in the Imphal city.

3 Standard Penetration Data

The city is situated along the river of Kongba, Imphal, and Nambul, mostly with Alluvial soil deposits. The Imphal valley mainly has soils of fluvio-lacustrine origin, whereas the foothill ferruginous red soils are traced. The soils in the valley region are rich in humus. Laiba (1992) has classified as virgin soil (clayey loam, dark clayey, and boggy type soils) the low lying areas of Imphal city viz., Lamphelpat, Takyelpat, Prompat, and Kakwapat (pat means lake),

Altogether, 144 Standard Penetration Tests (SPT) data are obtained from a different location in Imphal city. The SPT-N values are very low, mostly in the range of 15–20. According to international practices, the soil's engineering classification is the average standard penetration resistance ($\overline{N}$) is computed at all boreholes (IBC, 2009).

4 Methodology and Results

The approaches developed by Tokimatsu and Seed (1987) and Ishihara and Yoshimine (1992) are well known and widely used in practice. Although their approach is simple, they often require the use of charts, tables, or diagrams. The approach may be particularly time-consuming when estimations are required at sites with multiple soil layers with different properties. In this paper, a simplified and practical approach proposed by Cetin et al. (2009) is used to estimate the earthquake-induced settlements due to liquefaction in saturated sandy soils (Boulanger & Idriss, 2014). This direct and simplified approach consists of a set of equations which can be used to directly determine the settlements of saturated sandy soil layers subjected to earthquake loading. Cetin et al.'s (2009) approach have some limiting conditions [$5 \le N_{1,60,\mathrm{cs}}$(*corrected N-value for clay content*) ≤ 40 and $0.05 \le \mathrm{CSR}_{\mathrm{ss,20,1d,1\ atm}}$ (*corrected 1D-CSR value as per* (Cetin et al., 2009) ≤ 0.60].So, whenever these conditions are not met, the graphical procedure given by Ishihara and Yoshimine (1992) is considered and it assumes no fines content. For the settlement calculation procedure, the present study uses the equation given by Cetin et al. (2009)

$$\ln(\varepsilon_v) = \ln\left(1.879\ln\left[\frac{780.416\ln\left(CSR_{ss,20,1D,1\mathrm{atm}}\right) - N_{1,60,\mathrm{CS}} + 2442.465}{636.613N_{1,60,\mathrm{CS}} + 306.732}\right] + 5.583\right) \pm 0.689 \quad (1)$$

$$\text{Lim}: 5 \le N_{1,60,\mathrm{CS}} \le 40, 0.05 \le \mathrm{CSR}_{ss,20,1D,1\mathrm{atm}} \le 0.60$$

The procedure modifications used to eliminate the limitations are

1. The standard deviation term of ± 0.689 is neglected in order to get the determinate values of settlements. The modified version used in this study is

$$\varepsilon_v = \left(1.879\ln\left[\frac{780.416\ln\left(\mathrm{CSR}_{\mathrm{ss,20,1D,1atm}}\right) - N_{1,60,\mathrm{CS}} + 2442.465}{636.613N_{1,60,\mathrm{CS}} + 306.732}\right] + 5.583\right) \quad (2)$$

2. For the calculation of relative density (D_R), the expression given by Idriss and Boulanger (2006)

$$D_{\mathrm{R}} = \sqrt{\frac{(N_1)_{60}}{46}} \quad (3)$$

3. The expression for settlement given by Cetin et al. (2009) as

$$\ln\left(S_{\mathrm{cal}}\right) = \ln\left(\theta.S_{\mathrm{est}}\right) \pm \sigma_v$$

$$\varepsilon_{\mathrm{v,eq}} = \frac{\sum \varepsilon_{v,i} t_i DF_i}{\sum t_i DF_i}$$

Table 1 presents the sample calculation for Chingmeirong.

$$S_{\mathrm{est}} = \varepsilon_{\mathrm{v,eq}} \sum t_i \quad (4)$$

The results are presented in the form of contours in Fig. 3a for 3 m depth. It shows that the sites near Sanamahi Temple and Kangla palace area settle in the range of 0.65–0.3 m; whereas Manipur University and Tulihal Airport areas are in the range of 0.03–0.06 m. Further Overall settlement of all 114 sites has been estimated, and the settlement contour is shown in Fig. 3b. At Imphal city, the water table's depth varies from 0.5 to 0.79 m from the ground surface, and the settlement varies up to 0.78 m, which is relatively high compared to another place around the city. Therefore, caution should be taken while making a plan for any construction at this place. Chingmeirong, Ema market, Keisampat, and KhumanLampak have moderate settlements varying from 0.2 to 0.5 m. MantriPukhri and PWD areas have settlements varying from 0.05 cm to 0.25 m, which is the least compared to all settlements. So, these places will be safe from the earthquake-induced settlement due to liquefaction. Table 2 shows the comparison with corresponding Liquefaction Potential Index (LPI) and Liquefaction Severity Index (LSI) (Pallav et al., 2012).

5 Conclusions

The procedure used to find earthquake-induced settlement in this study is based on the latest research methods. The method is straightforward and easy to program in a personal

Table 1 Sample calculated data for a site at Chingmeirong

Average depth (m)	Density of soil (KN/m^3)	*N*-value	Total vertical stress (Kpa)	Effective vertical stress (Kpa)	CSR for $m=7.5$, $\sigma'v$	$N_{1,60CS}$ value	CRR for $m=7.5$, $\sigma'v$	FOS@ Liquefaction	Relative density D_R	Individual settlement, meters
1.725	19.23	13	33.17	32.42	0.106	21.2	0.222	2.10	0.68	0.0002
4.725	18.86	2	89.75	59.00	0.152	2.85	0.074	0.49	0.25	0.1651
7.725	18.8	7	146.15	85.40	0.165	7.72	0.103	0.62	0.41	0.0865
9.725	18.9	8	183.95	103.20	0.166	7.92	0.104	0.62	0.41	0.0568
12.225	19	24	231.45	125.70	0.165	21.90	0.232	1.40	0.69	0.0174
13.725	19.1	26	260.10	139.35	0.163	22.76	0.245	1.50	0.70	0.0089
16.725	19.58	25	318.84	168.09	0.157	20.00	0.206	1.31	0.66	0.0245
19.725	19.6	22	377.64	196.89	0.150	16.03	0.165	1.10	0.59	0
22.725	19.58	25	436.38	225.63	0.143	17.23	0.176	1.23	0.61	0
25.725	17	13	487.38	246.63	0.139	7.84	0.104	0.74	0.41	0
28.725	19.7	20	546.48	275.73	0.134	11.89	0.132	0.98	0.51	0
31.725	19.8	23	605.88	305.13	0.130	13.18	0.141	1.09	0.54	0
34.725	19.9	110[a]	665.58	334.83						Total = 0.3594 m

[a] Not considered for further CRR and settlement calculation because of very high SPT-N

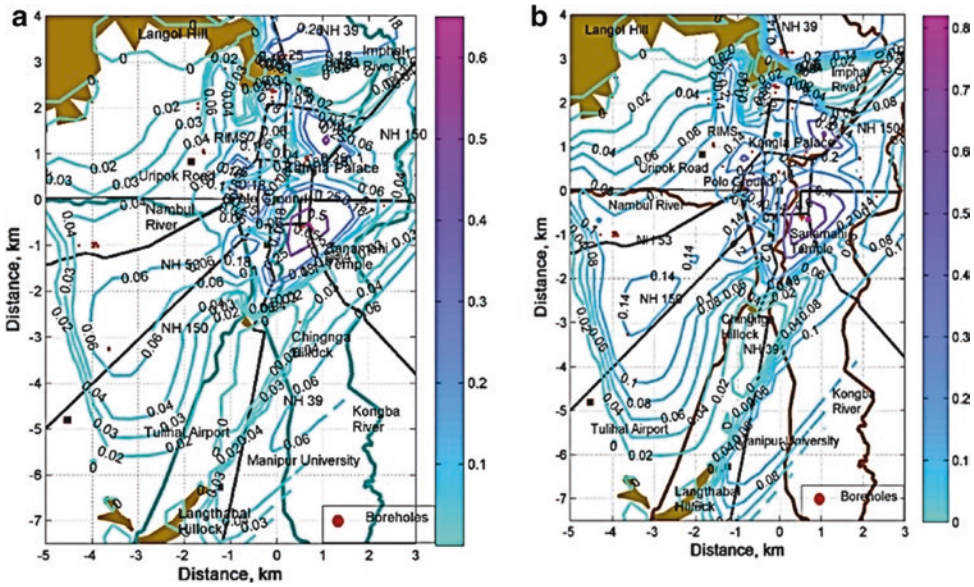

Fig. 3 **a** Imphal city contour map of settlements at 3 m depth due to earthquake-induced liquefaction after the Cachar earthquake, 1869 ($M_W = 7.5$). **b** Imphal city contour map of overall settlements (m) of sites due to earthquake-induced liquefaction after the Cachar earthquake, 1869 ($M_W = 7.5$)

Table 2 Comparison of settlement with LPI and LSI (Pallav et al., 2012)

Places	Settlement (m)	LPI	LSI
Kangla palace	0.4	60	70
RIMS	0.14	30	50
Polo ground	0.3	60	70
Sanamahi Temple	0.2	30	70

computer. This updated approach minimizes the use of charts, Tables, and diagrams. It can be conveniently implemented numerically, and allows the expeditious analysis of multi-layered soil profile. So, in the field, engineers, designers, and town planners can easily find the induced moment due to earthquake-induced settlement. If the induced moment is added while designing the structures, then the structures will be considered safe from the large settlement,

overturning, and excess moments in the members after the earthquake. This will help to prevent the loss of property and human life.

References

Adachi, T., Iwai, S., Yasui, M., Sato, Y. (1990). Settlement and inclination of reinforced concrete buildings in Dagupan City due to liquefaction during the 1990 Philippine earthquake, In *10th World Conf. on Earthquake Engineering, International Association for Earthquake Engineering (IAEE)*, 1992 (pp. 147–152) [Online]. Available: https://www.iitk.ac.in/nicee/wcee/article/10_vol1_147.pdf

Ambraseys, N. (1988). Engineering seismology. *Earthquake Engineering and Structural Dynamics, 17*, 1–105.

Boulanger, R., & Idriss, I. (2014). Cpt and Spt based liquefaction triggering procedures cpt and spt based liquefaction triggering procedures.

Cetin, K. O., Bilge, H. T., Wu, J., Kammerer, A. M., & Seed, R. B. (2009). Probabilistic model for the assessment of cyclically induced reconsolidation (Volumetric) settlements. *J. Geotech. Geoenvironmental Eng.* https://doi.org/10.1061/(ASCE)1090-0241(2009)135:3(387)

Dasgupta, S. et al., (2000). Seismotectonic atlas of India and its environs. *Geologica Survey India Special Publication.*

GMSR-Miscellaneous Publication No. 30, *Geological Survey of India*. http://www.portal.gsi.gov.in/gsiImages/information/map-manipur.gif

Idriss, I. M., & Boulanger, R. W. (2006). Semi-empirical procedures for evaluating liquefaction potential during earthquakes. *Soil Dynamics Earthquake Engneering, 26*(2–4), 115–130. ISSN 0267–7261. https://doi.org/10.1016/j.soildyn.2004.11.023

Idriss, I. M., & Boulanger, R. W. (2015). 2nd Ishihara Lecture: SPT- and CPT-based relationships for the residual shear strength of liquefied soils. *Soil Dynamics and Earthquake Engineering*.

IBC (2009). *International Buiding Code*. IL: International Code Council, INC.

IS. (1893). Criteria for Earthquake resistant design of structures, Part 1: general provisions and buildings. *Bureau. Indian Standards. New Delhi*, 2016.

Ishihara, K., & KOGA, Y. (1981). Case studies of liquefaction in the 1964 Niigata earthquake. *SOILS Found.* https://doi.org/10.3208/sandf1972.21.3_35

Ishihara, K., & Yoshimine, M. (1992). Evaluation of settlements in sand deposits following liquefaction during earthquakes. *Soils and Foundations*. https://doi.org/10.3208/sandf1972.32.173

Laiba, M. (1992). *The Geography of Manipur*. Public Book Store.

Lee, K.L., & A. Albaisa, A. (1974). Earthquake induced settlements in saturated sands. *ASCE Journal Geotechnical Engineering Division*. https://doi.org/10.1016/0148-9062(74)91814-2

Lee, C. J., Wei, Y. C., & Kuo, Y. C. (2012). Boundary effects of a laminar container in centrifuge shaking table tests. *Soil Dynamics and Earthquake Engineering*. https://doi.org/10.1016/j.soildyn.2011.10.011

Nagase, H., & Ishihara, K. (1988). Liquefaction-induced compaction and settlement of sand during earthquakes, *Soils and Foundation*, https://doi.org/10.3208/sandf1972.28.65

Oldham, T. (1869). The Cachar earthquake of January 10th, 1869, by T. Oldham & R. D. Oldham (Eds.), *Memoirs of the Geological Society of India*, (vol. 19, pp. 1–98).Calcutta, India.

Pallav, K., Raghukanth, S. T. G., & Singh, K. D. (2012). Liquefaction hazard scenario of Imphal city for 1869 cachar and a hypothetical earthquake. *Internation Journal Geotechnical Earthquake Engineering*. https://doi.org/10.4018/jgee.2012010103

Shahir, H., & Pak, A. (2010). Estimating liquefaction-induced settlement of shallow foundations by numerical approach. *Computers and Geotechnics*. https://doi.org/10.1016/j.compgeo.2009.10.001

Tatsuoka, F. (1984). Discussion of ‘ Stress ratio effects on shear modulus of dry sands ‘ by Peiji Yu and F. E. Richart, Jr.(Eds.), *Journal. Geotechnical. Engineering.* https://doi.org/10.1061/(asce)0733-9410(1985)111:9(1155)

Tokimatsu, K., & Seed, H. B. (1987). Evaluation of settlements in sands. *Journal Geotech. Geoenvironmental Engineering*. https://doi.org/10.1061/(ASCE)0733-9410(1987)113:8(861)

Youd, T. L., & Hoose, S. N. (1977). Liquefaction susceptibility and geologic setting. In Proc. *6th World Conf on Earthquake Engineering* (pp. 37–42).

Environmentally Benign Recovery of Precious Metals Using In-Situ Leaching

Ali Karrech and Ryan Azadi

Abstract

Recent research has shown that glycine–peroxide can be a viable solution to extract precious metals from deep pristine environments. In this study, we present our recent results of gold leaching using glycine as a key ingredient. We report our data analysis which highlights the potential of ISL as a future alternative to conventional mining methods and estimate the factors that influence it.

Keywords

In-situ leaching · Reactive transport · Lixiviants · Thermodynamics

1 Introduction

ISL consists of injecting lixiviants at depth to dissolve selected minerals in an orebody and transport the valuable species to the surface. The process requires one or several wells that are dedicated to the injection and extraction in a similar manner as oil and gas enhanced recovery. ISL is gaining momentum especially in the uranium industry with a global share of production amounting to 57%. However, the technology has not been yet used to extract precious metals due to the lack of environmentally benign lixiviants. In this study, we propose glycine as a an environmentally friendly lixiviant for ISL, which may open new horizons for ISL in the future.

2 Materials and Methods

Our approach consists of using microfluidic devices to mimic in-situ conditions. Figure 1 depicts the main steps of preparation at the University of Western Australia, which were discussed in detail by the authors (Azadi et al., 2019). Poly-methyl methacrylate (PMMA) plates, purchased from Goodfellow, were used as substrates. Inlet and outlet holes were then drilled in the substrates to inject and extract the lixiviant, respectively. A photoresist (AZ 4562) was applied to define the pattern of the microchannel on the PMMA substrate using UV light and a mask. Plasma (60% O_2 and 5% CF_4) was applied to etch a 12 μm groove in the substrate. A 5 nm layer of Cr followed by a 60 nm layer of gold were applied to the substrate by evaporation. The remaining photoresist was then cleaned up using a developer (AZ 340). Finally, a thin layer of PMM was bound to the substrate using UV-assisted glue.

After the microfluidic device preparation, the fluid was circulated in the microchannel at a constant rate using a syringe pump. While the fluid flowed over the gold nanolayer and eroded it away, a LED light was placed beneath the system to facilitate the monitoring of its thickness. In addition, a microscopic camera (Digitech) was placed over the microchannel to record the transmitted light which was then used to analyse the variation of gold thickness and deduce the gold dissolution kinetic.

Glycine, hydrogen peroxide, and sodium hydroxide, purchased from Sigma-Aldrich, were the key components of the lixiviants. These components were mixed with deionized water using a beaker, a magnetic stirrer, and a hot plate. The solution was agitated until a clear solution was obtained at the desired initial level of pH and temperature.

A. Karrech (✉) · R. Azadi
The University of Western Australia, 35 Stirling Highway, Crawley, WA 6009, Australia
e-mail: ali.karrech@uwa.edu.au

Z. A. Ergüler et al. (eds.), *Selected Studies in Geotechnics, Geo-Informatics and Remote Sensing*, Advances in Science, Technology & Innovation, https://doi.org/10.1007/978-3-031-43759-5_51

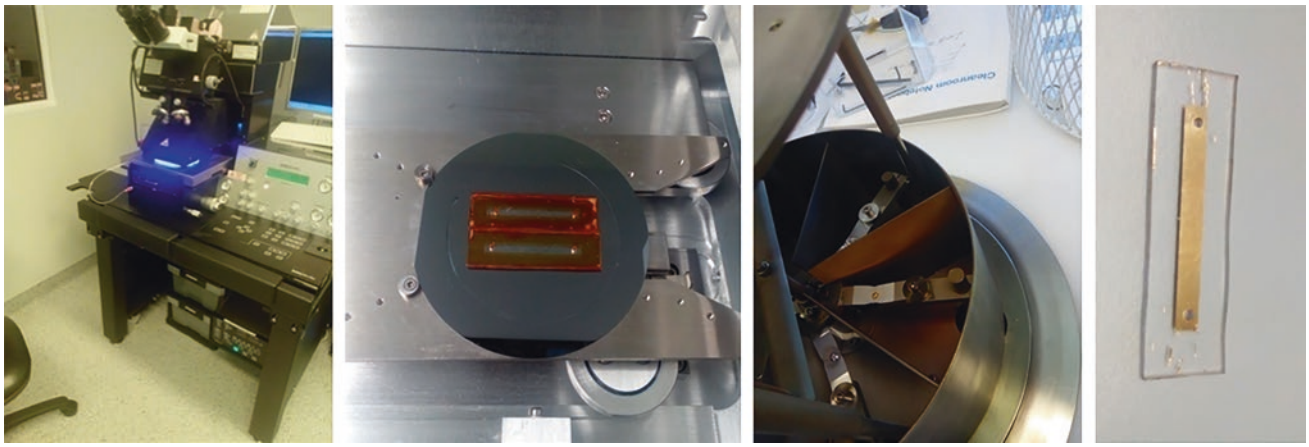

Fig. 1 Essential steps of microchannel preparation

3 Results and Discussion

The tests were performed at a flow rate of 7 mL/h (controlled by the syringe pump) and at a hydrogen peroxide concentration of 0.48 ($\pm$ 0.08)%. The response surface method (RSM) was used to interpret the results of this experimental campaign and establish the effect of the different factors (glycine concentrations, pH, and temperature) and their interactions. Three levels were chosen for glycine concentrations (0.5, 1, and 1.5 M), and two levels were chosen for temperature (60 and 75 ($\pm$ 2) °C) and pH (11 and 12). The specific conditions of gold leaching can be described by coding the independent variables according to the following expression:

$$X_{\mathrm{i}} = \frac{x_{\mathrm{i}} - x_{\mathrm{c}}}{\Delta x} \tag{1}$$

where X_{i} denotes the coded level, x_{i} is the uncoded level, x_{c} is the uncoded value of the central point, and Δx is the interval of change. The leaching results are depicted in Fig. 2, which indicates the variation of thickness with respect to time under various lixiviants concentrations, temperatures, and pH values.

3.1 Regression Model

RSM requires the description of the response with respect to the design factors (or experimental treatments). This arrangement can be resolved by adjusting the data to the following second-order polynomial:

$$Y = \beta_0 + \sum_i \beta_i X_i + \sum_i \beta_{ii} X_i^2 + \sum_{i,j,i\neq j} \beta_{ij} X_i X_j \tag{2}$$

where Y is the response, β_0 is the average of responses, β_i, β_{ii}, and β_{ij} are the response coefficients. The second term represents the linear response, the third indicates the quadratic influence of each factor, and the fourth term denotes the interaction effect. The quantities X_i and X_j represent the coded independent variables. Table 1 shows the etching rates of the gold layer obtained for a selected combination of conditions.

A regression analysis was used to fit the response function to Eq. (2) representing the etching rate. An empirical relationship has been obtained, which describes the response function in terms of coded levels of glycine concentration (G), temperature (T), and pH (P):

$$\begin{aligned}\mathrm{Rate}\left(\frac{\mathrm{nm}}{\mathrm{h}}\right) &= 45.98 + 36.23G + 38.96T \\ &\quad - 0.2P - 8.25G^2 + 34.125GT\end{aligned} \tag{3}$$

The model shows that the etching rate is linear and quadratic with respect to glycine concentration and linear with respect to temperature and pH. The model also shows that there is an interaction between glycine concentration and temperature.

3.2 Analysis of Variance

The analysis of variance (ANOVA) was used to examine the significance of the design factors influencing the gold leaching process. Table 2 summarizes the ANOVA results.

Among the important ANOVA results in Table 2, it is worth discussing the Fisher F-test defined as the ratio of mean square corresponding to the factor over the mean square error. The bigger the value, the more significant the corresponding factor. As such, it can be seen that

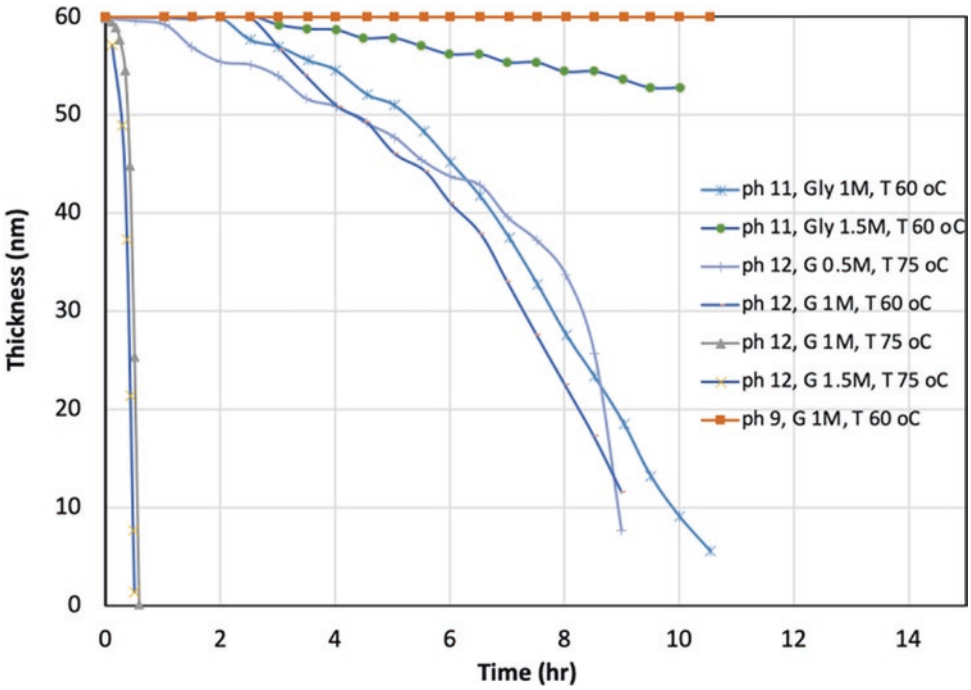

Fig. 2 Time-dependent changes in thickness

Table 1 Specific conditions of gold leaching

Experiment	Factors			Etching rate (nm/h)
	G	*T*	*P*	
Test 1	− 1	1	1	3.00
Test 2	− 1	− 1	− 1	0
Test 3	0	− 1	1	6.81
Test 4	0	1	1	91.02
Test 5	0	− 1	− 1	0.95
Test 6	1	1	1	143.72
Test 7	1	− 1	− 1	4.22

G, *T*, and *GT* are the most significant. Similarly, small *P*-values reflect strong evidence to reject the null hypothesis (the hypothesis that a given variable does not explain the response, which means that the corresponding regression coefficient would vanish to zero). The results in Table 2 indicate that glycine concentration, temperature, and their interaction presented *P*-values of 0.0947, 0.1134, and 0.1005, respectively. This implies that there is less than 11.34% probability that the response is independent of these variables. This is a strong evidence that glycine concentration, temperature, and their interaction influence the etching rate. However, Table 2 cannot confirm that pH influences the etching rate as much.

Table 2 Analysis of variance for the experimental data

Source of variation	Sum of squares	Degree of freedom	Mean square	*F* ratio	*P*-value
G: glycine concentration	10,001	1	10,001	84.71	0.0947
T: temperature	8302.537	1	8302.537	70.32	0.1134
P: pH	0.102	1	0.102	<0.01	0.9812
GG	90.750	1	90.750	0.768	0.5418
GT	4658.062	1	4658.062	39.45	0.1005
Regression	19,987.519	5	3997.503	33.85	0.1297
Residual	118.064	1	118.064		
Total	20,105.583	6	20,105.583		

Note $R^2 = 0.994$; adjusted $R^2 = 0.964$

4 Conclusions

In this study, we discussed the dissolution of gold using a glycine-based solution, which is relevant to the in-situ recovery of precious metals. The obtained results indicated that glycine concentration, temperature, and their interaction have a significant influence on the leaching of gold. Alkalinity (pH level) has exhibited lower influence.

Reference

Azadi, M. R., Karrech, A., Elchalakani, M., & Attar, M. (2019). Microfluidic study of sustainable gold leaching using glycine solution. *Hydrometallurgy, 185*, 186–193.

Potential of Using Dredged Marine Sediments as a Construction Material

Chau Lan Nguyen, Tuan Nghia Do, Hai Ha Nguyen and Viet Thanh Nguyen

Abstract

Dredging sediments is an important solution to maintain navigation in waterways and access to harbors. However, the management of dredged sediments is a worldwide issue. Dumping the sediments at sea is concerned due to its effects on the marine environment. This paper focuses on the utilization of dredged marine sediments for construction material. The dredged marine sediments taken from Hai Phong and Quang Ninh areas were modified by adding quicklime and Portland cement. Geotechnical test of the modified dredged marine sediments was conducted for samples after mixing for 7, 14, and 28 days. In addition, XRD and SEM are also conducted for dredged samples before and after mixing with lime and cement. Test results also indicate that less amount of cement is required to satisfy the construction material requirement than that of using quicklime.

Keywords

Dredging sediments · Portland cement · XRD · SEM

1 Introduction

Annually, there is a huge amount of marine sediments from the marine navigational channel needing to be dredged. Besides that, dredging marine sediments also has to be treated carefully. It is an important process to ensure environmental protection requirements and ecosystem balance at the dumpsite. In Vietnam, a large volume of dredged marine clay is accumulated (about 4.5 billion m^3) every year. Traditionally, cement, lime, and fly ash have been widely applied to the solidification of dredged material (Dong et al., 2011; Dubois et al., 2009; Taylor & Wang, 2013). Previous research had used solidified dredged sludge as a road material or an embankment material (Chan & Abdul Jalil, 2014; Rekik & Boutouil, 2009; Taylor & Wang, 2013; Wang et al., 2017).

However, only a small part of the sediment is used to repair constructions in the coastal area. Thus, it can be seen that the ability to improve dredged sediment as fill material is feasible and applicable to seaports in Vietnam, bringing great economical and environmental efficiency.

2 Materials and Methods

The dredged samples were taken from Hai Phong and Quang Ninh port in the northern part of Vietnam. At each port, a large sample of 500 L of the material was collected and transported to the laboratory for testing. Dredged samples were mixed with 150, 200, 250 kg/m^3 of lime, and with 75, 100, 150 kg/m^3 of cement ratios. The mixing process was conducted by mixing auto-machine for 5 min with 5 L capacity and 120 rpm speed.

Physical and mechanical tests were conducted for dredged samples before and after mixing with lime and cement, according to the ASTM standard.

In addition, the natural sample and mixture sample were dried and crushed. After that, solidified samples were grounded into powder and screened through a 200-mesh screener, and dried at 65°. SEM and XRD tests were conducted for samples before and after mixing.

C. L. Nguyen (✉) · H. H. Nguyen · V. T. Nguyen
University of Transport and Communications, 3 Cau Giay, Hanoi, Vietnam
e-mail: nguyenchaulan@utc.edu.vn

T. N. Do
Thuy Loi University, Hanoi, Vietnam

Z. A. Ergüler et al. (eds.), *Selected Studies in Geotechnics, Geo-Informatics and Remote Sensing*, Advances in Science, Technology & Innovation, https://doi.org/10.1007/978-3-031-43759-5_52

Table 1 Physical and geotechnical properties of sediment sample

	Quang Ninh sediment	Hai Phong sediment
Water content		
Mean water content (%)	75	39.7
Specific gravity (or density)		
Specific gravity Gs (t/m^3)	2.56	2.6
Grain size		
Gravel (> 2000 μm) (%)	0.000	0.000
Sand (63–2000 μm) (%)	0.403	6.224
Silt (2–63 μm) (%)	99.594	76.469
Clay (0–2 μm) (%)	14.396	17.303
Fine (0–80 μm) (%)	99.997	96.08
Liquid limit LL (%)	41.6	47.14
Plastic limit PL (%)	25.67	28.02
Unified soil classification system		
Classification	CL	CL

3 Results

3.1 Physical Test Result

See Table 1.

3.2 Unconfined Compression Test Results

The unconfined compression strength of samples are given in Table 2.

3.3 SEM and XRD Results

See Figs. 1 and 2.

The result from the above-mentioned SEM tests is shown in Figs. 3 and 4.

As shown in Figs. 1, 2, 3 and 4 from XRD and SEM tests, the natural sample has high porosity, and mineral

Table 2 Results of UC test for Quang Ninh and Hai Phong sample

Sample no.	Component	Ratio (kg/m^3)	q_u (kPa), 7 days		q_u (kPa), 14 days		q_u (kPa), 28 days	
			Quang Ninh	Hai Phong	Quang Ninh	Hai Phong	Quang Ninh	Hai Phong
1	Cement	75	50.1	37	148.02	105	168.04	123
2		100	92	43	164	109.3	259.10	130
3		150	180.4	50	215	96.63	321.25	170
4	Lime	150	7	22	22	25.2	6.2	27
5		200	22	40	25.2	50	13.2	35
6		250	40	43	50	55	50.5	70

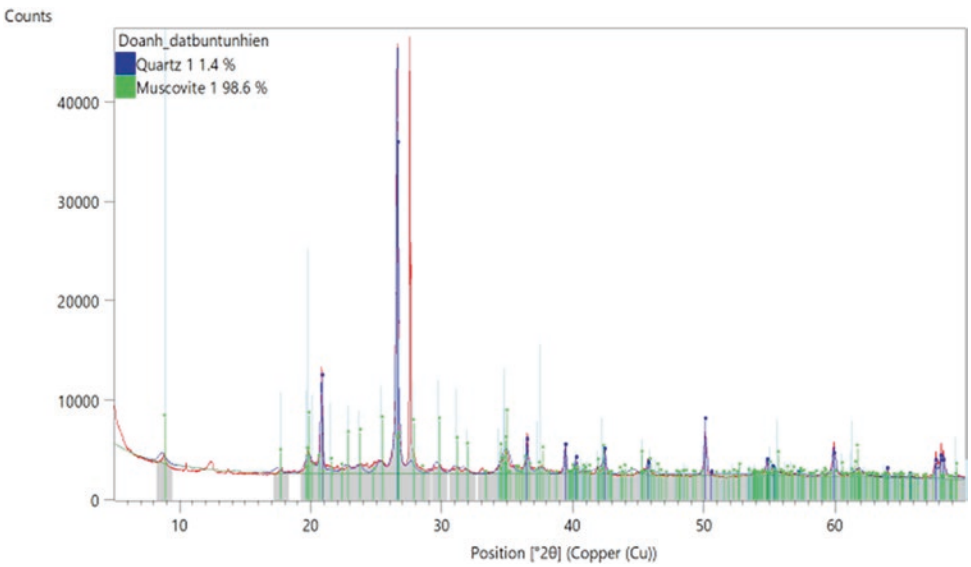

Fig. 1 XRD result for sample natural (Hai Phong)

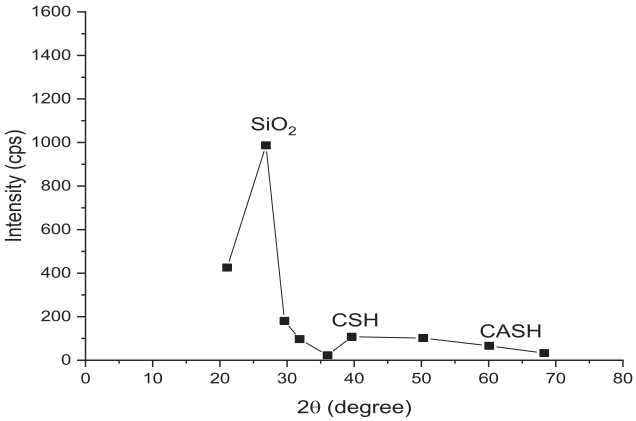

Fig. 2 XRD result for sample mixed with cement with a ratio of 150 kg/m^3, 28 days (Hai Phong)

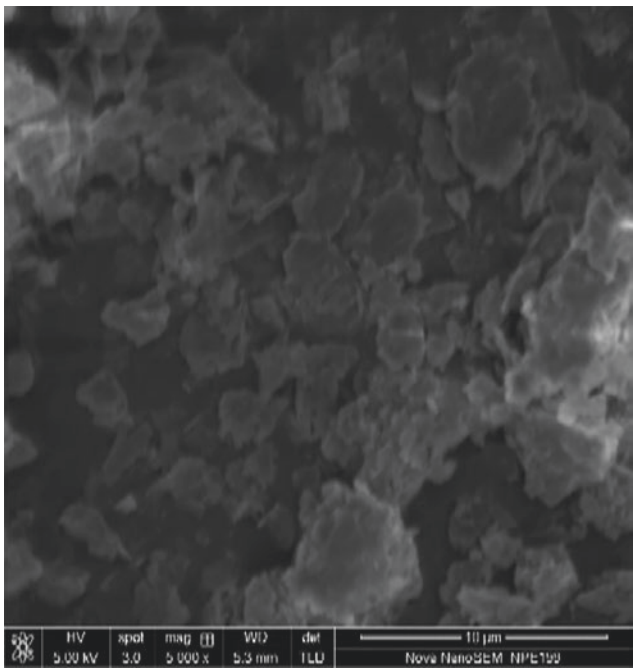

Fig. 3 SEM results for natural sample (Hai Phong)

composition has only SiO_2 and clay particles. Therefore, mixing lime and cement reduces the porosity and appeared hydration products such as calcium silicate hydrate (CSH) and CASH, forming a solid framework that can resist external effects.

Sample mixture with 75 kg/m^3 cement can be used for fill material (> 75 kPa). The results are consistent with other researches (Dubois et al., 2009; Huang et al., 2011, 2017; Kang et al., 2015).

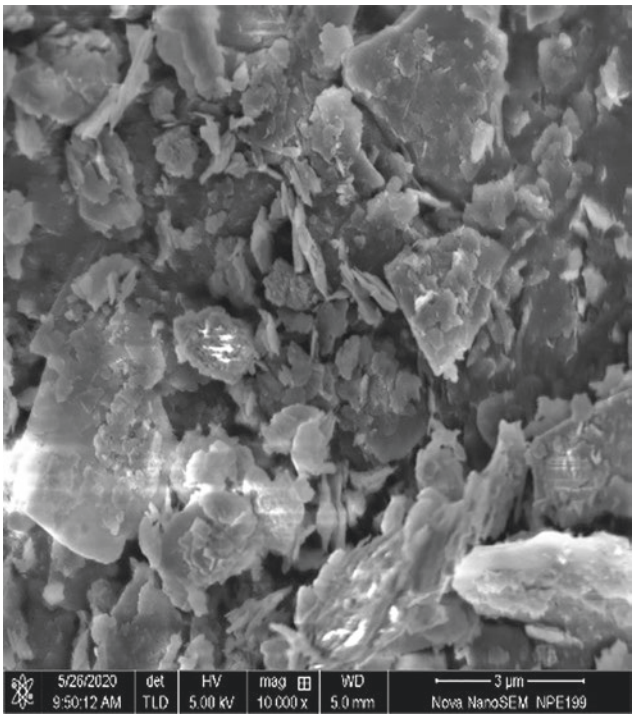

Fig. 4 SEM result for sample mixed with cement with a ratio of 150 kg/m^3, 28 days (Hai Phong)

4 Conclusions

From the experimental results of dredged sediment and dredged sediment mixed with cement and lime, the following conclusions can be drawn:

- Increased compressive strength will increase with increasing lime/cement content.
- The optimal content of 75 kg/m^3 of cement can be used as reinforcement material for marine sediments, which will be used as construction materials.
- SEM and XRD showed that hydration products are the main mechanisms leading to an increase in the strength of dredge material.

References

Chan, C. M., & Abdul Jalil, A. N. (2014). Some insights to the reuse of dredged marine soils by admixing with activated steel slag. *Advances in Civil Engineering, 2014*.

Dong, P. H., Hayano, K., Kikuchi, Y., Takahashi, H., & Morikawa, Y. (2011). Deformation and crushing of particles of cement treat granulate soil. *Soils and Foundations, 51*(4), 611–624.

Dubois, V., Abriak, N. E., Zentar, R., & Ballivy, G. (2009). The use of marine sediments as a pavement base material. *Waste Management, 29*(2), 774–782.

Huang, Y., Zhu, W., Qian, X., Zhang, N., & Zhou, X. (2011). Change of mechanical behavior between solidified and remolded solidified dredged materials. *Engineering Geology, 119*(3–4), 112–119.

Huang, Y., Dong, C., Zhang, C., & Xu, K. (2017). A dredged material solidification treatment for fill soils in East China: A case history. *Marine Georesources & Geotechnology, 35*(6).

Kang, G., Tsuchida, T., & Athapaththu, A. M. R. G. (2015). Strength mobilization of cement-treated dredged clay during the early stages of curing. *Soils and Foundations, 55*(2), 375–392.

Rekik, B., & Boutouil, M. (2009). Geotechnical properties of dredged marine sediments treated at high water/cement ratio. *Geo-Marine Letters, 29*, 171–179.

Taylor, P., & Wang, D. X. (2013). Solidification/stabilization of dredged marine sediments for road construction (pp. 37–41).

Wang, D., Abriak, N. E., & Zentar, R. (2017). Dredged marine sediments used as novel supply of filling materials for road construction. *Marine Georesources & Geotechnology, 35*(4), 472–480.